

# **On the accuracy of high redshift galaxy property estimation**

*Author:*

Paul HASKELL

*Supervised by:*

Dr D.J.B.Smith

Centre for Astrophysics Research  
School of Physics, Astronomy and Mathematics  
University of Hertfordshire

*Submitted to the University of Hertfordshire in partial fulfilment of the requirements of  
the degree of Doctor of Philosophy.*

December 2024

# *Abstract*

Spectral energy distribution (SED) fitting is now a cornerstone of galaxy research, enabling the recovery of properties across a wide range of galaxy configurations and redshifts. With the advent of increasingly powerful facilities able to probe deeper into the Universe, and surveys producing data on millions of galaxies, the need for fast and reliable SED fitting software is growing. Many SED fitting programs are now available using different theoretical models to build SEDs against which observations can be compared, and using different sampling techniques to find the model that best fits the observations. Testing SED fitting is problematic, results for local galaxies can be compared to results derived by other means, but higher redshifts must be tested by comparing different fitters' results or by testing against simulations where the property values are known in advance. We have taken four cosmological zoom-in simulations of dusty star-forming galaxies from the FIRE project and compared the results derived by the fitters MAGPHYS and PROSPECTOR with the true values; we have also investigated possible biases in the results caused by the size of the true values, by the galaxy inclination, by the choice of the star formation history (SFH) model used to create the templates, and by any offset between stellar emission and that from dust. This latter is of particular interest as many fitters rely on an energy balance between the energy absorbed by dust and that emitted by dust in the observer's line-of-sight. Recent works have suggested that energy-balance SED fitting may be of limited use for studying high-redshift galaxies for which the observed ultraviolet and far-infrared emission are offset. It has been proposed that such offsets could lead energy-balance codes to miscalculate the overall energetics, preventing them from recovering such galaxies' true properties.

To investigate this, we test how well the SED fitting code MAGPHYS can recover the stellar mass, star formation rate (SFR), specific SFR, dust mass and luminosity by fitting  $\approx 5900$  synthetic SEDs. Comparing our panchromatic results (using wavelengths  $0.4\text{--}500\ \mu\text{m}$ , and spanning  $1 < z < 8$ ) with fits based on either the starlight ( $\lambda_{\text{eff}} \leq 2.2\ \mu\text{m}$ ) or dust ( $\geq 100\ \mu\text{m}$ ) alone, we highlight the power of considering the full range of multi-wavelength data alongside an energy balance criterion. Overall, we obtain acceptable fits for 83 per cent of the synthetic SEDs, though the success rate falls rapidly beyond  $z \approx 4$ , in part due to the sparser sampling of the priors at earlier times since SFHs must be physically plausible (i.e. shorter than the age of the Universe). We use the ground truth from the simulations to show that when the quality of fit is acceptable, the fidelity of MAGPHYS estimates is independent of the degree of stellar and dust emission offset, with performance very similar to that previously reported for local galaxies.

We then investigate how the recovery of galaxy star formation rates depends on their recent star formation history. We use MAGPHYS and PROSPECTOR on the same simulations and identify a previously unknown systematic error in the MAGPHYS results due to bursty star formation:

the derived SFRs can differ from the truth by as much as 1 dex, at large statistical significance ( $> 5\sigma$ ), depending on the details of their recent SFH. SFRs inferred using PROSPECTOR with nonparametric SFHs do not exhibit this trend. We show that using parametric SFHs (pSFHs) causes SFR uncertainties to be underestimated by a factor of up to  $5\times$ . Although this undoubtedly contributes to the significance of the systematic, it cannot explain the largest biases in the SFRs of the starbursting galaxies, which could be caused by details of the stochastic prior sampling or the burst implementation in the MAGPHYS libraries. We advise against using pSFHs and urge careful consideration of starbursts when SED modelling galaxies where the SFR may have changed significantly over the last  $\sim 100$  Myr, such as recently quenched galaxies or those experiencing a burst. This concern is especially relevant, e.g., when fitting *JWST* observations of very high-redshift galaxies.

Finally, we re-run the PROSPECTOR on the simulations using four different SFH models, finding that PROSPECTOR can achieve successful SED fits at higher redshifts than MAGPHYS, with an overall success rate in excess of 93 per cent. We find three main causes for unsuccessful fits: simulations with zero dust-mass at redshifts where this would be unlikely; galaxies with atypically low stellar to dust mass ratios; PROSPECTOR significantly underestimating the visual attenuation. Where a fit has been successful, the derived properties are of similar accuracy to those successfully fitted by MAGPHYS. We also find that neither the offset between the stellar and dust emission, nor the galaxy inclination appear to bias the result in most cases. Contrary to previous works, we find that the four SFH models - three nonparametric and one parametric - produce similar results when averaged across all of our  $\approx 5900$  simulations. However, we note that the uncertainties are likely underestimated, particularly for the parametric model, and that for individual galaxies, different SFH models can lead to significantly different property recoveries. We re-enforce this finding by analysing the differences between each simulation for each pair of SFH models, revealing mean biases of low statistical significance, but with significant outliers indicating differing property recovery for different models.

# Declaration

I declare that no part of this work is being submitted concurrently for another award of the University or any other awarding body or institution. This thesis contains a substantial body of work that has not previously been submitted successfully for an award of the University or any other awarding body or institution.

The following parts of this submission have been published previously and/or undertaken as part of a previous degree or research programme:

1. Chapter 2: this has been published as Haskell et al., 2023, *Monthly Notices of the Royal Astronomical Society*, **525(1)**, 1535.
2. Chapter 3: this has been published as Haskell et al., 2024, *Monthly Notices of the Royal Astronomical Society Letters*, **530(1)**, L7.

Except where indicated otherwise in the submission, the submission is my own work and has not previously been submitted successfully for any award.

## *Acknowledgements*

I would like to thank my supervisor Professor Dan Smith for his patience, support and guidance over what must have seemed like a very long six years. I would also like to thank Dr Rachel Cochrane and Dr Chris Hayward, both now at the Flatiron Institute, for their support and encouragement over the same period. My colleague Soumyadeep Das has been a brilliant support, providing data and having the time and enthusiasm to perform more runs of PROSPECTOR whenever I needed them. I wish him all the very best for his future career.

Being a part-time student means that you are not really part of a single cohort, but I would like to acknowledge the support of my original class-of-2018, particularly Dr Tracy Garrett who helped me considerably in the early days. More recently Dr Marina Arnaudova and Shravya Shenoy have proved interesting and inspiring colleagues.

Finally, and perhaps most importantly, I would like to thank my family, particularly my wife Fiona who has stood by me as I struggled with different aspects of this work and put up with my exceptional grumpiness when my coding didn't do what I thought it should. Also my children - Tom, Pete and Lucy - for their encouragement and visible delight that their ageing father can still surprise them. And finally, my step-daughter Izzy who has been no less encouraging and who inadvertently set me on the path to starting this PhD in the first place.

# Contents

<b>Abstract</b>	<b>i</b>
<b>Acknowledgements</b>	<b>iv</b>
<b>Contents</b>	<b>v</b>
<b>List of Figures</b>	<b>viii</b>
<b>List of Tables</b>	<b>xviii</b>
<b>List of Abbreviations</b>	<b>xx</b>
<b>1 Introduction</b>	<b>1</b>
1.1 Formation and evolution of galaxies - the Big Bang to the present day . . . . .	1
1.2 Observed morphology, spectroscopy and photometry - our primary tools . . . . .	5
1.3 Classifying galaxies . . . . .	7
1.4 The interstellar medium . . . . .	12
1.4.1 Interstellar gas . . . . .	12
1.4.2 Interstellar dust . . . . .	14
1.5 Measuring individual properties . . . . .	15
1.5.1 Determining luminosity and distance . . . . .	16
1.5.2 Measuring the properties of the stellar population . . . . .	19
1.5.2.1 Determining the SFR . . . . .	19
1.5.2.2 Determining stellar mass . . . . .	22
1.5.3 Measuring the properties of the interstellar dust . . . . .	23
1.6 SED fitting . . . . .	26
1.6.1 A short history of SED fitting . . . . .	26
1.6.2 Modelling . . . . .	27
1.6.3 Fitting and interpreting . . . . .	32
1.6.4 Contemporary SED fitters . . . . .	34
1.6.4.1 Modelling the SFH . . . . .	34
1.6.4.2 Exploring the parameter space . . . . .	37
1.6.5 AI and machine learning technologies . . . . .	38
1.7 Galaxy simulations . . . . .	38
1.7.1 Simulating galaxy formation and evolution . . . . .	39
1.7.2 Radiative transfer . . . . .	42
1.7.3 Simulated Photometry . . . . .	44

1.8	Motivation and structure of this thesis . . . . .	46
<b>2</b>	<b>Energy balance with UV-FIR offsets</b>	<b>50</b>
2.1	Introduction . . . . .	50
2.2	Method . . . . .	54
2.2.1	Computing the SEDs of simulated galaxies . . . . .	54
2.2.2	MAGPHYS . . . . .	57
2.2.3	Processing the data . . . . .	61
2.3	Results . . . . .	63
2.3.1	The fraction of mock observations with acceptable fits . . . . .	63
2.3.2	Overall MAGPHYS performance . . . . .	65
2.3.2.1	The fidelity of MAGPHYS results over time . . . . .	66
2.3.2.2	Searching for systematic trends in the MAGPHYS fit results . . . . .	70
2.3.2.3	The importance of panchromatic data in energy balance fitting . . . . .	71
2.3.3	Measuring the effect of UV/FIR ‘decoupling’ on the fidelity of MAGPHYS results . . . . .	75
2.4	Discussion . . . . .	76
2.4.1	The redshift dependence of the MAGPHYS fit success rate . . . . .	76
2.4.2	The fidelity of MAGPHYS results for dusty, high-redshift galaxies . . . . .	78
2.5	Conclusions . . . . .	80
<b>3</b>	<b>Beware the recent past</b>	<b>83</b>
3.1	Introduction . . . . .	83
3.2	Method . . . . .	85
3.3	Results . . . . .	88
3.4	Discussion . . . . .	91
3.5	Conclusions . . . . .	93
<b>4</b>	<b>The performance of PROSPECTOR when measuring the properties of high-redshift galaxies</b>	<b>94</b>
4.1	Introduction . . . . .	94
4.2	Method . . . . .	96
4.2.1	Data . . . . .	96
4.2.2	PROSPECTOR . . . . .	96
4.2.3	SFH Priors . . . . .	98
4.2.4	Process . . . . .	99
4.3	Results . . . . .	100
4.3.1	Overall fitting performance . . . . .	101
4.3.2	Success in recovering property values . . . . .	102
4.3.3	The impact of the galaxy line-of-sight projection . . . . .	112
4.3.4	Impact of an offset between stellar and dust emission on the recovery of property values . . . . .	113
4.3.5	The impact of true property values . . . . .	115
4.3.6	The significance of scatter . . . . .	122
4.4	Discussion . . . . .	128
4.4.1	Why does PROSPECTOR fail to fit? . . . . .	128
4.4.1.1	Zero dust mass galaxies . . . . .	129
4.4.1.2	Low dust to stellar mass ratio galaxies . . . . .	129

4.4.1.3	Remaining unsatisfactory fits at $z < 2.5$ . . . . .	133
4.4.1.4	Remaining unsatisfactory fits at $z > 4.5$ . . . . .	135
4.4.1.5	Summary of fit failure modes . . . . .	135
4.4.2	The effect of prior choice on the fidelity of the derived properties. . . . .	136
4.4.3	How individual filters contribute to the $\chi^2$ value . . . . .	143
4.5	Summary and Conclusion . . . . .	146
<b>5</b>	<b>Summary and future work</b>	<b>149</b>
5.1	Summary . . . . .	149
5.1.1	MAGPHYS and energy-balance modelling . . . . .	150
5.1.2	Averaging results hides an SED bias in SFR recovery . . . . .	151
5.1.3	Using PROSPECTOR to derive galaxy properties . . . . .	151
5.2	Extrapolating from simulation to reality . . . . .	153
5.3	Future work . . . . .	156
5.4	Trends in SED fitting . . . . .	157
5.5	Concluding remarks . . . . .	158
<b>A</b>	<b>Using spectral energy distribution fitting to create catalogues of galaxy properties</b>	<b>159</b>
A.1	Introduction . . . . .	159
A.2	Method . . . . .	160
A.3	Contribution to science . . . . .	167
	<b>Bibliography</b>	<b>167</b>

# List of Figures

1.1	The history of the Universe according to the $\Lambda$ CDM theory. The initial Big Bang leads to an expansion and cooling of the baryonic matter which falls into the gravitational wells created by dark matter to form the stars and galaxies we see today. Image from <a href="https://science.nasa.gov/universe/overview">https://science.nasa.gov/universe/overview</a> .	4
1.2	Important factors in the formation and evolution of galaxies. The left-hand column contains the cosmological theories necessary to provide the environment for galaxy formation, the central column shows the processes that drive baryonic matter to form galaxies, and the right-hand column shows the observables providing the evidence to support or refute our theories. Image adapted from Cimatti et al. (2020). . . . .	4
1.3	The Hubble classification “tuning fork”. Elliptical galaxies, E0-E7, are shown with increasing ellipticity up to S0 a lenticular galaxy displaying characteristics of both ellipticals and spirals. Spiral galaxies are depicted Sa-Sc depending on the tightness of the spiral arms and spirals with a central bar as SBa-SBc. Irregulars on the far right are those which do not fit into the other categories. Image adapted from Hubble (1936) at <a href="http://www.physast.uga.edu">http://www.physast.uga.edu</a> . . . . .	8
1.4	Colour magnitude diagram for a subset of SDSS galaxies used in the ALFALFA survey (Giovanelli et al., 2005). The $M_r$ magnitude is plotted on the $x$ -axis against the $g - i$ colour on the $y$ -axis. The red line is drawn at $g - i = 0.0571(M_r + 24) + 1.25$ , the blue line is drawn parallel with an offset of 0.15 Mag. The plot shows the bi-modality of galaxy types with older, redder galaxies above the red line, and younger star-forming galaxies below the blue line. The green valley shows galaxies transitioning from star-forming to quenched, or <i>vice versa</i> . Image reproduced from Papastergis et al. (2013). . . . .	11
1.5	Example BPT diagram taken from Trouille et al. (2011). This plot of $\log([\text{NII}]/\text{H}\alpha)$ vs. $\log([\text{OIII}]/\text{H}\beta)$ for a subset of the SDSS galaxies, shows galaxies classified as star-forming in blue and AGN in red with composite galaxies shown in grey. The dashed curve shows the Kauffmann et al. (2003b) empirical division between star-forming galaxies and AGNs, the dotted curve shows the theoretical division proposed by Kewley et al. (2001). . . . .	11
1.6	The correlation between SFR and stellar mass for present day star-forming galaxies ( $0.04 < z < 0.1$ ) taken from the Great Observatories Origins Deep Survey (GOODS; Elbaz et al., 2007). The solid black line marks the track of equation 1.2 with $Y=1$ and $\kappa \approx 0.8$ , the dashed lines mark the 16th and 84th percentiles of the distribution. Star-forming galaxies are observed to lie close to the black line, while starburst galaxies, depicted by black circles, are positioned above the line reflecting their elevated SFR. Conversely, quiescent galaxies are found below the black line, signifying a lack of significant star formation activity. Figure reproduced from Cimatti et al. (2020) . . . . .	12

1.7	The evolution of the galaxy main sequence (MS) with redshift. The coloured lines show the track of the galaxy main sequence at the redshifts shown in the legend. this clearly shows how the MS evolves with redshift, the normalisation increasing with $z$ . The shaded coloured areas show a scatter of 0.2 dex. Image reproduced from Olsen (2015), data from Speagle et al. (2014) . . . . .	13
1.8	An SED produced using the fitting software MAGPHYS (da Cunha et al., 2008) as part of the work for Haskell et al. (2023). In the upper panel, the blue line shows the best-fit SED with the points marking the observed fluxes with associated error bars and the green squares marking the best-fit template fluxes at the observed wavelengths. The red line shows the MAGPHYS-derived intrinsic SED i.e. the luminosity density before processing by the ISM, the blue line shows the observed luminosity density. The lower panel shows the residuals for each observation - a measure of how closely the best-fit SED was to the observed wavelengths. This galaxy is part of the ELAIS-N1 field of the LOFAR Two Metre Sky Survey (LoTSS Shimwell et al., 2017) with the identifier shown in the title. . . . .	16
1.9	Plot demonstrating how three of the emission lines used for SFR estimation are affected by redshift. . . . .	21
1.10	Plots showing the different attenuation curves discussed in the text. The lines are coded as indicated in the legend. Image reproduced from SPARTAN (Thomas et al., 2020). . . . .	25
1.11	Flowchart depicting the step involved in creating SED templates. The initial stellar population synthesis stage builds the intrinsic spectrum of the galaxy by calculating the spectra of multiple simple stellar populations as the galaxy evolves. Once this stage is complete, the spectrum is adjusted to account for processing by the ISM - dust extinction and increased metallicity - and the effects of nebular emission. . . . .	29
1.12	Comparison of five IMF. The x-axis represents stellar mass in $M_{\odot}$ , and the y-axis indicates the number of stars per unit mass interval. Lines are colour-coded as indicated in the legend. Image reproduced from Colman and Teyssier (2019). . . . .	30
1.13	Examples of the different choices for non-parametric SFHs and the SFR behaviour they can produce. In each panel the blue shaded area shows the prior PDF for the SFH prior shown above the panel. The black solid lines mark the median value, the dashed and dotted lines the $1\sigma$ and $2\sigma$ values respectively; red lines show the results of five individual draws from the distribution. Figure reproduced from Leja et al. (2019) . . . . .	37
1.14	A view of a simulated cosmic web 300 million light years across as modeled by IllustrisTNG with dark matter shown in blue, galaxies in gold and circumgalactic gas in white. Image reproduced from science.org . . . . .	40
1.15	A flowchart of the steps and data structures involved in a SKIRT simulation. The simulation phases are shown in blue; the steps corresponding to these phases and their order of execution are shown in green; the major data structures are in purple. Image reproduced from Verstocken et al. (2017). . . . .	43
1.16	This figure shows the complexities of combining data from real galaxy observations compared to that for simulations. The upper panel shows images of a simulated galaxy, the lower images of a real galaxy . . . . .	47

- 2.1 An example SED obtained using MAGPHYS, demonstrating the generally close agreement between the true and MAGPHYS-derived SEDs. In the upper panel, the solid black line shows the best-fit MAGPHYS-derived SED, while the dashed black line indicates the MAGPHYS estimate of the unattenuated SED; the solid blue line represents the attenuated SED generated by SKIRT. The square markers represent the best-fit photometry, with the SKIRT photometry shown as the points with error bars (as described in the legend). The coloured lines above the lower horizontal axis show the normalised filter curves used in this study. The lower panel shows the residual value in  $\sigma$  units between each observation and the best-fit SED. The residual value is calculated as (observed flux - model flux)/observed error. This SED corresponds to simulated galaxy A1, snapshot 276, view 0,  $z = 1.00$ . . . . . 57
- 2.2 The properties of the simulated galaxies in their observational context. **Upper left:** the relationship between the simulated galaxies' SFRs and the galaxy main sequence (MS); for each snapshot, the y-axis shows the difference between the simulation SFR and the MS, with the magenta band indicating the typical  $\pm 0.3$  dex scatter associated with the MS (e.g. Tacchella et al., 2022a). **Upper right:** the relationship between the sub-mm flux density  $S_{870}$  and dust mass; the blue points represent the simulated data, while the orange points show galaxies from D20. **Lower left:** the variation in  $A_V$  as a function of redshift for the simulations (for which the median value at each  $z$  is shown by the solid line, within shading indicating values enclosed by the 16th and 84th percentiles of the distribution), along with a corresponding distribution from D20 (shown in purple). The SMG sample from Hainline et al. (2011) is shown by the red points. **Lower right:** the mean UV/FIR peak to peak (blue) and light-weighted mean (red) spatial offsets in redshift bins: the shading indicates the region enclosed by the 16th and 84th percentiles at each redshift, while the solid line indicates the median value. The red, green and black circles are values for individual sources taken from the literature (as indicated in the legend), while the solid green line marks the reported average spatial offset across 20 SMGs from Lang et al. (2019). . . . 58
- 2.3 Visualisations of two views of galaxy A1, in the later stages of its evolution, showing differing degrees of UV–FIR offsets ranging from kpc-scale projected separation (left) to approximately co-spatial (right). In each panel, the image in blue shows the UV emission, the side colourbars showing the flux density of the emission in MJy/sr. The coloured contours show flux density for the FIR emission, ranging from green ( $3 \times 10^4$  MJy/sr), to orange ( $5 \times 10^4$  MJy/sr) to black ( $10^5$  MJy/sr). In each panel, the base of the red vector is positioned at the peak FIR emission and the head at the peak UV emission, the base of the black vector is positioned at the light-weighted mean FIR emission and the head at the light-weighted mean UV emission. The title of each plot gives the galaxy name along with redshift, best-fit  $\chi^2$  and Spearman  $\rho$  value. . . . . 60

- 2.4 MAGPHYS produces statistically acceptable fits for virtually all snapshots at  $z < 5$ , irrespective of viewing angle. The best-fit  $\chi^2$  as a function of Universe age is shown for galaxy A1, colour-coded by view number. The  $\chi^2$  values have been averaged over bin widths of  $\Delta z = 0.2$  (relative to the top horizontal axis) for clarity. The horizontal line indicates the  $\chi^2$  threshold below which a fit is deemed acceptable using the Smith et al. (2012) criterion, this value varies with redshift (see Table 2.2). The dashed line indicates the number of stellar models (relative to the right-hand y-axis) available to MAGPHYS at a given redshift with which to compare the input SED. Although not shown here, qualitatively similar results are obtained for the other simulations (A2, A4 & A8). . . . . 65
- 2.5 MAGPHYS success rate in fitting SEDs. The percentage of successful fits averaged across all views and snapshots of all galaxies as a function of redshift, note that standard Poisson errors are too small to be visible. The horizontal line marks a success rate of 50 per cent. The fraction of fits that are statistically acceptable decreases with increasing redshift due to the constraint that the SFH must be shorter than the age of the Universe at that redshift, meaning that the size of the template library decreases with increasing redshift. . . . . 66
- 2.6 The overall MAGPHYS parameter estimation (red) compared with the true values from the simulation (black); MAGPHYS captures the overall true properties as a function of redshift. The columns refer to galaxies A1, A2, A4 and A8, respectively. In each row, the upper plot presents the evolution against Universe age (upper  $x$ -axis) and redshift (lower  $x$ -axis), and the lower plot shows the residuals on the same  $x$ -axes (note that the range for  $\Delta L_{\text{dust}}$  is smaller than that for other properties). The top row presents the evolution of stellar mass, while the four subsequent rows present the corresponding evolution of SFR, sSFR,  $M_{\text{dust}}$  and  $L_{\text{dust}}$  respectively. In each main panel, the black line indicates the true values, the red line plots the mean across all views of the median recovered value, and the shaded area indicates the region enclosed by the typical error bar on each parameter (i.e. the mean difference between the 16th/84th percentile and the median, for the upper and lower bounds, respectively). In the final row, the black and red lines in the upper plot show the true and recovered values of  $A_V$  for the different views, while the lower plot shows the residuals for each view. 67
- 2.7 The fidelity of MAGPHYS' recovery of  $M_{\text{star}}$  and SFR is remarkably consistent across the full range of true galaxy properties. The top five panels plot the relationship between the  $M_{\text{star}}$  residual and true value of the properties  $M_{\text{star}}$ , SFR, sSFR,  $M_{\text{dust}}$ , and  $L_{\text{dust}}$  respectively. The data points in black represent the median value for the residual in log-spaced bins; bin occupancy is shown by the background grey bar chart with log values read from the right-hand axis - note that bins with occupancy  $\leq 20$  have been removed for clarity. In each case the coloured band shows the median 16th and 84th percentile limits for the residuals within the bin and the bounded grey region shows the median 16th and 84th percentile limits for the scatter within the bin. The short coloured line on left-hand of each plot shows the average for the plotted value, residual values are read from the left-hand axis. The lower five panels show the same for the SFR residual. . . . . 72

- 2.8 Similar to figure 2.7, but showing the remarkably consistent recovery of sSFR and  $M_{\text{dust}}$  as a function of the true galaxy properties. The top five panels plot the relationship between the sSFR residual and true value of the properties  $M_{\text{star}}$ , SFR, sSFR,  $M_{\text{dust}}$ , and  $L_{\text{dust}}$  respectively. The data points in black represent the median value for the residual in log-spaced bins; bin occupancy is shown by the background grey bar chart with log values read from the right-hand axis - note that bins with occupancy  $\leq 20$  have been removed for clarity. In each case the coloured band shows the median 16th and 84th percentile limits for the residuals within the bin and the bounded grey region shows the median 16th and 84th percentile limits for the scatter within the bin. The short coloured line on left-hand of each plot shows the average for the plotted value, residual values are read from the left-hand axis. The lower five panels show the same for the  $M_{\text{dust}}$  residual. . . . . 73
- 2.9 Similar to figure 2.7, but showing the remarkably consistent recovery of  $L_{\text{dust}}$ . The five panels plot the relationship between the  $L_{\text{dust}}$  residual and true value of the properties  $M_{\text{star}}$ , SFR, sSFR,  $M_{\text{dust}}$ , and  $L_{\text{dust}}$  respectively. The data points in black represent the median value for the residual in log-spaced bins; bin occupancy is shown by the background grey bar chart with log values read from the right-hand axis - note that bins with occupancy  $\leq 20$  have been removed for clarity. In each case the coloured band shows the median 16th and 84th percentile limits for the residuals within the bin and the bounded grey region shows the median 16th and 84th percentile limits for the scatter within the bin. The short coloured line on left-hand of each plot shows the average for the plotted value, residual values are read from the left hand axis. . . . . 74
- 2.10 Using MAGPHYS to model panchromatic data gives better overall constraints on galaxy properties than sampling only a subset of the available wavelengths.  $\Delta \log(\text{parameter})$  for each parameter of interest, averaged across all galaxies for three different MAGPHYS runs: (i) including all available photometry, (ii) stellar only - including only those bands that sample the starlight ( $0.4\mu\text{m} < \lambda_{\text{eff}} < 2.2\mu\text{m}$ ), and (iii) FIR only - including only the FIR data ( $100\mu\text{m} < \lambda_{\text{eff}} < 500\mu\text{m}$ ), with each set of results colour-coded as in the legend. The error bars on each data point represent the mean uncertainty for each MAGPHYS estimate, based on using the 16th and 84th percentiles of the estimated PDFs. . . . . 76
- 2.11 The fidelity of MAGPHYS is largely independent of the extent of any UV/FIR offset, as measured by the three proxies, once the uncertainties are considered.  $\Delta \log(\text{parameter})$  as a function of three proxies for the difference between the UV and FIR images - panel (a) presents the data for  $M_{\text{star}}$ , (b) for SFR, (c) for sSFR, (d) for  $M_{\text{dust}}$  and (e) for  $L_{\text{dust}}$ . For each property, the data points represent the mean over all views and snapshots in that bin. The shaded area of the same colour indicates area enclosed by the mean 16th and 84th percentile values within the bin. The grey shaded area shows area enclosed by the 16th and 84th percentile values for the scatter within each bin. The top plot in each panel shows the logarithmic difference  $\Delta$ , as a function of the peak-to-peak distance between the UV and FIR images; the second and third panels show the corresponding  $\log \Delta$  as a function of the light-weighted mean UV-FIR offset and the Spearman rank correlation coefficient  $\rho$  between the 20 per cent brightest pixels in either the UV or FIR images. The short coloured lines adjacent to the left-hand y-axis represent the overall mean value. The grey histograms in each panel (a) to (e) show the bin occupancy relative to the right-hand axis. . . . . 77

- 2.12 The best-fit  $\chi^2$  depends on the size of the MAGPHYS library, which varies with the redshift assumed for the fit. This plot shows the ratio of best-fit  $\chi^2$  obtained for run A (at the native redshift) to that obtained in run B (where all SEDs were fixed to  $z = 2$ ). For galaxies on the left-hand side of this plot the prior gets larger in run B, while for galaxies viewed at later times, the opposite effect is apparent. 78
- 3.1 The recent SFHs (past 200 Myr) of three example simulated galaxies, showing a range of  $\eta$  values. The dark grey band encloses the previous 10 Myr, while the lighter band encloses the past 100 Myr;  $\eta$  is the ratio of the SFRs averaged over those two time periods. The black line shows an example of constant star formation with  $\eta \approx 0$ , while the red line shows a ‘temporarily quenched’ case ( $\eta = -0.64$ ). The blue line shows an example simulated galaxy observed during a burst, where the star formation activity averaged over the previous 10 Myr has increased compared to the average over the previous 100 Myr (giving  $\eta = 0.88$ ). 86
- 3.2 The LH panel shows the difference between the inferred and true SFRs averaged over the last 100 Myr,  $\Delta \log_{10} \psi = \log_{10}(\psi_{\text{inferred}}) - \log_{10}(\psi_{\text{true}})$ , as a function of the burst indicator  $\eta \equiv \log_{10}(\bar{\psi}_{10\text{Myr}}/\bar{\psi}_{100\text{Myr}})$ . The centre and RH panels show the same obtained using PROSPECTOR with the pSFH and bursty continuity SFH prior. In all panels the red line shows the mean residual averaged over 100 data points with the red shaded area enclosing the averaged 16th and 84th percentile residuals from the PDF. The grey shaded area indicates the 16th and 84th percentiles of the scatter in  $\Delta \log_{10} \psi$  within each averaged point, and the blue markers show values for individual SEDs. The MAGPHYS SFRs exhibit a systematic bias: the SFR tends to be underestimated for ‘temp-quenched’ galaxies and overestimated for galaxies that have experienced a burst within the past 10 Myr. . . . . 90
- 3.3 The distributions of  $\eta$  values for 50,000 SFHs in the MAGPHYS high- $z$  libraries (in blue), overlaid with the ground truth values from the simulations (hatched) and for the PROSPECTOR bursty continuity prior in red. Note the significantly larger  $\eta$  range relative to Figure 3.2. . . . . 92
- 4.1 Percentage of successful fits by redshift averaged over bins of width  $\Delta z = 0.1$ . The lines plot the percentage of simulated SEDs successfully fitted by PROSPECTOR and MAGPHYS for each of the different SFH priors in colours defined in the legend, shaded areas in the same colour enclose the binomial standard deviation within each bin calculated using the Python package `astropy.stats`. The black horizontal line marks the 50 per cent success level for reference; the background bar chart shows the bin occupancy read from the right-hand y-axis. . . . 103
- 4.2 PROSPECTOR best-fit  $\chi^2$  values by redshift for the simulated galaxies identified in the upper left of each panel. The best-fit  $\chi^2$  values are averaged over bins of width  $\Delta z = 0.1$  and plotted for each of the PROSPECTOR SFH priors along with those for MAGPHYS - colour coded as in the central legend. The horizontal black lines in each panel define the  $\chi^2$  value below which a fit is deemed successful (see Section 4.2.4). . . . . 104

4.3	Visual depiction of the residuals and uncertainties returned by PROSPECTOR. Each row presents the data for a specific property (see $y$ -axis labels), the first four columns showing the data averaged across a specific galaxy (see $x$ -axis labels) at all redshifts, and the final column that averaged over all galaxies. The plots are colour coded to the prior as shown in the legend, with MAGPHYS added for reference. Each point plots the average of the median residual delivered by the relevant fitter/prior with the value read from the $y$ -axis, the error bars are the 16th and 84th residual percentiles of the differences similarly averaged. . . . .	105
4.4	Evolution of properties over time for galaxy A1. The evolution of the true and derived values for each of the five properties is presented, each pair of rows showing a different property as labelled on the $y$ -axis, and each column a different fitter/prior as shown by the column title. For the first four pairs of rows, the large panel's grey-shaded area encloses the 16th and 84th percentiles of the derived value averaged over the seven views within each snapshot; the true value is shown in green. The smaller panels plot the residual of the derived value again enclosing the 16th and 84th percentiles of the snapshot's seven views; the black line marks $\Delta \log(\text{property}) = 0$ . The final pair of rows show the results for $A_V$ , here all seven views are plotted independently as overlapping grey areas. . . . .	106
4.5	Evolution of properties over time for galaxy A2 - see Figure 4.4 for details. . . . .	107
4.6	Evolution of properties over time for galaxy A4 - see Figure 4.4 for details. . . . .	108
4.7	Evolution of properties over time for galaxy A8 - see Figure 4.4 for details. . . . .	109
4.8	Average median residuals by view. Each panel shows the residual plots for the property labelled on the $y$ -axis. The bars are grouped by view (see $x$ -axis labels) and show the mean of the 50th percentile of the residuals averaged across all galaxies and snapshots. The bars are colour coded as per the legend. The black error bars show the 16th and 84th percentiles of the residual similarly averaged. . . . .	114
4.9	The variability of the stellar mass residual with the stellar and dust emission offset. Each panel shows how the residual of PROSPECTOR's recovery of stellar mass varies against the proxies defined in the text for the offset between UV and FIR emitting regions. Each prior is shown in a different panel (see panel caption), in each panel the stellar mass recovery is plotted against the simple peak-to-peak proxy in the upper plot, the light-weighted mean proxy in the centre plot, and the Spearman rank correlation coefficient $\rho$ in the lower plot. The coloured line marks the median of the difference between the true and recovered values averaged over each bin; the coloured region marks the 16th and 84th percentiles of this difference similarly averaged and the grey-shaded area the 16th and 84th percentiles of the scatter within each bin. The short coloured lines adjacent to the left-hand $y$ -axis mark the mean value of the difference across all galaxies and snapshots for which a satisfactory fit was achieved; the background bar chart shows the bin occupancy read from the right-hand $y$ -axis. . . . .	116
4.10	The variability of the SFR residual with the stellar and dust emission offset - see 4.9 for details. . . . .	117
4.11	The variability of the sSFR residual with the stellar and dust emission offset - see Figure 4.9 for details. . . . .	118
4.12	The variability of the dust luminosity residual with the stellar and dust emission offset - see Figure 4.9 for details. . . . .	119
4.13	The variability of the $A_V$ residual with the stellar and dust emission offset - see Figure 4.9 for details. . . . .	120

4.14	The variation in the stellar mass median residual value against the range of true stellar mass values available from the simulations. Each panel plots the results for the different fitters and SFH priors as shown in the label at the top left. In each panel, the coloured line plots the 50th percentile of the residual averaged over log-spaced bins of the true stellar mass values. The shaded area of the same colour shows the 16th and 84th residual percentiles similarly averaged, the grey-shaded area encloses the 16th and 84th percentiles of the scatter within each bin. The background bar chart shows the bin occupancy read from the right-hand y-axis. . . . .	123
4.15	Plots of the variation in the SFR median recovery as a function of the range of SFR true values - see Figure 4.14 for details. . . . .	124
4.16	Plots of the variation in the sSFR median recovery as a function of the range of sSFR true values - see Figure 4.14 for details. . . . .	125
4.17	Plots of the variation in the dust luminosity recovery as a function of the range of dust luminosity true values - see Figure 4.14 for details. . . . .	126
4.18	Plots of the variation in the $A_V$ median recovery as a function of the range of $A_V$ true values - see Figure 4.14 for details. . . . .	127
4.19	The relationship between $A_V$ and the 10 Myr averaged SFR. The upper panel plots the true value of $A_V$ against the true 10 Myr average SFR; the background points are the data, the blue line shows the trend with the data averaged over equal log-spaced bins. The lower panel plots the recovery of $A_V$ for the Bursty SFH prior against the 10 Myr averaged SFR; the background points are the data, the blue line shows the trend in recovery accuracy averaged over equal log-spaced bins with the coloured area enclosing the 16th and 84th percentiles of the recovered accuracy similarly averaged. . . . .	128
4.20	PROSPECTOR generated SED of a snapshot with zero true dust mass. . . . .	130
4.21	PROSPECTOR generated SED of a snapshot at $z = 1.14$ showing the alignment between the true and derived unattenuated SEDs. . . . .	130
4.22	The percentage of PROSPECTOR failed fits against the dust to stellar mass ratio across all snapshots of all galaxies. The $x$ -axis shows the dust to stellar mass ratio, the blue bars present the number of successful fits achieved using the Bursty SFH prior, read from the left-hand $y$ -axis, in equal log-spaced bins; the red bars show the number of unsuccessful fits. The blue line plots the percentage of failed fits read from the right-hand $y$ -axis. . . . .	131
4.23	Plots of the dust to stellar mass ratio against redshift for each of the four galaxies. Black points mark successful fits, red points unsuccessful fits, note that failed fits due to zero dust mass have been removed. The horizontal line marks a mass ratio of $6 \times 10^{-5}$ for reference; the shaded area encloses $2.5 < z < 4.5$ within which there are no failed fits. . . . .	132
4.24	Bar chart showing the proportion of failed fits for each view for MAGPHYS and PROSPECTOR using the Bursty prior, with Poisson errors. . . . .	132
4.25	PROSPECTOR generated SED of galaxy A1 at $z = 1.56$ , which was successfully fitted ( $\chi^2 = 23.8$ ) using the Bursty SFH prior, showing the underestimation of the intrinsic FIR leading to the underestimation of the IR emission in the derived SED. . . . .	134
4.26	SEDs of two views of the same galaxy snapshot - galaxy A8, snapshot 249 at $z = 1.2$ . The left-hand panel shows view 0 to which PROSPECTOR was unable to fit an SED, the right-hand panel shows view 4 which PROSPECTOR was successful in fitting. . . . .	134

- 4.27 Plot of the difference between the true value of  $A_V$  and that derived by PROSPECTOR for all galaxies, successful fits are shown in blue, failed fits are shown in red; the vertical line marks  $z = 2.5$ , the upper end of the range for failed fits likely caused by  $A_V$  underestimation. Note that failed fits due to zero dust mass or low dust to stellar mass ratio have been removed. . . . . 135
- 4.28 Z-score distributions of stellar mass for all pairs of priors, the z-scores were determined by taking the difference between the residuals (i.e. the difference in the logs of the median values) and dividing by the sum of the errors in quadrature. Each panel presents the results of comparing the accuracy of all observations (i.e. all views, all snapshots, all galaxies), the x-axis is labelled with the two priors compared in each panel (Cont=Continuity, Burs=Bursty, Diri=Dirichlet, para=PROSPECTOR parametric and MAGP=MAGPHYS), the dotted vertical line marks the sample mean which, together with the standard deviation, is shown in the legend. The standard normal distribution ( $\mu = 0 \sigma = 1$ ) is shown in green for reference with the zero point marked by the vertical green line. . . . . 138
- 4.29 Plots showing the distribution of z-scores for SFR values, see Figure 4.28 for details. . . . . 139
- 4.30 Plots showing the distribution of z-scores for sSFR values, see Figure 4.28 for details. . . . . 140
- 4.31 Plots showing the distribution of z-scores for  $L_{\text{dust}}$  values, see Figure 4.28 for details. . . . . 141
- 4.32 Plots showing the distribution of z-scores for  $A_V$  values, see Figure 4.28 for details. . . . . 142
- 4.33 The mean  $\chi^2$  values for each filter produced for galaxy A1 by the four PROSPECTOR SFH priors. The grey-shaded area encloses the 16th and 84th percentiles within the Bursty prior filter  $\chi^2$ . . . . . 144
- 4.34 The rest wavelength coverage of the filters used for this work, together with the  $\chi^2$  values for the MIPS24, PACS100, PACS160, and SPIRE250 filters, delivered by the PROSPECTOR Bursty SFH prior. The named filters are colour coded as shown in the legend and their  $\chi^2$  values read from the LH y-axis, the other filters are shown in grey. The horizontal lines mark the rest frame wavelengths covered by each filter (read from the RH y-axis) over the redshift range provided by the simulations with the four named filters colour coded as shown in the legend. . . . . 145
- 4.35 The mean  $\chi^2$  values for each filter produced for galaxy A1 by the Bursty non-parametric SFH prior and MAGPHYS. The grey-shaded area encloses the 16th and 84th percentiles within the Bursty prior filter  $\chi^2$ , the red area that for MAGPHYS. . . . . 145
- 4.36 The rest wavelength coverage of the filters used for this work, together with the  $\chi^2$  values for the *ugrizy* filters, delivered by MAGPHYS, colour coded as shown in the legend and read from the LH y-axis; the  $\chi^2$  values for the other filters are shown in grey. The horizontal lines mark the rest frame wavelengths covered by each filter (read from the RH y-axis) over the redshift range provided by the simulations with the *ugrizy* filters colour coded as shown in the legend. . . . . 146
- A.1 The program stack for processing the deepfield observations. Usual flowchart notation applies; the boxes coloured green are FORTRAN or Python programs written specifically for this project, boxes coloured orange are the MAGPHYS processing suite. The numbers in brackets are referred to in the text. . . . . 161

- A.2 Examples of the plots produced by MAGPY. The main plot in the upper panel is an SED produced by MAGPHYS the key to the symbols is shown in the legend. The lower part of this panel shows the residuals -  $\log_{10}(\text{model value}) - \log_{10}(\text{observed value})$  - of the observations in  $\sigma$  units for each filter. The lower panel shows the probability density functions (PDFs) of 16 of the galaxy properties returned by MAGPHYS, the blue lines mark the median. These plots are for galaxy ILTJ103253.60+582642.9 in the Lockman Hole field. . . . . 165

# List of Tables

1.1	Comparative overview of the models used in popular SED fitting tools. The column headings present the model type, and EB indicates whether energy balance is assumed. Within the columns: Mult. means the user can choose the model, Own means the fitter uses the authors' own model, Nest.sam. is nested sampling, Exp.dec. is exponentially declining (the $\tau$ model), FSPS is Flexible Stellar Population Synthesis (Conroy and Gunn, 2010b), BC03 is Bruzual and Charlot (2003), C03 is Chabrier (2003), CF00 is Charlot and Fall (2000), C07 is Capak et al. (2007), DL07 is Draine and Li (2007) and D14 is Dale et al. (2014). Some data reproduced from Pacifici et al. 2023. <sup>1</sup> Note that MAGPHYS uses delayed $\tau$ with additional starbursts. . . . .	35
1.2	Some of the hydrodynamic galaxy simulators currently available. The first column lists the name of the simulation; the second indicates the numerical method used to model gas dynamics with the relevant simulation code in brackets, these are described in the text; the third column presents the simulated volume, typically expressed as the side length of the cubic simulation box, for zoom-in simulations which focus on individual galaxies or galaxy groups at high resolution, only a limited number of objects are simulated in detail rather than an entire cosmological volume; the final column describes the primary focus of each simulation. . . . .	39
2.1	The filters used to create synthetic observations from the simulated photometry. The first column gives the telescope/survey, the second the instrument/filter name, and the third the effective wavelength of the filter. . . . .	59
2.2	The number of filters available and the value of $\chi^2_{\max}$ for different redshift ranges.	64
2.3	Mean residuals – $\Delta \log(\text{parameter})$ , as defined in Equation 2.3 – for each property for each galaxy and the average across all galaxies; a negative value indicates an underestimate. The quoted uncertainties indicate the typical uncertainty that MAGPHYS derives on that galaxy parameter (equal to half the difference between the 16th and 84th percentiles of the derived PDF). . . . .	68
3.1	SED fit success rate and typical SFR estimate fidelity, $\Delta \log_{10}(\psi)$ , for the MAGPHYS and PROSPECTOR fits to our synthetic observations. For the four sets of PROSPECTOR fits, the different SFH priors are indicated. . . . .	89
4.1	Input parameters for FSPS relevant to this work and their priors. Column 2 describes each variable, column 3 shows the value or range and distribution of the priors. (Table adapted from Das et al. 2024.) . . . . .	97

4.2	The percentage of simulations for which PROSPECTOR and MAGPHYS were able to find a satisfactory fit. The total number of simulation SEDs available for each galaxy is shown in column 2, the percentage success rate for each galaxy achieved by PROSPECTOR using four different SFH priors is shown in columns 3 to 6, MAGPHYS results are shown in column 7 for reference. Errors are $1\sigma$ binomial errors calculated using the Python package <code>astropy.stats</code> (see footnote), all percentages are rounded to one decimal place. . . . .	102
4.3	The average median residuals for each galaxy, property and SFH prior. Each entry shows the mean of the 50th percentile of the given property as recovered by the SFH prior shown in the column headings. The uncertainties are the 16th and 84th percentiles calculated from the true value and the appropriate percentile taken from the recovered PDF. The entries are colour coded black for $\leq 3\sigma$ result and red for $> 3\sigma$ result. . . . .	110
4.4	The different fitting failure modes for PROSPECTOR. The first column shows the galaxies, the second the total number of observations of that galaxy and the third the number of unsuccessful fits. The subsequent columns show the number of unsuccessful fits in each category, these are defined and discussed in the text. . . . .	129
A.1	Telescopes, instruments and filters used for the deep fields catalogues. MAGPHYS filter sets were built for each of the three survey fields using the instruments shown. Details were taken from private communications or the SVO Filter Profile Service - <a href="http://svo2.cab.inta-csic.es/svo/theory/fps3/index.php">http://svo2.cab.inta-csic.es/svo/theory/fps3/index.php</a> . . . . .	162
A.2	Columns in the LOFAR Deepfields catalogues. The 8 values associated with the property <code>fmu_sfh</code> are repeated for each property marked * . . . . .	166
A.3	Details of the six published catalogues. The first column lists the survey field, the second the method of galaxy selection, the third the number of galaxies in the catalogue, and the fourth the percentage of galaxies to which MAGPHYS was able to satisfactorily fit an SED. . . . .	166

# List of Abbreviations

<b>2dFGRS</b>	<b>Two-degree Field Rhift Survey</b>
<b>AGB</b>	<b>Asymptotic Giant Branch</b>
<b>AGN</b>	<b>Active Galactic Nucleus</b>
<b>AI</b>	<b>Artificial Intelligence</b>
<b>ALFALFA</b>	<b>Arecibo Legacy Fast - Arecibo L-band Feed Array</b>
<b>ALMA</b>	<b>Atacama Large Millimetre Aarray</b>
<b>AMR</b>	<b>Adaptive Mesh Refinement</b>
<b>BC</b>	<b>Birth Cloud</b>
<b>BPT</b>	<b>Baldwin Phillips Terlevich</b>
<b>CDM</b>	<b>Cold Dark Matter</b>
<b>CMB</b>	<b>Cosmic Microwave Background</b>
<b>CMD</b>	<b>Colour Magnitude Diagram</b>
<b>COBE</b>	<b>COsmic Background Explorer</b>
<b>DoF</b>	<b>Degrees of Freedom</b>
<b>EELG</b>	<b>Extreme Emission Line Galaxy</b>
<b>ELAIS</b>	<b>European Large Area ISO Survey</b>
<b>EW</b>	<b>Equivalent Width</b>
<b>FIR</b>	<b>Far InfraRed</b>
<b>FIRE</b>	<b>Feedback In Realistic Environments</b>
<b>FSPS</b>	<b>Flexible Stellar Population Synthesis</b>
<b>FUV</b>	<b>Far UltraViolet</b>
<b>GALEX</b>	<b>Galaxy Explorer</b>
<b>GOODS</b>	<b>Great Observatories Origins Deep Survey</b>
<b>ICM</b>	<b>Intra-Cluster Medium</b>
<b>IGM</b>	<b>Inter-Gallactic Medium</b>

---

<b>IMF</b>	<b>I</b> nitial <b>M</b> ass <b>F</b> unction
<b>ISM</b>	<b>I</b> nter- <b>S</b> tellar <b>M</b> edium
<b>IR</b>	<b>I</b> nfra <b>R</b> ed
<b>IUE</b>	<b>I</b> nternational <b>U</b> ltraviolet <b>E</b> xplorer
<b>JWST</b>	<b>J</b> ames <b>W</b> ebb <b>S</b> pace <b>T</b> elescope
<b>KINGFISH</b>	<b>K</b> ey <b>I</b> nsights on <b>N</b> earby <b>G</b> alaxies: a <b>F</b> ar <b>I</b> nfrared <b>S</b> urvey with <b>H</b> erschel
<b>LAMOST</b>	<b>L</b> arge <b>S</b> ky <b>A</b> rea <b>M</b> ulti- <b>O</b> bject <b>F</b> ibre <b>S</b> pectroscopic <b>T</b> elescope
<b>LINER</b>	<b>L</b> ow- <b>I</b> onisation <b>N</b> uclear <b>E</b> mission-line <b>R</b> egion
<b>LMC</b>	<b>L</b> arge <b>M</b> agellanic <b>C</b> loud
<b>LOFAR</b>	<b>L</b> Ow <b>F</b> requency <b>A</b> Rray
<b>LoTSS</b>	<b>L</b> OFAR <b>T</b> wo-metre <b>S</b> ky <b>S</b> urvey
<b>M/L</b>	<b>M</b> ass to <b>L</b> ight
<b>MCMC</b>	<b>M</b> arkov <b>C</b> hain <b>M</b> onte <b>C</b> arlo
<b>MIR</b>	<b>M</b> id <b>I</b> nfra <b>R</b> ed
<b>MS</b>	<b>M</b> ain <b>S</b> equence
<b>NIR</b>	<b>N</b> ear <b>I</b> nfra <b>R</b> ed
<b>PAH</b>	<b>P</b> olycyclic <b>A</b> romatic <b>H</b> ydrocarbons
<b>PDF</b>	<b>P</b> robability <b>D</b> istribution <b>F</b> unction
<b>PSF</b>	<b>P</b> oint <b>S</b> pread <b>F</b> unction
<b>pSFH</b>	<b>p</b> arametric <b>S</b> tar <b>F</b> ormation <b>H</b> istory
<b>SDSS</b>	<b>S</b> loan <b>D</b> igital <b>S</b> ky <b>S</b> urvey
<b>SED</b>	<b>S</b> pectral <b>E</b> nergy <b>D</b> istribution
<b>SF</b>	<b>S</b> tar <b>F</b> orming
<b>SFH</b>	<b>S</b> tar <b>F</b> ormation <b>H</b> istory
<b>SFR</b>	<b>S</b> tar <b>F</b> ormation <b>R</b> ate
<b>SINGS</b>	<b>S</b> pitzer <b>I</b> nfrared <b>N</b> earby <b>G</b> alaxy <b>S</b> urvey
<b>SKIRT</b>	<b>S</b> tellar <b>K</b> inematics <b>I</b> ncluding <b>R</b> adiative <b>T</b> ransfer
<b>SMC</b>	<b>S</b> mall <b>M</b> agellanic <b>C</b> loud
<b>SMG</b>	<b>S</b> ub- <b>M</b> illimetre <b>G</b> alaxy
<b>SNR</b>	<b>S</b> ignal to <b>N</b> oise <b>R</b> atio
<b>SPH</b>	<b>S</b> moothed <b>P</b> article <b>H</b> ydrodynamics
<b>SPS</b>	<b>S</b> tellar <b>P</b> opulation <b>S</b> ynthesis
<b>sSFR</b>	<b>s</b> pecific <b>S</b> tar <b>F</b> ormation <b>R</b> ate

---

<b>SSP</b>	<b>S</b> imple <b>S</b> tellar <b>P</b> opulation
<b>TIR</b>	<b>T</b> otal <b>I</b> nfra <b>R</b> ed
<b>TP-AGB</b>	<b>T</b> hermally <b>P</b> ulsing- <b>A</b> symptotic <b>G</b> iant <b>B</b> ranch
<b>TMSS</b>	<b>T</b> wo <b>M</b> icron <b>S</b> ky <b>S</b> urvey
<b>UHHPC</b>	<b>U</b> niversity of <b>H</b> ertfordshire <b>H</b> igh <b>P</b> erformance <b>C</b> luster
<b>UKIRT</b>	<b>U</b> nited <b>K</b> ingdom <b>I</b> nfra <b>R</b> ed <b>E</b> xplorer
<b>UV</b>	<b>U</b> ltraviolet
<b>VLA</b>	<b>V</b> ery <b>L</b> arge <b>A</b> rray
<b>WEAVE</b>	<b>W</b> illiam <b>H</b> erschel <b>E</b> nhanced <b>A</b> rea <b>V</b> elocity <b>E</b> xplorer
<b>WHIM</b>	<b>W</b> arm- <b>h</b> ot intergalactic <b>M</b> edium
<b>WMAP</b>	<b>W</b> ilkinson <b>M</b> icrowave <b>A</b> nistropy <b>P</b> robe

# Chapter 1

## Introduction

Despite originating from relatively simple components in the early Universe, galaxies exhibit a broad range of morphologies, sizes, masses, luminosities, compositions, and spectra, reflecting the diverse processes that have shaped their evolution. Understanding these processes and the resulting diversity remains a key focus of astrophysical research.

### 1.1 Formation and evolution of galaxies - the Big Bang to the present day

To study the formation of galaxies and their subsequent evolution, it is necessary to first establish a cosmological framework and then determine how this framework can lead to the creation of luminous objects. The  $\Lambda$  Cold Dark Matter model ( $\Lambda$ CDM) provides such a framework, setting the initial conditions of the Universe such as the expansion rate, baryonic matter fractions, and the properties of cold dark matter (CDM; see review by Bull et al., 2016).

According to the  $\Lambda$ CDM model, the Universe begins as a hot, super-dense point-like singularity which starts to expand - the Big Bang. Then, between  $\approx 10^{-36}$  and  $\approx 10^{-32}$  seconds after the initial expansion, it undergoes a period of exponential expansion, referred to as inflation (Guth, 1981), during which quantum fluctuations are stretched to macroscopic scales, seeding the large-scale structure of the Universe (e.g. Turner, 1999).

Cimatti et al. (2020) describes the early stages of Universal evolution; when the inflationary period completes, the Universe continues to expand and cool, now composed of dark matter,

radiation, and a plasma of electrons and protons. After approximately 400,000 years, the Universe has cooled sufficiently for electrons and protons to combine, forming predominantly neutral hydrogen, this recombination epoch marks a significant transition as the Universe becomes transparent, allowing cosmic microwave background (CMB) photons to travel freely without frequent scattering by electrons.

Concurrently, dark matter begins to cluster in regions of over-density resulting from the initial quantum fluctuations (e.g. Baumann, 2009). This process is thought to lead to the formation of the “cosmic web”, a large-scale structure that serves as the scaffolding for the subsequent formation of galaxies and the observable Universe (e.g. Cautun et al., 2014).

Baryonic matter, formed of  $\approx 75$  per cent neutral hydrogen,  $\approx 25$  per cent helium and traces of lithium (e.g. Fields et al., 2014), falls into the gravitational wells (haloes) formed by dark matter and begins to contract (e.g. Benson, 2010). As the gas compresses, gravity continues to dominate over the increasing gas pressure and temperature, aided by the escape of photons that cool the compressing gas (e.g. Cimatti et al., 2020). This process leads to the formation of the first stars approximately 100 million years after the Big Bang (e.g. Larson and Bromm, 2001). Over the following 100 million years, galaxies start to form within the larger dark matter halos, evolving into disk-like structures where stars continue to form (e.g. Cimatti et al., 2020; Fall and Efstathiou, 1980; Somerville and Davé, 2015). A timeline depicting this early history of the Universe is presented in Figure 1.1.

The subsequent evolution of these early galaxies has been a topic of discussion with two main competing theories - hierarchical growth and monolithic collapse. The hierarchical growth model asserts that galaxies merge over time to form the mature systems observed today (White and Rees, 1978). In contrast, the monolithic collapse model, also known as the ELS model after Eggen et al. (1962), posits that galaxies formed early in the Universe through the rapid collapse of gas clouds, creating massive galaxies in a single, intense period of star formation, and so explaining the early formation of massive elliptical galaxies.

There is evidence supporting both of these theories. “Downsizing” refers to the observed trend that more massive galaxies form stars earlier and at a faster rate than their lower-mass counterparts (e.g. Cowie et al., 1996). As a result, massive galaxies experience quenching of star formation relatively early in cosmic history, whereas smaller galaxies continue to evolve and form stars over extended periods (e.g. Cattaneo et al., 2008). This phenomenon is consistent with the monolithic collapse contention that massive galaxies form rapidly and then become

quiescent. In contrast, within the framework of the hierarchical model, downsizing must be explained through mechanisms such as internal feedback processes or external environmental influences (e.g., Scannapieco et al., 2005).

The  $\Lambda$ CDM cosmological model favours the hierarchical, bottom-up scenario (e.g. Bell et al., 2004; Gawiser, 2006) and this is now the predominant theory for the evolution of massive galaxies (e.g. White and Rees, 1978; Merrifield et al., 2000; Kauffmann and Haehnelt, 2000). Evidence in favour of the hierarchical model has come from several studies. Observations of the CMB, particularly from missions such as the Wilkinson Microwave Anisotropy Probe (WMAP; Bennett et al., 2003) and Planck (Planck Collaboration et al., 2011), show initial density fluctuations that grow over time into the large-scale structures we see today (Spergel et al., 2003; Planck Collaboration et al., 2016), an observation which fits the predictions of the hierarchical model. Additionally, studies of the metallicity gradients among early-type galaxies suggest a more complex formation history than that which monolithic collapse can provide. They note that while some galaxies exhibit gradients consistent with monolithic collapse, the overall distribution indicates that many galaxies likely formed through a hybrid scenario involving mergers and accretion processes (e.g. Ogando et al., 2005). Similarly, Forbes et al. (2005) highlight that the correlation between metallicity gradients and galaxy mass is more consistent with hierarchical formation models. Studies of the colour-magnitude diagrams (see Section 1.3) of elliptical galaxies have revealed that, while some features align with monolithic collapse predictions, the overall complexity of observed structures suggests that multiple formation pathways are at play (e.g. Ikuta, 2007). Kaviraj et al. (2005) also examined the colour-magnitude relation of elliptical galaxies, finding that the presence of young stars in these systems is inconsistent with the monolithic collapse model. This complexity is further emphasized by the work of Lintott et al. (2006), who demonstrated that the evolution of massive elliptical galaxies is dominated by the merging of smaller dark matter haloes, contradicting the simplistic view of monolithic collapse. Their results suggest that these galaxies have undergone significant merging events that introduced younger stars into the population - see also Conselice (2003).

Together, these studies have shown that the hierarchical model is more consistent with observations than monolithic collapse.

Figure 1.2, taken from Cimatti et al. (2020), outlines the main components required to develop theories of galaxy formation and evolution, alongside the observables available to validate these theories.

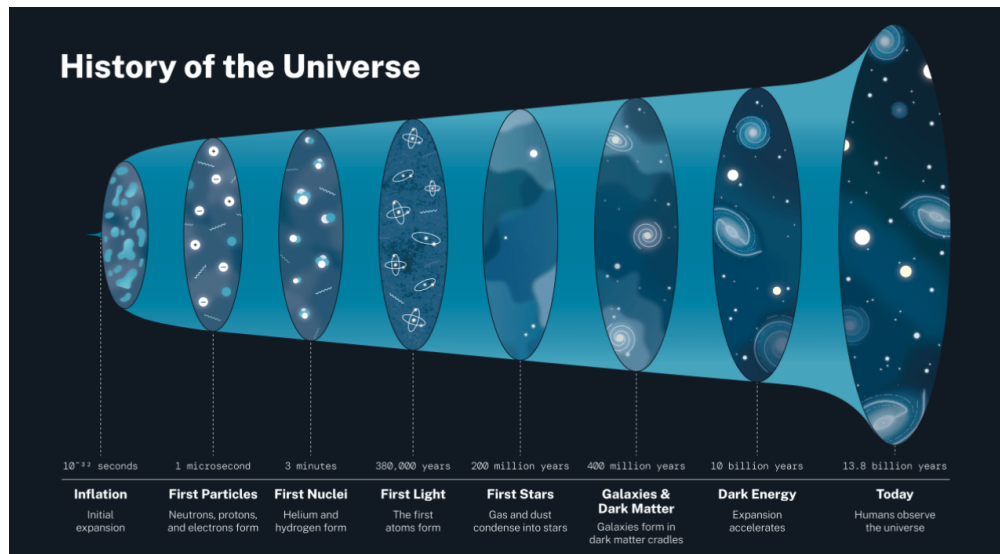


FIGURE 1.1: The history of the Universe according to the  $\Lambda$ CDM theory. The initial Big Bang leads to an expansion and cooling of the baryonic matter which falls into the gravitational wells created by dark matter to form the stars and galaxies we see today. Image from <https://science.nasa.gov/universe/overview>

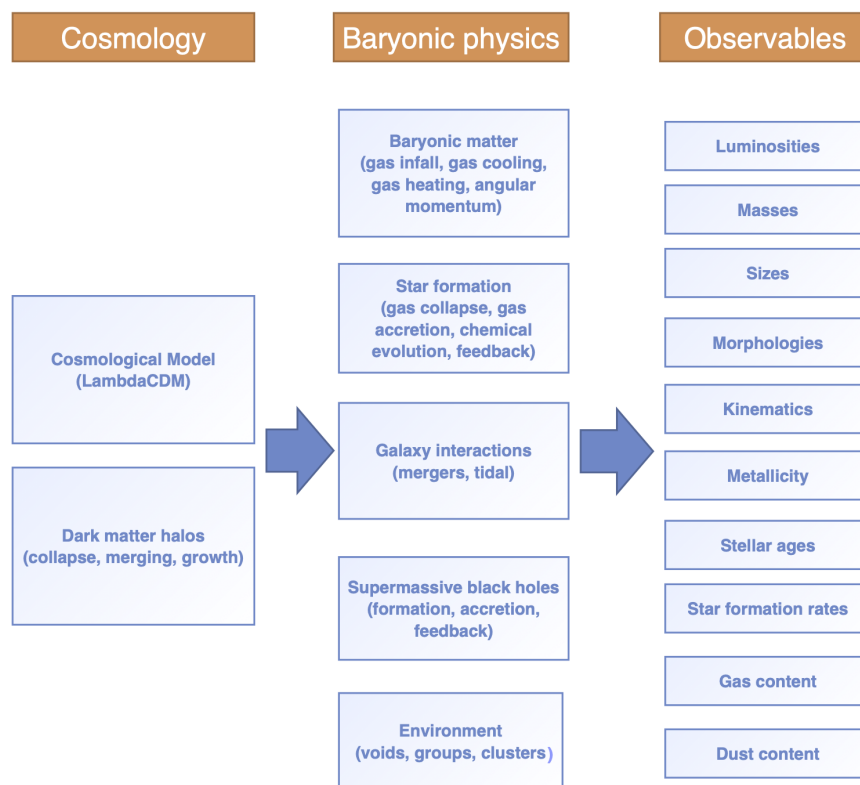


FIGURE 1.2: Important factors in the formation and evolution of galaxies. The left-hand column contains the cosmological theories necessary to provide the environment for galaxy formation, the central column shows the processes that drive baryonic matter to form galaxies, and the right-hand column shows the observables providing the evidence to support or refute our theories. Image adapted from Cimatti et al. (2020).

The continuing expansion of the Universe is central to the  $\Lambda$ CDM model. The initial evidence for this came from Hubble (1929), though it remained contentious with rival theories (e.g. Einstein, 1917; de Sitter, 1917; Hoyle, 1948) proposing static models. However, the development of the Big Bang theory (first proposed by Lemaître, 1927) and the discovery of the CMB (Penzias and Wilson, 1965) provided the evidence needed to support an expanding Universe model. Riess et al. (1998) and Perlmutter et al. (1999) have demonstrated that this expansion is now accelerating after a period of decline; the nature of the “dark energy” that powers this expansion remains an active topic of research.

The expansion of the Universe leads to the phenomenon of redshift whereby light from a distant object is stretched and so received by an observer at a wavelength longer than that at which it was emitted (see Gray and Dunning-Davies, 2008, for a review of the interpretation of redshift). The value of the redshift of an object is calculated by:

$$z = \frac{\lambda_o - \lambda_e}{\lambda_e} = \frac{\lambda_o}{\lambda_e} - 1 \quad (1.1)$$

Where  $\lambda_o$  is the observed wavelength and  $\lambda_e$  is the wavelength at which the light was emitted, the so-called rest wavelength typically derived by laboratory experiment. By determining the redshift, it is possible to estimate the distance to an object, a necessary first step in determining its luminosity. Redshifts are routinely used to calculate galaxy distances, and are frequently used as proxies for both distance and the age of the Universe at the point of observation.

## **1.2 Observed morphology, spectroscopy and photometry - our primary tools**

We can observe the emission from distant galaxies using a number of different observational methods. Most simply, the shape and extent of a galaxy, its morphology, can be observed. This was initially confined to the optical part of the spectrum, where visible light can reveal structural features, such as spiral arms or elliptical shapes, and provide insights into star formation and galaxy morphology (e.g. Cimatti et al., 2020). However, with the development of advanced telescopes observing the morphology of galaxies at different wavelengths can now be performed, including X-ray telescopes such as Chandra (Weisskopf, 2000) and XMM-Newton (de Chambure et al., 1999), ultraviolet (UV) telescopes such as GALEX (Martin et al., 2005) and the International Ultraviolet Explorer (IUE; Gondhalekar, 1981), infrared (IR) telescopes

such as the James Webb Space Telescope (JWST; Gardner, 2009), the Spitzer telescope (Gehrz et al., 2007) and the Herschel space telescope (Pilbratt, 2003), and radio wavelength telescopes such as the Very Large Array (VLA; Selina et al., 2018), the Atacama Large Millimetre Array (ALMA; Tarengi, 2008) and the Low Frequency Array (LOFAR; van Haarlem et al., 2013).

The second observational method is spectroscopy which involves dispersing light from a galaxy into its constituent wavelengths to create and measure a spectrum. This process enables the identification of specific spectral features, such as emission or absorption lines, which correspond to transitions between energy levels in atoms or molecules (e.g. Pavia et al., 2012). Each element or molecule has a spectral fingerprint, enabling the determination a galaxy's chemical composition by analyzing the presence and intensity of these features. In addition to composition, spectroscopy provides key information about the physical conditions within a galaxy, for example, the width and shape of spectral lines can reveal the temperature, density, and velocity of gas in different regions (e.g. Cimatti et al., 2020).

The final method is photometry which measures the flux from a galaxy at different wavelengths. Telescopes use different filters to selectively capture flux measurements at different wavelengths, enabling the observation of a galaxy's light output in a broad range of wavelengths and providing information about its stellar populations, dust content, and star formation rates (SFR) - see Section 1.5. Photometric data are often presented as a Spectral Energy Distribution (SED), which plots luminosity against wavelength, providing a visual representation of a galaxy's energy output across the electromagnetic spectrum (e.g. Cimatti et al., 2020).

Spectroscopy is inherently more time-consuming than photometry, due to the need to extend observing time to compensate for the weakened signal caused by dispersing the incoming light and so longer integration times are required to achieve a sufficient signal-to-noise ratio (SNR) for detailed analysis (e.g. Cimatti et al., 2020). Furthermore, spectroscopic datasets include multi-dimensional data structures that require greater computational resources for storage, reduction, and analysis (e.g. Burger and Gowen, 2011). For surveys employing multi-object spectroscopy where the spectra of numerous objects are captured simultaneously, e.g. the Large Sky Area Multi-Object Fibre Spectroscopic Telescope (LAMOST; Chu and Cui, 1996) and the William Herschel Telescope Enhanced Area Velocity Explorer (WEAVE; Dalton et al., 2012), the complexity escalates further. In these surveys, the extraction of individual spectra from multiple slits or fibres introduces additional challenges, as it requires spatial separation of the objects'

signals and precise corrections for any overlaps or background contamination (e.g. Shimono et al., 2012; Guerra et al., 2016).

### 1.3 Classifying galaxies

Aristotle is often credited with the idea that “before you study something, you must classify it” (Lennox, 2001), and efforts to classify galaxies can be traced back to at least 1802, when William and Caroline Herschel proposed eight subcategories of nebulae (Herschel, 1802). In 1926, Edwin Hubble published a seminal classification system based on optical morphology, defining four categories of galaxies: ellipticals, spirals, barred spirals, and irregulars. This classification, often referred to as the Hubble sequence or the tuning fork diagram, is shown in Figure 1.3 which is adapted from the original image from Hubble (1936). Subsequent categorisation schemes have been proposed by various astronomers, including De Vaucouleurs (1959), Sandage (1961), and Sandage et al. (1975), all of which, like Hubble’s system, are grounded in optical morphology. In the local Universe, such classifications correlate well with specific galactic properties. For example, elliptical galaxies typically contain old, red stars and exhibit little or no star-forming activity, while spiral galaxies generally have old stars in their central bulges but feature young stars and active star formation in their spiral arms (e.g. Cimatti et al., 2020). However, to study the evolution of galaxies we must look back in time beyond the local Universe and observe distant galaxies as they were in the past, here we cannot rely solely on optical morphology for a number of reasons.

Firstly, the nature of galaxies changes over time (e.g. Conselice, 2014) with the familiar Hubble sequence only emerging between redshifts  $1 < z < 2$  (e.g. Kajisawa and Yamada, 2001). Secondly, many galaxies are not visible, or are only faintly visible, at optical wavelengths. The Cosmic Background Explorer satellite (COBE; Kelsall et al., 1998), launched in 1989, revealed that at  $z = 1.5$  star formation rates were twice as high as those inferred from UV/optical observations alone (Dwek et al., 1998; Hauser et al., 1998). This discrepancy is due to stellar energy being absorbed by dust within the interstellar medium (ISM), either in enshrouded galaxies or dusty star-forming regions within observed galaxies (Dwek et al., 1998). Thirdly, at redshifts greater than 1.5, optical wavelengths are shifted into the near-infrared (NIR). Systematic observation of these wavelengths only became feasible from 1979 when the United Kingdom Infrared

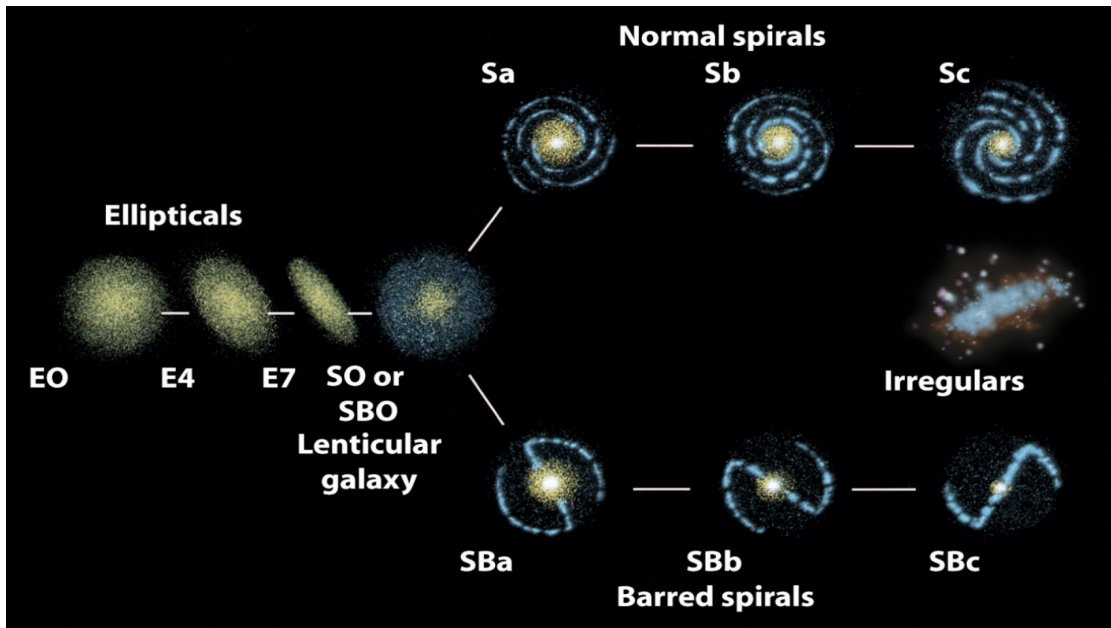


FIGURE 1.3: The Hubble classification “tuning fork”. Elliptical galaxies, E0-E7, are shown with increasing ellipticity up to S0 a lenticular galaxy displaying characteristics of both ellipticals and spirals. Spiral galaxies are depicted Sa-Sc depending on the tightness of the spiral arms and spirals with a central bar as SBa-SBc. Irregulars on the far right are those which do not fit into the other categories. Image adapted from Hubble (1936) at <http://www.physast.uga.edu>.

Telescope (UKIRT) became operational <sup>1</sup>. Finally, a wealth of information is encoded in wavelengths outside the optical range: dust emits in the mid-infrared (MIR) and far-infrared (FIR), new stars emit strongly in the UV, and some galaxies exhibit significant radio emission from active galactic nuclei (AGN), supernovae, and ionised atomic hydrogen (HII) regions (Jansky, 1933; Reber, 1944).

Given the limitations of optical morphology for classifying galaxies, alternative classification methods have been developed. One such method is the photometric colour-magnitude diagram (CMD), which plots galaxy colour against absolute magnitude and can provide information about galaxy types and star formation history (SFH) (e.g. Wyder et al., 2007). Figure 1.4 shows a CMD from Papastergis et al. (2013) for a selection of galaxies from the Sloan Digital Sky Survey (SDSS; York et al., 2000) used in the Arecibo Legacy Fast ALFA (ALFALFA) 21 cm survey (Giovanelli et al., 2005), the diagram plots the  $r$ -band absolute magnitude against the  $g-i$  colour. This plot illustrates the characteristic bi-modality in galaxy colour first identified by Kauffmann et al. (2003b) and later confirmed by Bell et al. (2004) and Baldry et al. (2004). The region above the red line is known as the red sequence, while the region below the blue line is referred to as the blue cloud. The red sequence is predominantly populated by elliptical and lenticular galaxies,

<sup>1</sup>The earliest NIR sky survey was the Two Micron Sky Survey (TMSS), conducted in the late 1960s. However, this was mainly focused on stars within the Milky Way (Neugebauer and Leighton, 1969).

although some spiral, star-forming galaxies may also occupy this region, particularly those with a substantial bulge or significant dust extinction. In contrast, the blue cloud consists primarily of star-forming galaxies (e.g. Cimatti et al., 2020). The area between the red sequence and the blue cloud is termed the green valley, a more sparsely populated region occupied by galaxies in transition between the two states. It is widely accepted that these galaxies are undergoing star formation quenching<sup>2</sup>, moving from the star-forming blue cloud to the quiescent red sequence (e.g. Martin, 2007; Walker et al., 2013; Salim, 2014; Phillipps et al., 2019). The relative scarcity of galaxies in the green valley reflects the short time spent in this transitional phase, typically around 2 Gyr (e.g. Trayford et al., 2016). The precise positions of the red and blue lines defining the two regions are determined empirically, as demonstrated in works such as Bell et al. (2004).

This diagram provides a diagnostic tool for distinguishing between star-forming and quiescent galaxies when these galaxies are unresolved. By effectively separating galaxies based on their star formation activity, it enables the investigation into the evolution of star formation rates over cosmic time. For instance, Gilbank et al. (2008) used the CMD to demonstrate how the distribution of red and blue galaxies changes with redshift, indicating that star-forming galaxies, i.e. those in the blue section of the diagram, were more numerous at higher redshifts.

A second technique for galaxy classification is the Baldwin, Phillips, and Terlevich (BPT) diagram first introduced by Baldwin et al. (1981). The BPT diagram employs spectroscopy to measure the ratios between specific emission lines to differentiate between various ionization sources, effectively separating star-forming galaxies from AGN. In star-forming galaxies, the primary ionisation source is hot OB type stars which ionise hydrogen gas producing  $H_\alpha$  and  $H_\beta$  emission, but only weakly ionise other gases such as oxygen, nitrogen and sulphur; in contrast, AGN produce harder radiation and higher ionisation states in these gases leading to stronger emission lines (e.g. Draine, 2011). The most widely used BPT diagram plots the ratio of  $[NII]\lambda 6583\text{\AA}/H_\alpha$  against  $[OIII]\lambda 5007\text{\AA}/H_\beta$  (e.g. Sánchez et al., 2024). An example of this diagram is illustrated in Figure 1.5, adapted from Trouille et al. (2011), where star-forming galaxies are represented in blue, AGN in red, and composite galaxies in grey. The demarcation line separating SF galaxies from composite galaxies is derived from Kauffmann et al. (2003a), while the boundary distinguishing composite galaxies from AGN is based on Kewley et al. (2001). Other

<sup>2</sup>Quenching refers to the slowing or halting of star formation in galaxies, leading to a transition from star forming to quiescent states. Quenching may be temporary, i.e. star formation will at some point restart, or permanent. It can be driven by various mechanisms, including feedback from AGN, environmental influences such as ram pressure stripping in galaxy clusters, and the exhaustion of available gas for star formation (e.g. Cimatti et al., 2020)

BPT diagrams plot  $[\text{OIII}]\lambda 5007\text{\AA}/\text{H}\beta$  against  $[\text{SII}]\lambda 6716\text{\AA}, 6731\text{\AA}/\text{H}\alpha$  which aids the differentiation of AGN and Low-Ionization Nuclear Emission-line Region galaxies (LINER), and  $[\text{OIII}]\lambda 5007\text{\AA}/\text{H}\beta$  against  $[\text{OI}]\lambda 6300\text{\AA}/\text{H}\alpha$  which can further assist in identifying LINERs (e.g. Draine, 2011). While BPT diagrams are a valuable tool, they have several limitations. Firstly, they are only applicable to galaxies where strong emission lines are present, limiting their use for quiescent galaxies or those with weak emission (e.g. Sánchez et al., 2024). Secondly, the calibration of BPT diagrams is primarily based on local galaxies, and the evolution of ionization conditions and metallicity with redshift can impact the accuracy of these calibrations when applied to high-redshift galaxies (e.g. Brinchmann et al., 2008; Juneau et al., 2014; Coil et al., 2015; Katz et al., 2019; Shapley et al., 2019). Finally, there can be ambiguity between diagrams and problems interpreting the galaxies in the "composite" area (e.g. Ji and Yan, 2020).

The final classification method we examine is the galaxy main sequence (MS) for star-forming galaxies, a relationship between SFR and stellar mass that was first introduced by Noeske et al. (2007a). The MS is commonly expressed as:

$$\log_{10}(\text{SFR}) = Y + \kappa \log_{10}(M_*) \quad (1.2)$$

where the SFR is measured in  $M_{\odot}\text{yr}^{-1}$ ,  $M_*$  is the stellar mass in  $M_{\odot}$ ,  $Y$  is a normalization factor, and  $\kappa$  is the slope, typically in the range  $0.6 \leq \kappa \leq 1.0$ . The MS provides a framework for distinguishing between star-forming and quiescent galaxies, as well as identifying starburst galaxies that show unusually high SFR for their stellar mass. Galaxies on the MS exhibit a characteristic relationship between SFR and stellar mass, allowing consistent classification based on the specific star formation rate (sSFR), defined as the SFR per unit stellar mass,  $s\text{SFR} = \frac{\text{SFR}}{M_{\text{star}}}$  (e.g. Cimatti et al., 2020), which determines whether the star formation activity of a galaxy is typical for its mass. An example of the MS, based on data from the Great Observatories Origins Deep Survey (GOODS; Elbaz et al., 2007), is shown in Figure 1.6. In this diagram, star-forming galaxies lie along or near the MS, while quiescent galaxies fall below the sequence, and starburst galaxies occupy a region above it, indicating elevated star-formation activity. The typical scatter around the MS is approximately  $\pm 0.3$  dex (Speagle et al., 2014; Lindholmer and Pimblet, 2019). Figure 1.7 illustrates how the MS evolves with redshift, primarily in terms of its normalisation, the MS moving upward with increasing redshift, indicating a higher sSFR at earlier cosmic times (e.g. Speagle et al., 2014; Cimatti et al., 2020), and implying that the definition of a star-forming, starburst, and quiescent galaxy changes with redshift.

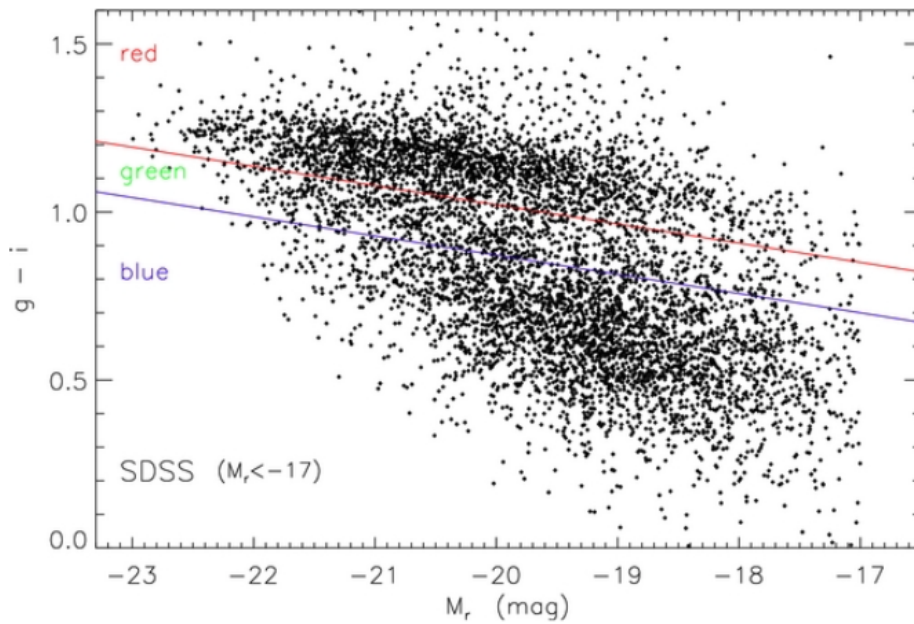


FIGURE 1.4: Colour magnitude diagram for a subset of SDSS galaxies used in the ALFALFA survey (Giovanelli et al., 2005). The  $M_r$  magnitude is plotted on the  $x$ -axis against the  $g - i$  colour on the  $y$ -axis. The red line is drawn at  $g - i = 0.0571(M_r + 24) + 1.25$ , the blue line is drawn parallel with an offset of 0.15 Mag. The plot shows the bi-modality of galaxy types with older, redder galaxies above the red line, and younger star-forming galaxies below the blue line. The green valley shows galaxies transitioning from star-forming to quenched, or *vice versa*. Image reproduced from Papastergis et al. (2013).

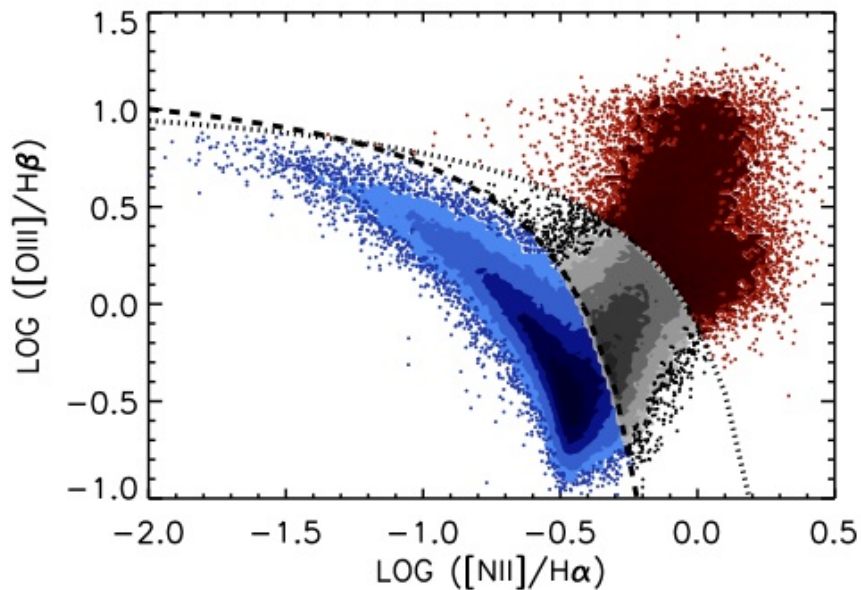


FIGURE 1.5: Example BPT diagram taken from Trouille et al. (2011). This plot of  $\log([\text{NII}]/\text{H}\alpha)$  vs.  $\log([\text{OIII}]/\text{H}\beta)$  for a subset of the SDSS galaxies, shows galaxies classified as star-forming in blue and AGN in red with composite galaxies shown in grey. The dashed curve shows the Kauffmann et al. (2003b) empirical division between star-forming galaxies and AGNs, the dotted curve shows the theoretical division proposed by Kewley et al. (2001).

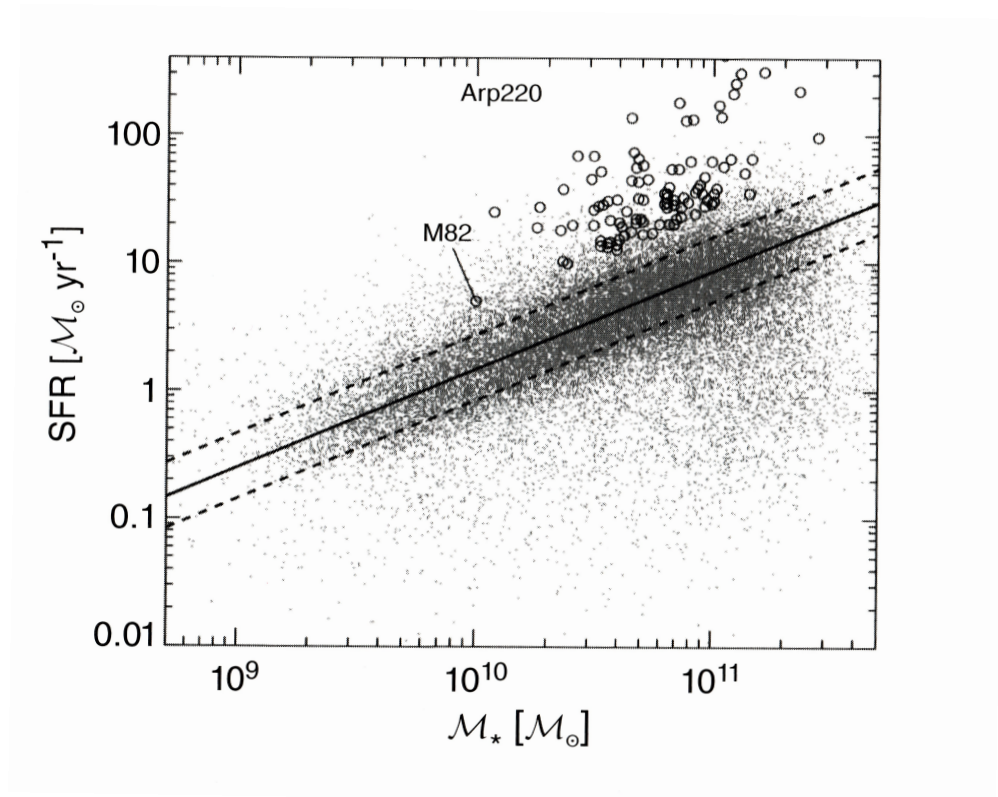


FIGURE 1.6: The correlation between SFR and stellar mass for present day star-forming galaxies ( $0.04 < z < 0.1$ ) taken from the Great Observatories Origins Deep Survey (GOODS; Elbaz et al., 2007). The solid black line marks the track of equation 1.2 with  $Y=1$  and  $\kappa \approx 0.8$ , the dashed lines mark the 16th and 84th percentiles of the distribution. Star-forming galaxies are observed to lie close to the black line, while starburst galaxies, depicted by black circles, are positioned above the line reflecting their elevated SFR. Conversely, quiescent galaxies are found below the black line, signifying a lack of significant star formation activity. Figure reproduced from Cimatti et al. (2020)

## 1.4 The interstellar medium

In this section, we turn our attention to two of the most important constituents of the ISM, gas and dust (Draine, 2011).

### 1.4.1 Interstellar gas

Draine (2011) describes the ISM as being composed primarily of gas with the ratio of gas mass to dust typically quoted as  $\approx 100/1$ , although it varies considerably between and within galaxies. The gas, in the main, is left over from the Big Bang and consists primarily of hydrogen and helium with traces of heavier elements produced by stellar reprocessing. It is present in a number of different forms:

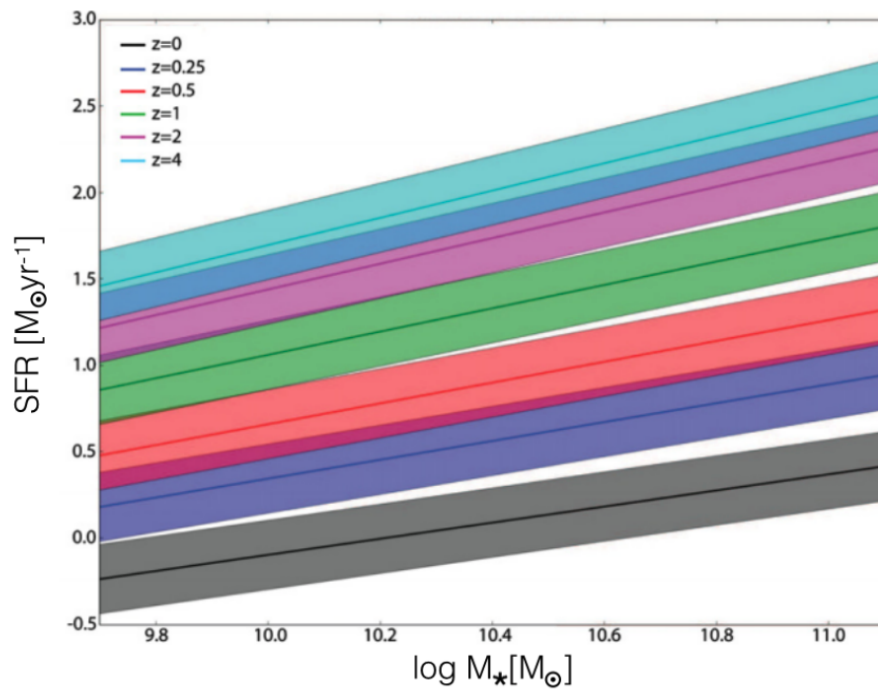


FIGURE 1.7: The evolution of the galaxy main sequence (MS) with redshift. The coloured lines show the track of the galaxy main sequence at the redshifts shown in the legend. This clearly shows how the MS evolves with redshift, the normalisation increasing with  $z$ . The shaded coloured areas show a scatter of 0.2 dex. Image reproduced from Olsen (2015), data from Speagle et al. (2014)

- Coronal gas - this comprises gas heated to  $T \geq 10^{5.5} K$  and collisionally ionised by shock waves from supernovae; it is detected by observing UV and X-ray emission, and nonthermal radio synchrotron emission (Draine, 2011). However, it should be noted that these emissions may also be produced by AGN (e.g. Cimatti et al., 2020);
- HII gas - this is hydrogen photoionised by UV radiation from hot massive type O stars. Clouds of HII (HII regions) can form close to a massive star with dimensions of a few pc and a lifetime of 3-10 Myr; they can also be present as planetary nebulae, created during the latter stages of a star's life when the core becomes exposed. HII may also exist in lower densities in diffuse inter-cloud regions. This gas is detected by optical line emission and thermal radio emission caused by the random motion of charged particles (e.g. Draine, 2011);
- Warm HI - warm atomic hydrogen,  $T \approx 10^4 K$ , typically detected by the 21cm emission line and UV/optical absorption lines (Draine, 2011). The 21cm emission is produced by the hyperfine transition in which the spins of protons and electrons in hydrogen transition

from a parallel alignment to a lower-energy anti-parallel state, resulting in the emission of photons at a wavelength of  $\lambda = 21$  cm (e.g. Sparke and Gallagher, 2007);

- Cool HI - cool atomic hydrogen,  $T \approx 10^3$  K. This can also be detected by the 21cm emission line (e.g. Draine, 2011), though the line will be narrower than that for warm HI;
- Diffuse molecular gas - this comprises molecular hydrogen gas,  $H_2$ , in the centre of molecular clouds. It survives photo-disassociation as a result of the outer layers of the cloud absorbing the UV and protecting the  $H_2$  molecules within - so-called self-shielding (e.g. Draine, 2011). It can be detected in the same way as neutral hydrogen atoms or using the CO 2.6mm emission as a proxy. CO is used as it is commonly found with  $H_2$ , though in significant lower abundances (e.g. Bolatto et al., 2013) but, unlike  $H_2$ , is detectable as it is heteronuclear and therefore has a dipole moment which enables CO to undergo rotational transitions which emit radiation (e.g. Draine, 2011);
- Dense molecular gas - gravitationally bound clouds within which star formation may take place, typically detected using CO or dust FIR emission<sup>3</sup>(e.g. Draine, 2011).

## 1.4.2 Interstellar dust

The second major component of the ISM is dust. Dust comprises particles originating from the winds of massive stars (Hoyle and Wickramasinghe, 1967), novae, and supernovae (e.g. Gehrz, 1989; Michałowski et al., 2010; Ginolfi et al., 2018). These particles undergo continuous evolution within the ISM, where they are fragmented by collisions with gas and other dust particles, and subsequently reconstituted by absorbing molecules from the surrounding gas (e.g. Tielens, 2005).

Dust grains are composed of a number of elements, including carbon, magnesium, silicon, and iron, identified primarily by their under-abundance in the interstellar gas (Draine, 2011). Grain sizes vary considerably, Mathis et al. (1977) investigated the grain size distribution, concluding that  $n(a) \propto a^{-3.5}$  where  $n(a)$  is the number of grains of radius  $a$ . Practically, grains are often categorised as either small or large. Small grains, ranging from 0.3 to 100 nm in radius, include polycyclic aromatic hydrocarbons (PAH: large organic molecules composed of aromatic rings of carbon and hydrogen) and small carbonaceous or silicate grains. Large grains have radii

<sup>3</sup>Note that “dense” refers to  $n_H \approx 10^3 \text{ cm}^{-3}$  which would qualify as a high vacuum in a terrestrial laboratory (Draine (2011))

between 0.01 and 0.25  $\mu\text{m}$  (e.g. da Cunha et al., 2008; Draine, 2011). Dust grains lack well-defined structures, although a minority such as forsterite and enstatite are crystalline and produce sharp spectral features (e.g. Juhász et al., 2010; Draine, 2011).

Dust grains significantly impact galaxy evolution by cooling the interstellar gas (e.g. Natale et al., 2012) and shielding gas clouds from ionizing UV radiation (e.g. Gnedin et al., 2009). Grains of different sizes and compositions affect the ISM and its emission in different ways. PAHs emit in the MIR and play a crucial role in the photoelectric heating of the ISM (e.g. Tielens, 2008). Small silicate or carbonaceous grains absorb UV photons and re-emit in the IR (e.g. Draine, 2003), while large silicate or graphite grains, which are in thermal equilibrium with the surrounding gas and radiation field, absorb and scatter optical and NIR photons, re-emitting in the FIR (e.g. Rawlings et al., 2005; Planck Collaboration et al., 2015).

The effect of dust on the emission from galaxies is referred to as dust extinction and involves two separate processes: scattering and absorption (e.g. Cimatti et al., 2020). Scattering refers to the preferential scattering of UV and blue optical photons away from or into the observer's line-of-sight; absorption is the process of absorbing and re-emitting photons, converting a proportion of the UV/optical stellar energy into IR.

From an observational perspective, dust attenuates and reddens stellar emission, emitting radiation that provides insight into its mass and chemical composition (e.g. Draine, 2011). This effect is demonstrated in Figure 1.8, an SED plotting luminosity density against wavelength, derived using the SED fitting software MAGPHYS (da Cunha et al., 2008), the blue line plots the observed emission from the galaxy while the red line plots the estimated emission before processing by the ISM.

## 1.5 Measuring individual properties

Section 1.6 deals with the recovery of galaxy properties using SED fitting, but first in this section we discuss alternative methods to derive estimates for the values of some of the individual properties of galaxies.

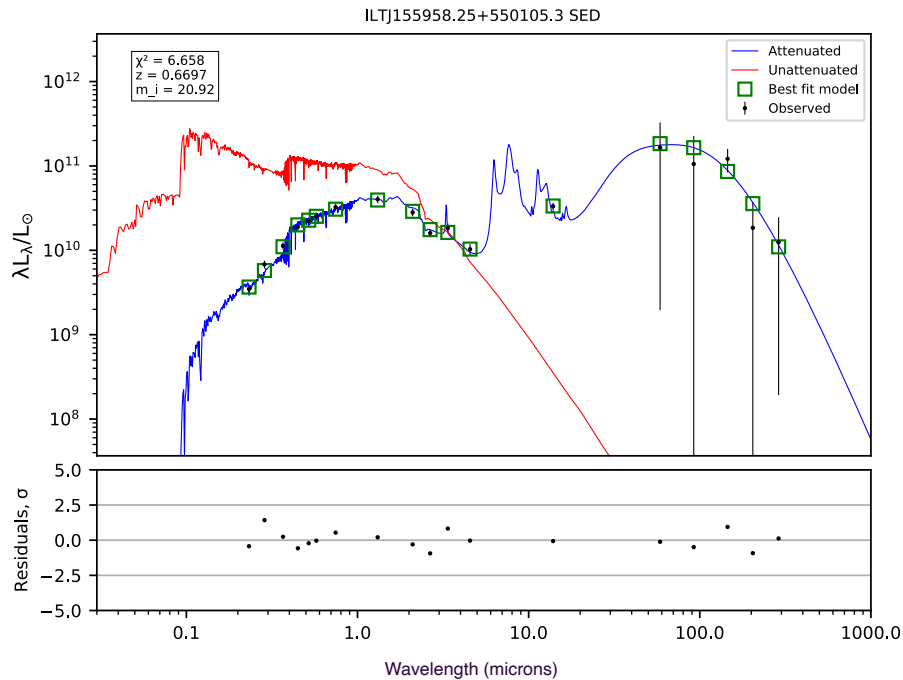


FIGURE 1.8: An SED produced using the fitting software MAGPHYS (da Cunha et al., 2008) as part of the work for Haskell et al. (2023). In the upper panel, the blue line shows the best-fit SED with the points marking the observed fluxes with associated error bars and the green squares marking the best-fit template fluxes at the observed wavelengths. The red line shows the MAGPHYS-derived intrinsic SED i.e. the luminosity density before processing by the ISM, the blue line shows the observed luminosity density. The lower panel shows the residuals for each observation - a measure of how closely the best-fit SED was to the observed wavelengths. This galaxy is part of the ELAIS-N1 field of the LOFAR Two Metre Sky Survey (LoTSS Shimwell et al., 2017) with the identifier shown in the title.

### 1.5.1 Determining luminosity and distance

In order to determine the luminosity of a galaxy, its distance must first be calculated, this is typically done by determining the redshift which can be estimated using either spectroscopy or photometry. A spectroscopic redshift is determined by identifying common emission or absorption lines or continuum features such as the  $4000\text{\AA}$  break, caused by increased absorption at shorter wavelengths (e.g. Cimatti et al., 2020), the Balmer jump at  $3647\text{\AA}$  caused by the ionisation of hydrogen at the second energy level leading to increased absorption (e.g. Draine, 2011) or the Lyman break at  $912\text{\AA}$  caused by photons blueward of this wavelength being absorbed in the photoionisation of hydrogen (e.g. Phillipps et al., 2019). Once the observed wavelength ( $\lambda_{\text{obs}}$ ) of one or more of these features has been determined, the redshift ( $z$ ) is calculated using the rest-frame wavelength and Equation 1.1. Although spectroscopic redshifts are highly accurate (see Lilly et al. 2009, Pentericci et al. 2018 but note Fernández-Soto et al. 2001), they are time-consuming and may be impossible to obtain for faint sources, as discussed in Section

1.2. Nevertheless, the Two-Degree Field Galaxy Redshift Survey (2dFGRS; Colless et al., 2001) serves as an example of the power of spectroscopy, obtaining redshifts for over 220,000 galaxies and mapping the three-dimensional distribution of galaxies across the sky. This has enabled detailed studies of large-scale structures, such as the clustering of galaxies (Croft et al., 2002) and the identification of cosmic voids and filaments (Croton et al., 2004; Patiri et al., 2006). Similarly, SDSS has provided high-quality spectra for over 3 million galaxies (Data Release 16; Ahumada et al., 2020), yielding precise redshifts up to  $z \sim 6$ , alongside measurements of stellar populations, element abundances (metallicity), and SFR.

For large astronomical surveys, it is generally impractical to obtain spectroscopic redshifts for all sources due to the significant telescope time required for faint, high-redshift galaxies (e.g. Duncan et al., 2018a; Cimatti et al., 2020). Photometric redshifts provide a feasible alternative, though they are typically less accurate than those derived spectroscopically (e.g. Ilbert et al., 2006; Dahlen et al., 2013; Laigle et al., 2018).

Two methods are commonly used to estimate photometric redshifts: template matching and machine learning (e.g. Duncan et al., 2018a). The template fitting method involves matching photometric data to templates derived from empirical observations or theoretical models. A statistical goodness-of-fit test, such as a  $\chi^2$  minimization or maximum likelihood approach, is then applied to identify the best-fitting redshift; this can be done using a photometric redshift code such as EAZY (Brammer et al., 2008).

A commonly used machine learning method trains algorithms (e.g. ANNz Collister and Lahav, 2004) on datasets with known spectroscopic redshifts, allowing the software to learn correlations between galaxy colours, magnitudes, and redshift. Once trained, these models can efficiently recognize patterns in new photometric data to estimate redshifts. Machine learning techniques generally produce lower scatter in redshift estimates compared to template fitting (Carrasco Kind and Brunner, 2014; Sánchez et al., 2014) and are computationally faster once the training phase is complete (e.g. Duncan et al., 2018a). However, the effectiveness of machine learning models is contingent upon adequate coverage of the target sources within the parameter space of the training set (e.g. Beck et al., 2017).

Recent studies, such as Duncan et al. (2018b), have demonstrated that a hybrid approach combining these methods yields more precise and reliable redshift estimates.

Once the redshift has been estimated, the luminosity distance can be calculated, this is the distance light would have to travel to produce the observed flux for a given luminosity. In a static Universe, this would be a simple application of the inverse-square law (e.g. Carroll and Ostlie, 2017), however in an expanding Universe the calculation must include several cosmological variables - the mass density  $\Omega_m$ , the dark energy density  $\Omega_\Lambda$ , and the curvature of space  $\Omega_k$ . These variables are defined as follows:

$$\Omega_m = \frac{8\pi G\rho_0}{3H_0^2} \quad (1.3)$$

$$\Omega_\Lambda = \frac{\Lambda c^2}{3H_0^2} \quad (1.4)$$

$$\Omega_k = 0 \quad (1.5)$$

where  $\rho_0$  is the current mass density of the Universe,  $G$  is the gravitational constant,  $H_0$  is the current value of the Hubble parameter  $H(t)$  and  $\Lambda$  is the cosmological constant (Hogg, 1999). The Hubble parameter describes the rate of expansion of the Universe, it is a measure of the energy density per unit volume ( $J/m^3$ ) and represents the repulsive force of dark energy. If the curvature of the Universe,  $\Omega_k$ , is set to zero under the assumption of a flat Universe, the luminosity distance can be calculated by (Hogg, 1999):

$$D_L = \frac{c}{H_0} \int_0^z [\Omega_m(1+z')^3 + \Omega_\Lambda(1+z')^2]^{-0.5} dz' \quad (1.6)$$

For this work, we have adopted the values  $H_0 = 70 \text{ km s}^{-1} \text{ Mpc}^{-1}$ ,  $\Omega_m = 0.3$ , and  $\Omega_\Lambda = 0.7$  which are generally accepted as good approximations (e.g. Driver and Robotham, 2010; Schmidt et al., 2014; Hidaka et al., 2015; Haskell et al., 2023; Arnaudova et al., 2024). Using these values the above equation simplifies to:

$$D_L \approx 0.01c \int_0^z [0.3(1+z')^3 + 0.7(1+z')^2]^{-0.5} dz' \quad (1.7)$$

This calculation can be performed using the Python *astropy* package<sup>4</sup> or the Mattig approximation (Mattig, 1958).

The luminosity ( $L_\lambda$ ) of a galaxy at a wavelength  $\lambda$  can now be calculated using:

$$L_\lambda = 4\pi D_L^2 F_\lambda \times 10^{0.4K(\lambda)} \quad (1.8)$$

---

<sup>4</sup><https://docs.astropy.org>

where  $F_\lambda$  is the flux at wavelength  $\lambda$ ,  $D_L$  is the luminosity distance and  $K(\lambda)$  is the K-correction for wavelength  $\lambda$ . The K-correction adjusts for a number of factors that reduce the observed flux in relation to the emitted flux: the shape of the SED, the fixed bandpass of the observing instrument, and energy loss caused by the observed wavelength being longer than the emitted wavelength, the K-correction reverses this effect (e.g. Cimatti et al., 2020), see (Hogg et al., 2002) for details of the derivation of  $K(\lambda)$ .

## 1.5.2 Measuring the properties of the stellar population

Two of the most important stellar properties are SFR and stellar mass (Calzetti, 2013) as they position a galaxy on the star-forming main sequence plot, enabling the determination of its overall state as discussed in Section 1.3.

### 1.5.2.1 Determining the SFR

The SFR for unresolved galaxies can be estimated by measuring the monochromatic or integrated luminosity over a specific wavelength range which targets continuum or line emission sensitive to short-lived massive stars (Calzetti, 2013). The general form of the SFR calculation is  $SFR = C_\lambda L_\lambda$  where  $L_\lambda$  is the luminosity at wavelength  $\lambda$  and  $C_\lambda$  is a constant. These calculations rest on three key assumptions: (1) the SFR is constant over the timescale probed by  $L_\lambda$ , (2) the initial mass function (IMF) is known, allowing extrapolation from the SFR for massive stars to all stellar types, and (3) that the emission contribution from a potential AGN has been removed (Calzetti, 2013).

Removing the contribution of AGN emission is crucial as it can significantly contaminate the emission needed to determine SFR. Several methods can be used to expedite this. One of the most common approaches involves the use of SED fitting (discussed in Section 1.6). Ciesla et al. (2015) demonstrated that by modelling the SEDs of AGN host galaxies, the contributions from AGN can be separated from those due to star formation. Rosario et al. (2016) emphasizes that FIR emission is less influenced by AGN, a view supported by Mullaney et al. (2012) who argues that FIR emission arises from dust heated by star-forming processes, making them reliable tracers of SFR even in the presence of AGN. However, Dai et al. (2018) noted that AGN emission

can extend significantly into the far-infrared spectrum emphasising the need for careful SED-based AGN/SF decomposition. Other methods to identify AGN include the use of diagnostic tools such as the BPT diagrams (see Section 1.3).

SFR indicators have been derived for several wavelengths including the UV, optical, or IR bands (see e.g. Kennicutt 1998a; Kennicutt et al. 2007, 2009, and for a comprehensive review Calzetti 2013). The following formulae provide the values for SFR from the observed luminosity of emission at different wavelengths:

$$SFR = \begin{cases} 1.3 \times 10^{-28} L_{1500\text{\AA}} \\ 7.9 \times 10^{-42} L_{H\alpha} \\ 2.04 \times 10^{-43} L_{24\mu m} & \text{for } 4 \times 10^{42} \leq L_{24\mu m} \leq 5 \times 10^{43} \\ 2.04 \times 10^{-43} L_{24\mu m} \times [2.03 \times 10^{-44} L_{24\mu m}]^{0.048} & \text{for } L_{24\mu m} > 5 \times 10^{43} \end{cases}$$

Where  $L_{1500\text{\AA}}$  is the luminosity at  $1500\text{\AA}$ ,  $L_{H\alpha}$  is the luminosity of the  $H\alpha$  line ( $656.3\text{ nm}$ ) and  $L_{24\mu m}$  is the luminosity of the  $24\mu m$  emission, All luminosities are in units of  $\text{erg s}^{-1}$ , and assume the IMF derived by Salpeter (1955, see Section 1.5.2.1); the constants for  $L_{24\mu m}$  are from Rieke et al. (2009). Calzetti (2013) notes that each indicator has specific advantages and disadvantages: the UV indicator is sensitive to the age of young stars but may need adjustment for galaxies with recent star bursts, while the  $H\alpha$  indicator assumes that all ionizing photons are absorbed and re-emitted which is likely to lead to an underestimate of the true SFR - Pellegrini et al. (2012) estimated that, as a minimum, between 4 and 9 percent of ionising photons escaped from the Small Magellanic Cloud (SMC) and between 10 and 20 per cent from the Large Magellanic Cloud (LMC). Also, the  $24\mu m$  indicator is effective in heavily dust-shrouded areas, but may not be sensitive enough to capture low SF regions. Figure 1.9 illustrates how these indicators move at higher redshifts, making the choice of indicator also dependent on the available instruments.

The integrated IR luminosity,  $L_{\text{IR}}$ , typically measured between wavelengths  $8\mu m$  and  $1000\mu m$  (e.g. Sanders and Mirabel, 1996; Kartaltepe et al., 2010; Solarz et al., 2016), can also be used as an SFR indicator. This measures the dust grains heated by UV radiation to temperatures of  $T_d \approx 20 - 60\text{K}$ . SFR in this case is given by:  $SFR = 1.73 \times 10^{-10} \left( \frac{L_{\text{IR}}}{\text{erg s}^{-1}} \right) M_{\odot} \text{ yr}^{-1}$  (Cimatti et al., 2020). This measure may be biased by IR emission from AGNs or where IR emission from mature stars is significant, such as from circumstellar dust around asymptotic giant branch (AGB) or red giant stars (Calzetti, 2013).

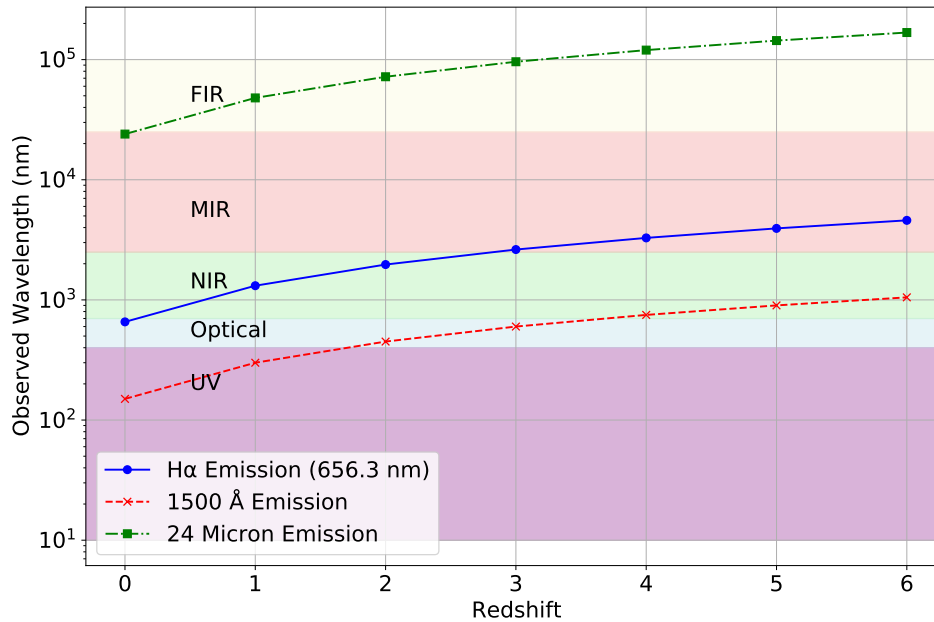


FIGURE 1.9: Plot demonstrating how three of the emission lines used for SFR estimation are affected by redshift.

Correlations between radio emission and SFR have been reported in the literature (e.g. Condon et al., 1982; Cram et al., 1998; Kennicutt and Evans, 2012). These correlations are primarily attributed to two mechanisms: non-thermal synchrotron radiation, and thermal free-free emission. Synchrotron radiation dominates the radio emission (e.g. Condon, 1992; Becker et al., 2009; Motha and Razzaque, 2021), as supernova remnants accelerate electrons which interact with the galaxy’s magnetic field. Free-free emission is primarily related to young, massive stars ionizing their surrounding medium and producing radio emission that traces regions of active star formation (e.g. Cimatti et al., 2020).

In a recent study, Smith et al. (2021) demonstrated a strong correlation between galaxy radio luminosity at 150 MHz and the SFR. 150 MHz radiation is predominantly due to synchrotron radiation (Choudhuri et al., 2020). The relationship is expressed as:  $L_{150MHz} = L_1 \psi^\beta$  where  $L_1 = 22.221 \pm 0.008$ ,  $\beta = 1.058 \pm 0.007$  for  $-2 < \log_{10}(\psi) < 2$  and  $\psi$  is the SFR in units of  $M_\odot \text{ yr}^{-1}$ . A mass dependence for this relationship was observed, indicating that more massive galaxies exhibit higher  $L_{150MHz}$  for a given SFR.

Using radio emission as a tracer of star formation offers several significant advantages over shorter wavelengths. One of the primary benefits is its immunity to attenuation by dust (e.g.

Condon, 1992; Calzetti, 2013), making radio emission particularly valuable for studying star formation in dusty environments. Furthermore, radio observations, especially at longer wavelengths, can be conducted with relative ease using ground-based telescopes, and can be applied over large cosmological distances (e.g. Kennicutt and Evans, 2012; Delvecchio et al., 2021; Smith et al., 2021). However, using longer wavelengths such as radio has certain drawbacks. The first is reduced spatial resolution compared to shorter wavelengths (e.g. Carroll and Ostlie, 2017), which limits the ability to resolve fine details. Secondly, AGN emit strong non-thermal radio waves from processes around the central supermassive black hole which can mimic or overshadow radio emissions stemming from star formation (e.g. Zinn et al., 2013; Brown et al., 2023).

For galaxies with high SFRs, typically  $> 10 M_{\odot} \text{yr}^{-1}$ , the use of a combination of tracers, often referred to as hybrid indicators, tends to yield more reliable SFR estimates (e.g. Kennicutt and Evans, 2012; Calzetti, 2013). This approach accounts for different sources of emission and provides a more comprehensive measurement of star formation. For example, combining an ionised gas tracer such as  $L_{H\alpha}$  and a dust tracer such as  $L_{24\mu m}$  enables the measurement of UV photons absorbed by both gas and dust. This is important in high-SFR environments, where significant amounts of UV can be absorbed by dust causing the SFR to be otherwise underestimated (Calzetti, 2001).

For galaxies with low SFRs, extrapolating from the formation rate of massive stars to the general stellar population can introduce uncertainties in SFR estimates. In these cases, long-lived UV tracers may be more appropriate, as they reflect the ongoing star formation over longer timescales, smoothing out the fluctuations caused by the small number of massive stars (e.g. Calzetti, 2013).

### 1.5.2.2 Determining stellar mass

Stellar mass estimation can be performed using one of two methods: colour-based and spectra-based (Cimatti et al., 2020). Both methods aim to determine the mass-to-light ratio (M/L) of a galaxy, which serves as a key parameter for translating observed luminosity into stellar mass.

The colour-based method relies on broad-band photometric measurements, where the galaxy's integrated colours are used to estimate M/L ratios based on empirical or model-derived relationships between colour and stellar population properties (Wilkins et al., 2013). Empirical relations

for M/L ratios corresponding to different colour indices have been provided by various studies, including those by Bell and Jong (2001) and Bell et al. (2003). The relationship in Bell and Jong (2001) was derived using the Tully-Fisher relation (Tully and Fisher, 1977), which correlates a galaxy’s luminosity to its rotational velocity and, by extension, to its dynamical mass. In contrast, Bell et al. (2003) used a more theoretical approach, deriving M/L ratios from stellar population synthesis (SPS) models, which simulate the integrated light of a galaxy or star cluster, incorporating the evolutionary tracks of different stellar populations.

Spectra-based stellar mass estimation involves obtaining the galaxy’s spectrum in the optical wavelength range, which is processed to produce a continuum which can be fitted against a library of spectra using software such as STARLIGHT (Asari et al., 2007), FIREFLY (Wilkinson et al., 2017), or PPXF (Cappellari, 2023). Roediger and Courteau (2015) demonstrated that both colour-based and spectra-based methods for stellar mass estimation yield comparable results, although Drory et al. (2004) found that the colour-based method produced dynamical masses in better agreement with velocity dispersion mass estimates than the spectra-based estimates. Each method has its own advantages and limitations. Spectra-based mass estimates tend to cost more in telescope time (e.g. Duncan et al., 2018a; Cimatti et al., 2020) but are more precise and less affected by degeneracies related to age and dust (e.g. Gallazzi et al., 2005).

In contrast, colour-based estimates are simpler to implement, and more cost-effective. However, they are more vulnerable to degeneracies and dust extinction effects (e.g. Courteau et al., 2014), which can introduce greater uncertainties. Both methods are sensitive to systematic uncertainties inherent in the SPS models upon which they rely. Gallazzi and Bell (2009) pointed out that these uncertainties are strongly influenced by the SFH of the stellar population; for older stellar populations, spectroscopic mass-to-light (M/L) ratios exhibit narrower uncertainties, ranging from 0.05 to 0.1 dex whereas in galaxies with smoother SFHs or recent starbursts, the uncertainties rise, with spectroscopic methods producing uncertainties of approximately 0.15 dex and colour-based methods yielding uncertainties around 0.2 dex.

### 1.5.3 Measuring the properties of the interstellar dust

As described in Section 1.4.2, dust absorbs UV and optical photons and re-emits in the IR causing a reddening of galaxy emission which can be quantified as the colour excess:

$$E(B - V) = (B - V) - (B - V)_0 = A_B - A_V \quad (1.9)$$

Where  $(B - V)$  is the observed difference in magnitude between the B and V bands,  $(B - V)_0$  is the difference it would have in the absence of dust, and  $A_B$  and  $A_V$  are the extinctions in the B and V bands respectively. This leads to the parameter:

$$R_V = \frac{A_V}{A_B - A_V} = \frac{A_V}{E(B - V)} \quad (1.10)$$

Which is a measure of the steepness of the attenuation curve which plots the extinction, measured in magnitudes, against wavelength. Several attenuation curves have been derived to characterize the impact of dust on observed starlight, including the curve developed by Calzetti et al. (2000) for starburst galaxies which quantifies the attenuation as:

$$k(\lambda) = \begin{cases} 2.659 \left( -2.156 + \frac{1.509}{\lambda} + \frac{0.198}{\lambda^2} + \frac{0.011}{\lambda^3} \right) + R_V & \text{for } 0.12\mu\text{m} < \lambda < 0.63\mu\text{m}. \\ 2.659 \left( -1.857 + \frac{1.040}{\lambda} \right) + R_V & \text{for } 0.63\mu\text{m} \leq \lambda \leq 2.20\mu\text{m} \end{cases}$$

For the Calzetti curve,  $R_V$  is typically set to 4.05, a value derived empirically by Calzetti et al. (2000). Alternative attenuation curves have been established for different environments, including the Milky Way (Cardelli et al., 1989), the LMC (Fitzpatrick, 1986), and the SMC (Prevot et al., 1984). More recent studies by Reddy et al. (2015) and Narayanan et al. (2018) have proposed modified Calzetti curves tailored for high-redshift galaxies.

Once an appropriate attenuation curve is selected, the observed flux can be corrected for attenuation by:

$$F_{\text{int}}(\lambda) = F_{\text{obs}}(\lambda) \times 10^{0.4 \times A(\lambda)} \quad (1.11)$$

Where  $F_{\text{int}}$  and  $F_{\text{obs}}$  are the intrinsic and observed fluxes, respectively, and  $A(\lambda)$  is the attenuation determined from the chosen curve. Figure 1.10 presents examples of the Calzetti, Milky Way, LMC, and SMC attenuation curves. Note the 2175Å 'bump' which is evident in the Milky Way and LMC curves but absent in the Calzetti and SMC curves. The source of this feature, first noted by Stecher (1965), remains a subject for discussion, but is typically attributed to UV absorption by PAHs and possibly small carbonaceous grains (e.g. Bradley et al., 2005; Mao et al., 2014).

Determining the attenuation curve allows the recovery of important dust properties. As smaller dust grains are more efficient at absorbing shorter wavelengths, the slope of the attenuation curve informs the distribution of grain sizes within the galaxy. and the size of the 2175Å bump

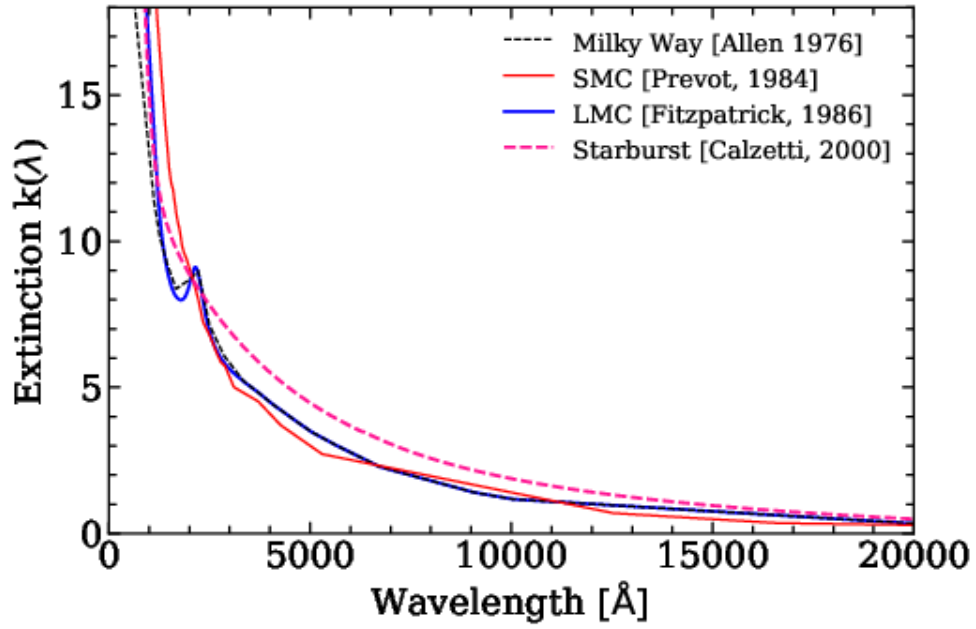


FIGURE 1.10: Plots showing the different attenuation curves discussed in the text. The lines are coded as indicated in the legend. Image reproduced from SPARTAN (Thomas et al., 2020).

may provide evidence of the presence of PAHs and small carbonaceous grains. In addition, the degree of reddening, measured by the colour excess, can give an indication of the amount of dust along the line-of-sight, though this should be treated with caution as the same reddening effect can be caused by older stellar populations or high metallicity within the ISM (e.g. Worthey, 1994; Cimatti et al., 2020).

An important property is that of dust mass; assuming that dust particles are spherical with an average radius  $a$  and density  $\rho_d$ , the dust mass can be estimated from observations by:

$$M_d = \frac{S_\lambda D_L^2}{\kappa_\lambda B_\lambda(T_d)} \quad (1.12)$$

Where  $S_\lambda$  is the flux density at  $\lambda$  (i.e. the flux per unit area per unit time),  $D_L$  is the luminosity distance,  $\kappa_\lambda$  is the dust opacity,  $B_\lambda$  is the Planck function for black-body emission and  $T_d$  is the dust temperature (e.g. Hildebrand, 1983; Dunne et al., 2000).  $T_d$  can be approximated using Wien's law<sup>5</sup> if observations in the IR sample the emission near the IR peak. The dust opacity ( $\kappa_\lambda$ ) modifies the Planck black-body calculation to the appropriate value (i.e. producing a grey-body), it is calculated by  $\kappa_\lambda = \frac{3}{4} \frac{Q_\lambda}{a\rho_d}$  where  $Q_\lambda$  is the efficiency of emission and  $\rho_d$  is the average density of the dust particles (Draine and Lee, 1984). The efficiency of emission  $Q \propto \lambda^\beta$  is determined empirically with  $\beta \approx 1$  for amorphous material and  $\beta \approx 2$  for metals and crystals

<sup>5</sup> $T = \frac{b}{\lambda_{\text{peak}}}$  where  $b$  is Wien's displacement constant

(Cimatti et al., 2020). The assumed values for other parameters can be chosen from the dust size range proposed by Mathis et al. (1977) and the dust density values proposed by Draine and Lee (1984). Emission efficiency values can be referenced from studies such as Draine and Lee (1984), Weingartner and Draine (2001), and Draine (2003).

## 1.6 SED fitting

In the preceding sections, we have discussed how various galaxy properties can be inferred through an array of observational methods and analytical techniques. However, “the different physical processes occurring in galaxies all leave their imprint on the global and detailed shape of the spectrum, each dominating at different wavelengths” (Walcher et al., 2011). Consequently, a detailed analysis of the SED enables a more comprehensive recovery of galaxy properties, allowing the simultaneous derivation of multiple properties instead of isolating single spectral features to constrain individual values.

The SED of a galaxy, which can be derived from photometric or spectroscopic observations, offers a detailed view of the galaxy’s energy output across a wide range of the electromagnetic spectrum (e.g. Cimatti et al., 2020). The primary objective of SED fitting is to analyze this energy distribution by matching an observed SED with a model SED generated using theoretical predictions combined with empirical data. By comparing the observed SED to the model, the inferred properties of the model can be ascribed to the observed galaxy (See Walcher et al., 2011, for a comprehensive review of SED fitting).

### 1.6.1 A short history of SED fitting

The origins of SED fitting for galaxies can be traced back to early photometric studies of galaxy populations in the mid-20th century when photometry in optical bands provided a relatively simple way to estimate the basic properties of galaxies such as their stellar populations and ages (e.g. Baum, 1959). Early observational work focused largely on broad-band colours and magnitudes, which offered the first clues about the relationship between a galaxy’s colour and its evolutionary state. Later, Tinsley (1968) recognized that a galaxy’s light is the composite output of many different generations of stars, this realization leading to the development of SPS models which enabled the construction of theoretical templates describing how a galaxy’s spectrum evolves over time based on its SFH and IMF (see Conroy, 2013, for a review of SPS

models and their role in SED fitting). These models provided the foundation for what would become SED fitting.

A further significant step forward came with the advent of multi-wavelength observations, particularly with the launch of space-based observatories that could probe galaxies at UV and IR wavelengths. The first large-scale infrared surveys of galaxies revealed a significant population of dust-enshrouded, star-forming galaxies (Dwek et al., 1998; Hauser et al., 1998). This discovery demonstrated the need to account for dust attenuation and re-emission in any model attempting to fit the full SED of a galaxy. SPS models continued to evolve (e.g. Bruzual and Charlot, 2003), incorporating detailed treatments of SFHs, chemical enrichment, and dust extinction, enabling the first attempts to fit observed galaxy SEDs using a combination of theoretical templates and photometric data.

The late 1990s and early 2000s saw the beginning of large-scale galaxy surveys, such as SDSS, which provided photometric and spectroscopic data for millions of galaxies across multiple wavelength bands. This wealth of data necessitated the development of more efficient and automated methods for SED fitting, as manual fitting techniques were impractical for such large datasets. In response, more sophisticated tools were developed, such as MAGPHYS (da Cunha et al., 2008) and CIGALE (Boquien et al., 2019), which enabled rapid fitting of observed galaxy SEDs to theoretical models, accounting for factors such as SFH, SFR and dust attenuation. The motivation behind these automated methods was not only efficiency but also the ability to derive statistically robust properties for large samples of galaxies. For example, Kauffmann et al. (2003b) used SED fitting to derive stellar masses and SFH for SDSS galaxies, while Salim et al. (2007) applied SED fitting to UV data from the Galaxy Evolution Explorer (GALEX) to study star formation rates across a wide range of galaxy types.

Appendix A of this thesis is included as an example of the use SEDs to derive galaxy properties from large survey catalogues. The work was undertaken by the author and resulted in catalogues of MAGPHYS-derived properties for  $\approx 850,000$  galaxies.

## 1.6.2 Modelling

SED templates are generated by combining theoretical models with empirical data which encapsulate a range of galaxy properties such as age, metallicity, SFR, and dust content that influence

the shape of the SED. By comparing observed SEDs with these templates, the underlying physical properties of galaxies can be inferred, establishing a link between the observed energy output and the galaxy characteristics likely responsible for producing such a distribution.

Theoretical models provide details for stellar population synthesis, dust attenuation, and gas emission processes that define the SED, while empirical data from observed galaxy spectra provide calibration and validation.

Figure 1.11 illustrates a process for generating these SED templates. Stellar populations within galaxies are modelled using SPS (e.g. Tinsley, 1972; Searle et al., 1973; Larson and Tinsley, 1978), which integrates the spectra of individual stars. Bruzual and Charlot (2003) and Conroy et al. (2010) have both developed SPS that are widely used in current SED fitting programs.

As depicted in Figure 1.11, creating an SED template can be broken down into several steps. (Walcher et al., 2011; Cimatti et al., 2020). A simple stellar population (SSP), is a group of coeval stars assumed to be created in a single burst of star formation with the same metallicity. Creating the spectrum for an SSP requires a number of elements:

1. Import a set of isochrones, these trace the positions of stars of varying masses on a Hertzsprung-Russell diagram, all with the same age and metallicity. Isochrone synthesis libraries of isochrones are available from several sources, including: PARSEC (Bressan et al., 2012), MIST (Dotter, 2016), Dartmouth (Dotter et al., 2008) and BaSTI (Hidalgo et al., 2018);
2. Apply an IMF, this defines the number of stars of each mass in a single-age stellar population. Many IMFs have been proposed, beginning with the Salpeter (1955) IMF, which follows a simple power law,  $\xi(M) \propto M^{-2.5}$  where  $\xi(M)$  is the number of stars of mass  $M$  per unit mass interval, however, various studies have questioned the slope of this function (e.g. Bell and Jong, 2001; Worthey and Dotter, 2009; Lee, 2014). Other commonly used IMFs include the Kroupa (2001) IMF, which features three power laws for different mass ranges, and the Chabrier (2003) IMF, which combines a power law for  $M \geq M_{\odot}$  with a log-normal distribution for less massive stars. Figure 1.12 compares these IMFs over a mass range of  $0.01M_{\odot} < M \leq 10M_{\odot}$ , together with the revised Chabrier IMF (Chabrier, 2005) and a more recent IMF based on theoretical models by Parravano et al. (2011).
3. Use a stellar library to provide spectra for stars of each relevant mass, age, and metallicity. Several libraries are available, including STELIB (Le Borgne et al., 2003), MILES

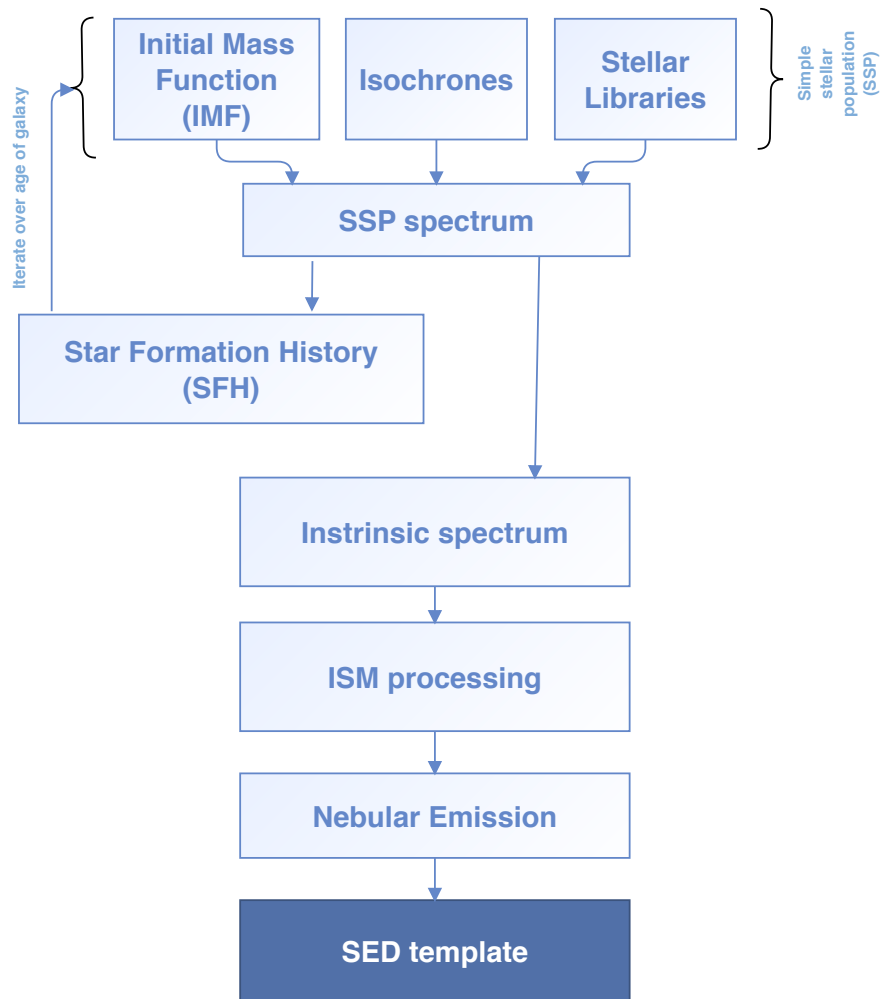


FIGURE 1.11: Flowchart depicting the steps involved in creating SED templates. The initial stellar population synthesis stage builds the intrinsic spectrum of the galaxy by calculating the spectra of multiple simple stellar populations as the galaxy evolves. Once this stage is complete, the spectrum is adjusted to account for processing by the ISM - dust extinction and increased metallicity - and the effects of nebular emission.

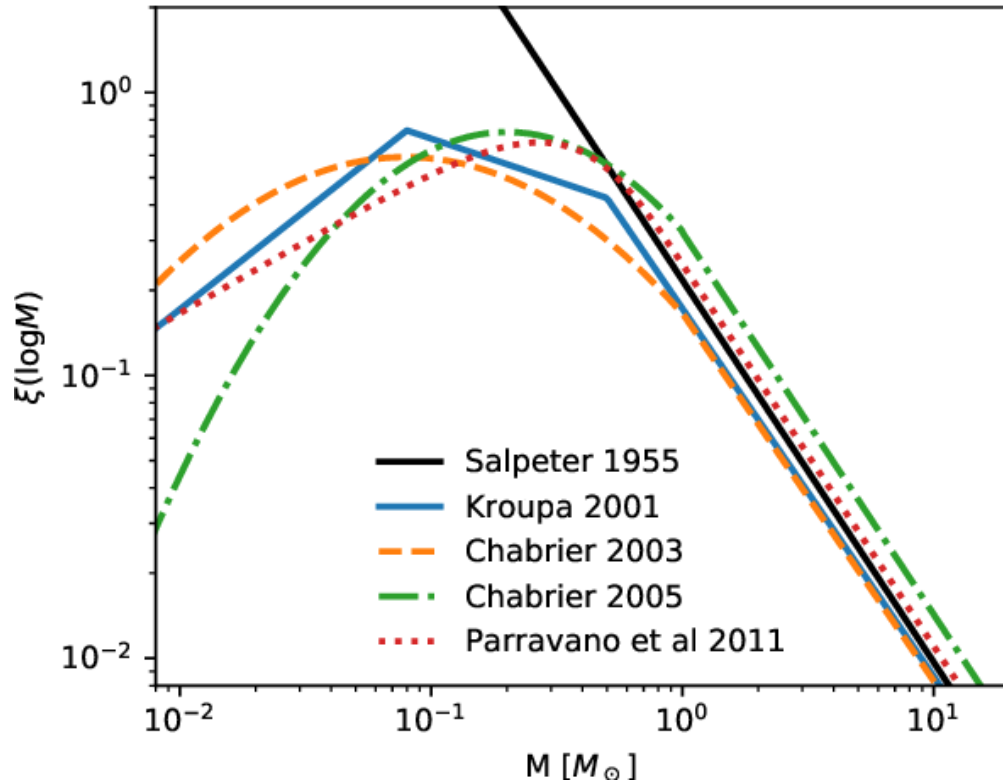


FIGURE 1.12: Comparison of five IMF. The x-axis represents stellar mass in  $M_{\odot}$ , and the y-axis indicates the number of stars per unit mass interval. Lines are colour-coded as indicated in the legend. Image reproduced from Colman and Teyssier (2019).

(Falc3n-Barroso et al., 2011), ELODIE (Prugniel and Soubiran, 2001), and PHOENIX (Husser et al., 2013).

However, to construct the spectrum of a galaxy, this process must be extended over the galaxy’s lifetime, from zero age to the age of the template galaxy. This requires the selection of an SFH; as illustrated in Figure 1.11, the SSP process is iterated multiple times to compile the spectra of a galaxy that has experienced various phases, as dictated by its SFH.

The choice of SFH determines how a galaxy builds its stellar population over time. SFHs can be modelled in one of two ways: parametric, using a formula to describe the SFR at any point in the galaxy’s history, or non-parametric, where the galaxy’s lifetime is divided into distinct periods, with the SFR being free to vary within each period. Some fitters also introduce a stochastic element to the parametric form to model bursts of star formation. The relative merits of parametric versus non-parametric SFHs continue to be debated in the literature (e.g. Carnall et al., 2019; Leja et al., 2019; Lower et al., 2020). Parametric SFHs are straightforward, computationally efficient and easy to interpret, yet they may oversimplify the history of a galaxy (e.g. Smith and Hayward, 2018). Non-parametric SFHs exhibit a greater number of degrees of freedom due to

their separation of the SFH into multiple bins. This has the benefit of providing greater flexibility and potentially a more accurate representation, but can require significantly more computational resource (Leja et al., 2017, 2019).

The result of the SPS process is an SED representing the integrated light from stars over the galaxy's SFH. In Figure 1.8, the red line exemplifies such an output.

Once the stellar spectrum of a galaxy has been constructed, it must be adjusted to account for the effects of the ISM and, in the case of high-redshift galaxies, the intergalactic medium (IGM). This adjustment transforms the estimated intrinsic spectrum (the red line in Figure 1.8) into an estimated observed SED (the blue line in Figure 1.8). The impact of ISM dust was described in Section 1.4.2, dust attenuation is applied using a chosen attenuation law such as Calzetti et al. (2000) or Charlot and Fall (2000) with most fitters also adopting the Draine and Li (2007) emission model. Such adjustment should account for the evolved ISM metallicity; this chemical enrichment enhances the strength of metal absorption and emission lines altering the overall spectral shape, especially in the UV, optical, and infrared regions. Bellstedt et al. (2020, 2021) and Thorne et al. (2022) have highlighted the benefits of modelling galaxies using an evolving metallicity. However, few SED fitters incorporate this evolution (the exception being PROSPECT Robotham et al., 2020), instead, metallicity is treated as a tunable parameter, constant over the galaxy's lifetime.

Finally, nebular emission arises from ionized gas clouds, mainly consisting of hydrogen, helium, and trace amounts of heavier elements, which emit light at specific wavelengths (e.g. Osterbrock and Ferland, 2006). One of the most prominent sources of nebular emission is ionisation by UV photons from young OB type stars leading to characteristic emission lines such as  $H_\alpha$  at 656.3 nm and [OIII] at 495.9 nm and 500.7 nm. Planetary nebulae and supernova remnants also contribute to nebular emission, with planetary nebulae displaying strong lines from ionised elements such as oxygen, nitrogen, and sulphur, while supernova remnants exhibit a broader spectrum including X-ray and radio emissions due to high-energy processes (e.g. Osterbrock and Ferland, 2006). Nebular emission can significantly impact SED templates, as highlighted by Raiter et al. (2010), who noted that it can dominate the SED under certain conditions, and by Terao et al. (2022) who emphasized the importance of including the  $H_\alpha$  line in SED templates. More recently, the SED fitting software BEAGLE-AGN (Vidal-García et al., 2024) has included nebular emission from the narrow line region of AGN in its modelling, see Silcock et al., *submitted* for an example of its deployment.

For high-redshift galaxies, additional attenuation may occur due to the IGM. The IGM comprises of cool gas (predominantly HI and HII) at temperatures of  $10^3$  to  $10^4$  K; and warm-hot intergalactic medium (WHIM) consisting of HII, HeIII and metals at temperatures between  $10^5$  and  $10^7$  K (e.g. Meiksin, 2009; Patidar et al., 2024). Some SED fitting tools, such as the high-redshift version of MAGPHYS (da Cunha et al., 2015) and CIGALE (Boquien et al., 2019), incorporate the IGM attenuation model proposed by Madau (1995) to account for these effects at high redshifts.

### 1.6.3 Fitting and interpreting

The method of assessing the goodness-of-fit for each model remains largely consistent across most SED fitting codes. In most cases, this assessment is conducted using a  $\chi^2$  calculation (Pearson, 1900), which provides a measure of how well the model describes the observed data (Wall and Jenkins, 2003). The  $\chi^2$  statistic is given by the expression:

$$\chi^2 = \sum_{i=1}^n \left( \frac{o_i - m_i}{\sigma_i} \right)^2 \quad (1.13)$$

Where  $n$  is the number of observed fluxes (i.e. the number of filters used),  $o_i$  is the observed flux through the  $i$ -th filter,  $m_i$  is the flux through the  $i$ -th filter in the template, and  $\sigma_i$  is the error in the  $i$ -th observation. From the  $\chi^2$  values, the SED fitting software computes a likelihood value, which quantifies the probability of the observed data given the model. For example, in MAGPHYS, the likelihood  $\mathcal{L}$  is derived from the relation:

$$\mathcal{L} \propto e^{-\frac{\chi^2}{2}} \quad (1.14)$$

The likelihood values obtained are then used to generate probability density functions (PDFs) for specific physical properties by marginalizing to isolate the distribution for the parameter of interest. The resulting PDFs provide a statistical representation of the most probable values for each property.

Alongside these PDFs, SED fitting software typically outputs the property values associated with the model that has the lowest  $\chi^2$  value, known as the best-fit model. This model represents the set of parameters that yields the closest match to the observed data. While the best-fit model offers a point estimate, the PDFs give a more complete picture of the range and likelihood of different parameter values.

To assess the quality of the fit, it is necessary to define a satisfactory level of agreement between the model and the observed data. This is typically done by establishing a threshold for the  $\chi^2$  value below which the fit is considered acceptable. The threshold is determined by calculating a  $p$ -value from the  $\chi^2$  distribution and comparing it to a predetermined significance level, commonly set at 0.05 for a 95 per cent confidence level or 0.01 for a 99 per cent confidence level.

The statistical distribution of the  $\chi^2$  function, and consequently the probability value ( $p$ ), is governed by the number of degrees of freedom ( $N_{\text{dof}}$ ). The probability density function of  $\chi^2$  is given by:

$$p \propto \frac{(\chi^2)^{(N_{\text{dof}}/2)-1} e^{-\chi^2/2}}{2^{(N_{\text{dof}}/2)} \Gamma(N_{\text{dof}}/2)} \quad (1.15)$$

where  $\Gamma$  represents the Gamma function,  $N_{\text{dof}}$  is the number of degrees of freedom, and  $\chi^2$  is the statistic derived from the observational data. In an ideal case, the number of degrees of freedom is commonly taken to be the number of independent observations minus one. However, in the context of photometric measurements, individual data points may not be fully independent due to correlations between bands, systematics in calibration, and the effects of photometric noise (e.g. Scranton et al., 2005). As a result, the effective number of degrees of freedom must be determined empirically.

Smith et al. (2012) performed a statistical analysis to estimate  $N_{\text{dof}}$  for SED fitting using MAGPHYS. Generating synthetic variations of the observed photometry they applied Gaussian perturbations to each photometric measurement, with a standard deviation defined by the minimum photometric uncertainty in each band. By performing 1000 such Monte Carlo realizations, a distribution of  $\chi^2$  values was obtained and the effective number of degrees of freedom was then determined by fitting Equation 1.15 to the resulting histogram, with  $N_{\text{dof}}$  as a free parameter. Using this approach, Smith et al. (2012) derived the following empirical relation:

$$N_{\text{dof}} \approx (-2.820 \pm 0.745) + (0.661 \pm 0.132)N_{\text{bands}} + (7.91 \pm 5.50 \times 10^{-3})N_{\text{bands}}^2 \quad (1.16)$$

Throughout this work, the central values from Equation 1.16 are adopted to determine  $N_{\text{dof}}$ , which in turn is used to establish the threshold  $\chi_{\text{max}}^2$  corresponding to a 99 per cent confidence level based on standard  $\chi^2$  tables.

### 1.6.4 Contemporary SED fitters

We now review how some of the contemporary fitting software implements the general principles described above. Table 1.1 presents details of some of the prominent fitters currently available, outlining how each fitter samples the parameter space, as well as specifying the models used for the SFH, SPS, IMF, and dust attenuation and emission. The majority of fitters assume that the energy absorbed from stellar emission in the UV and optical wavebands is fully re-emitted in the IR. Of the fitters in Table 1.1 only AGNFITTER (Calistro Rivera et al., 2014) explicitly avoids energy-balance. The energy-balance assumption is useful for constraining the amount of dust attenuation in galaxies. Several papers have cast doubt on whether this assumption holds for galaxies where UV/optical and IR emissions are physically separated (e.g. Casey et al., 2017; Miettinen et al., 2017; Simpson et al., 2017; Buat et al., 2019), for instance, galaxies with clumpy dust clouds where some star-forming regions are unobscured in the observer's line-of-sight. However, Hayward and Smith (2015) and Haskell et al. (2023) showed that, on average, the assumption holds across a range of galaxy configurations.

A consistent feature across all the fitters listed is the use of Bayesian statistics, though some not listed do still use a frequentist approach - e.g. LEPHARE (Arnouts et al., 1999; Ilbert et al., 2006) and ZPHOT (Fontana et al., 2000). Bayesian statistics allows the incorporation of prior knowledge (the prior distribution) and results in a posterior distribution that easily demonstrates the uncertainties. In contrast, a frequentist approach will return only a point-best estimate with a confidence interval that gives no sense of the probability that a parameter is within a certain range.

Table 1.1 highlights that some fitters, such as AGNFITTER, BEAGLE, MAGPHYS and PROSPECTOR, are prescriptive in the underlying models available while others, such as BAGPIPES, CIGALE, PROSPECT allow the user to determine which model to use; while this latter approach appears to be an advantage, it can make comparing results from different teams challenging.

We now discuss two key features in which contemporary fitters differ - the modelling of the SFH and the method used to explore the parameter space.

#### 1.6.4.1 Modelling the SFH

The two main approaches to SFH modelling were introduced in Section 1.6.2 - parametric and non-parametric. Parametric SFHs use an analytic function to determine the SFR at any point in

TABLE 1.1: Comparative overview of the models used in popular SED fitting tools. The column headings present the model type, and EB indicates whether energy balance is assumed. Within the columns: Mult. means the user can choose the model, Own means the fitter uses the authors' own model, Nest.sam. is nested sampling, Exp.dec. is exponentially declining (the  $\tau$  model), FSPS is Flexible Stellar Population Synthesis (Conroy and Gunn, 2010b), BC03 is Bruzual and Charlot (2003), C03 is Chabrier (2003), CF00 is Charlot and Fall (2000), C07 is Capak et al. (2007), DL07 is Draine and Li (2007) and D14 is Dale et al. (2014). Some data reproduced from Pacifici et al. 2023.

<sup>1</sup>Note that MAGPHYS uses delayed  $\tau$  with additional starbursts.

Fitter	Sampler	SFH	SPS	IMF	Dust att.	Dust em.	EB
AGNFITTER	MCMC	Exp.dec.	BC03	C03	C07	Mult.	N
BAGPIPES	Nest.sam.	Mult.	Mult.	Mult.	Mult.	Own	Y
BEAGLE	Nest.sam.	Mult.	BC03	C03	CF00	Mult.	Y
CIGALE	Grid	Mult.	Mult.	Mult.	Mult.	Mult.	Y
MAGPHYS	Atlas	Exp.dec. <sup>1</sup>	BC03	C03	CF00	Own	Y
PROSPECT	MCMC	Mult.	Mult.	Mult.	CF00	D14	Y
PROSPECTOR	Nest.sam.	Mult.	FSPS	C03	CF00	DL07	Y

a galaxy's evolution, imposing constraints on the shape of the SFH. In contrast, non-parametric SFHs provide greater flexibility, enabling the SFR to be independently determined across user-defined time intervals of a galaxy's SFH.

One of the most common parametric forms is the exponential decay model (Carnall et al., 2019), often referred to as the  $\tau$  model. This assumes that star formation reaches some maximum at  $t_0$  and then declines exponentially as a fixed pool of gas is consumed.

$$\text{SFR}(t) \propto \begin{cases} e^{-\frac{(t-t_0)}{\tau}} & \text{for } t \geq t_0, \\ 0 & \text{for } t < t_0 \end{cases}$$

Where  $t_0$  is the time taken for light to reach the observer (the lookback time) and  $\tau$  is a constant determined by comparing the SFR of a model to that of the observed data.

An extension to this is the delayed exponential decay model which avoids the unrealistic assumption of an instantaneous burst of star formation by introducing a delay before the SFR begins to decline. Additionally, if the parameter  $\tau$  is sufficiently large, this version of the model can accommodate rising SFRs, allowing for a more gradual build-up of star formation in the early stages of a galaxy's evolution.

$$\text{SFR}(t) \propto \begin{cases} (t-t_0)e^{-\frac{(t-t_0)}{\tau}} & \text{for } t \geq t_0, \\ 0 & \text{for } t < t_0 \end{cases}$$

MAGPHYS takes this one step further by adding random star bursts to the declining continuum as described in Section 2.2.2 of this thesis.

However, there is good evidence to suggest that, while computationally efficient, parametric SFHs do not provide an adequate representation of galaxy evolution. Studies such as those by Simha et al. (2014), Diemer et al. (2017), Ciesla et al. (2017), and Carnall et al. (2018) have demonstrated that parametric SFH models often fail to capture the full diversity of galaxies as observed in both surveys and simulations. Carnall et al. (2019)'s overview concludes with "Our analyses demonstrate the challenges involved in using parametric SFH models as tools for understanding the history of galaxy stellar-mass assembly. Non-parametric SFH models are a promising alternative...."

Non-parametric SFH models divide a galaxy's history into discrete time bins, with the SFR in each bin sampled from a prior distribution, see Leja et al. (2019) for an overview of this method. Non-parametric priors avoid the assumption that the SFR follows a predictable path throughout a galaxy's history but the method is more computationally demanding; additionally, the number and timing of bins needs to be decided in advance along with the prior distribution from which the SFR is drawn for each bin. They have been shown to return more accurate estimates for stellar mass, to better capture the true shape of the SFH, and to produce more realistic error bars for both SFR (Leja et al., 2019; Haskell et al., 2024) and for stellar mass (Lower et al., 2020).

Leja et al. (2019), Lower et al. (2020) and Harvey et al. (2024) have shown that the choice of prior has a significant impact on the modelled SFH with different prior distributions producing either smooth or discontinuous SFRs between time bins and different SFH posteriors. Despite these variations, Leja et al. (2019) comments that non-parametric priors remain the better choice as parametric models rule out plausible solutions and can produce unrealistically constrained error bars. Figure 1.13, reproduced from Leja et al. (2019), provides an example of the effects of choosing different priors, from this figure it is evident that while some priors such as Dirichlet  $\alpha = 1$  and continuity produce smooth SFHs with little SFR difference between time bins, Log(M) and Dirichlet  $\alpha = 0.2$  allow for bursts of star formation. The flexible time bin option differs from the others in this figure by selecting time bins such that equal stellar mass is formed within each bin (Leja et al., 2019; Iyer et al., 2019).

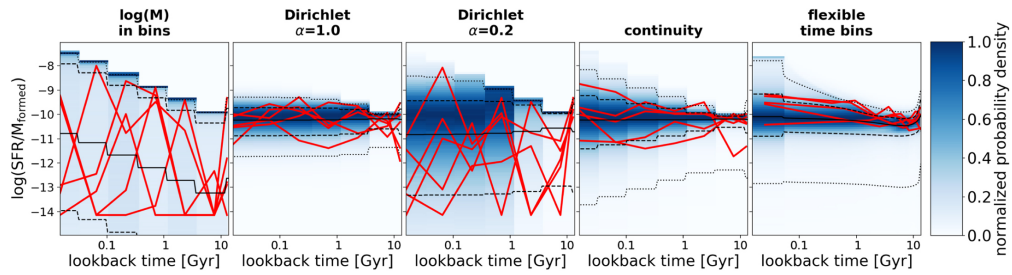


FIGURE 1.13: Examples of the different choices for non-parametric SFHs and the SFR behaviour they can produce. In each panel the blue shaded area shows the prior PDF for the SFH prior shown above the panel. The black solid lines mark the median value, the dashed and dotted lines the  $1\sigma$  and  $2\sigma$  values respectively; red lines show the results of five individual draws from the distribution. Figure reproduced from Leja et al. (2019)

### 1.6.4.2 Exploring the parameter space

The second major difference between fitting codes is the method by which the software explores the likelihoods across the parameter space. In Table 1.1 column 2 we have adopted the descriptions used by Pacifici et al. (2023) to describe the different approaches available. These varying strategies affect the sampling the parameter space and the evaluation of the likelihood of each model which in turn impacts the accuracy and speed of the fitting process. The sampling strategy options are:

- **Atlas** refers to the use of pre-built SED libraries. This technique is suitable for very large data sets where computational time is important. This is the method used by MAGPHYS;
- **Grid** is similar to Atlas, but with the pre-built library's entries consistently spaced within the parameter space;
- **MCMC** refers to the Markov Chain Monte Carlo technique used to traverse a smooth parameter space. In this case, the SEDs are created as the fitting proceeds, guided by the MCMC results. This technique is more computationally demanding but can produce improved fitting;
- **Nested sampling** uses the technique developed by Skilling (2004) which determines the posterior and evidence simultaneously. Like MCMC, this samples the parameter space smoothly and so requires models to be built on-the-fly. PROSPECTOR uses an extension of this - dynamic nested sampling (Speagle, 2020) - in which the sampling is dynamically adjusted as the fitting proceeds which can lead to a more efficient exploration of the parameter space.

PROSPECTOR's sampling of the parameter space is performed by DYNESTY, an implementation of the last of these options. DYNESTY is a dynamic nested sampling package using techniques defined by Higson et al. (2019) which is a generalisation of the nested sampling algorithm of Skilling (2004). Nested sampling places a number of live points randomly within a parameter space and then iterates, replacing the point with the lowest likelihood with one of a higher likelihood at each iteration so ensuring that, as the process continues, the points converge on areas of higher likelihood. Dynamic nested sampling is an extension of this process, adjusting the number of live points as new evidence is found. When the process terminates, the live points are weighted according to their likelihood to produce the PDF.

### **1.6.5 AI and machine learning technologies**

One technology not included in Table 1.1 is that incorporating machine learning, examples of fitters using this technique are ANNZ (Collister and Lahav, 2004) and MIRKWOOD (Gilda et al., 2021). ANNZ has been trained using observations of galaxies with known redshift to rapidly determine photometric redshifts. MIRKWOOD has been trained using simulated galaxies from SIMBA (Davé et al., 2019), EAGLE (Schaller et al., 2015), and ILLUSTRIS (Vogelsberger et al., 2014) to derive stellar mass, dust mass, metallicity, and SFR from the photometry. Gilda et al. (2021) has shown that MIRKWOOD produces superior results to those of PROSPECTOR using the same data. While this class of fitter will undoubtedly make an impact in the future, they are not included in this thesis.

## **1.7 Galaxy simulations**

Simulated galaxies can be used to study the formation and evolution of galaxies, enabling the modeling of dark matter, dark energy, baryonic matter, and feedback processes within the framework of a  $\Lambda$ CDM cosmology. Simulations provide a theoretical foundation for understanding key observables, including galaxy morphology, star formation histories, and mass distributions, and assist in understanding the mechanisms governing galaxy evolution (Somerville and Davé, 2015; Vogelsberger et al., 2020). Simulations also enable testing of theoretical predictions against observational data, facilitating the investigation of complex physical processes such as supernova-driven outflows, black hole feedback, and the enrichment of the ISM and IGM with metals (Hopkins et al., 2018; Pillepich et al., 2018).

TABLE 1.2: Some of the hydrodynamic galaxy simulators currently available. The first column lists the name of the simulation; the second indicates the numerical method used to model gas dynamics with the relevant simulation code in brackets, these are described in the text; the third column presents the simulated volume, typically expressed as the side length of the cubic simulation box, for zoom-in simulations which focus on individual galaxies or galaxy groups at high resolution, only a limited number of objects are simulated in detail rather than an entire cosmological volume; the final column describes the primary focus of each simulation.

Simulator	Hydrodynamics	Scale	Focus
EAGLE	SPH (GADGET)	100 Mpc	Observational realism, feedback
FIRE	Meshless (GIZMO)	Zoom-in	Stellar feedback, bursty SF
Horizon-AGN	AMR (RAMSES)	100 Mpc	Galaxy evolution, morphologies
NewHorizon	AMR (RAMSES)	Zoom-in	High resolution galaxy structure
IllustrisTNG	Moving mesh (AREPO)	300 Mpc	Galaxy statistics, AGN feedback
SIMBA	Meshless (GIZMO)	100 Mpc	Black holes, AGN quenching

### 1.7.1 Simulating galaxy formation and evolution

Cosmological simulations primarily model the evolution of dark matter under the influence of gravity, demonstrating the emergence of large-scale structures such as filaments, voids, and clusters. Notable examples of such simulations include the ThreeHundred project (Cui et al., 2018), MillenniumTNG (Pakmor et al., 2023), and Dianoga (Bassini et al., 2020). However, to investigate galaxy formation and evolution within this framework, it is necessary to incorporate baryonic physics, requiring the use of hydrodynamic simulations.

Hydrodynamic simulations extend dark matter-only models by incorporating gas dynamics, star formation, and feedback processes within the evolving cosmic web, and so enable the study of galaxy formation within dark matter halos. Figure 1.14 illustrates an example from the IllustrisTNG simulation (Pillepich et al., 2018), depicting the structure of the cosmic web and the formation of galaxies within its filamentary network. Several major hydrodynamic simulation projects have been developed to model these processes, including EAGLE (Crain et al., 2015; Schaye et al., 2015), FIRE (Hopkins et al., 2014, 2018), Horizon-AGN and NewHorizon (Dubois et al., 2014, 2021), Illustris and IllustrisTNG (Vogelsberger et al., 2014; Pillepich et al., 2018), and Simba (Davé et al., 2019).

Hydrodynamic simulations can differ in their numerical techniques, feedback prescriptions, and primary scientific goals. Table 1.2 provides an overview of some of the major simulation projects, outlining their key characteristics and particular focus.

The numerical methods listed in column two of Table 1.2 employ different approaches to modeling gas dynamics, each with distinct advantages and limitations. These methods broadly fall

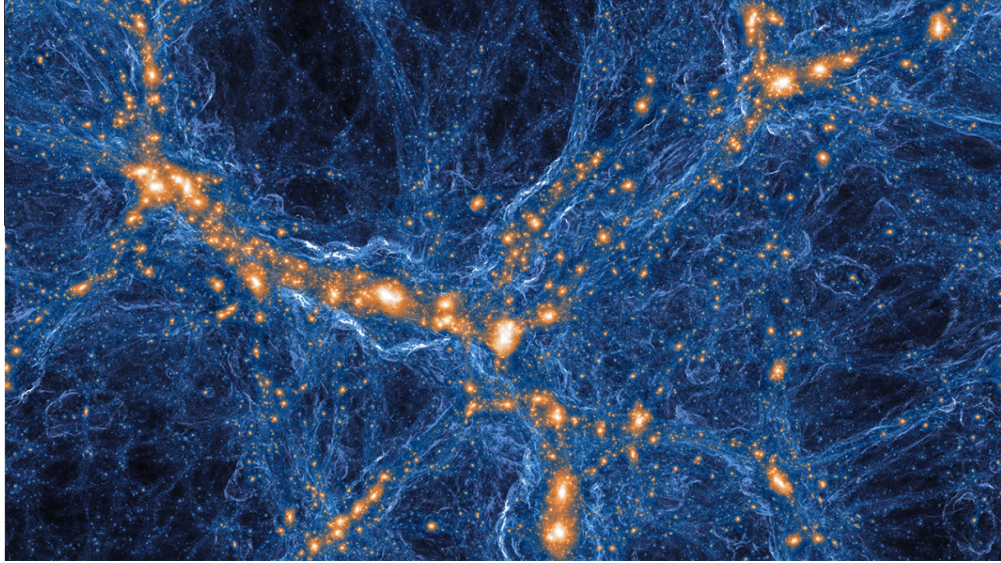


FIGURE 1.14: A view of a simulated cosmic web 300 million light years across as modeled by IllustrisTNG with dark matter shown in blue, galaxies in gold and circumgalactic gas in white. Image reproduced from science.org

into four categories: meshless (Lagrangian), moving mesh, smoothed particle hydrodynamics (SPH), and adaptive mesh refinement (AMR).

Meshless methods treat gas in discrete elements that move with the fluid flow. This technique is implemented in the GIZMO code (Hopkins, 2015), which is used by the FIRE and SIMBA simulations. Unlike traditional SPH, GIZMO employs a mesh-free finite volume method, improving accuracy in handling shocks and turbulence (Hopkins and Raives, 2016).

Moving mesh methods differ from meshless techniques in using a grid of cells that move dynamically with the gas flow, adapting their positions to follow mass distribution. The AREPO code (Springel, 2010) is an implementation of this approach and forms the basis of simulations such as Illustris and IllustrisTNG. This method combines the advantages of both SPH and Eulerian grid-based techniques, reducing numerical diffusion<sup>6</sup> while maintaining high spatial resolution (Springel, 2011).

SPH represents gas as a set of particles that interact according to smoothed kernel functions (Gingold and Monaghan, 1977; Springel, 2010). This method, used in simulations such as GADGET, is used in large-scale cosmological simulations due to its conservation properties and ability to handle highly dynamic fluid flows (Springel et al., 2001).

<sup>6</sup>Numerical diffusion refers to the tendency of numerical simulations to smooth out peaks some quantities such as (e.g.) temperature.

AMR, in contrast, employs a fixed grid but refines the resolution in regions of interest, such as dense galactic environments, where higher spatial resolution is required. The RAMSES code (Teyssier, 2002) is an implementation of AMR and is used in simulations such as Horizon-AGN and NewHorizon.

The choice of hydrodynamic method can significantly impact simulation outcomes. For instance, Few et al. (2016) conducted a comparative study simulating the evolution of a gas disk into a spiral galaxy using three different hydrodynamic codes: SPH (SPHNG; Benz 1990), AMR (RAMSES; Teyssier 2002), and meshless (GIZMO; Hopkins 2015). Their findings indicated that the resulting spiral galaxies exhibited differences in gas density within their spiral arms, which could have implications for subsequent SFRs.

Hydrodynamic simulations track the large-scale movement of gas, however many key astrophysical processes occur on spatial and temporal scales smaller than the typical resolution limits of these simulations. To account for these unresolved processes, sub-grid physics models are implemented, providing parameterized prescriptions for complex phenomena that cannot be directly resolved. These sub-grid models include star formation, supernova feedback, stellar winds, radiation feedback, AGN feedback, and metal enrichment (e.g. Kelly et al., 2022; Butsky et al., 2024; Nobels et al., 2024; Semenov, 2024).

The choice of sub-grid prescriptions can significantly impact the outcomes of simulations, influencing key galaxy properties such as star formation histories, gas dynamics, and the thermodynamics of the ISM, ICM and IGM. For instance, variations in feedback efficiency, cooling mechanisms, or the treatment of turbulence can lead to different galaxy morphologies, mass distributions, and baryon fractions. Comparisons between simulations employing different sub-grid models have demonstrated that these assumptions can introduce systematic variations in the predicted evolution of galaxies and their environments (Crain et al., 2015; Li et al., 2020).

The FIRE simulations used in this thesis incorporate strong stellar feedback mechanisms, which result in a highly variable, bursty mode of star formation (Sparre et al., 2017; Flores Velázquez et al., 2021a). Faucher-Giguère (2018) demonstrated that all galaxies in the FIRE simulations exhibit bursty star formation at  $z > 1$ . However, this interpretation is nuanced, as Stern et al. (2021) found that star formation in FIRE transitions from a bursty to a more steady-state mode at lower redshifts. This evolution is correlated with changes in the gas cooling time, suggesting that the thermodynamic state of the ISM and ICM plays a key role in regulating star formation variability.

Bursty star formation has important implications for the interpretation of observational SFR indicators. Short-term indicators such as  $H_\alpha$  emission, which traces star formation on timescales of a few Myr (Calzetti, 2013), may accurately capture individual starbursts. However, longer-term indicators, such as UV or IR luminosity, which trace star formation over longer periods (Calzetti, 2013), may smooth out or entirely miss the impact of these bursts, leading to a systematic under-estimation of SFR and potentially an incorrect shape for the SFH (Sparre et al., 2017). An additional source of possible bias arises for this work due to the time intervals between simulation snapshots, which range between 10 and 25 Myr. This snapshot timing may fail to capture rapid bursts of star formation, leading to errors in the derived SFR-to-stellar mass ratio and, consequently, affecting a galaxy’s inferred position on the star-forming main sequence. Finally, the FIRE simulations produce a clumpy, patchy dust distribution (Ma et al., 2019) that may be inconsistent with the uniform screen model (Charlot and Fall, 2000) used by many SED fitters (e.g. MAGPHYS and PROSPECTOR). Lower et al. (2020) has showed that using a non-uniform model improves the accuracy with which both dust attenuation and SFR can be recovered.

### 1.7.2 Radiative transfer

Generating the SED of a simulated galaxy requires processing the topology of stars and ISM produced by the simulation through a radiative transfer code that accounts for the effects of dust absorption, scattering, and re-emission. In this study, the radiative transfer package SKIRT (Camps and Baes, 2020) is employed to model the propagation of radiation through the ISM and produce realistic multi-wavelength SEDs.

The workflow for SED generation in SKIRT involves multiple steps, including importing simulated galaxy data, defining dust and stellar emission properties, performing Monte Carlo radiative transfer calculations, and extracting synthetic photometry and spectra. The structure of these processes, along with the data dependencies, is illustrated in Figure 1.15 (Verstocken et al., 2017).

SKIRT uses a Monte Carlo technique to model the interaction of radiation with dust, simulating the propagation of photon packets through a three-dimensional spatial domain containing both sources of radiation and dust distributions. Each photon packet interacts probabilistically with dust grains via scattering, absorption, and re-emission, allowing for a realistic treatment of radiative transfer in dusty galaxies (Camps and Baes, 2015).

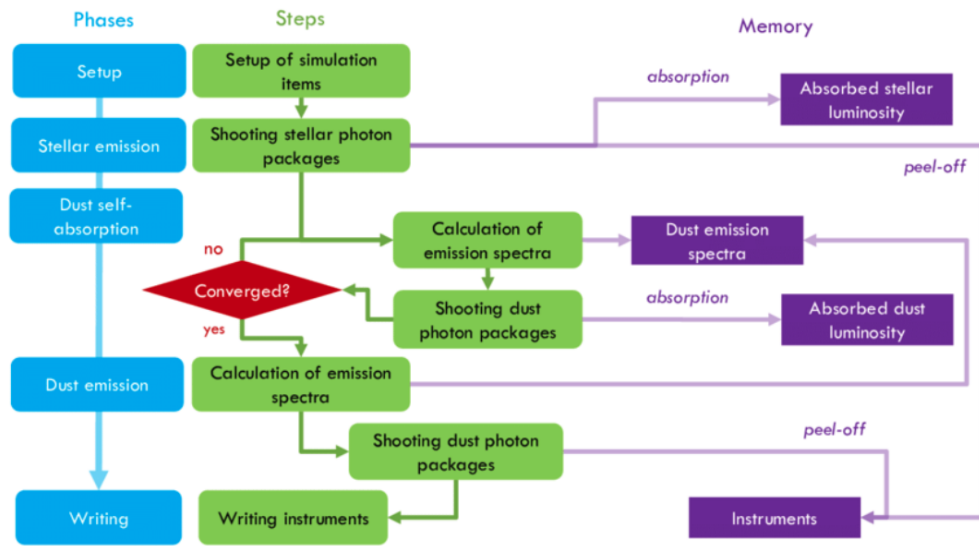


FIGURE 1.15: A flowchart of the steps and data structures involved in a SKIRT simulation. The simulation phases are shown in blue; the steps corresponding to these phases and their order of execution are shown in green; the major data structures are in purple. Image reproduced from Verstocken et al. (2017).

Users can specify custom grain size distributions and select from various dust compositions (Baes et al., 2003), including models representative of the Milky Way, the Large Magellanic Cloud, and the Small Magellanic Cloud. The choice of dust model can significantly influence the resulting SED and the derived galaxy properties, as different compositions exhibit varying extinction and emission characteristics (Faucher and Blanton, 2024). Throughout this thesis, the Milky Way dust prescription of Weingartner and Draine (2001) was adopted.

SKIRT has known limitations, particularly when applied to dusty galaxies with high optical depths. The Monte Carlo method becomes unreliable for optical depths exceeding  $\tau \approx 20$  as photon packets experience multiple interactions, leading to inefficient propagation through the medium (Lee et al., 2016; Camps and Baes, 2018). This limitation affects heavily obscured regions, such as the dense central regions of star-forming or infrared-luminous galaxies, where the radiative transfer calculations may become computationally expensive or yield inaccurate results (Camps and Baes, 2018; Krieger and Wolf, 2023). To mitigate these issues, SKIRT incorporates several explicit absorption schemes and path length stretching methods to enhance the efficiency of photon packet propagation through optically thick regions<sup>7</sup>. However, these limitations imply that mock SEDs should be treated with some caution and viewed in the context of the simulated galaxy morphology.

<sup>7</sup>[https://skirt.ugent.be/root/\\_user\\_photon\\_cycle.html](https://skirt.ugent.be/root/_user_photon_cycle.html)

### 1.7.3 Simulated Photometry

Simulated photometry is inherently less affected by systematic observational challenges compared to real-world astronomical data. The creation of SEDs using data from different instruments is complicated by the need to match apertures and point spread functions (PSF) across the different datasets (e.g. Kuijken, 2008; Aniano et al., 2011; Jiménez-Teja et al., 2015). These issues arise due to variations in the spatial resolution, PSF shapes, and sensitivities of different instruments, and require careful pre-processing to ensure consistency in flux measurements across bands.

Aperture matching ensures that flux measurements across different wavelengths sample the same physical region of a galaxy. This issue becomes particularly relevant when comparing observations from instruments with varying spatial resolutions, where flux measurements at different wavelengths may correspond to different parts of the galaxy. Gil de Paz et al. (2007) and Auld et al. (2013) comment on offsets possibly caused by aperture effects. Also, differences in aperture size and detector resolution can result in inconsistent SEDs if they are not properly accounted for (e.g. Iglesias-Páramo et al., 2013).

PSF matching ensures that images at different wavelengths have comparable spatial resolution, so that structures appear similar across bands. The PSF describes the response of an imaging system to a point source, and its width is a key determinant of an image's spatial resolution (Cimatti et al., 2020). If the PSF varies significantly across bands, the degree of blurring will differ, making direct comparisons between flux measurements challenging (e.g. Zhuang and Shen, 2024).

While aperture matching ensures that flux is measured over a consistent area across wavelengths, PSF matching ensures that light is spread in a consistent manner across images. The two processes are inherently linked: if the PSF differs between bands, aperture matching becomes non-trivial, as a single aperture may capture different amounts of flux in each image. This is particularly problematic for extended sources such as resolved galaxies, where different wavelengths trace distinct physical structures (e.g. UV emission tracing star-forming regions, while IR emission traces dust). Failure to correctly match apertures and PSFs can lead to systematic biases in galaxy properties derived from SED fitting (e.g. Sorba and Sawicki, 2015).

To mitigate the challenges posed by aperture mismatching and PSF variations, observational data must undergo post-processing. The most common approach is PSF matching, where higher-resolution images are degraded to match the PSF of the lowest-resolution dataset - often corresponding to FIR or radio wavelengths<sup>8</sup>. This process involves constructing a blurring kernel for each image, which determines the amount of smoothing required to match the target PSF. The transformation is then applied uniformly across all images, ensuring consistent spatial resolution. PSF matching can be performed using dedicated software packages such as IRAF (Tody, 1986) and Photutils (Bradley et al., 2025).

Once PSF matching is completed, aperture corrections are applied to ensure that flux measurements are consistent across wavelengths (Kuijken, 2008). This typically involves adopting a fixed aperture size for all bands and applying corrections to compensate for missing flux outside the chosen region. These corrections are particularly important for extended sources such as galaxies, where variations in flux distribution across bands may lead to systematic biases in multi-wavelength photometry. For an example of these techniques in practice, see Nayyeri et al. (2017); Best et al. (2023).

When analyzing simulated galaxies, the idealized nature of the environment eliminates the need for PSF matching, as there is no observational imaging system introducing wavelength-dependent resolution constraints. Simulated images and SEDs can be extracted at arbitrarily high resolution, meaning that intrinsic structural details are not subject to instrumental blurring or diffraction effects. However, aperture selection remains a critical factor that can significantly influence flux measurements and the derived galaxy properties (Kewley et al., 2005; Gebek et al., 2024).

To ensure homogeneous photometry across wavelengths, aperture definitions in simulations must be considered; unlike observational studies, where aperture sizes are often dictated by instrumental limitations, simulated datasets allow for more flexible approaches to aperture definition. Several common methods are used to define apertures in simulated data:

- Fixed physical apertures: A predetermined physical size (e.g. 5 kpc, 10 kpc) is applied across all wavelengths (e.g. Snyder et al., 2015). While this approach ensures uniformity, it may fail to capture all of the galaxy's emission at longer wavelengths or introduce biases for extended structures (e.g. Klaas et al., 2006).

---

<sup>8</sup>The spatial resolution of a telescope is determined by the Rayleigh criterion  $\theta_{\min} = 1.22 \times \lambda/D$  where  $\theta_{\min}$  is the minimum detectable angular separation,  $\lambda$  is the wavelength, and  $D$  is the telescope diameter (Carroll and Ostlie, 2017)

- Fraction of total light: Apertures may be defined as a fraction of the total light, such as the Petrosian radius (Petrosian, 1976) or a multiple of the effective radius (e.g. Tacchella et al., 2022d). This method accounts for variations in galaxy size and morphology but may still introduce biases due to wavelength-dependent flux distributions (e.g. Nersesian et al., 2023).
- Surface brightness thresholds: Flux measurements can be extracted based on a surface brightness isophote, typically in the rest-frame optical or near-infrared, to ensure consistency across wavelengths (e.g. Cochrane et al., 2019). This method aligns well with observational approaches but requires careful selection of threshold values to avoid missing flux contributions in different bands <sup>9</sup>.

The choice of aperture used for measuring the photometry can significantly influence the measured fluxes and colours, and therefore the SFRs, stellar masses, and other derived galaxy properties, especially in the presence of extended emission components such as diffuse dust re-radiation in the infrared or stellar halos in the optical and near-infrared (Kewley et al., 2005; Iglesias-Páramo et al., 2013). Figure 1.16 illustrates this point showing the different images that must be processed to form a consistent SED (Panel b) for a real galaxy compared to the relative simplicity of combining simulated images (Panel a).

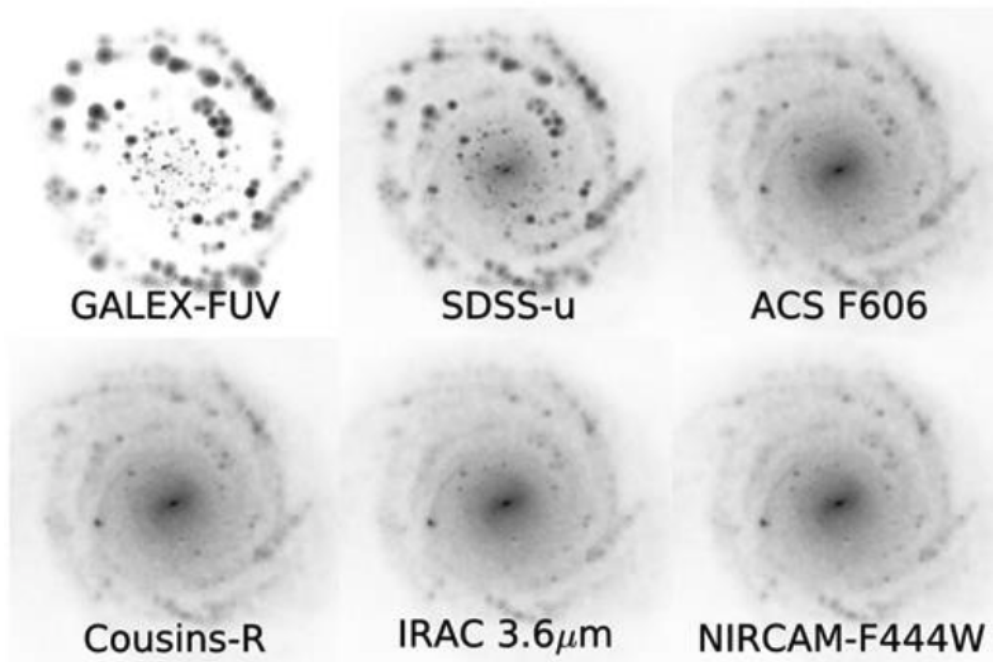
## 1.8 Motivation and structure of this thesis

The preceding sections’ description of the process for creating SED templates has highlighted how each step of construction involves choices of models each with its own theoretical background, assumptions, approximations, uncertainties and biases. Therefore, it is reasonable to approach the results of such modelling with some skepticism and to ask “Should we believe the results of UV-mm galaxy spectral energy distribution modelling” - the question posed by Hayward and Smith (2015) which serves as the inspiration for this work.

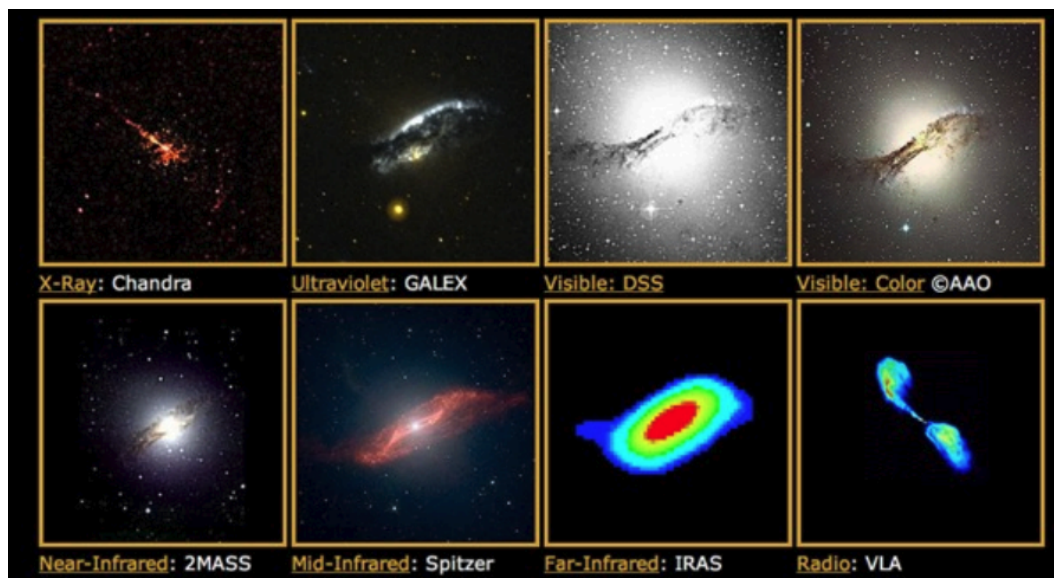
This thesis aims to further address this question by exploring the fidelity of results from two major SED fitters: MAGPHYS and PROSPECTOR. These packages encompass a range of options in terms of their fitting methodology and basic assumptions, as well as differing competencies concerning fitting high-redshift galaxies. Their different approaches to SFH make this work

---

<sup>9</sup><https://ned.ipac.caltech.edu/level5/Tyson3/Tyson2.html>



(A) Images of a simulated galaxy from the Illustris project ( ) taken at (from top left to bottom right) 2316, 5820, 5917, 6407, 36000 and 44000 Å. Image reproduced from Torrey et al. (2015).



(B) Images of NGC 5128 (Centaurus A) taken at different wavelengths as shown, image reproduced from <https://scipp.ucsc.edu/~tesla/multiwave.pdf>.

FIGURE 1.16: This figure shows the complexities of combining data from real galaxy observations compared to that for simulations. The upper panel shows images of a simulated galaxy, the lower images of a real galaxy

particularly relevant to the ongoing debate on the merits of parametric versus non-parametric SFHs.

While the primary objective of this work is to assess the suitability of different SED fitting methods for studying high-redshift galaxies, our investigation addresses several aspects of the fitting process:

- Energy balance assumption: we determine whether the energy balance assumption, which links the UV/optical and FIR emission through dust reprocessing, holds true when these emissions may be spatially separated.
- Projection: we investigate the ability of the models to accurately derive galaxy properties across a range of viewing angles onto the same galaxy.
- Changes in SFR: we evaluate the different methods' ability to capture rapid changes in star formation history, such as starbursts or periods of temporary quenching.
- Dependence on true property values: we investigate whether the accuracy of the derived galaxy properties, such as stellar mass or SFR, is dependent on the true values of these properties.
- Model fitting accuracy: Finally, we determine the overall ability of different fitting methods to produce reliable and accurate fits to the observed data of high-redshift galaxies.

This framework will allow for a comprehensive evaluation of SED fitting techniques in the context of high-redshift galaxy studies, informing future applications of these models to distant, evolving galaxies.

This thesis is structured as follows:

Chapter 2 published in Haskell et al. (2023) presents the work performed using simulated galaxies to investigate concerns that energy balance SED fitters cannot accommodate spatially separated UV/optical and FIR emitting regions.

Chapter 3 published in Haskell et al. (2024) highlights issues concerning a MAGPHYS bias under certain SF conditions.

Chapter 4 reports on the results of running the PROSPECTOR SED fitter on the simulated galaxies, comparing the results with those of MAGPHYS and examining the capabilities of different SED techniques and SFH models.

Chapter 5 synthesizes the results and suggests future work to enhance our confidence in the results of SED fitting for high-redshift galaxies.

## Chapter 2

# Energy balance SED modelling can be effective at high redshifts regardless of UV-FIR offsets

### 2.1 Introduction

Spectral energy distribution (SED) fitting offers a powerful method of estimating galaxy physical properties from photometry. SED fitting programs take as input the available photometry, which can be  $> 30$  bands in the best studied fields to  $< 10$  elsewhere, then use models of varying complexity to infer the shape of the full SED and hence the underlying physical properties (for an introduction to SED fitting see e.g. Walcher et al., 2011; Conroy, 2013).

The energy-balance code MAGPHYS (da Cunha et al. 2008 - hereafter DC08) performs  $\chi^2$  fitting using two sets of pre-built libraries of model SEDs with a representative range of SFHs and dust models for star-forming galaxies. The energy balance criterion works in such a way that MAGPHYS considers only combinations of SFH and dust emission that are energetically consistent, in the sense that the energy absorbed by dust in the rest-frame UV is re-radiated in the FIR. During the fit, MAGPHYS finds the SFH and dust model that best fits the data, and calculates probability density functions (PDFs) for a variety of property values by marginalising over all of the models which satisfy the energy balance criterion.

To determine the fidelity of the properties derived from SED fitting, three testing techniques have been used in previous studies. The first is to compare the derived physical parameters to those derived using simpler methods. DC08 tested how well MAGPHYS could fit observations from the *Spitzer* Infrared Nearby Galaxy Survey (SINGS Kennicutt et al., 2003), producing acceptable best-fit  $\chi^2$  results for 63 of the 66 galaxies. They also tested how well MAGPHYS could recover the properties of 100 of its own, randomly selected, models with noise added to the photometry. Here,  $M_{\text{star}}$ , SFR and  $L_{\text{dust}}$  were reported to be recovered to a high degree of accuracy. Similarly, Noll et al. (2009) tested the alternative energy balance SED fitting code CIGALE (Boquien et al., 2019) using the SINGS galaxies, replacing DC08's UVB observations with those from Muñoz-Mateos et al. (2009). Here,  $L_{\text{dust}}$  estimates compared well ( $\pm 0.03$  dex) with those derived by Draine et al. (2007), similarly the SFR estimates compared well ( $0.06 \pm 0.05$  dex) with those provided by Kennicutt (1998b) based on  $H\alpha$  emission (e.g. Kennicutt 1998a).

An alternative testing technique is to compare the results of different fitting programs when applied to the same dataset. This will not provide evidence that the results are correct, but does give confidence that a given code performs similarly to others. Best et al. (2023) tested three energy balance based fitters - MAGPHYS, CIGALE and BAGPIPES (Carnall et al., 2018) - together with AGNFITTER (Calistro Rivera et al., 2016). The four codes were each used to estimate  $M_{\text{star}}$  and SFR for galaxies in the Boötes, Lockman Hole and ELAIS-N1 fields of the LOFAR Two Metre Sky Survey (LoTSS Shimwell et al., 2017) deep fields first data release (Duncan et al. 2021, Kondapally et al. 2021, Sabater et al. 2021 and Tasse et al. 2021). The results of the runs were compared to determine how well they agreed with each other. For galaxies with no AGN, MAGPHYS, CIGALE and BAGPIPES typically agreed to within 0.1 dex for stellar mass, with AGNFITTER differing by 0.3 dex. Similar levels of agreement were found for the SFRs of galaxies found not to contain an AGN. For galaxies with an AGN the situation was more mixed as neither MAGPHYS nor BAGPIPES are designed to handle AGN emission.

Hunt et al. (2019) compared the results of applying MAGPHYS, CIGALE and GRASIL (Silva et al., 1998) to a sample of 61 galaxies from the Key Insights on Nearby Galaxies: a Far-Infrared Survey with *Herschel* (KINGFISH) survey (Kennicutt et al., 2011), including 57 of the SINGS galaxies. They found that stellar masses estimated using  $3.6\mu\text{m}$  luminosity agreed with all three codes to within 0.2 dex. Similarly, SED derived SFR estimates were within 0.2 dex of those derived using FUV+TIR luminosities and  $H\alpha + 24\mu\text{m}$  luminosities. The results for  $M_{\text{dust}}$  were

more mixed, with GRASIL giving values 0.3 dex higher than MAGPHYS or CIGALE or the value determined using a single temperature modified black body. A similar approach with an even broader selection of fourteen SED fitting codes was taken by Pacifici et al. (2023), who found agreement on stellar mass estimates across the ensemble, but some discrepancies in their SFR and dust attenuation results. More recently, Cheng et al. (2023) used a modified version of MAGPHYS (MAGPHYS +photo-z; Battisti et al. 2019) to determine the photometric redshifts of 16 sub-millimetre galaxies (SMGs). The results were compared to the redshifts derived using EAZY (Brammer et al., 2008), finding that for most sources the results were consistent.

The final, and perhaps most promising technique for validating SED fitting is to use simulated galaxies where the ‘right’ answer is known in advance. Wuyts et al. (2009) used the HYPERZ (Bolzonella et al., 2000) SED fitting code on GADGET-2 (Springel, 2005) simulations to recover mass, age,  $E(B-V)$  and  $A_V$  under a variety of conditions. They concluded that recovery of properties for ellipticals was generally good (residuals between 0.02 and 0.03 dex) with slightly poorer results for disks (residuals of 0.03 to 0.35 dex), with residuals increasing further to 0.02 to 0.54 dex during periods of merger-triggered star formation. Hayward and Smith (2015, hereafter HS15) used MAGPHYS on two GADGET-3 (Springel, 2005) simulations of an isolated disk and a major merger of two disk galaxies at  $z = 0.1$ . Snapshots were taken at 10 Myr intervals and the radiative transfer code SUNRISE (Jonsson, 2006) used to produce observations from 7 different lines of sight around the simulation. In both scenarios, the attenuated SED was recovered with an acceptable fit ( $\chi^2$  within the 99 per cent confidence threshold; see Smith et al. 2012 for details) except for the time around the peak starburst/coalescence phase of the merger simulation. In both scenarios,  $L_{\text{dust}}$  was recovered well with  $M_{\text{star}}$  recovered to within 0.3 dex and SFR within 0.2 dex.  $M_{\text{dust}}$  was recovered less well, but still within 0.3 dex for the isolated galaxy and 0.5 dex for the merger. The conclusion from this study is that these properties of local galaxies can typically be recovered to within a factor of 1.5 – 3. Smith and Hayward (2018) studied a resolved simulated isolated disk, using spatial resolution as fine as 0.2 kpc. They found that MAGPHYS produced statistically acceptable results for  $M_{\text{star}}$ ,  $L_{\text{dust}}$ , SFR, sSFR and  $A_V$  for over 99 per cent of pixels within the r-band effective radius. At higher redshifts, Dudzevičiūtė et al. (2020, hereafter D20), used EAGLE (Schaye et al. 2015, Crain et al. 2015) simulations with SKIRT generated photometry (Baes et al. 2011, Camps and Baes 2020) to validate the performance of MAGPHYS for studying galaxies with redshifts up to 3.4. They found that MAGPHYS gave a remarkably linear correlation with the true (simulated) values, though with significant scatter (at the level of 10, 15 and 30 per cent for the dust mass, SFR and stellar masses, respectively) and significant

systematic offsets (of up to  $0.46 \pm 0.10$  dex for the recovered stellar mass).

These studies all provide evidence that SED fitting, particularly energy balance SED fitting, is working remarkably well and providing results often consistent with the ground truth once the uncertainties are accounted for.

However, several authors have questioned whether using an energy balance criterion is appropriate when viewing galaxies for which the UV and FIR are spatially offset from one another (e.g. Casey et al., 2017; Miettinen et al., 2017; Simpson et al., 2017; Buat et al., 2019). In such cases, while ‘energy balance’ is still expected overall (i.e. energy conservation is presumably not violated), significant spatial decoupling may lead to difficulties in recovering the true properties. Under such circumstances, the attenuation – and thus the intrinsic UV luminosity – may be underestimated because the UV-bright, relatively dust-free regions can result in a blue UV-optical slope even if the bulk of the young stars are heavily dust-obscured.

This concern has recently become testable with the sub-arcsecond resolution provided by the Atacama Large Millimetre/submillimetre Array (ALMA)<sup>1</sup>, enabling direct observation of UV/optical and FIR offsets. There are now numerous papers reporting spatial offsets. Hodge et al. (2016), Rujopakarn et al. (2016), Gómez-Guijarro et al. (2018) and Rujopakarn et al. (2019) have discovered kpc offsets between star forming regions and centres of stellar mass while investigating the star formation and dust distributions in  $2 < z < 4.5$  galaxies. Along these lines, Chen et al. (2017) found a significant offset in ALESS67.1, a SMG at  $z = 2.12$ , Cochrane et al. (2021) reported the same in the massive star-forming galaxy SHiZELS-14 at  $z = 2.24$ , and Bowler et al. (2018) detected a 3 kpc offset between the rest-frame FIR and UV emission in the Lyman-break galaxy ID65666 at  $z \approx 7$ .

The concern over the impact of decoupling between the dust and starlight is such that new SED fitting codes such as MICH12 (Liu, 2020) and Stardust (Kokorev et al., 2021) mention the *absence* of energy balance as a key advantage in favour of using these codes for studying galaxies where spatial offsets are likely to be a factor. In Liu et al. (2021), MICH12 produced results very similar to MAGPHYS and CIGALE for a sample of high redshift galaxies, with stellar mass and dust luminosity estimates obtained to within 0.2 - 0.3 dex of those obtained using the two energy-balance codes. Similarly, Kokorev et al. (2021) used Stardust to fit 5,000 IR bright galaxies in the GOODS-N and COSMOS fields, producing results which compared well

---

<sup>1</sup><http://www.alma.info>

with those derived using CIGALE with a mean  $M_{\text{dust}}$  residual of 0.09 dex, a mean  $L_{\text{IR}}$  residual of 0.2 dex and a mean  $M_{\text{star}}$  residual of 0.1 dex (albeit with a significant scatter of 0.3 dex).

An additional test of the likely impact of spatial offsets was conducted by Seillé et al. (2022), who used the CIGALE code to model the Antennae Galaxy, Arp244, which is known to have very different UV and IR distributions (Zhang et al., 2010). Seillé et al. (2022) found that the total stellar mass and SFR were consistent, whether they attempted to fit the integrated photometry of the galaxy or sum the results of fitting 58 different regions of Arp244 independently and summed the results (i.e. performance very similar to that found by Smith and Hayward 2018 for simulated galaxies without spatial offsets).

In this context, we now seek to further test the efficacy of energy balance SED fitting for these more challenging dusty, high redshift, star-forming galaxies by using high-resolution simulations with differing degrees of spatial offset between the apparent UV/FIR emission.

This paper is structured as follows. Section 2.2 describes the tools and methods used to create the observations and to fit the SEDs; Section 2.3 presents the results of the fitting including the derived values for several galaxy properties; Section 2.4 discusses these in the context of previous papers and Section 2.5 summarises the conclusions. Throughout this work we adopt a standard cosmology with  $H_0 = 70 \text{ km s}^{-1} \text{ Mpc}^{-1}$ ,  $\Omega_M = 0.3$ , and  $\Omega_\Lambda = 0.7$ .

## 2.2 Method

This section describes the simulation data and the creation of the synthetic observations. It also provides a brief introduction to MAGPHYS, details of the simulations, and how they were subsequently analysed.

### 2.2.1 Computing the SEDs of simulated galaxies

We analyze a set of 4 cosmological zoom-in simulations from the FIRE project<sup>2</sup> that were run using the FIRE-2 code (Hopkins et al., 2018) down to  $z = 1$ . The simulations use the code

---

<sup>2</sup><http://fire.northwestern.edu>

GIZMO (Hopkins, 2015)<sup>3</sup>, with hydrodynamics solved using the mesh-free Lagrangian Godunov “MFM” method. Both hydrodynamic and gravitational (force-softening) spatial resolution are set in a fully-adaptive Lagrangian manner with fixed mass resolution. The simulations include cooling and heating from a meta-galactic background and local stellar sources from  $T \approx 10 - 10^{10}$  K; star formation in locally self-gravitating, dense, self-shielding molecular, Jeans-unstable gas; and stellar feedback from OB & AGB mass-loss, SNe Ia & II, multi-wavelength photo-heating and radiation pressure with inputs taken directly from stellar evolution models. The FIRE-2 physics, source code, and all numerical parameters are *exactly* identical to those in Hopkins et al. (2018).

The specific sample of simulations studied in this paper include the halos first presented in Feldmann et al. (2016). The FIRE-2 simulations for these halos were introduced, along with a novel on-the-fly treatment of black hole seeding and growth in Anglés-Alcázar et al. (2017). These halos were chosen because they are representative of the high-redshift, massive, dusty star-forming galaxies found in infrared-selected observational samples, Cochrane et al. (2019) showing that they present a clumpy dust distribution together with very different morphologies for stellar mass, dust, gas and young stars. At  $z = 2$ , the galaxies central to the halos have half-light radii of 0.73, 0.98, 0.81 and 0.91 kpc; for additional information on these galaxies see Anglés-Alcázar et al. (2017) as well as Cochrane et al. (2019), Wellons et al. (2020), Parsotan et al. (2021) and Cochrane et al. (2022).

To generate synthetic SEDs, Monte Carlo dust radiative transfer was performed on each time snapshot of the simulated galaxies in post-processing using the code SKIRT<sup>4</sup>. SKIRT assigns single-age stellar population SEDs to star particles in the simulations according to their ages and metallicities. It then propagates photon packets through the simulated galaxies’ ISM to compute the effects of dust absorption, scattering, and re-emission. Snapshots of the galaxies’ evolution were taken at 15 - 25 Myr intervals with each galaxy ‘observed’ from 7 positions that uniformly sampled inclination angles from view 0 (aligned with the angular momentum vector) in steps of 30° to view 6 (anti-aligned). For full details of the SKIRT calculations, see Cochrane et al. (2019, 2022). This procedure yielded 6,706 SEDs across the four simulated galaxies, spanning  $1 < z < 8$ .

To compute photometry from the SEDs, we convolved the SEDs with appropriate filter response curves for the 18 bands listed in Table 2.1. These filters were chosen for similarity with previous

<sup>3</sup><http://www.tapir.caltech.edu/~phopkins/Site/GIZMO.html>

<sup>4</sup><http://www.skirt.ugent.be/>

work in the LoTSS deep fields (e.g. Smith et al., 2021), providing good coverage of the spectrum from the UV to the FIR with which to test how MAGPHYS performs in these idealised conditions. Figure 2.1 shows the filter coverage for an example SED at  $z = 1$ , along with the emergent SED generated by SKIRT.

Figure 2.2 examines the relationship between the properties of our simulated galaxies and those of high redshift sub-millimetre galaxy populations in which spatial UV–FIR offsets have been observed. We compared four properties with observations, specifically the SFR relative to the galaxy main sequence (MS; upper left panel), the relationship between sub-mm flux density and  $M_{\text{dust}}$  (upper right), the degree of  $V$  band extinction (lower left), as well as the magnitude of the UV/IR offsets (lower right) in relation to studies in the literature. In the upper left panel we have compared the SFR in each snapshot with the MS parameterisation from Schreiber et al. (2015) modified for our adopted Chabrier (2003) IMF using the method of Madau and Dickinson (2014), as a function of redshift. The magenta band indicates the typical  $\pm 0.3$  dex scatter associated with the MS (e.g. Tacchella et al., 2022a). The simulated galaxies lie either on or above the MS in the vast majority of cases, and are therefore consistent with dusty, star forming galaxies. The upper right panel of Figure 2.2 shows the sub-millimetre flux density,  $S_{870}$ , as a function of the dust mass for the simulated galaxies and for the SMGs published in D20. While the simulations do not occupy the parameter space of the brightest SMGs, there is significant overlap, and they do lie along the same submm/dust mass relationship (see Hayward et al. 2011, Cochrane et al. 2023b). The lower left panel shows how the  $V$ -band extinction ( $A_V$ ) for the simulations (the blue solid line indicates the median, with shading indicating the values enclosed by the 16th and 84th percentiles of the distribution at each redshift) compares with the corresponding values for the SMG samples from D20 (in purple) and Hainline et al. (2011, indicated by the red points with error bars). Although the D20 sample is on average more obscured than our simulations, similarity to the Hainline et al. (2011) SMGs is evident. The lower right panel shows the range of offsets between the UV and FIR emission in redshift bins. The solid lines indicate the mean simulated offset (blue for peak-to-peak, red for light-weighted mean), with shaded regions indicating the area enclosed by the 16th and 84th percentiles at each redshift. The black, red and green symbols indicate ALMA sources from Rujopakarn et al. (2016), Rujopakarn et al. (2019) and Lang et al. (2019). Finally, the short green line marks the mean offset from Lang et al. (2019) over 20 SMGs with  $1.6 < z < 2.5$ .

To summarise, Figure 2.2 demonstrates that the simulated sources are predominantly dusty star-forming galaxies. While the D20 SMG sample is more extreme, the degree of extinction and the

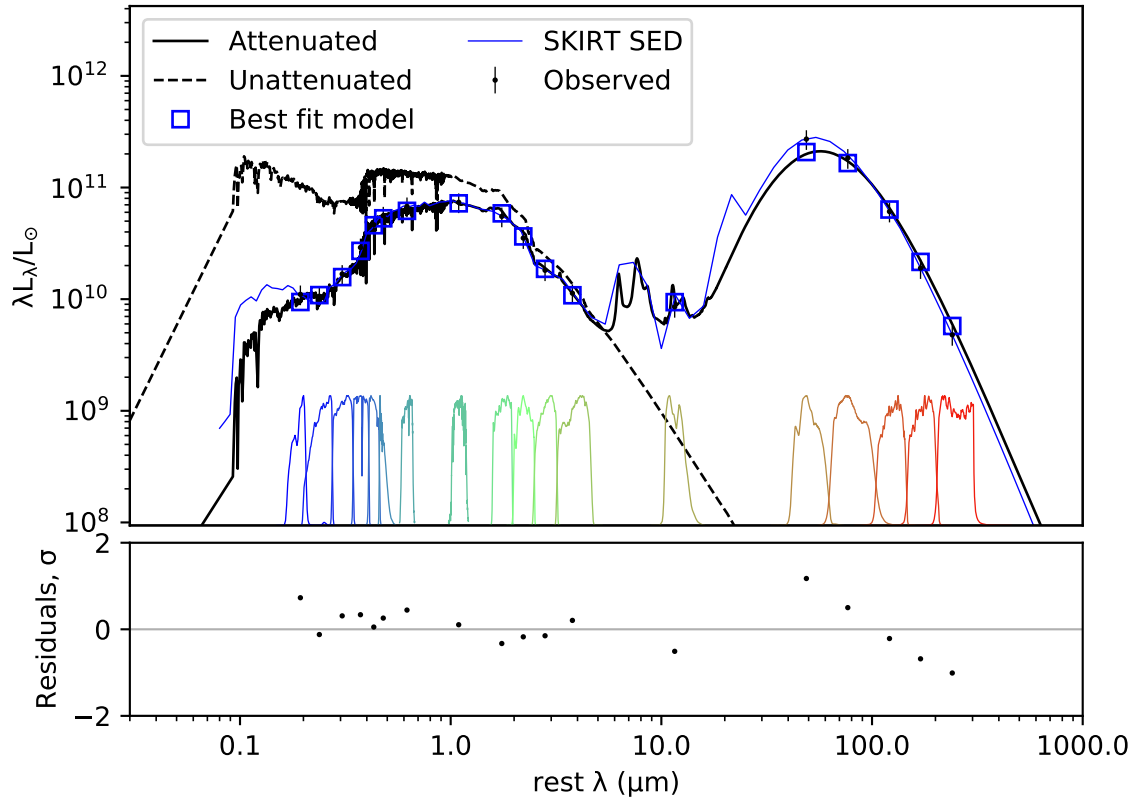


FIGURE 2.1: An example SED obtained using MAGPHYS, demonstrating the generally close agreement between the true and MAGPHYS-derived SEDs. In the upper panel, the solid black line shows the best-fit MAGPHYS-derived SED, while the dashed black line indicates the MAGPHYS estimate of the unattenuated SED; the solid blue line represents the attenuated SED generated by SKIRT. The square markers represent the best-fit photometry, with the SKIRT photometry shown as the points with error bars (as described in the legend). The coloured lines above the lower horizontal axis show the normalised filter curves used in this study. The lower panel shows the residual value in  $\sigma$  units between each observation and the best-fit SED. The residual value is calculated as (observed flux - model flux)/observed error. This SED corresponds to simulated galaxy A1, snapshot 276, view 0,  $z = 1.00$ .

magnitude of the UV-FIR spatial offsets in the simulations show significant overlap with values published in the literature. The simulations are therefore a useful testing ground for determining the extent of our ability to recover the true properties of galaxies with plausible UV-FIR offsets using MAGPHYS.

## 2.2.2 MAGPHYS

MAGPHYS is an SED modelling code using Bayesian inference to derive best-fit SEDs as well as estimates (best-fit, median likelihood, and probability distribution functions) for a wide range

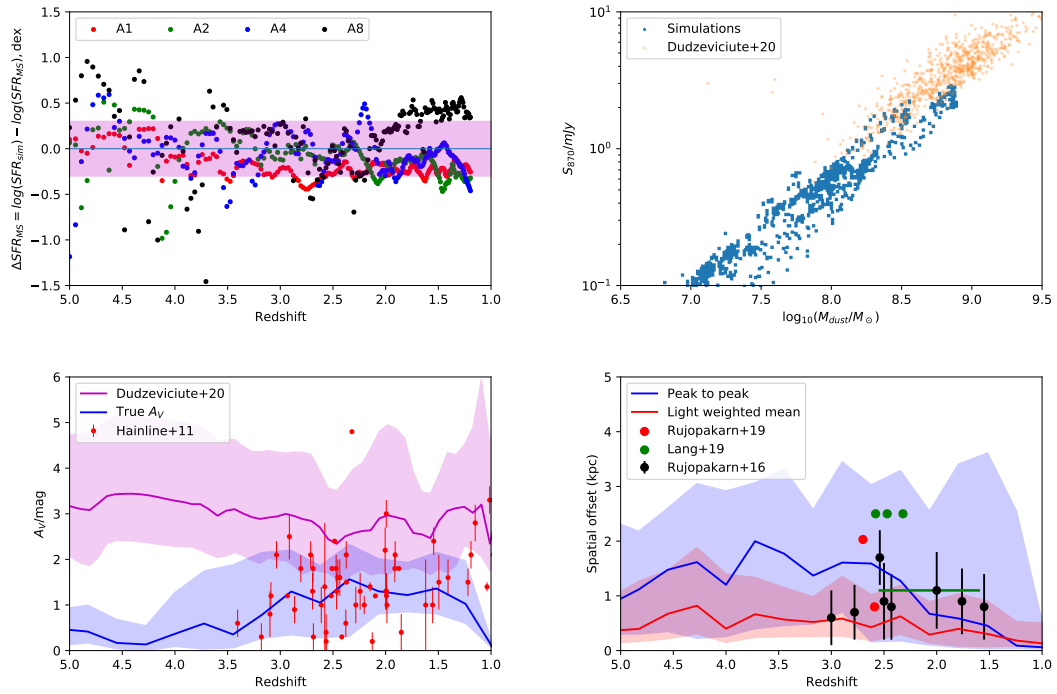


FIGURE 2.2: The properties of the simulated galaxies in their observational context. **Upper left:** the relationship between the simulated galaxies’ SFRs and the galaxy main sequence (MS); for each snapshot, the y-axis shows the difference between the simulation SFR and the MS, with the magenta band indicating the typical  $\pm 0.3$  dex scatter associated with the MS (e.g. Tacchella et al., 2022a). **Upper right:** the relationship between the sub-mm flux density  $S_{870}$  and dust mass; the blue points represent the simulated data, while the orange points show galaxies from D20. **Lower left:** the variation in  $A_V$  as a function of redshift for the simulations (for which the median value at each  $z$  is shown by the solid line, within shading indicating values enclosed by the 16th and 84th percentiles of the distribution), along with a corresponding distribution from D20 (shown in purple). The SMG sample from Hainline et al. (2011) is shown by the red points. **Lower right:** the mean UV/FIR peak to peak (blue) and light-weighted mean (red) spatial offsets in redshift bins: the shading indicates the region enclosed by the 16th and 84th percentiles at each redshift, while the solid line indicates the median value. The red, green and black circles are values for individual sources taken from the literature (as indicated in the legend), while the solid green line marks the reported average spatial offset across 20 SMGs from Lang et al. (2019).

of galaxy properties. A full description can be found in DC08 and da Cunha et al. (2015), but we include a brief overview. MAGPHYS uses two libraries of model galaxies: the first, the library of star-formation histories (SFH), consists of 50,000 models each comprising a UV/optical SED and associated galaxy properties; the second, the dust library, comprises 25,000 models each with an IR SED and associated properties.

The SFH library is built using the IMF of Chabrier (2003) and the stellar population synthesis (SPS) model of Bruzual and Charlot (2003). Exponentially declining star formation histories are superposed with random bursts, in such a way that a burst of star formation has occurred in half of the SFH library models within the last 2 Gyr.

TABLE 2.1: The filters used to create synthetic observations from the simulated photometry. The first column gives the telescope/survey, the second the instrument/filter name, and the third the effective wavelength of the filter.

Facility	Filter	$\lambda_{\text{eff}}(\mu\text{m})$
CFHT	Megacam <i>u</i>	0.39
PanSTARRS	<i>g</i>	0.48
PanSTARRS	<i>r</i>	0.61
PanSTARRS	<i>i</i>	0.75
PanSTARRS	<i>z</i>	0.87
PanSTARRS	<i>y</i>	0.96
UKIDSS	<i>J</i>	1.2
UKIDSS	<i>K</i>	2.2
<i>Spitzer</i>	IRAC ch1	3.4
<i>Spitzer</i>	IRAC ch2	4.5
<i>Spitzer</i>	IRAC ch3	5.6
<i>Spitzer</i>	IRAC ch4	8.0
<i>Spitzer</i>	MIPS 24 $\mu\text{m}$	24
<i>Herschel</i>	PACS green	100
<i>Herschel</i>	PACS red	160
<i>Herschel</i>	SPIRE	250
<i>Herschel</i>	SPIRE	350
<i>Herschel</i>	SPIRE	500

Common to both libraries is the use of the Charlot and Fall (2000) two-component dust model. In this model, stellar populations younger than 10 Myr are attenuated by a greater amount than older stellar populations, under the assumption that these young stars are still embedded within their ‘birth clouds’. These stellar populations are subject to a total optical depth  $\tau_{\text{BC}} + \tau_{\text{ISM}}$ , whereas older populations ‘see’ an optical depth of only  $\tau_{\text{ISM}}$ , from the diffuse ISM. Charlot and Fall (2000) define the optical depth seen by stellar emission as

$$\hat{\tau}_{\lambda} = \begin{cases} \hat{\tau}_{\lambda}^{\text{BC}} + \hat{\tau}_{\lambda}^{\text{ISM}} & \text{for stars } < 10 \text{ Myr,} \\ \hat{\tau}_{\lambda}^{\text{ISM}} & \text{for stars } \geq 10 \text{ Myr.} \end{cases}$$

where  $\hat{\tau}_{\lambda}$  is the total optical depth for  $\lambda$ ,  $\hat{\tau}_{\lambda}^{\text{BC}}$  is the optical depth of the birth clouds and  $\hat{\tau}_{\lambda}^{\text{ISM}}$  is the optical depth of the ISM. These latter two are defined in MAGPHYS such that:

$$\hat{\tau}_{\lambda}^{\text{BC}} = (1 - \mu) \hat{\tau}_V (\lambda / 5500 \text{ \AA})^{-1.3}, \text{ and} \quad (2.1)$$

$$\hat{\tau}_{\lambda}^{\text{ISM}} = \mu \hat{\tau}_V (\lambda / 5500 \text{ \AA})^{-0.7}, \quad (2.2)$$

where  $\hat{\tau}_V$  is the mean *V* band optical depth and  $\mu$  represents the fraction of  $\hat{\tau}_V$  arising from the ISM.

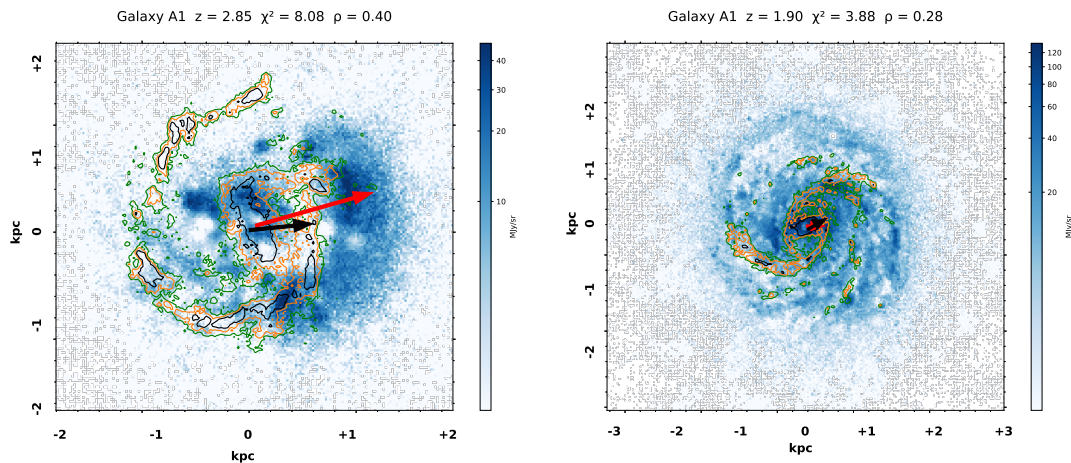


FIGURE 2.3: Visualisations of two views of galaxy A1, in the later stages of its evolution, showing differing degrees of UV–FIR offsets ranging from kpc-scale projected separation (left) to approximately co-spatial (right). In each panel, the image in blue shows the UV emission, the side colourbars showing the flux density of the emission in MJy/sr. The coloured contours show flux density for the FIR emission, ranging from green ( $3 \times 10^4$  MJy/sr), to orange ( $5 \times 10^4$  MJy/sr) to black ( $10^5$  MJy/sr). In each panel, the base of the red vector is positioned at the peak FIR emission and the head at the peak UV emission, the base of the black vector is positioned at the light-weighted mean FIR emission and the head at the light-weighted mean UV emission. The title of each plot gives the galaxy name along with redshift, best-fit  $\chi^2$  and Spearman  $\rho$  value.

The dust library is built from three main components: emission from very small grains ( $< 0.01 \mu\text{m}$ ) which can reach high temperatures if they absorb a UV photon; large grains (between  $0.01 - 0.25 \mu\text{m}$ ) in thermal equilibrium with the interstellar radiation field; and polycyclic aromatic hydrocarbons (PAHs) which are responsible for emission line features in the mid-infrared. The contribution of each component to the SEDs of the birth clouds and the ISM is chosen to broadly reproduce the range of SEDs found in nearby star-forming galaxies. The total IR SED is then modelled as the sum of the ISM and the birth cloud components.

The SFH and dust libraries are linked together in such a manner that the starlight absorbed by dust at short wavelengths is re-radiated at longer wavelengths, i.e. the energy is balanced. During the fit, as well as ensuring that energy conservation (i.e. energy balance) is satisfied by construction (i.e. the luminosity absorbed by dust equals that emitted by dust), MAGPHYS combines those models in the optical library with those in the IR library that have similar contributions from dust in the ISM to the overall dust energy budget (the fraction of luminosity absorbed by the diffuse ISM component and that emitted by the diffuse ISM component, respectively). This is parameterised in MAGPHYS using the  $f_\mu$  parameter; in the high-redshift version used in this work, values for the SFH and dust libraries must have  $\Delta f_\mu < 0.2$  for the

combination to be acceptable. In this way, each galaxy is fitted against a wide variety of ‘empirical but physically-motivated’ (DC08) SFHs and dust content. By calculating the best-fit  $\chi^2$  for each model combination that satisfies the conditions, a likelihood function is built for each galaxy property by assuming that  $L \propto \exp(-\frac{\chi^2}{2})$ . When all combinations of models in the libraries have been processed, a PDF is produced for each property by marginalising the individual likelihoods. MAGPHYS outputs a pair of files for each fitted galaxy: one containing the best-fit SED (an example of both the attenuated and unattenuated versions are shown, alongside the model photometry in Figure 2.1), while the other contains the best-fit model values and the PDFs.

This study uses the high-redshift version of MAGPHYS (da Cunha et al., 2015), which differs from the low-redshift version in two important ways: firstly, the prior distributions are modified to include higher dust optical depths, higher SFRs and younger ages; secondly, the effects of absorption in the inter-galactic medium (IGM) at UV wavelengths are taken into account.

Some studies have sought to determine the extent to which AGN can influence the results of SED fitting (e.g. HS15, Best et al., *in preparation*). However, neither the simulations nor the SED fitting code used in this paper include AGN, and so this important aspect will not be discussed further.

### 2.2.3 Processing the data

To test how well MAGPHYS is able to recover the intrinsic properties of the simulated galaxies, we ran MAGPHYS four times on each synthetic SED, using different combinations of photometry and assumed redshift:

- Run A - used all 18 filters;
- Run B - used all 18 filters, but with all SEDs shifted to a redshift of 2. This run was used as a comparison to detect any bias in the results due to redshift effects. This is discussed in section 2.4.1;
- Run C - used only the UV to near-IR filters ( $u - K$ );
- Run D - used only the FIR filters (PACS  $100 \mu\text{m}$  – SPIRE  $500 \mu\text{m}$ ).

Runs C & D are discussed in section 2.3.2.3. We assumed a signal-to-noise ratio of 5 in every band, following Smith and Hayward (2018).

One of the key aims of this work is to determine how MAGPHYS performs when analyzing galaxies for which the observed UV and FIR emission are spatially ‘decoupled.’ To do this, we characterise the offset between the UV and FIR emission in three different ways:

1. the peak to peak offset: this is defined as the distance in parsecs between the points of maximum flux in the UV ( $0.3\ \mu\text{m}$ ) and FIR ( $100\ \mu\text{m}$ ) images;
2. the light-weighted mean offset: this is defined as the distance in parsecs between the light-weighted centres for the UV ( $0.3\ \mu\text{m}$ ) and FIR ( $100\ \mu\text{m}$ ) emission.
3. the Spearman rank coefficient (Myers and Well, 2003) comparing the degree of correlation between the UV ( $0.3\ \mu\text{m}$ ) image and the FIR ( $100\ \mu\text{m}$ ) image. A Spearman rank coefficient of  $\rho > 0.8$  is considered necessary for a strong correlation. Spearman also returns a  $p$  value indicating a correlation confidence level, 99 per cent of our results returned  $p$  values indicating that the probability of the reported correlation being due to chance was  $< 0.0001$ . The images were filtered to allow only the data points with intensity above the 80th percentile in either the UV or FIR images to be included in the analysis. This was done to avoid the comparatively very large number of low intensity pixels from unduly dominating the result. The 80th percentile was chosen as a reasonable value after comparing the results using different percentile values of the UV and FIR images by eye.

The three proxies were each calculated using the rest-frame UV and FIR maps for each snapshot and view to provide values that would be possible using real observational data with high enough spatial resolution and sensitivity. As an example, Figure 2.3 shows two images of the simulated galaxy A1 in the later stages of its evolution, other examples can be seen in Cochrane et al. 2019. The image on the left shows a significant offset between the UV (shown as the blue image) and FIR (shown as contours) intensity, while in the right image (which has the same colour scheme) the UV and FIR appear almost coincident. In both panels the red vectors show the peak-to-peak offset, while the black vectors show the light-weighted offset. The Spearman  $\rho$  value is given in the title of each panel. We also calculated the offsets using the projected maps of the simulated young stars (age  $< 10$  Myr) and dust; however, there was no significant difference in the results and so the observed offsets are used throughout this paper.

In the following sections, where we compare derived values to true (simulated) values these are expressed as residuals in dex between the 50th percentile of the derived value's likelihood function and the true value:

$$\Delta \log(\text{parameter}) = \log_{10}(\text{derived value}) - \log_{10}(\text{true value}). \quad (2.3)$$

It follows that positive offsets ( $\Delta$ ) represent MAGPHYS over-estimates, and negative values indicate under-estimates. Throughout this work, where MAGPHYS results are shown averaged across the seven views of a snapshot, they are the mean of the individual median likelihood estimates.

## 2.3 Results

In this section we present results from the four runs described in Section 2.2.3. In all runs a successful fit was defined as one where the  $\chi^2$  value was equal to or below the 99 per cent confidence limit ( $\chi_{\text{max}}^2$ ), this was taken from standard  $\chi^2$  tables. The number of degrees of freedom was calculated as in Smith et al. (2012), which perturbed the output best-fit SEDs from MAGPHYS with random samples from the standard normal distribution and found that it depended on the number of bands in the manner shown in Appendix B of that work. We are using the same MAGPHYS model and have assumed that the relation does not vary with the particular choice of bands or the redshifts of the sources being studied.

### 2.3.1 The fraction of mock observations with acceptable fits

From run A we find that MAGPHYS achieved a statistically acceptable fit (i.e.  $\chi^2 \leq \chi_{\text{max}}^2$ ) for 83 per cent (5,567 out of 6,706) of the snapshots. Note that the value of  $\chi_{\text{max}}^2$  varies with redshift because the SKIRT SEDs do not include wavelengths  $< 0.08 \mu\text{m}$ , meaning that we are unable to generate synthetic photometry for the bluest filters at  $z \gtrsim 3.9$ .

The derived  $\chi^2$  values are broadly independent of viewing angle for all galaxies; as an example, Figure 2.4 shows the  $\chi^2$  results for all snapshots and views for the galaxy A1. Figure 2.5 shows how the fit success rate, averaged across all snapshots and views for all four galaxies, changes with redshift. We see from this that MAGPHYS can routinely produce acceptable fits to the

TABLE 2.2: The number of filters available and the value of  $\chi_{\max}^2$  for different redshift ranges.

$z$	filters	$\chi_{\max}^2$
$8.4 \leq z < 6.6$	15	21.67
$6.6 \leq z < 5.0$	16	23.01
$5.0 \leq z < 3.9$	17	24.75
$3.9 \leq z < 1.0$	18	26.72

synthetic photometry up to  $z = 4$ , but that the success rate drops to 50 per cent at  $z \approx 4.85$  and to zero after  $z \approx 5.9$ . Different factors may be contributing to this effect. Firstly, the number of SFHs from the MAGPHYS libraries that are compared with observations is a strong function of redshift. MAGPHYS does not consider SFHs longer than the age of the Universe at a given redshift (the number of SFHs shorter than the Hubble time at each redshift is shown as the dashed line, relative to the right-hand axis in Figure 2.4) and at  $z \approx 5$  the number of such SFHs in the library is only 20 per cent of those available at  $z \approx 1$ . It is therefore clear that the prior is significantly more densely sampled at lower redshifts, leading to more acceptable fits in cases such as this, where the SFH itself is constrained only weakly by the photometry (e.g. Smith and Hayward, 2018). Secondly, at these very early times in the simulations ( $z > 5$ ), the model galaxies are low mass ( $< 10^9 M_{\odot}$ ) and bursts of star formation have a disproportionate influence on a galaxy’s bolometric luminosity. This highly stochastic star formation is not well-modelled by the star formation histories included in the MAGPHYS libraries. It is possible that including additional bands of model photometry may provide better results, e.g. by an additional sub-millimetre datapoint providing an ‘anchor’ point to the Rayleigh-Jeans tail of the dust SED and in doing so enabling tighter constraints on the overall energy balance (though we note that the  $500 \mu\text{m}$  band does sample this side of the dust SED out to  $z \approx 4$ ). However, in this work we have chosen to focus on an example set of photometric data appropriate for studying dusty star-forming galaxies in general, and with an enforced  $\text{SNR} = 5$  in every band we are not subject to some of the sensitivity (or resolution) limitations associated with using real *Herschel* data to study galaxies at the highest redshifts. We therefore defer testing our results with different photometric coverage for a future work. Throughout the remainder of this study, we follow the same approach used in previous MAGPHYS works both observational and numerical (e.g. HS15; Smith et al., 2012; Smith and Hayward, 2018; Smith et al., 2021), and consider only those views for which an acceptable fit was obtained.

To investigate the influence of redshift on the MAGPHYS fit rate further, we used Run B, in which the photometry is modified such that all SEDs were placed at  $z = 2$ . In this run, the

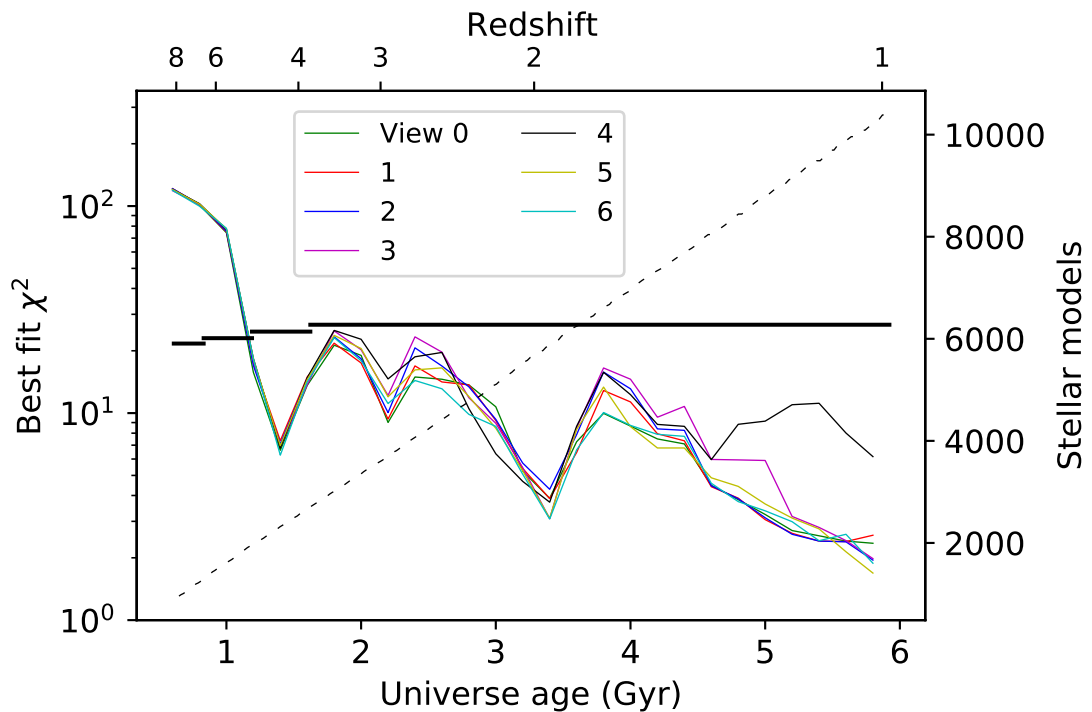


FIGURE 2.4: MAGPHYS produces statistically acceptable fits for virtually all snapshots at  $z < 5$ , irrespective of viewing angle. The best-fit  $\chi^2$  as a function of Universe age is shown for galaxy A1, colour-coded by view number. The  $\chi^2$  values have been averaged over bin widths of  $\Delta z = 0.2$  (relative to the top horizontal axis) for clarity. The horizontal line indicates the  $\chi^2$  threshold below which a fit is deemed acceptable using the Smith et al. (2012) criterion, this value varies with redshift (see Table 2.2). The dashed line indicates the number of stellar models (relative to the right-hand y-axis) available to MAGPHYS at a given redshift with which to compare the input SED. Although not shown here, qualitatively similar results are obtained for the other simulations (A2, A4 & A8).

size of the libraries and therefore the sampling of the priors used for SED fitting is the same for all snapshots. We find that the fit success rate increases to 93 per cent for the forced  $z = 2$  runs, from 83 per cent for run A. Although it is tempting, we cannot attribute this change solely to the weakening of the SFH prior, since it is also possible that sampling different rest-frame wavelengths could impact the fit success rate (e.g. because of individual spectral features being redshifted into a particular observed bandpass; Smith et al., 2012). These effects are discussed further in section 2.4.1.

### 2.3.2 Overall MAGPHYS performance

In studying the fidelity of the MAGPHYS parameter estimates, we have chosen to focus on five properties likely to be of the widest interest, namely SFR and sSFR (both averaged over the last 100 Myr),  $M_{\text{star}}$ ,  $M_{\text{dust}}$  and  $L_{\text{dust}}$ . The true values for  $M_{\text{star}}$ , SFR (averaged over the last 100 Myr),

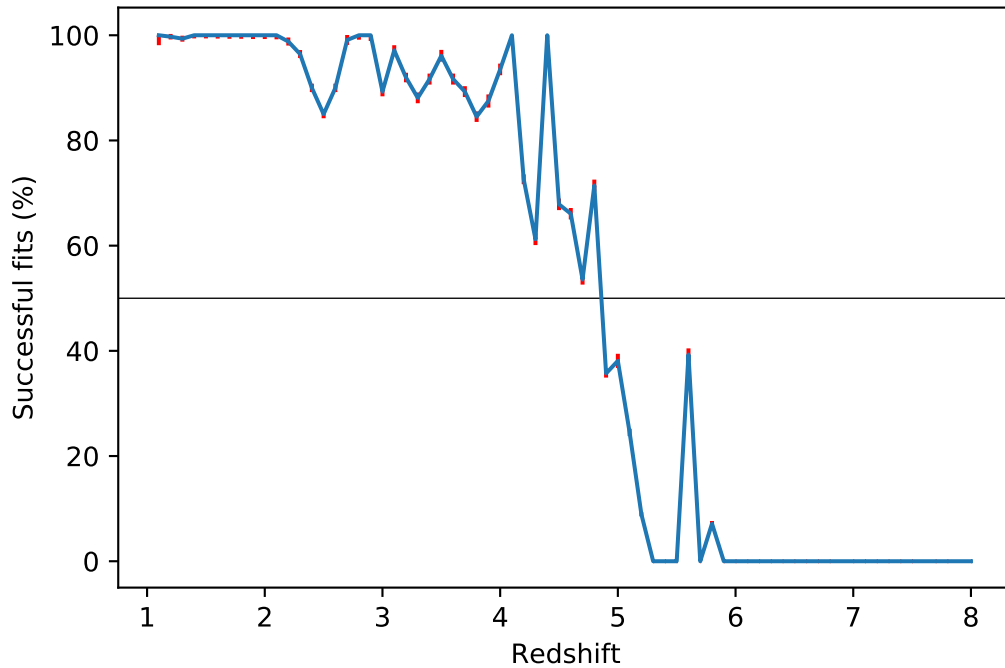


FIGURE 2.5: MAGPHYS success rate in fitting SEDs. The percentage of successful fits averaged across all views and snapshots of all galaxies as a function of redshift, note that standard Poisson errors are too small to be visible. The horizontal line marks a success rate of 50 per cent. The fraction of fits that are statistically acceptable decreases with increasing redshift due to the constraint that the SFH must be shorter than the age of the Universe at that redshift, meaning that the size of the template library decreases with increasing redshift.

and  $M_{\text{dust}}$  were available from the simulation. The true values for  $L_{\text{dust}}$  were calculated by integrating under the SKIRT-produced rest frame SED from  $8\mu\text{m} < \lambda < 1000\mu\text{m}$ , following Kennicutt (1998a).

### 2.3.2.1 The fidelity of MAGPHYS results over time

Figure 2.6 shows the evolution in the true and derived physical properties of our simulated galaxies as a function of redshift (with a second horizontal axis at the top of each column showing the age of the Universe at each redshift in our adopted cosmology). The different physical properties are shown along successive rows, while the different simulated galaxies are shown in successive columns, as indicated in the text at the top of each column. In each panel, the black line indicates the true values for each property, taken from the simulations, while the red line indicates the mean of the median-likelihood MAGPHYS estimates, where the averaging has been conducted over the seven different viewing angles. Similarly, the shaded red region in each

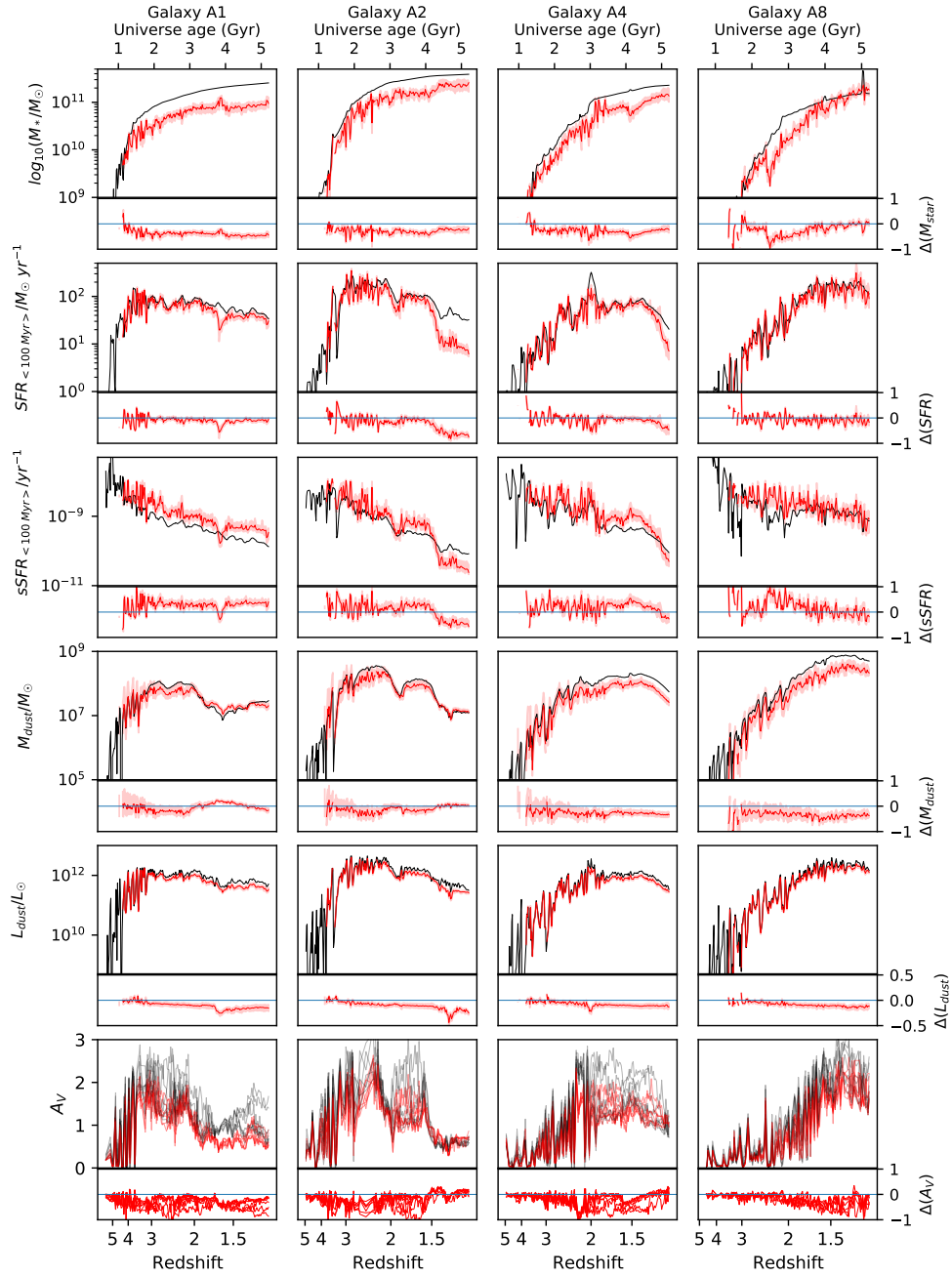


FIGURE 2.6: The overall MAGPHYS parameter estimation (red) compared with the true values from the simulation (black); MAGPHYS captures the overall true properties as a function of redshift. The columns refer to galaxies A1, A2, A4 and A8, respectively. In each row, the upper plot presents the evolution against Universe age (upper  $x$ -axis) and redshift (lower  $x$ -axis), and the lower plot shows the residuals on the same  $x$ -axes (note that the range for  $\Delta L_{\text{dust}}$  is smaller than that for other properties). The top row presents the evolution of stellar mass, while the four subsequent rows present the corresponding evolution of SFR, sSFR,  $M_{\text{dust}}$  and  $L_{\text{dust}}$  respectively. In each main panel, the black line indicates the true values, the red line plots the mean across all views of the median recovered value, and the shaded area indicates the region enclosed by the typical error bar on each parameter (i.e. the mean difference between the 16th/84th percentile and the median, for the upper and lower bounds, respectively). In the final row, the black and red lines in the upper plot show the true and recovered values of  $A_V$  for the different views, while the lower plot shows the residuals for each view.

TABLE 2.3: Mean residuals –  $\Delta\log(\text{parameter})$ , as defined in Equation 2.3 – for each property for each galaxy and the average across all galaxies; a negative value indicates an underestimate. The quoted uncertainties indicate the typical uncertainty that MAGPHYS derives on that galaxy parameter (equal to half the difference between the 16th and 84th percentiles of the derived PDF).

Galaxy	$\Delta\log(M_{\text{star}})$	$\Delta\log(\text{SFR})$	$\Delta\log(\text{sSFR})$	$\Delta\log(M_{\text{dust}})$	$\Delta\log(L_{\text{dust}})$	$\Delta A_V$
A1	$-0.37 \pm 0.08$	$-0.10 \pm 0.06$	$0.26 \pm 0.12$	$-0.05 \pm 0.14$	$-0.10 \pm 0.04$	$-0.30 \pm 0.07$
A2	$-0.28 \pm 0.08$	$-0.21 \pm 0.07$	$0.06 \pm 0.13$	$-0.11 \pm 0.15$	$-0.10 \pm 0.04$	$-0.20 \pm 0.07$
A4	$-0.27 \pm 0.08$	$-0.08 \pm 0.06$	$0.18 \pm 0.13$	$-0.26 \pm 0.19$	$-0.07 \pm 0.04$	$-0.20 \pm 0.07$
A8	$-0.24 \pm 0.09$	$-0.05 \pm 0.06$	$0.19 \pm 0.14$	$-0.35 \pm 0.21$	$-0.08 \pm 0.03$	$-0.19 \pm 0.07$
Mean	$-0.29 \pm 0.09$	$-0.11 \pm 0.06$	$0.18 \pm 0.13$	$-0.19 \pm 0.17$	$-0.09 \pm 0.04$	$-0.22 \pm 0.07$

panel indicates the area enclosed by the mean of the 16th and 84th percentiles of each parameter’s MAGPHYS PDF (once more averaged over the seven views), to give the reader a feel for the typical error bar. Each lower panel shows the residual, e.g.  $\Delta\log(\text{SFR})$ , as defined in Equation 2.3.

In general, MAGPHYS-derived values show a significant degree of consistency, both in the temporal sense and by comparison to the true values. The temporal sense is a valuable test in its own right as, although MAGPHYS fits each snapshot independently, the true values shown in Figure 2.6 mostly vary smoothly with time. That this is reflected in the MAGPHYS estimates once the error bars are taken in to account, offers broad encouragement for the use of MAGPHYS with observational data.

Below, we discuss the degree of fidelity in the MAGPHYS parameter estimates overall by comparing with the true (simulated) values. It is clear based on even a cursory inspection of the trends visible in Figure 2.6 that the MAGPHYS estimates have broadly captured the behaviour visible in the true parameter values, such as increasing stellar mass and generally decreasing sSFR. Similar encouragement was found in the earlier work of HS15, though we now extend this to higher-redshift, dustier galaxies for the first time with a sample of very high-resolution simulations. The mean residuals,  $\Delta\log(\text{parameter})$ , averaged over the full evolution of each simulated galaxy, are shown in Table 2.3.

Averaging the results across all views of all snapshots of all galaxies, we find that the stellar mass is typically underestimated by MAGPHYS, recovered with a mean residual of  $\Delta\log(M_{\text{star}}) = -0.29 \pm 0.09$ . This  $3.22\sigma$  result covers a wide range of simulated scenarios, ranging from the early stages of formation, through periods of starburst, tidal disruptions and merger events. By way of comparison, in HS15 the stellar mass was recovered to within 0.2 dex (which was also

the typical uncertainty in that work) for the vast majority of snapshots, across both the isolated disk and major merger simulations. The principal exception to this excellent recovery being a 0.4 dex underestimate of the stellar mass during the peak period of AGN activity (which we do not simulate here). D20 also reported a larger systematic underestimation of stellar mass, with a deviation of  $-0.46 \pm 0.10$  dex; our results therefore fall between those of these two previous studies. We suggest two factors which may be contributing to this systematic underestimation of the stellar mass. Firstly, a sub-optimal choice of SFH (such as we know we have made in this work, since we can see that the simulated galaxies do not have parametric SFHs in Figure 2.6) has been shown to produce biased results (Carnall et al., 2019) and in particular an underestimate for stellar mass when applied to star forming galaxies (Mitchell et al., 2013; Michałowski et al., 2014). Secondly, Mitchell et al. (2013) and Małek et al. (2018) have shown that the choice of attenuation law has an impact on the estimation on stellar mass (and it is also clear that the two-component geometry assumed by MAGPHYS is not consistent with the ground truth in the simulations where the radiative transfer calculates the attenuation due to ISM dust *in situ*).

In the second row of Figure 2.6, we show that the MAGPHYS SFRs for our simulated galaxies are typically accurate to within  $\Delta \log(\text{SFR}) = -0.11 \pm 0.06$  of the true values ( $1.83\sigma$ ). Of the five properties highlighted in this study, Figure 2.6 shows SFR to be the one for which MAGPHYS produces perhaps the most accurate reflection of the true values once the uncertainties are considered. However, there are some points of disagreement that are worth mentioning. The first example of this is for galaxy A1 at  $z \approx 1.7$ : this deviation of  $\approx -0.59 \pm 0.16$  dex ( $3.7\sigma$ ) coincides with a local minimum of  $M_{\text{dust}}$ , perhaps resulting from a strong outflow, and is associated with a brief reduction in the SFR that is not apparent when averaging over 100 Myr. The second example is for galaxy A2 around  $1.0 \leq z \leq 1.5$  at the point where the galaxy has the highest stellar mass ( $M_{\text{star}} > 10^{11} M_{\odot}$ ), and is the most quiescent that we have simulated ( $\text{sSFR} \approx 10^{-10} \text{ yr}^{-1}$ ). For comparison, HS15 found that SFR was typically recovered to around 0.2-0.3 dex accuracy<sup>5</sup>. D20 reported that SFR was typically underestimated by approximately 20 per cent – very similar to our value of  $\Delta \log(\text{SFR}) = -0.11 \pm 0.06$  dex – attributing this to differences in their adopted SFHs, dust model and geometry.

The observed effects in sSFR mirror those in stellar mass and SFR as expected. Averaging over all snapshots and views, we obtain a mean offset of  $\Delta \log(\text{sSFR}) = 0.18 \pm 0.13$ , a  $1.38\sigma$  result

<sup>5</sup>We note that HS15 compared MAGPHYS 100 Myr-averaged SFRs with instantaneous SFRs rather than values averaged over 100 Myr, as we do here. Due to the bursty SFHs of the simulated galaxies, these values can differ significantly (Sparre et al., 2017; Flores Velázquez et al., 2021b). This topic is further discussed below in connection with  $A_V$  recovery.

which is consistent with the findings of HS15.

Figure 2.6 highlights the excellent recovery of the true dust mass; averaging over all snapshots reveals a mean residual of  $\Delta \log(M_{\text{dust}}) = -0.19 \pm 0.17$  ( $1.12\sigma$ ), suggesting that the results are typically consistent with the true values once the uncertainties are taken into account, consistent with the findings of D20.

Overall  $L_{\text{dust}}$  is well recovered with a mean residual of  $\Delta \log(L_{\text{dust}}) = 0.09 \pm 0.04$ ; this  $2.25\sigma$  result is again in line with the results of HS15. However, the fifth row of Figure 2.6 may suggest a weak trend for a larger  $|\Delta \log(L_{\text{dust}})|$  in the sense that the MAGPHYS estimates increasingly underestimate the true values as the simulations progress and the galaxies develop lower sSFR (though note that the scale of the residual panel for  $L_{\text{dust}}$  is half as large as for the other parameters, which exaggerates the size of the effect). It is possible that the assumptions inherent in the two-component dust model used by MAGPHYS, originally optimised to reproduce the observations of local star-forming galaxies (DC08), are no longer appropriate for the high-mass ( $M_{\text{star}} \approx 10^{11}$ ), highly star-forming ( $\text{SFR} > 20 M_{\odot} \text{yr}^{-1}$ ) galaxies that are simulated here.

Finally, while it is not always the case,  $A_V$  is in general underestimated, with a mean residual of  $\Delta A_V = -0.22 \pm 0.07$  ( $3.14\sigma$ ), similar to the overall fidelity of the stellar mass recovery. This underestimation of the degree of extinction at  $V$  band may be linked to the typical underestimation of the overall dust luminosity, though it is interesting to note this does not prevent excellent recovery of the star formation rate for the majority of snapshots.

### 2.3.2.2 Searching for systematic trends in the MAGPHYS fit results

We used our simulations to determine the consistency of the MAGPHYS-derived galaxy properties across the range of values presented by the simulations. To do this, we binned the residuals defined using equation 2.3 across the full range of each property (stellar mass, SFR, sSFR, dust mass and dust luminosity) from the simulations and plotted the median bin residual. To gauge the significance of our results, we also averaged across all occupants of each bin to calculate the typical uncertainty associated with each MAGPHYS fit (although this is by no means constant in our results), and the scatter within each bin. The median residual, typical error bar, and the 16th and 84th percentile values for the scatter were plotted - see Figures 2.7, 2.8 and 2.9. Systematic trends might be expected to appear as deviations from horizontal lines in these figures; however, our results show that in all cases, the MAGPHYS results are remarkably consistent across the full

range of values once the two sources of scatter are taken into account, and no further systematic trends can be identified.

### 2.3.2.3 The importance of panchromatic data in energy balance fitting

We now discuss runs C and D, originally mentioned in section 2.2.3. Run C used only the UV-NIR photometry from  $u$  to  $K$  band ( $0.4 \mu m < \lambda_{\text{eff}} < 2.2 \mu m$ ), while run D retained only the FIR data from the PACS and SPIRE instruments ( $100 \mu m < \lambda_{\text{eff}} < 500 \mu m$ ). While it is not possible to ‘switch off’ the energy balance criterion in MAGPHYS, runs C and D enable us to make a direct comparison of the results of ‘traditional’ SED fitting (i.e. attempting to recover the stellar mass or dust content of a galaxy from the optical/NIR data alone) with both the true values and the full panchromatic run. In both the starlight-only and FIR-only runs, MAGPHYS must rely on the physically-motivated model and the energy balance assumption to estimate the properties usually associated with the missing observations (e.g. estimating the dust mass purely on the basis of the observed starlight, or the stellar mass using only FIR data).

Figure 2.10 shows the results of these runs comparing the mean  $\log \Delta$  and typical uncertainty for the five properties for each of the three runs A, C & D: full filter set, stellar-only and FIR-only.

The left panel of Figure 2.10 shows the view and snapshot-averaged  $\Delta \log(M_{\text{star}})$  for the three runs. It is immediately clear that although the average  $\Delta \log(M_{\text{star}})$  is very similar for the stellar-only (0.31 dex) and all-filter (0.29 dex) runs, including the full set of data does reduce the typical uncertainty (shown by the error bars) from  $\pm 0.20$  dex to  $\pm 0.09$  dex. Unsurprisingly, attempting to estimate the stellar mass using only the FIR data leads not only to a large  $\Delta \log(M_{\text{star}})$  but also a significantly larger typical uncertainty ( $\approx 0.42$  dex).

In the second panel, we show the corresponding results for  $\Delta \log(\text{SFR})$ . The power of panchromatic fitting is again clear, since the largest  $\Delta \log(\text{SFR})$  and typical uncertainty occur for the stellar-only fits, which can be influenced by the dominance of the lowest-attenuation sightlines (meaning that the amount of obscured star formation can be underestimated) as well as subject to the well-known age-dust degeneracy (e.g. Cimatti et al., 1997). Our results show that FIR-only SFR estimates are more reliable than those using the  $u$  to  $K$ -band photometry alone, since the FIR-only mean  $\Delta \log(\text{SFR}) \approx 0.19 \pm 0.11$  is significantly closer to the true values than the corresponding stellar-only fits which have  $\Delta \log(\text{SFR}) \approx 0.30 \pm 0.29$ .

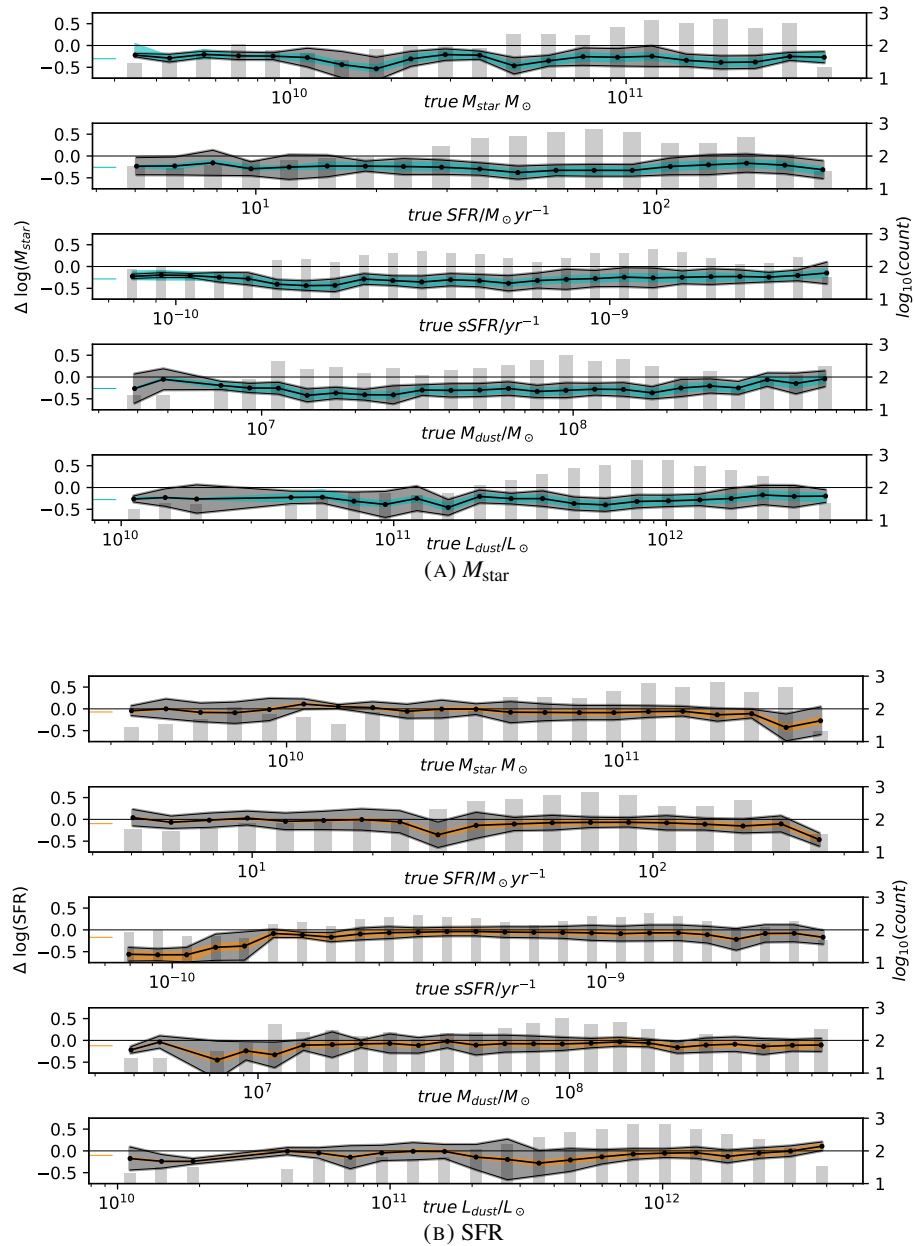


FIGURE 2.7: The fidelity of MAGPHYS' recovery of  $M_{\text{star}}$  and SFR is remarkably consistent across the full range of true galaxy properties. The top five panels plot the relationship between the  $M_{\text{star}}$  residual and true value of the properties  $M_{\text{star}}$ , SFR, sSFR,  $M_{\text{dust}}$ , and  $L_{\text{dust}}$  respectively. The data points in black represent the median value for the residual in log-spaced bins; bin occupancy is shown by the background grey bar chart with log values read from the right-hand axis - note that bins with occupancy  $\leq 20$  have been removed for clarity. In each case the coloured band shows the median 16th and 84th percentile limits for the residuals within the bin and the bounded grey region shows the median 16th and 84th percentile limits for the scatter within the bin. The short coloured line on left-hand of each plot shows the average for the plotted value, residual values are read from the left-hand axis. The lower five panels show the same for the SFR residual.

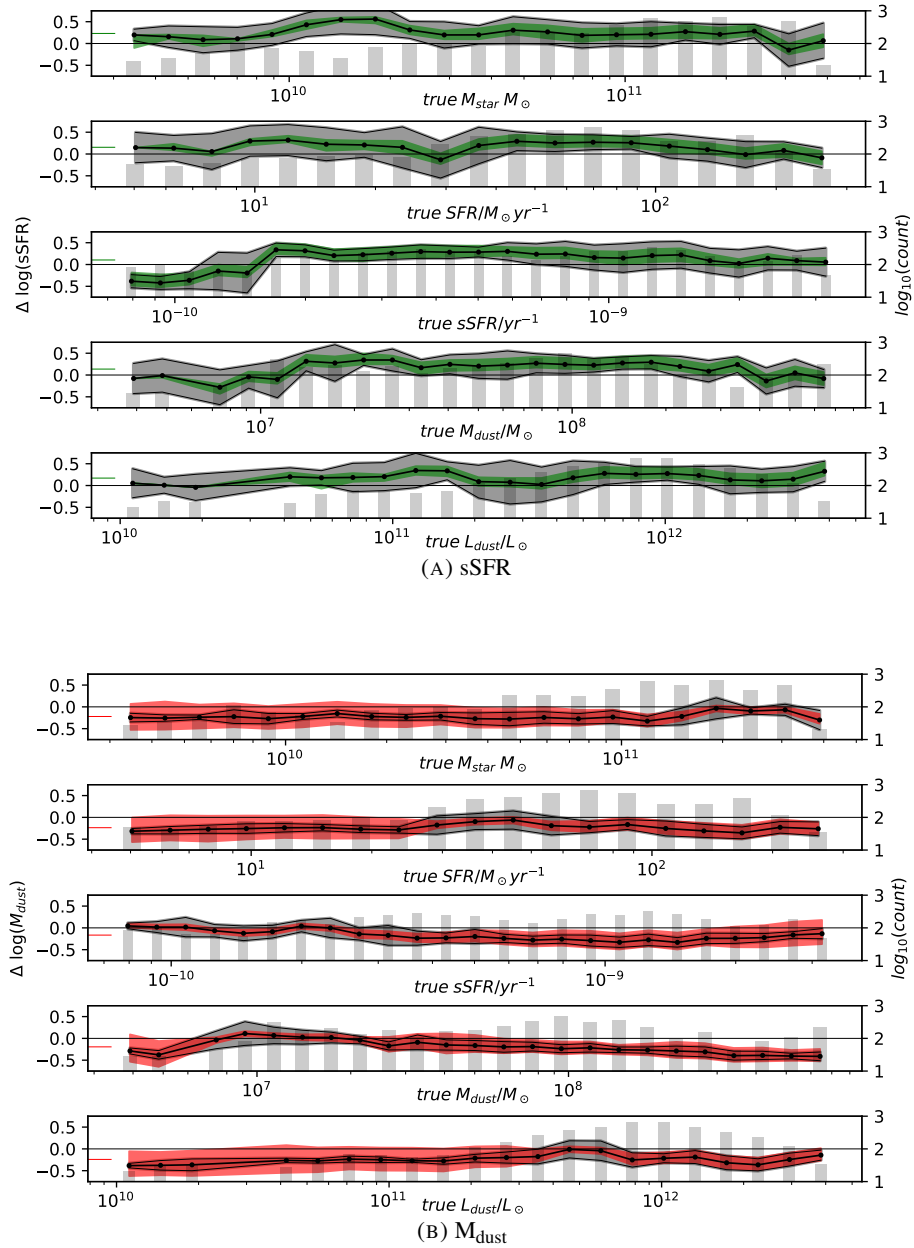


FIGURE 2.8: Similar to figure 2.7, but showing the remarkably consistent recovery of sSFR and  $M_{\text{dust}}$  as a function of the true galaxy properties. The top five panels plot the relationship between the sSFR residual and true value of the properties  $M_{\text{star}}$ , SFR, sSFR,  $M_{\text{dust}}$ , and  $L_{\text{dust}}$  respectively. The data points in black represent the median value for the residual in log-spaced bins; bin occupancy is shown by the background grey bar chart with log values read from the right-hand axis - note that bins with occupancy  $\leq 20$  have been removed for clarity. In each case the coloured band shows the median 16th and 84th percentile limits for the residuals within the bin and the bounded grey region shows the median 16th and 84th percentile limits for the scatter within the bin. The short coloured line on left-hand of each plot shows the average for the plotted value, residual values are read from the left-hand axis. The lower five panels show the same for the  $M_{\text{dust}}$  residual.

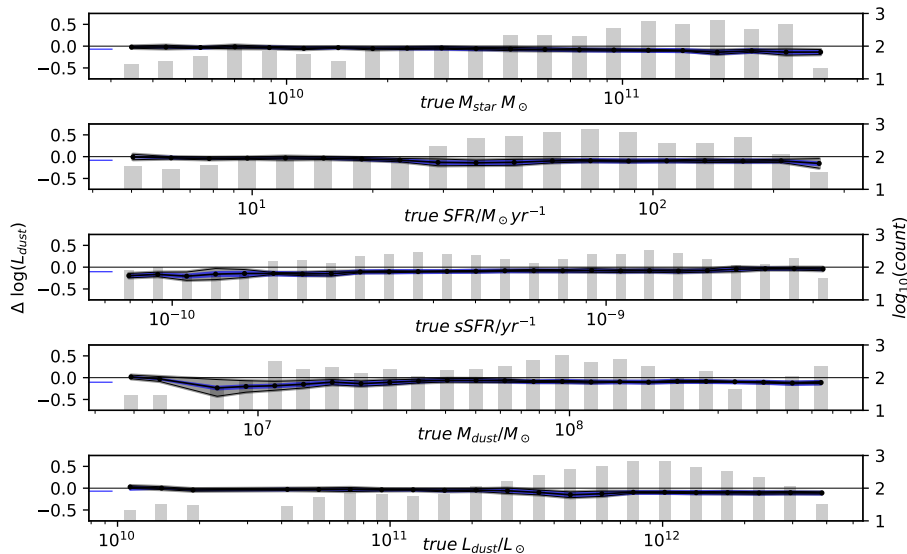


FIGURE 2.9: Similar to figure 2.7, but showing the remarkably consistent recovery of  $L_{\text{dust}}$ . The five panels plot the relationship between the  $L_{\text{dust}}$  residual and true value of the properties  $M_{\text{star}}$ , SFR, sSFR,  $M_{\text{dust}}$ , and  $L_{\text{dust}}$  respectively. The data points in black represent the median value for the residual in log-spaced bins; bin occupancy is shown by the background grey bar chart with log values read from the right-hand axis - note that bins with occupancy  $\leq 20$  have been removed for clarity. In each case the coloured band shows the median 16th and 84th percentile limits for the residuals within the bin and the bounded grey region shows the median 16th and 84th percentile limits for the scatter within the bin. The short coloured line on left-hand of each plot shows the average for the plotted value, residual values are read from the left hand axis.

The situation is even more pronounced for the recovery of the sSFR, with  $\Delta \log(\text{sSFR})$  for the three runs shown in the central panel of Figure 2.10. Although the mean  $\Delta \log(\text{sSFR})$  for the stellar-only run is closest to the true values, the typical uncertainties on the panchromatic run are more than a factor two smaller than the stellar-only estimates. The larger error bar represents a wide range of possible activity levels, making it impossible to unravel the age/dust degeneracy; by adding FIR data, the sSFR is better constrained. This, in turn, enables a constrained determination of the SFR and hence the cause of any observed reddening.

For  $M_{\text{dust}}$ , Figure 2.10 shows that the addition of stellar data makes very little difference to the mean  $\Delta \log(M_{\text{dust}})$  with FIR-only giving results within 0.18 dex and the full filter set 0.19 dex; this is comparable to the typical uncertainties (0.20 dex as opposed to 0.17 dex). Using only the stellar data, the mean  $\Delta \log(M_{\text{dust}})$  is 0.26 dex but the typical uncertainty is significantly increased to 0.64 dex, reflecting the difficulty associated with estimating the dust content of distant galaxies using data probing the starlight alone.

Finally, the right-hand panel of Figure 2.10 shows the recovery of  $L_{\text{dust}}$  across the three runs. Interestingly, although the typical uncertainties are similar for the FIR-only and panchromatic

runs, the inclusion of the UV/NIR data along with the energy balance criterion perhaps increases the mean  $\Delta \log(L_{\text{dust}})$ , although the significance of this difference is low.

### 2.3.3 Measuring the effect of UV/FIR ‘decoupling’ on the fidelity of MAGPHYS results

As discussed above, the primary goal of this work is to examine the fidelity of the MAGPHYS results as a function of the degree of correlation or apparent offset between UV and FIR emission using the three proxies for this ‘decoupling’ described in Section 2.2.3. The results are shown in Figure 2.11, in which the mean  $\Delta$  in dex for each parameter is plotted against the different measures for the degree of separation. Each of the five panels shows the residuals for one of the properties plotted against the degree of separation/correlation as measured by the three proxies. The coloured lines indicate the median residual in log-spaced bins, while the coloured shaded areas show the mean range enclosed by the 16th and 84th percentiles (i.e. the typical  $1\sigma$  error in the limit of Gaussian statistics), and the grey shaded area shows the 16th and 84th percentile range of the scatter within each bin. The bin occupancy is shown by the grey background histogram relative to the right-hand axis. In many cases the scatter is larger than the typical uncertainties, this is likely to be the result of two effects. Firstly, it reflects the fact that the MAGPHYS results contain a range of uncertainties that cannot be adequately summarized by a single error bar (the uncertainties show significant variation and contain outliers). Secondly, the uncertainties produced by MAGPHYS are likely to be underestimates. This is inevitably the case since the range of SEDs contained in any pre-computed library must by definition be smaller than the actual range of galaxy SEDs in the Universe; for example neither real galaxies or those in our simulations have truly parametric SFHs. In addition, the MAGPHYS libraries may not be equally appropriate at all stages of our simulations.

The average performance of MAGPHYS is remarkably consistent, both as a function of the peak-to-peak distance between the UV and FIR images, and as a function of the light-weighted mean UV to FIR distance. In these cases, the mean  $\Delta$  is less than  $\pm 0.3$  dex for all parameters, across the separations ranging from 0 to 10 kpc. In the lower plot of each panel we show the corresponding variation in  $\Delta$  (in dex) as a function of the Spearman  $\rho$  calculated by comparing the UV and FIR images (recall that only the brightest 20 per cent of pixels were included in this calculation). Here again, the logarithmic difference between the derived and true properties appears independent of  $\rho$  once the mean uncertainties are taken in to account.

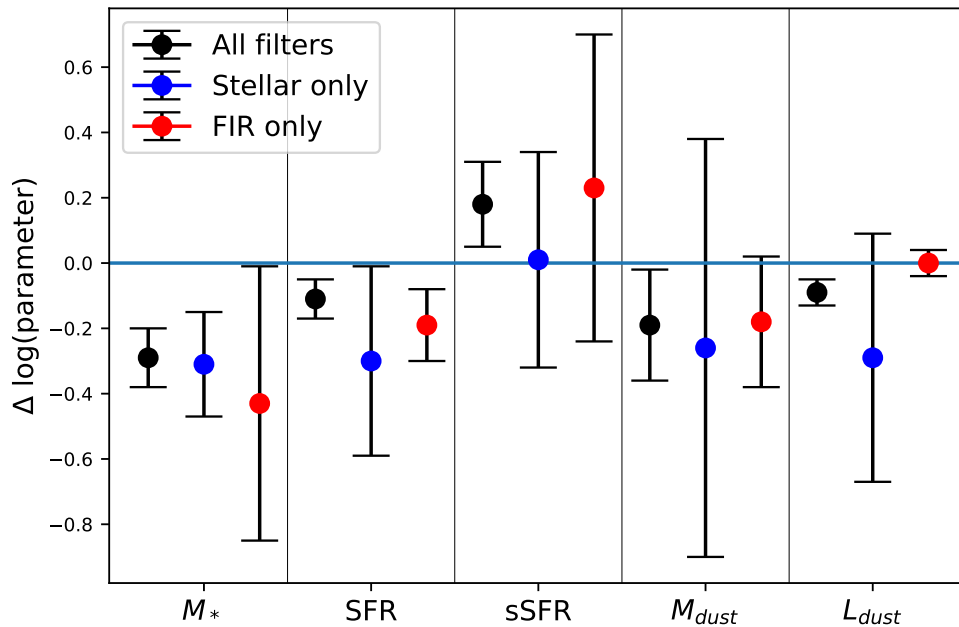


FIGURE 2.10: Using MAGPHYS to model panchromatic data gives better overall constraints on galaxy properties than sampling only a subset of the available wavelengths.  $\Delta \log(\text{parameter})$  for each parameter of interest, averaged across all galaxies for three different MAGPHYS runs: (i) including all available photometry, (ii) stellar only - including only those bands that sample the starlight ( $0.4\mu\text{m} < \lambda_{\text{eff}} < 2.2\mu\text{m}$ ), and (iii) FIR only - including only the FIR data ( $100\mu\text{m} < \lambda_{\text{eff}} < 500\mu\text{m}$ ), with each set of results colour-coded as in the legend. The error bars on each data point represent the mean uncertainty for each MAGPHYS estimate, based on using the 16th and 84th percentiles of the estimated PDFs.

## 2.4 Discussion

### 2.4.1 The redshift dependence of the MAGPHYS fit success rate

In section 2.3.1 we showed that the fit success rate was a strong function of redshift, with 83 per cent of the mock observations having acceptable  $\chi^2$  overall, but no good fits being obtained at  $z > 5.9$ . Fixing each mock to be observed at  $z = 2$  (Run B) resulted in an increase in the overall success rate to 93 per cent. A likely explanation for this is that the number of SFHs in the MAGPHYS library is a strong function of redshift (shown as the dashed line in figure 2.4, due to the requirement of considering only SFHs shorter than the Hubble time at the observed redshift), which results in significantly worse sampling of the priors at early epochs, particularly when the SFHs of galaxies are so weakly constrained by photometry (e.g. Smith and Hayward, 2018).

In support of this idea, Figure 2.12 shows the ratio of the best-fit  $\chi^2$  obtained for our fiducial results (native redshift run A) to the corresponding value for the SEDs fixed to  $z = 2$  (run B).

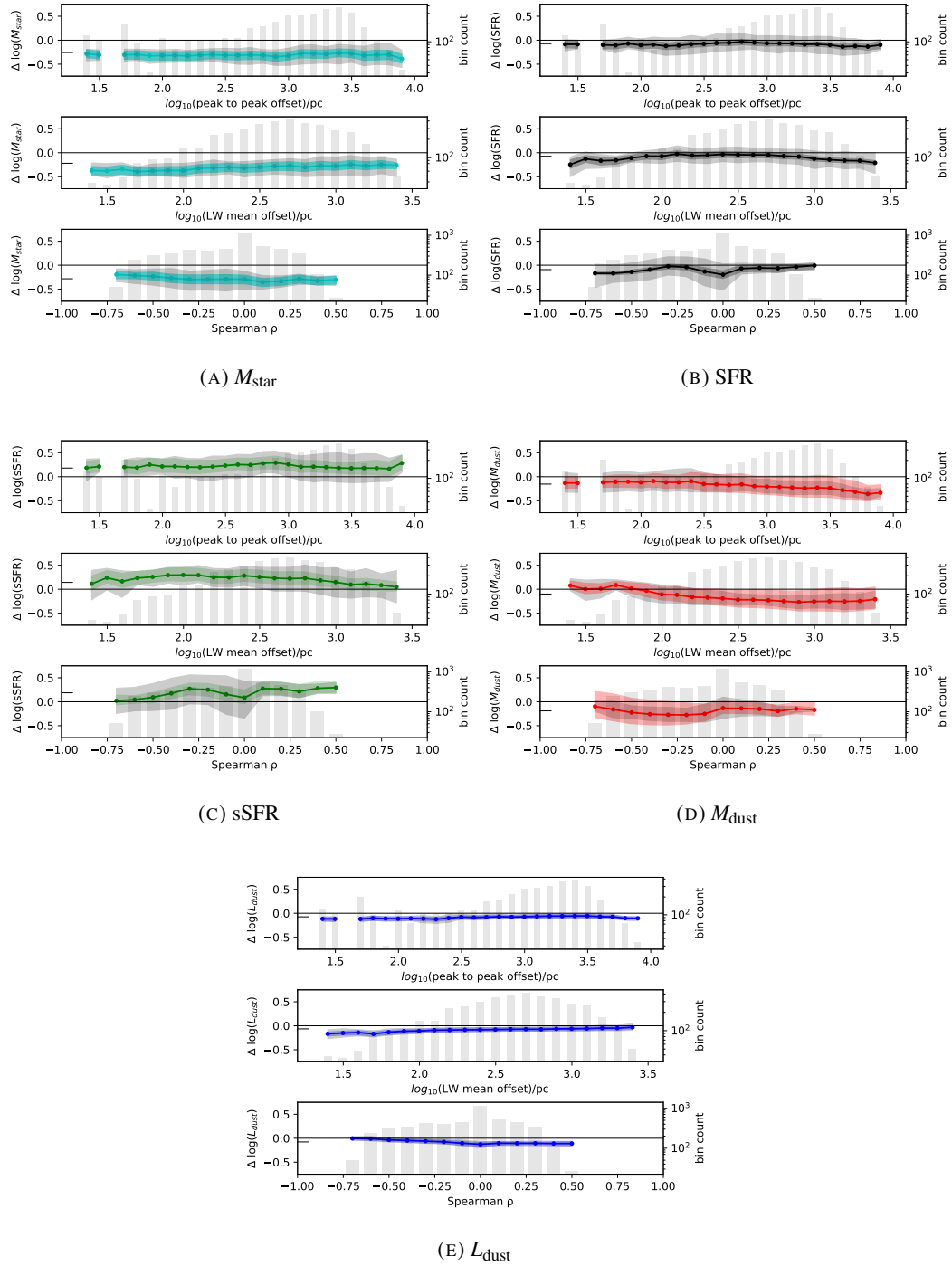


FIGURE 2.11: The fidelity of MAGPHYS is largely independent of the extent of any UV/FIR offset, as measured by the three proxies, once the uncertainties are considered.  $\Delta \log(\text{parameter})$  as a function of three proxies for the difference between the UV and FIR images - panel (a) presents the data for  $M_{\text{star}}$ , (b) for SFR, (c) for sSFR, (d) for  $M_{\text{dust}}$  and (e) for  $L_{\text{dust}}$ . For each property, the data points represent the mean over all views and snapshots in that bin. The shaded area of the same colour indicates area enclosed by the mean 16th and 84th percentile values within the bin. The grey shaded area shows area enclosed by the 16th and 84th percentile values for the scatter within each bin. The top plot in each panel shows the logarithmic difference  $\Delta$ , as a function of the peak-to-peak distance between the UV and FIR images; the second and third panels show the corresponding  $\log \Delta$  as a function of the light-weighted mean UV-FIR offset and the Spearman rank correlation coefficient  $\rho$  between the 20 per cent brightest pixels in either the UV or FIR images. The short coloured lines adjacent to the left-hand y-axis represent the overall mean value. The grey histograms in each panel (a) to (e) show the bin occupancy relative to the right-hand axis.

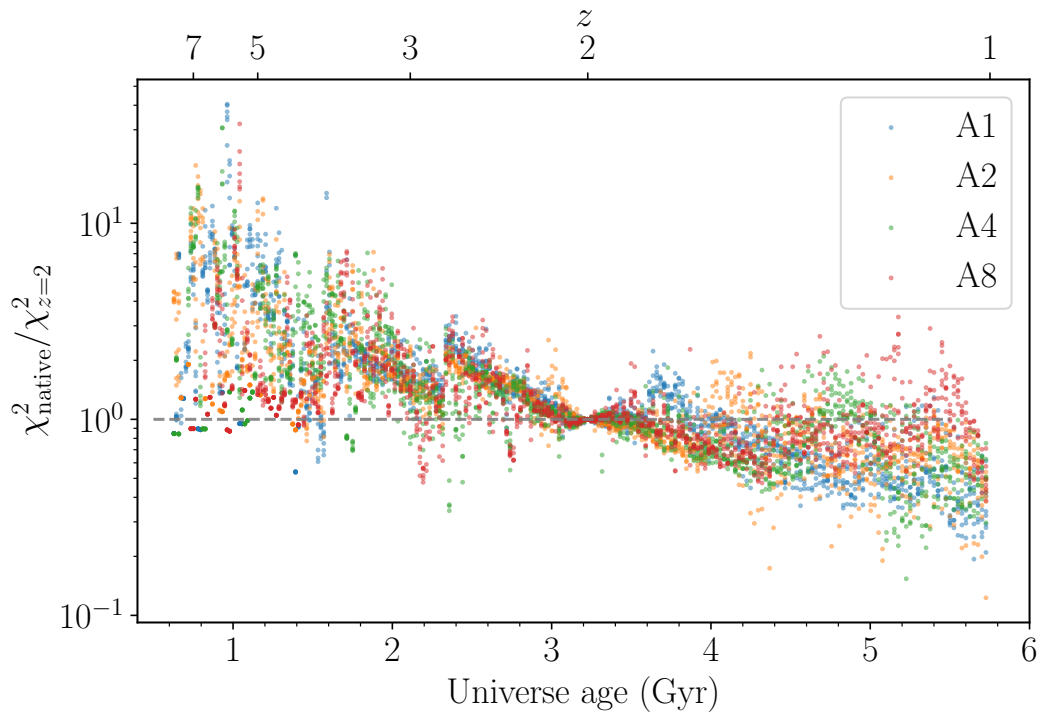


FIGURE 2.12: The best-fit  $\chi^2$  depends on the size of the MAGPHYS library, which varies with the redshift assumed for the fit. This plot shows the ratio of best-fit  $\chi^2$  obtained for run A (at the native redshift) to that obtained in run B (where all SEDs were fixed to  $z=2$ ). For galaxies on the left-hand side of this plot the prior gets larger in run B, while for galaxies viewed at later times, the opposite effect is apparent.

It is clear that there is a systematic trend for the native  $\chi^2$  to be worse at  $z > 2$  (corresponding to a Universe age of  $\leq 3.2$  Gyr in our adopted cosmology) and better at  $z < 2$ . However this trend is by no means absolute, indicating that other effects such as the precise details of the rest-wavelengths being sampled and the number of available filters may also be playing a role.

Interestingly, that the ratio of  $\chi^2$  for run A to that of run B does not converge on the right-hand side of this plot may indicate that the size of the MAGPHYS prior library still impacts the fit quality even at  $z < 2$ , though of course the difference is that at these comparatively late epochs the priors are sufficiently well-sampled to obtain statistically acceptable fits to the data.

#### 2.4.2 The fidelity of MAGPHYS results for dusty, high-redshift galaxies

The principal aim of this study is to determine how the fidelity of the energy balance code MAGPHYS is impacted when it is applied to high-redshift galaxies for which the observed UV and FIR emission are offset, or spatially ‘decoupled’. For such galaxies, the observed UV light potentially originates from young star clusters that are not spatially co-located with the young

stars that dominate the dust heating and thus FIR emission. Consequently, it is possible that the relatively unobscured young stars could yield a blue UV-optical slope and cause SED modelling codes to underestimate the attenuation. It has been shown that the use of panchromatic data is important when fitting such galaxies (Roebuck et al., 2019), and fitters such as MAGPHYS use energy balance to produce physically motivated, panchromatic models that seek to minimise this underestimation. We determine the efficacy of this approach by analyzing the logarithmic difference,  $\Delta$ , between the true and median-likelihood estimates for stellar mass, SFR, specific SFR, dust mass and dust luminosity as a function of three proxies for the degree of ‘decoupling’ between the UV and FIR data.

In all cases, the performance of MAGPHYS appears independent of the degree of UV/FIR ‘decoupling’ as measured by all three proxies. We therefore conclude that energy balance SED fitting codes can perform just as well in the presence of such effects as they do when the dust and young stars are co-located within a galaxy.

We suspect that the explanation for this success is that the Charlot and Fall (2000) dust attenuation model used by MAGPHYS is sufficiently flexible to handle this ‘decoupling’ in many cases and that the  $\chi^2$  algorithm is doing its job by identifying cases for which the model cannot yield a self-consistent solution (i.e. very low attenuation but high FIR luminosity). This has been shown to be the case for an un-modeled AGN contribution to the SED: Smith et al. (2021) noted that using the  $\chi^2$  threshold from Smith et al. (2012), which we have also implemented here, had the effect of flagging the vast majority of LOFAR-detected AGN as bad fits unless the AGN contribution to the emergent luminosity was very small. Of course, it is expected (e.g. Witt and Gordon, 2000) and observed (e.g. Kriek and Conroy, 2013; Boquien et al., 2022; Nagaraj et al., 2022) that the attenuation law is not universal and instead varies by galaxy type. Should additional flexibility be required in future, we note that other works have explored implementing modifications to the standard dust law, including Battisti et al. (2019) who added a 2175Å feature to remove a systematic redshift effect, as well as Lo Faro et al. (2017) and Trayford et al. (2020) who allowed the power law indices of equations 2.1 & 2.2 to vary. However, the fact that there is no scope to easily modify the dust parameterisation assumed in MAGPHYS leaves us no option but to defer further investigation of this potentially important aspect for a future work.

The reason that some have claimed that energy balance should fail in galaxies with significant IR-UV offsets is that the unobscured lines of sight should dominate the UV emission, meaning that the attenuation that would be inferred from the observed UV-optical emission would be less

than the total attenuation experienced by the stellar population as a whole. However, energy balance codes such as MAGPHYS use the FIR luminosity as a simultaneous constraint on the attenuation, and it would simply not be possible to obtain a satisfactory fit to both the UV-optical and FIR regions of the SED assuming low attenuation when the FIR luminosity is high.<sup>6</sup> Furthermore, we note that even in ‘normal’ galaxies that do not exhibit significant UV-FIR offsets, stars of a given age are not all subject to the same amount of attenuation (e.g. the Charlot and Fall 2000 dust model). Instead, even for a single age and line of sight, there is a distribution of dust optical depths, and this distribution varies with both the stellar age and line of sight considered. The Charlot and Fall (2000) model attempts to capture this complex age and line of sight dependence using only two effective optical depths. Though this underlying model is certainly very crude compared to both the simulations and real galaxies, HS15 have already shown that it is adequate to correct for the effects of dust attenuation in at least some low-redshift galaxies. There is no *a priori* reason to believe that it should ‘break’ above some offset threshold (which was the motivation for this study). Our results demonstrate that even when the width of the optical depth distribution experienced by young stars is very wide (i.e. in our simulations some young stars are almost completely unobscured, whereas others have line-of-sight UV optical depths  $\gg 1$ ), the Charlot and Fall (2000) model can still adequately capture the overall effects of dust attenuation in most cases.

## 2.5 Conclusions

Recent works (e.g. Hodge et al. 2016; Casey et al. 2017; Miettinen et al. 2017; Simpson et al. 2017; Buat et al. 2019) have questioned whether energy balance SED fitting algorithms are appropriate for studying high-redshift star-forming galaxies, due to observations of offsets between the UV and FIR emission (e.g. Hodge et al., 2016; Rujopakarn et al., 2016; Chen et al., 2017; Bowler et al., 2018; Gómez-Guijarro et al., 2018; Rujopakarn et al., 2019). Clumpy dust distributions within these galaxies may cause a small fraction of relatively unobscured young stars to influence the blue UV-optical slope and result in an underestimation of the attenuation even if the bulk of the young stars are completely dust-obscured. We have used four cosmological zoom-in simulations of dusty, high-redshift galaxies from the FIRE-2 project, together with the

<sup>6</sup>It is tempting to investigate this by making a plot similar to figure 2.11 but including only those fits that exceed the  $\chi^2$  threshold we use to identify the bad fits. However, since the best-fit model is statistically unacceptable, we cannot believe the parameter estimates produced by MAGPHYS in these cases, meaning that such a test is not meaningful.

radiative transfer code SKIRT, to generate over 6,700 synthetic galaxy SEDs spanning a redshift range  $8 > z > 1$ . We used these model data to test the fidelity of the galaxy properties recovered using the energy balance fitting code MAGPHYS with 18 bands of UV–FIR photometry, building on our previous related studies (HS15, Smith and Hayward 2015, 2018). Our principal findings are as follows:

- We find that the high- $z$  version of MAGPHYS was able to produce statistically acceptable best-fit SEDs for 83 per cent of the synthetic SEDs that we trialed. The fit success rate fell to 50 per cent for galaxies at  $z > 4.85$  and zero for galaxies at  $z > 5.9$ . This reduction in fit success rate has two main contributing factors:
  1. the fixed MAGPHYS libraries, combined with the requirement that model SFHs should be shorter than the age of the Universe at any given redshift reduces the size of the MAGPHYS library available at higher redshifts, mean that the priors become increasingly poorly sampled at earlier times;
  2. the evolution of the simulated galaxies is increasingly stochastic at the earliest times in our simulations due to their lower mass, causing bursts of star formation to have a disproportionate influence on a galaxy’s bolometric luminosity that cannot be reconciled with the MAGPHYS prior libraries.
- Where statistically acceptable best-fits were obtained, we found that MAGPHYS fits are able to broadly capture the true evolution of the four zoom-in simulations that we studied (steady build-up of stellar mass, generally decreasing sSFR, evolution of dust mass), despite individual snapshots being fit independently. In addition, we find that the fidelity of this recovery is remarkably consistent across a broad range of galaxy properties sampled by the simulations, showing no evidence for strong systematics as a function of stellar mass, SFR, sSFR, dust mass or dust luminosity.
- Combining UV to FIR observations with an energy balance SED fitting code provides a powerful way to combine multi-wavelength data, and obtain the most reliable estimates of the ground-truth galaxy properties. The panchromatic results outperform those obtained by using either the stellar or dust emission alone.
- We find no evidence that the performance of MAGPHYS depends on the degree of spatial ‘decoupling’ between the UV and FIR data, despite suggestions to the contrary by several other works. Indeed, our results show that the fidelity of the galaxy properties derived is

very similar to that observed for local galaxies, e.g. in our previous work (Hayward and Smith, 2015).

## Chapter 3

# Beware the recent past: a bias in spectral energy distribution modelling due to bursty star formation

### 3.1 Introduction

Star formation rates (SFRs) and star formation histories (SFHs) are both of great importance to our understanding of galaxies. SFRs are critical since (along with their stellar mass) they enable us to put galaxies in their contemporary context relative to the evolving SFR–stellar mass relation (e.g. Noeske et al., 2007b). SFHs encode the build-up of stellar mass in the Universe (Dye, 2008), potentially yielding insight into the physical processes that drive galaxy evolution (e.g. Madau et al., 1996; Behroozi et al., 2013; Wang et al., 2022). SFRs and other galaxy properties can be inferred for high-redshift galaxies by fitting a model spectral energy distribution (SED) to available data, which can include spectroscopy as well as photometry. There are many freely-available SED fitting codes able to do this (as discussed by e.g. Walcher et al., 2011; Conroy, 2013; Baes, 2020).

SED models frequently differ in their approach and assumptions in important ways which potentially impact the fidelity of inferred galaxy properties (Hunt et al. 2019, Pacifici et al. 2023). For example, they may employ different stellar population synthesis models (e.g. Bruzual and Charlot 2003, Maraston 2005, Conroy et al. 2009; see also Baldwin et al. 2018), initial mass

functions (IMFs; e.g. Salpeter 1955, Kroupa 2001, Chabrier 2003; see also Kroupa and Jerabkova 2019), dust models (e.g. Calzetti 1997, Charlot and Fall 2000, Draine and Li 2007, da Cunha et al. 2008) and SFH forms. These can be parametric or non-parametric; while the former typically use one of many simple functional forms to represent the SFH (e.g. Behroozi et al., 2013; Simha et al., 2014; Carnall et al., 2019), the latter can be implemented e.g. by partitioning the history into time bins and allocating stellar mass to each bin from a chosen prior distribution as the observations allow (e.g. Leja et al. 2019).

Many SED fitters, including those used in this study, assume balance between the energy absorbed by dust at short wavelengths and that re-radiated in the far-infrared. While this must be true overall, strict equality should not hold for every line of sight since dust attenuation is non-isotropic. Recent observations of spatial offsets between the starlight and dust in high-redshift galaxies (e.g. Hodge et al., 2016, 2019; Cochrane et al., 2021) cast doubt on whether these codes are appropriate in such cases. However Haskell et al. (2023, hereafter H23/Chapter 2) showed that the performance of MAGPHYS is similar for galaxies with UV/FIR spatial offsets as it is for local galaxies (Hayward and Smith, 2015); energy-balance codes remain the gold standard for deriving the properties of galaxies from photometric surveys.

With myriad codes available, with different physics and underlying assumptions, it is critical to validate the performance of each method. As well as the works of this group, which have compared the physical properties inferred using energy-balance SED fitting with MAGPHYS to simulated galaxies for which the ‘ground truth’ properties are known (Hayward and Smith 2015; Smith and Hayward 2015, 2018; H23/Chapter2), there is a large body of work by other authors aiming to understand how well SED fitting works in different ways (e.g. da Cunha et al. 2008, Lee et al. 2009, Noll et al. 2009, Wuyts et al. 2009, Lee 2010, Pforr et al. 2012, Simha et al. 2014, Mobasher et al. 2015, Hunt et al. 2019, Dudzevičiūtė et al. 2020, Lower et al. 2020, Pacifici et al. 2023, Best et al. 2023). Since validation tests are often accomplished by averaging over a large population of galaxies, there is always danger of “washing out” important details or systematic effects that could impact our understanding of how well SED fitting methods work in real-Universe situations. For example, recent papers have shown that non-parametric models are better able to recover model SFHs with recent sharp changes than fitters using parametric SFHs (hereafter pSFHs; e.g. Leja et al. 2019, Carnall et al. 2019, Suess et al. 2022, Narayanan et al. 2023a).

Here, we build on H23/Chapter 2 and run the PROSPECTOR SED fitting code on the same

synthetic galaxy SEDs for which we already have MAGPHYS fits, focusing on how the inferred SFR depends on the recent SFH within the last 100 Myr. Galaxies experiencing rapid changes in SFR over short ( $\sim 10$ s-100s of Myr) timescales have been identified both observationally (e.g. Guo et al. 2016, Faisst et al. 2019, Broussard et al. 2022, Looser et al. 2023, Wang et al. 2023, Woodrum et al. 2023) and in simulations (e.g. Sparre et al. 2017, Iyer et al. 2020, Flores Velázquez et al. 2021a, Hopkins et al. 2023a, Narayanan et al. 2023a, Dome et al. 2024). In the FIRE simulations, massive galaxies at high redshift and dwarfs at all redshifts exhibit very bursty SFHs, with short ( $\sim 10$ -Myr) bursts followed by temporarily quenched periods<sup>1</sup> lasting a few 100 Myr; see Sparre et al. (2017) for a detailed analysis and Hayward and Hopkins (2017) and Hopkins et al. (2023a) for discussions of the physical origin of this behavior. They thus provide an excellent test data set for exploring the effects of bursty star formation on SED modelling inferences.<sup>2</sup>

In this work, we demonstrate that MAGPHYS results exhibit a systematic bias in the inferred SFR: the SFR is overestimated (underestimated) for simulated galaxies experiencing a burst (temporarily quenched period). We also show that PROSPECTOR SFRs do not exhibit this bias. This Letter is structured as follows. In Section 3.2 we outline the tools and methods used to create the observations and to fit the SEDs, while in Section 3.3 we present the results of the fitting, and in Section 3.4 discuss the implications. In Section 3.5 we make some concluding remarks. We adopt a standard cosmology with  $H_0 = 70 \text{ km s}^{-1} \text{ Mpc}^{-1}$ ,  $\Omega_M = 0.3$ , and  $\Omega_\Lambda = 0.7$ .

## 3.2 Method

To provide the synthetic SEDs used for this test, we used four cosmological zoom-in simulations of massive high-redshift galaxies from the FIRE project.<sup>3</sup> The halos were first presented in Feldmann et al. (2016), and subsequently resimulated by Anglés-Alcázar et al. (2017) using the FIRE-2 code (Hopkins et al., 2018); we use the simulations from that work. The simulations use the code GIZMO (Hopkins, 2015),<sup>4</sup> with hydrodynamics solved using the mesh-free Lagrangian Godunov ‘MFM’ method. The simulations include cooling and heating from a

<sup>1</sup>We will use the shorthand ‘temp-quenched’ to refer to the periods of low-specific SFR between bursts that are common in the FIRE simulations analysed here. We use the term ‘starburst’ to refer to simulated galaxies that are currently undergoing a burst, i.e. the 10 Myr-averaged SFR is greater than the 100 Myr-averaged value.

<sup>2</sup>Owing to the lack of AGN feedback in these simulations, none of the simulated galaxies are permanently quenched. However, since the bias depends on the SFH over the past 100 Myr, our conclusions should apply equally to permanently- as well as temp-quenched galaxies.

<sup>3</sup><http://fire.northwestern.edu>

<sup>4</sup><http://www.tapir.caltech.edu/~phopkins/Site/GIZMO.html>

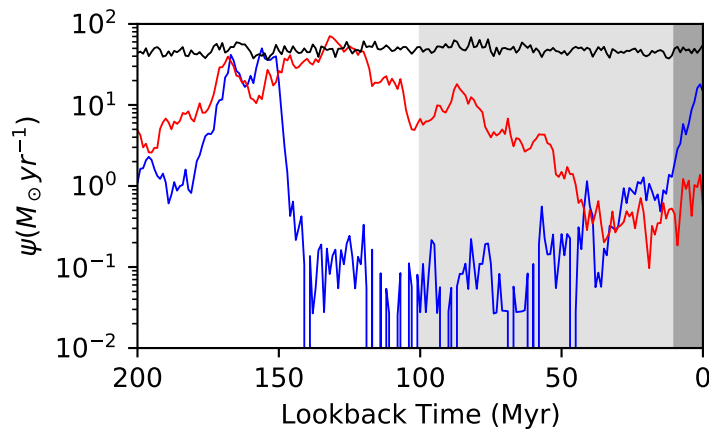


FIGURE 3.1: The recent SFHs (past 200 Myr) of three example simulated galaxies, showing a range of  $\eta$  values. The dark grey band encloses the previous 10 Myr, while the lighter band encloses the past 100 Myr;  $\eta$  is the ratio of the SFRs averaged over those two time periods. The black line shows an example of constant star formation with  $\eta \approx 0$ , while the red line shows a ‘temporarily quenched’ case ( $\eta = -0.64$ ). The blue line shows an example simulated galaxy observed during a burst, where the star formation activity averaged over the previous 10 Myr has increased compared to the average over the previous 100 Myr (giving  $\eta = 0.88$ ).

meta-galactic background and local stellar sources from  $T \sim 10 - 10^{10}$  K; star formation in locally self-gravitating, dense, self-shielding molecular, Jeans-unstable gas; and stellar feedback from OB & AGB mass-loss, SNe Ia & II, and multi-wavelength photo-heating and radiation pressure, with inputs taken directly from stellar evolution models. The FIRE physics, source code, and all numerical parameters are identical to those in Hopkins et al. (2018).

Snapshots of the halos’ central galaxies were taken from  $1 < z < 8$  at intervals of 15 – 25 Myr. For each snapshot, we compute the true 10 Myr and 100 Myr-averaged SFRs,  $\bar{\psi}_{10\text{Myr}}$  and  $\bar{\psi}_{100\text{Myr}}$ , respectively. Following Broussard et al. (2019), we quantify the recent star forming activity using the ‘burst indicator’  $\eta = \log_{10}(\bar{\psi}_{10\text{Myr}}/\bar{\psi}_{100\text{Myr}})$ , such that

$$\eta \begin{cases} < 0, & \text{galaxy has reduced SFR within the last 10 Myr;} \\ \approx 0, & \text{galaxy has had a constant SFR over the last 100 Myr;} \\ > 0, & \text{galaxy has increased SFR in the last 10 Myr.} \end{cases}$$

Figure 3.1 shows three example SFHs of snapshots used in this study with  $\eta \approx 0$  (black line),  $\eta < 0$  (red line) and  $\eta > 0$  (blue line).

Cochrane et al. (2019) calculated synthetic SEDs for these simulated galaxies using the radiative

transfer code SKIRT.<sup>5</sup> Each snapshot was ‘observed’ at 7 viewing angles spaced at 30° intervals, ranging from aligned with the angular momentum vector to anti-aligned. This resulted in 6,706 forward-modeled SEDs. See Cochrane et al. (2019, 2022, 2023c,a) and Parsotan et al. (2021) for further details about the SKIRT calculations and other applications of these and similar simulations/SEDs. We convolved these SEDs with the filter response curves for 18 photometric bands spanning observed-frame wavelengths  $0.39 < \lambda/\mu\text{m} < 500$  (we refer the interested reader to H23/Chapter 2 for further details) assuming a signal-to-noise ratio of 5 in every band (following Smith and Hayward, 2018). We fit the synthetic SEDs using two SED fitting codes, MAGPHYS (da Cunha et al., 2008, hereafter DC08) and PROSPECTOR (Leja et al. 2017, 2019, Johnson et al. 2021), fixing the redshift to the true value (i.e. photometric redshift errors do not contribute to the bias demonstrated here). We use the high-redshift version of MAGPHYS (da Cunha et al., 2015) which builds model UV–FIR SEDs by linking a stellar library containing 50,000 pre-computed SFHs with those which satisfy the energy balance criterion among another pre-computed library of 25,000 Charlot and Fall (2000) dust models; see DC08 and H23/Chapter 2 for detailed discussions. By calculating the  $\chi^2$  goodness-of-fit parameter between the observed photometry and every combination which satisfies the energy balance, MAGPHYS is able to marginalise over the prior distribution to estimate posterior probability distributions for each property in the model. MAGPHYS assumes an initial mass function (IMF) from Chabrier (2003), and stellar models from Bruzual and Charlot (2003) for metallicity between 0.02 and 2 times solar.

For the PROSPECTOR fits, we followed the process described in Das et al. (2024). PROSPECTOR uses the Flexible Stellar Populations Synthesis (FSPS; Conroy et al., 2009) code assuming a Kroupa (2001) IMF and solar metallicity. Dust attenuation is modelled using the two-component Charlot and Fall (2000) model and the Kriek and Conroy (2013) attenuation curve. The three-parameter Draine and Li (2007, hereafter DL07) dust emission templates are used to model the shape of the IR SED. The dynamic nested sampling library Dynesty (Speagle, 2020) is used to estimate Bayesian posteriors and evidences.

For both fitters, we consider an SED fit to be acceptable if the best fit  $\chi^2$  is below the 99 per cent confidence limit taken from standard  $\chi^2$  tables with the degrees of freedom calculated following Smith et al. (2012, who calculated this only for MAGPHYS; here we assume that it applies equally well to the PROSPECTOR results, though this is perhaps unlikely to be true given the differences between the two sets of models). Throughout the subsequent analysis, we consider

---

<sup>5</sup><http://www.skirt.ugent.be/>

only those SEDs with satisfactory fits, though our conclusions are qualitatively unchanged if we also consider the “bad fits”.

Based on these analyses, we obtained five sets of SFR estimates for each snapshot. The MAGPHYS SFRs assume a fixed parameterisation of the SFH based on a parametric model overlaid with random starbursts (as detailed in DC08). In addition, we have four sets of results from PROSPECTOR, assuming different SFH priors: parametric, Dirichlet, continuity, and bursty continuity. The parametric prior assumes a delayed exponentially declining SFH, and does not account for bursts.<sup>6</sup> The Dirichlet prior assumes that the fractional specific star formation rate (sSFR) in each time bin follows a Dirichlet distribution, with a concentration parameter,  $\alpha$ , that controls the shape of the SFH (Leja et al., 2017, 2019), and which we set to unity. The continuity prior directly fits for  $\Delta \log(\text{SFR})$  between neighbouring time bins using a Student’s  $t$ -distribution with scale factor  $\sigma = 0.3$  and two degrees of freedom. This prior discourages abrupt changes in SFR between adjacent bins but remains flexible enough to fit both star-forming and quenched galaxies (Leja et al., 2019; Johnson et al., 2021). Following Tacchella et al. (2022b), we also consider the bursty continuity prior – a modified form of the continuity prior with  $\sigma = 1$  and  $\nu = 2$ , which allows greater variability in the SFH. For each of these priors, we adopt the following binning scheme: the first two and the last bins are kept the same for all sources, covering  $0 < t_l < 10$  Myrs,  $10 < t_l < 100$  Myrs, and  $0.85t_z < t_l < t_z$ , respectively. Here,  $t_z$  represents the age of the Universe at the object’s redshift, and  $t_l$  is the lookback time. The remaining time between 100 Myrs and  $0.85t_z$  is evenly spaced in logarithmic time. The number of bins is chosen to ensure that  $\log_{10}(\text{bin width}/\text{Gyr}) > 0.02$ , ranging from eight bins (for the lowest redshifts in our simulations), to five (for the highest).

To quantify the fidelity of the 100Myr averaged SFR inferred using MAGPHYS and PROSPECTOR, following H23/Chapter 2, we use the residual between the inferred SFR and the true value from the simulation:  $\Delta \log_{10} \psi = \log_{10}(\psi_{\text{inferred}}) - \log_{10}(\psi_{\text{true}})$ .

### 3.3 Results

Table 3.1 shows the fit success rate and the average SFR residual for each of the five runs. It is immediately apparent that PROSPECTOR is able to produce acceptable fits for a larger fraction of the snapshots ( $> 90$  per cent fit success rate irrespective of the prior assumed) than MAGPHYS

<sup>6</sup>Using PROSPECTOR with bursts is not recommended in the documentation.

TABLE 3.1: SED fit success rate and typical SFR estimate fidelity,  $\Delta \log_{10}(\psi)$ , for the MAGPHYS and PROSPECTOR fits to our synthetic observations. For the four sets of PROSPECTOR fits, the different SFH priors are indicated.

Fitter/prior	% Fit success	$\Delta \log_{10}(\psi)$
MAGPHYS (pre-defined)	83	$-0.11 \pm 0.06$
PROSPECTOR (pSFH; delayed $\tau$ model)	92	$-0.11 \pm 0.05$
PROSPECTOR (Bursty-continuity)	91	$-0.09 \pm 0.24$
PROSPECTOR (Dirichlet, $\alpha = 1$ )	92	$-0.30 \pm 0.19$
PROSPECTOR (Continuity)	92	$-0.12 \pm 0.12$

(83 per cent). This may reflect the effect that the MAGPHYS pre-computed libraries – coupled with the requirement that it consider only SFHs shorter than the age of the Universe at a given redshift – result in the priors becoming increasingly poorly-sampled at higher redshifts, and acceptable MAGPHYS fits increasingly hard to obtain at earlier epochs. Secondly, we note that the typical SFR uncertainties for the non-parametric runs shown in Table 3.1 are significantly larger than those yielded by the pSFH runs (with both MAGPHYS and PROSPECTOR) and we will return to this point below. These details notwithstanding, it is clear from Table 3.1 that there is no significant difference in the overall  $\Delta \log_{10} \psi$  once the uncertainties are considered, meaning that both codes do a similarly acceptable job of recovering the true SFR on average.

We now investigate the fidelity of the MAGPHYS and PROSPECTOR SFR estimates as a function of the recent SFH. In Figure 3.2, we plot  $\Delta \log(\psi)$  against  $\eta$ , with MAGPHYS results shown in the left-hand panel, PROSPECTOR pSFH results in the centre panel, and the PROSPECTOR bursty continuity prior results in the right-hand panel. The axes are chosen such that ‘starburst’ snapshots appear to the right of each plot, and ‘temp-quenched’ ones to the left. The values for individual SEDs are shown as points, with red lines showing a running average of  $\Delta \log_{10}(\psi)$  for 100 data points. The red areas enclose the 16th and 84th percentiles of the inferred SFR PDF using the same running average, while the grey shading encloses the 16th and 84th percentiles of the scatter within each corresponding subsample.

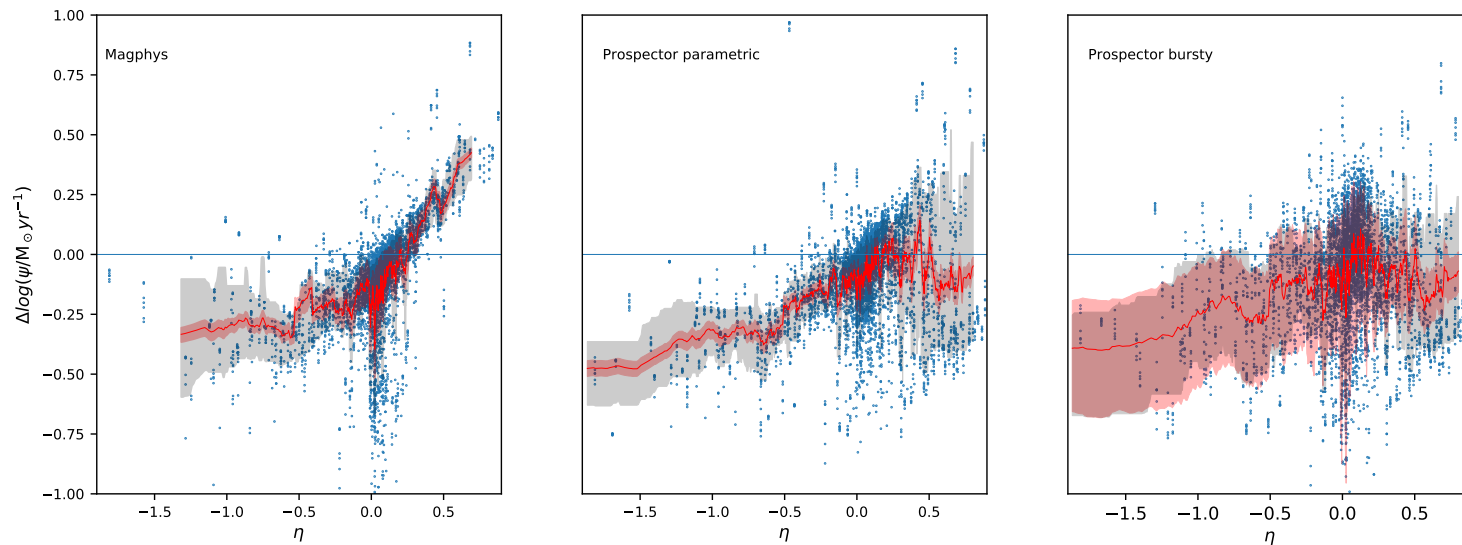


FIGURE 3.2: The LH panel shows the difference between the inferred and true SFRs averaged over the last 100 Myr,  $\Delta \log_{10} \psi = \log_{10}(\psi_{\text{inferred}}) - \log_{10}(\psi_{\text{true}})$ , as a function of the burst indicator  $\eta \equiv \log_{10}(\bar{\psi}_{10\text{Myr}}/\bar{\psi}_{100\text{Myr}})$ . The centre and RH panels show the same obtained using PROSPECTOR with the pSFH and bursty continuity SFH prior. In all panels the red line shows the mean residual averaged over 100 data points with the red shaded area enclosing the averaged 16th and 84th percentile residuals from the PDF. The grey shaded area indicates the 16th and 84th percentiles of the scatter in  $\Delta \log_{10} \psi$  within each averaged point, and the blue markers show values for individual SEDs. The MAGPHYS SFRs exhibit a systematic bias: the SFR tends to be underestimated for ‘temp-quenched’ galaxies and overestimated for galaxies that have experienced a burst within the past 10 Myr.

Two effects are immediately apparent. Firstly, there is a systematic trend in the MAGPHYS SFRs, such that while they are typically overestimated by  $\sim 0.4$  dex at  $\eta > 0.5$  (the ‘starburst’ snapshots), the converse is true at  $\eta < -0.5$  (the ‘temp-quenched’ snapshots) where MAGPHYS typically underestimates the true SFRs by  $\sim 0.3$  dex. This is clearly of concern, since we know that both ‘starburst’ and ‘temp-quenched’ galaxies exist in the real Universe (e.g. Guo et al., 2016; Faisst et al., 2019; Broussard et al., 2022; Looser et al., 2023) and this effect could result in a systematic error in the SFRs of galaxies that could be 1 dex in magnitude in the worst cases. Secondly, and underscoring the severity of the first issue, there is a clear tendency for the typical pSFH uncertainties to underestimate the degree of scatter visible in the data points (grey shading). This effect becomes increasingly noticeable as  $|\eta|$  increases.

The equivalent PROSPECTOR bursty continuity plot shows the SFR recovery is approximately independent of  $\eta$  with reasonable uncertainties at  $\eta_{\text{true}} < 0.5$  (where  $\sim 90$  per cent of the snapshots lie). At these  $\eta$ , the  $\sim 0.3$  dex offset in the PROSPECTOR SFRs relative to the ground truth is similar to that returned by MAGPHYS at  $\eta < -0.5$ ; however, in the PROSPECTOR non-parametric results the deviation from zero is not statistically significant due to the realistic error bars (and we obtain similar results with the other non-parametric SFHs).

### 3.4 Discussion

Fundamental to SED fitting codes’ abilities to recover the true properties of galaxies are (i) wavelength sampling (including range covered, and resolution), (ii) priors, and (iii) sensitivity of the available observations. The first of these is closely related to the extent of our ability to estimate  $\eta$  using SED fitting (since different wavelengths have different “response functions” between the luminosity and the SFH; e.g. Kennicutt and Evans, 2012; Sparre et al., 2017). In this work we focus solely on our ability to recover 100 Myr-averaged SFRs using an example 18 bands of photometry similar to that used in Smith et al. (2021) and Best et al. (2023) to fit galaxies in the LOFAR deep fields (Tasse et al., 2021; Sabater et al., 2021; Kondapally et al., 2021; Duncan et al., 2021). This good wavelength sampling, in addition to the fact that we have not added noise to photometry, means that this test represents a best-case scenario: the bias that we have identified is fundamental, not due to noise or poor SED sampling, and thus cannot be addressed with ‘better data’.

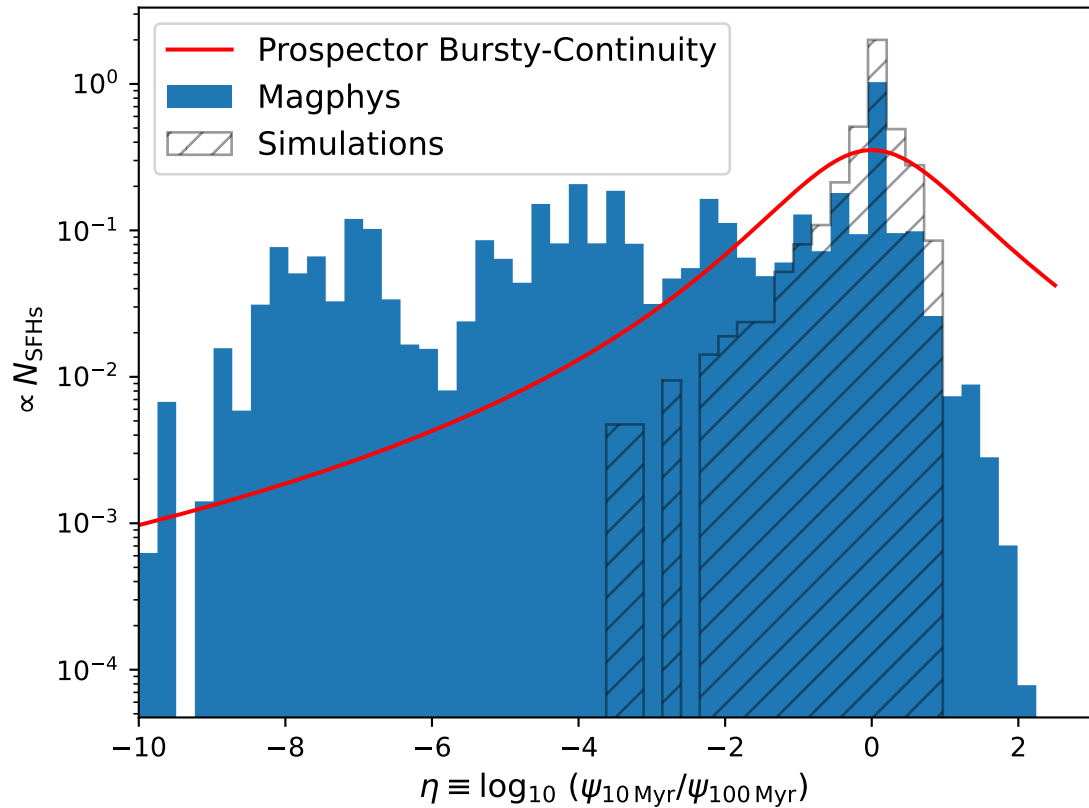


FIGURE 3.3: The distributions of  $\eta$  values for 50,000 SFHs in the MAGPHYS high- $z$  libraries (in blue), overlaid with the ground truth values from the simulations (hatched) and for the PROSPECTOR bursty continuity prior in red. Note the significantly larger  $\eta$  range relative to Figure 3.2.

In the MAGPHYS model, the priors are immutable since it uses pre-computed SFH libraries with fixed sampling. The high- $z$  MAGPHYS SFHs assume a delayed exponential parametric form, with random bursts superposed in such a manner that during the previous 2 Gyr, 75 per cent of SFHs include a burst lasting between 30-300 Myr and forming between 0.1 and 100 times the stellar mass formed by the underlying distribution (da Cunha et al., 2015). The  $\eta$  distribution for the MAGPHYS high- $z$  SFHs is shown in Figure 3.3, overlaid with the distribution of values for the true SFHs of the simulated galaxies and for the assumed PROSPECTOR bursty continuity prior. It is clear that both the MAGPHYS libraries and the PROSPECTOR bursty continuity prior allow for a significantly broader range of  $\eta$  values than the simulations contain, so the prior on  $\eta$  is not the source of the bias.

In Section 3.3 we noted that the pSFH SFR uncertainties are increasingly underestimated as  $|\eta|$  moves away from 0. Alongside the similarity in the mean  $\Delta\psi$  between the PROSPECTOR pSFH and non-parametric plots, this leads us to speculate that while the choice of prior may affect the

uncertainties and crucially the statistical significance of the systematic trend, the cause of the largest upturn in the MAGPHYS  $\Delta \log_{10} \psi$  for the most bursty galaxies lies elsewhere.

### 3.5 Conclusions

We have used four cosmological zoom-in simulations spanning  $1 < z < 8$ , together with the radiative transfer code SKIRT, to generate 6,706 synthetic galaxy SEDs. We attempted to recover their true SFRs based on fitting the synthetic observations using MAGPHYS and PROSPECTOR. Although there is little difference between the fidelity of the recovered  $\bar{\psi}_{100\text{Myr}}$  values averaged across all of the simulated recovery tests using the two codes, we find that the accuracy of the MAGPHYS-inferred SFRs is strongly dependent on the recent SFH. This trend is sufficiently large that the MAGPHYS 100 Myr-averaged SFRs of individual galaxies could be overestimated (underestimated) by as much as 1 dex in the worst cases for galaxies experiencing starbursts (temporarily quenched periods). The trend is not evident in the 100 Myr SFRs from PROSPECTOR, and is significantly weakened in PROSPECTOR results assuming parametric SFHs (pSFHs). We therefore speculate that this effect could be due to MAGPHYS's burst recipe or the use of pre-defined libraries with fixed parameter sampling which may be unsuitable for some galaxies. Given this bias, and the significantly underestimated SFR uncertainties produced using pSFHs, we urge caution when employing pSFHs and/or pre-defined libraries to study the SEDs of observed galaxies that are likely to have bursty SFHs, such as high-redshift galaxies observed with *JWST*.

## Chapter 4

# The performance of PROSPECTOR when measuring the properties of high-redshift galaxies

### 4.1 Introduction

The importance of SED fitting to astrophysics research, and the breadth of choice available when implementing models against which observations can be compared, were described in Chapter 1. Chapter 2 then described the use of one of the SED fitting codes in common use today, MAGPHYS (da Cunha et al., 2008). It described how FIRE simulations (Hopkins et al., 2018) were used to test the suggestion by other authors that the energy balance assumption could be a problem when dealing with dusty galaxies with apparent UV/FIR spatial offsets, and also to investigate the fidelity of derived property values as a function of redshift, true property values, and stellar and dust emission offsets. MAGPHYS uses prebuilt templates (the atlas approach as described in Section 1.6.4.2) and a modified delayed- $\tau$  parametric SFH prior to create the model spectra. Both of these approaches have their drawbacks, though both are computationally efficient, and so an investigation into different techniques, in the form of that undertaken by Hayward and Smith (2015) and Haskell et al. (2023) for MAGPHYS, is warranted.

PROSPECTOR (Leja et al., 2017) offers a choice of SFH priors as well as using a nested sampling technique to explore the parameter space. By running different configurations of PROSPECTOR, it is possible to address a number of interesting questions:

1. To what extent do these methodologies demonstrate statistical success in fitting SEDs at redshifts comparable to or exceeding those modeled by MAGPHYS?
2. How significantly are the outcomes influenced by spatial offsets between regions of stellar emission and FIR emission, particularly in systems with complex dust distributions?
3. Do the derived results exhibit systematic biases as a function of intrinsic galaxy properties or with variations in the orientation of the line-of-sight?
4. What are the quantitative and qualitative differences in the recovered galaxy properties when employing nonparametric SFH models as opposed to parametric forms?
5. Does the computationally intensive nested sampling approach yield superior estimates of physical parameters compared to results derived from pre-computed template libraries?

In this chapter we extend the work on MAGPHYS described in Chapter 2 to perform some of the same tests on the fitter PROSPECTOR using the same simulations. PROSPECTOR offers considerably more configuration flexibility than MAGPHYS, and we exploit this flexibility to investigate the impact of SFH priors on the fidelity of the derived values, using three nonparametric priors and the delayed- $\tau$  parametric prior.

This chapter is structured as follows: Section 4.2 describes the data, the configuration of PROSPECTOR, and the SFH priors used for this chapter; Section 4.3 presents the results of the fitting as a function of different variables, namely: redshift, the projection of the galaxy geometry (view angle), the offsets between the stellar and FIR emission, and the true values of the properties ; Section 4.4 discusses the reasons for PROSPECTOR failing to find a satisfactory fit, the effect of SFH prior choice and the fidelity of the results and Section 4.5 presents a summary with conclusions.

Throughout this work we again adopt a standard cosmology with  $H_0 = 70 \text{ km s}^{-1} \text{ Mpc}^{-1}$ ,  $\Omega_M = 0.3$ , and  $\Omega_\Lambda = 0.7$ .

## 4.2 Method

### 4.2.1 Data

To examine the fidelity of PROSPECTOR results, we employ the same simulations, radiative transfer and filters to produce the same observation data as those processed by MAGPHYS in Chapter 2 and described in Section 2.2. In brief, these consist of four cosmological zoom-in simulations from the FIRE project<sup>1</sup> using the FIRE-2 code of Hopkins et al. (2018). The simulations cover the redshift range  $1 < z < 8$  with snapshots taken approximately every 25 Myr. Each snapshot consists of seven views of the simulated galaxy taken at different angles relative to the angular momentum vector, delivering 6706 datasets, radiative transfer calculations were provided by SKIRT<sup>2</sup>. We convolved the results with the profiles of 18 filters from UV to FIR. Of the resulting datasets 5894, were processed through PROSPECTOR with  $1.2 < z < 8$ .

### 4.2.2 PROSPECTOR

PROSPECTOR is fully described in Leja et al. (2017) and Johnson et al. (2021), here we outline the configuration options used in this thesis.

Section 1.6.2 of this thesis describes the process of stellar population synthesis, which is described in full in three papers by Conroy et al (Conroy et al., 2009, 2010; Conroy and Gunn, 2010b). PROSPECTOR uses the Flexible Stellar Population Synthesis (FSPS) package described in Conroy and Gunn (2010a). For the PROSPECTOR runs for this thesis, FSPS was configured to use the Padova isochrones to follow stellar evolution from the main sequence to the TP-AGB stage (Bertelli et al. 1994; Girardi et al. 2000; Marigo et al. 2008), and Vassiliadis and Wood (1994) to track the post-AGB phase. FSPS was also configured to use the Kroupa (2001) IMF, the MILES spectral library (Sánchez-Blázquez et al., 2006), the Charlot and Fall (2000) dust attenuation model, the Kriek and Conroy (2013) attenuation curve, and the Draine and Li (2007) dust emission templates; stellar metallicity was fixed at  $Z_{\odot}$ .

The input to FSPS calculations consists of a multi-dimensional parameter space with defined limits and distributions; those relevant to this work are presented in Table 4.1.

<sup>1</sup><http://fire.northwestern.edu>

<sup>2</sup><http://www.skirt.ugent.be/>

TABLE 4.1: Input parameters for FSPS relevant to this work and their priors. Column 2 describes each variable, column 3 shows the value or range and distribution of the priors. (Table adapted from Das et al. 2024.)

	Description	Prior distribution/Value
Stellar Mass	$\log_{10}(\text{stellar mass})$	Uniform from 6.5 to 13.5
Dust attenuation	$\left\{ \begin{array}{l} \text{Diffuse dust V-band optical depth } (\tau_{\lambda,2}) \\ \text{Diffuse dust attenuation index } (n) \\ \text{Ratio of optical depth of the birth cloud to} \\ \text{optical depth of dust screen } (\tau_{\lambda,1}/\tau_{\lambda,2}) \end{array} \right.$	Uniform from $-1$ to $4$
		Uniform from $-2$ to $0.5$
		Clipped normal $\mu = 1, \sigma^2 = 0.3$ from $0$ to $2$
Dust emission	$\left\{ \begin{array}{l} \text{The minimum intensity of stellar emission heating} \\ \text{the ISM } (U_{\min}) \\ \text{Fraction of total dust mass affected by the above } (\gamma_e) \\ \text{The fraction of total dust mass coming from} \\ \text{polycyclic aromatic hydrocarbons } (Q_{\text{PAH}}) \end{array} \right.$	Uniform from $0.1$ to $25$
		Log uniform from $0.001$ to $0.15$
		Uniform from $0.1$ to $10$
Fixed parameters	$\left\{ \begin{array}{l} \text{Stellar metallicity } (Z_{\odot}) \\ \text{Additional optical depth attenuating the light } (\tau_{\lambda,1}) \\ \text{from young stars} \\ \text{Dust attenuation } k(\lambda) \\ \text{Discrete time binning scheme } (F_{\text{bins}}) \\ \text{Gas-phase metallicity } (Z_{\text{gas}}) \end{array} \right.$	Fixed at solar
		Function of $\tau_{\lambda,1}/\tau_{\lambda,2}$ above
		Kriek and Conroy (2013)
		Fixed
		Fixed at solar

PROSPECTOR employs the dynamic nested sampling package DYNESTY to explore the parameter space using the priors shown in Table 4.1- note that parameters associated with AGN and nebular emission are not shown as these features are not present in our simulations; for a full description see Das et al. (2024). Samples drawn from this parameter space are combined with the snapshot's redshift and processed through FSPS to create a plausible model SED. When the SED is returned, a  $\chi^2$  statistic is computed to evaluate the goodness of fit between the model and observed data. On the basis of this, DYNESTY will update the prior values and FSPS will run again, the process continuing until a pre-defined stop condition is met - typically when successive iterations produce matching likelihoods which differ by only a small predetermined value.

The PROSPECTOR approach explores the parameter space in a smoother fashion than the grid-like approach enforced by the MAGPHYS pre-built libraries, though this improved parameter-space coverage is paid for by longer computation times. For this thesis, PROSPECTOR took up to 20 minutes per SED compared to MAGPHYS's  $\approx 4$  minutes - however, parallel running alleviates this issue to some extent and the multi-core University of Hertfordshire High Performance Cluster (UHHPC) was used to facilitate this.

### 4.2.3 SFH Priors

PROSPECTOR was run using four different SFH priors - three nonparametric priors we refer to as Continuity, Continuity-Bursty (hereafter Bursty) and Dirichlet and one parametric prior - see Figure 1.13.

To implement nonparametric priors, the SFH must be divided into discrete time bins. These were divided such that the first two and the last are the same for all redshifts, covering  $0 < t_l < 10$  Myrs,  $10 < t_l < 100$  Myrs, and  $0.85t_z < t_l < t_z$ , respectively where  $t_l$  is the look back time and  $t_z$  is the age of the Universe at the redshift of the snapshot. The remaining time between 100 Myrs and  $0.85t_z$  was evenly spaced in logarithmic time such that  $\log_{10}(\Delta t_l) > 0.02$  for each bin. This binning strategy resulted in nine bins for the lowest redshift sources reducing to six for the highest.

Two prior distributions were used for this work - Dirichlet and the Student's t. The Dirichlet distribution is a probability density function with three free parameters, namely the total stellar mass formed, the number of time bins ( $K$ ) and the concentration parameter vector ( $\vec{\alpha}$ ). It is defined as:

$$p(\vec{x}|\vec{\alpha}) = \frac{1}{B(\vec{\alpha})} \prod_{i=1}^K x_i^{\alpha_i-1} \quad (4.1)$$

Where  $\vec{x}$  is the vector of the fractional stellar mass produced in each bin, such that  $\sum_{i=1}^K x_i = 1$  and  $B(\vec{\alpha})$  is the multivariate beta function:

$$B(\vec{\alpha}) = \frac{\prod_{i=1}^K \Gamma(\alpha_i)}{\Gamma\left(\sum_{i=1}^K \alpha_i\right)} \quad (4.2)$$

The mass formed in each bin is calculated as:

$$m_n = \frac{x_n t_n}{\sum_{i=1}^K x_i t_i} \quad (4.3)$$

Where  $t_n$  is the width of the  $n$ th time bin. The Dirichlet distribution is useful in our context because of the intuitive interpretation of two of its three free parameters. The third, the concentration parameter controls the weighting across the bins, with  $\alpha_i < 1$  distributing the majority of weight in a few bins and  $\alpha_i > 1$  distributing the weight more evenly. For this work we have used a

symmetric concentration parameter of 1 ( $\alpha_i = 1 \forall i$ ) following Leja et al. (2019). This makes every point in the  $K$ -dimensional space equally likely to produce a smooth and tightly constrained SFR as shown in Figure 1.13. However, it does not force continuity between adjacent bins, and so can produce sharp quenching or star-forming events, although the high-concentration parameter value will mitigate against this.

The Student's  $t$ -distribution differs from Dirichlet by weighting against sharp changes in SFR between bins. In this implementation we apply the Student's  $t$ -distribution such that the prior for the SFR in the  $(n + 1)$ th bin has a mean equal to the SFR in the  $n$ th bin. The Student's  $t$ -distribution distribution requires three free parameters, namely the number of degrees of freedom ( $\nu$ ) which determines the shape of the distribution, the location parameter ( $\mu$ ) which is analogous to the Gaussian mean, and the scale parameter ( $\sigma$ ) which is analogous to the Gaussian standard deviation.

The Student's  $t$ -distribution is defined as:

$$P(x|\nu) = \frac{\Gamma(\frac{\nu+1}{2})}{\sqrt{\nu\pi\sigma}\Gamma(\frac{\nu}{2})} \left( 1 + \frac{1}{\nu} \left( \frac{x-\mu}{\sigma} \right)^2 \right)^{-\frac{\nu+1}{2}} \quad (4.4)$$

Where  $\nu, \mu, \sigma$  are as described above. For this work we have set  $\nu = 2$  and  $\sigma = 0.3$  for the Continuity prior, and  $\nu = 2$  and  $\sigma = 1$  for the more variable Bursty prior, following Tacchella et al. (2022c).

The Parametric prior is a delayed- $\tau$  model, chosen because it is one of the most widely used (Carnall et al., 2019). It has the form:

$$\text{SFR}(t) = (t - t_a)e^{-(t-t_a)/\tau} \quad (4.5)$$

For this work  $\tau$  is varied between  $0.1 < \tau < 10$  Gyr within a uniform logarithmic prior, and the parameter  $t_a$  with a uniform prior between 1 Myr and the age of the Universe at the snapshot's redshift, following Tacchella et al. (2022a).

#### 4.2.4 Process

The observations were input to PROSPECTOR assuming a signal-to-noise ratio of 5 in every filter band to enable direct comparison of the results with those from MAGPHYS (see Chapter 2). Four

separate runs of PROSPECTOR were executed, each using a different SFH prior - nonparametric priors Bursty, Continuity and Dirichlet, and the  $\tau$  model parametric prior.

We analyze the median-likelihood values for five properties output by PROSPECTOR- stellar mass, SFR, sSFR, dust luminosity, and  $A_V$  - together with their implicit uncertainties. The fidelity of the results was measured in the same way as used in Chapter 2 for MAGPHYS, by taking the residual of each value and noting that over-estimates result in positive residuals:

$$\text{residual} = \log_{10}(\text{derived}) - \log_{10}(\text{true}) \quad (4.6)$$

An acceptable fit was determined using the same  $\chi^2_{\text{max}}$  values as those for MAGPHYS in Chapter 2, following Smith et al. (2012) where the  $\chi^2$  number of degrees of freedom is calculated from the number of filter bands used in the fitting. We note that this technique is based on MAGPHYS and may not be entirely applicable to PROSPECTOR or other SED fitters. Further work is needed to fully validate this approach which we defer to a future publication, however, the use of this method is suitable for the comparisons between the SED fitters used in this thesis.

In Section 4.3.2 we seek to determine whether the fidelity of the property estimates derived by PROSPECTOR is sensitive to offsets between the observed stellar and dust emission. To test this we used the three proxies defined in section 2.2.3; these are referred to in the text as peak-to-peak (measuring the distance in kpc between the points of maximum flux at  $\lambda = 0.3 \mu\text{m}$  and  $100 \mu\text{m}$ ), light-weighted mean (measuring the distance in kpc between the light-weighted mean centres of maximum flux as above), and the Spearman rank coefficient  $\rho$  (Myers and Well, 2003) to test the degree of correlation between the image at  $\lambda = 0.3 \mu\text{m}$  and that at  $100 \mu\text{m}$ .

### 4.3 Results

In this section we present the results of PROSPECTOR SED fitting using the four different SFH priors described in the Section 4.2.3. Where relevant we compare the results to those reported in Haskell et al. (2023) using MAGPHYS on the same data, and to the benchmark values from Hayward and Smith (2015). Where MAGPHYS results are quoted they are those from Run A (see Section 2.2.3) using all available photometry and at the redshift appropriate to the Universe age at the time of the simulation snapshot.

In Section 4.3.1 we report on PROSPECTOR’s ability to fit SEDs across the range of redshifts and in Section 4.3.2 on the fidelity of the derived property values, using the different SFH priors, when averaged throughout a galaxy’s evolution and when averaged across all galaxies; in Section 4.3.3 we leverage the different view angles provided by the simulations to determine whether the fidelity of the recovered property values is affected by the different line-of-sight projections of the galaxy’s stellar and dust spatial distribution; in Section 4.3.4 we show how the fidelity of the derived values is affected by any offset between the stellar and dust emission within the galaxy (using the proxies defined in Section 2.2.3); and finally, in Section 4.3.5 we determine whether the fidelity of a derived property value is sensitive to the property’s true value.

### 4.3.1 Overall fitting performance

First, we determine PROSPECTOR’s success in fitting SEDs to the synthetic photometry; Table 4.2 shows the percentage success rate of PROSPECTOR fitting using each of the four SFH priors with the MAGPHYS results from Haskell et al. (2023) included for reference. The uncertainties are binomial errors calculated using the Python package `astropy.stats` with a confidence level of 68 percent ( $1\sigma$ ) and the Wilson formula for the confidence interval<sup>3</sup>. The binomial distribution is suitable for this as each bin contains a fixed number of independent observations each with only two possible outcomes - a successful or unsuccessful fit. It is evident from this that PROSPECTOR has a higher fit success rate than MAGPHYS regardless of which SFH prior is used. In addition, when examining the success rates of all four galaxies combined as presented in the final row of Table 4.2, it is clear that the results for the four PROSPECTOR SFH priors are not significantly different, with a two-sample z-score between each pair of results of typically  $< 1\sigma$ .

Figure 4.1 presents the percentage of successful fits against redshift, colour coded by prior, averaged across bins of width  $\Delta z = 0.1$ ; the uncertainties are enclosed by shaded areas of the same colour with the MAGPHYS results shown in blue for reference. The background bar chart shows the bin occupancy read from the right-hand y-axis; note that the simulations create an almost consistent number of observations when binned by age leading to the exponentially declining bin occupancy as redshift increases. We can see that PROSPECTOR delivers success rates in excess of 95 per cent for  $2.5 \lesssim z \lesssim 4.5$ , but there is some deterioration outside this range, this is discussed in the Section 4.4.1.

<sup>3</sup>[https://docs.astropy.org/en/stable/api/astropy.stats.binom\\_conf\\_interval.html](https://docs.astropy.org/en/stable/api/astropy.stats.binom_conf_interval.html)

TABLE 4.2: The percentage of simulations for which PROSPECTOR and MAGPHYS were able to find a satisfactory fit. The total number of simulation SEDs available for each galaxy is shown in column 2, the percentage success rate for each galaxy achieved by PROSPECTOR using four different SFH priors is shown in columns 3 to 6, MAGPHYS results are shown in column 7 for reference. Errors are  $1\sigma$  binomial errors calculated using the Python package `astropy.stats` (see footnote), all percentages are rounded to one decimal place.

Galaxy	Total Obs	PROSPECTOR successful fits (per cent)				MAGPHYS successful fits (per cent)
		Bursty	Continuity	Dirichlet	Parametric	
A1	1512	92.3 <sup>+0.7</sup> <sub>-0.7</sub>	92.9 <sup>+0.6</sup> <sub>-0.7</sub>	92.4 <sup>+0.7</sup> <sub>-0.7</sub>	91.9 <sup>+0.7</sup> <sub>-0.7</sub>	84.8 <sup>+0.9</sup> <sub>-0.9</sub>
A2	1491	90.9 <sup>+0.7</sup> <sub>-0.8</sub>	91.0 <sup>+0.7</sup> <sub>-0.8</sub>	91.3 <sup>+0.7</sup> <sub>-0.8</sub>	91.4 <sup>+0.7</sup> <sub>-0.8</sub>	78.1 <sup>+1.1</sup> <sub>-1.1</sub>
A4	1477	94.7 <sup>+0.6</sup> <sub>-0.6</sub>	94.8 <sup>+0.5</sup> <sub>-0.6</sub>	95.8 <sup>+0.5</sup> <sub>-0.6</sub>	94.1 <sup>+0.6</sup> <sub>-0.6</sub>	85.0 <sup>+0.9</sup> <sub>-1.0</sub>
A8	1414	95.3 <sup>+0.5</sup> <sub>-0.6</sub>	95.3 <sup>+0.5</sup> <sub>-0.6</sub>	95.3 <sup>+0.5</sup> <sub>-0.6</sub>	95.3 <sup>+0.5</sup> <sub>-0.6</sub>	79.8 <sup>+1.0</sup> <sub>-1.1</sub>
All	5894	93.1 <sup>+0.3</sup> <sub>-0.3</sub>	93.3 <sup>+0.3</sup> <sub>-0.3</sub>	93.6 <sup>+0.3</sup> <sub>-0.3</sub>	93.4 <sup>+0.3</sup> <sub>-0.3</sub>	82.0 <sup>+0.5</sup> <sub>-0.5</sub>

It is evident that the different nonparametric priors are mutually consistent in their performance throughout the full redshift range. This is supported by the fact that of the 5894 simulations processed by PROSPECTOR at least one of the nonparametric SFH prior runs failed to fit an SED 417 times, but all three failed to fit 356 times. This leaves only 61 of the observations ( $\approx 1$  per cent) for which the choice of nonparametric prior made a difference to PROSPECTOR’s ability to obtain a statistically acceptable fit. This result is in agreement with Leja et al. (2019) who found that, in the majority of cases, the photometry was recovered equally well by all of the nonparametric priors: in that work the Dirichlet and Continuity priors, amongst others, were used.

Figure 4.2 presents the best-fit  $\chi^2$  values, averaged over bins of width  $\Delta z = 0.1$ , for each of the four galaxies against redshift. The black horizontal lines mark the value of  $\chi^2_{\max}$  for each redshift, this varies as parts of the SKIRT SED are redshifted out of the range of the filter bands at higher  $z$  values (see Section 2.3.1). This figure re-enforces the view that the four PROSPECTOR priors are producing very similar results which are an improvement on those produced by MAGPHYS in the majority of cases.

### 4.3.2 Success in recovering property values

We now look at how accurately PROSPECTOR was able to recover the true galaxy properties from its successful SED fits. For each property, we present the results in two ways. Firstly, we average the difference between the true and derived property values (the residual) as defined in Equation 4.6 for each prior across each galaxy to enable us to compare the different runs, with

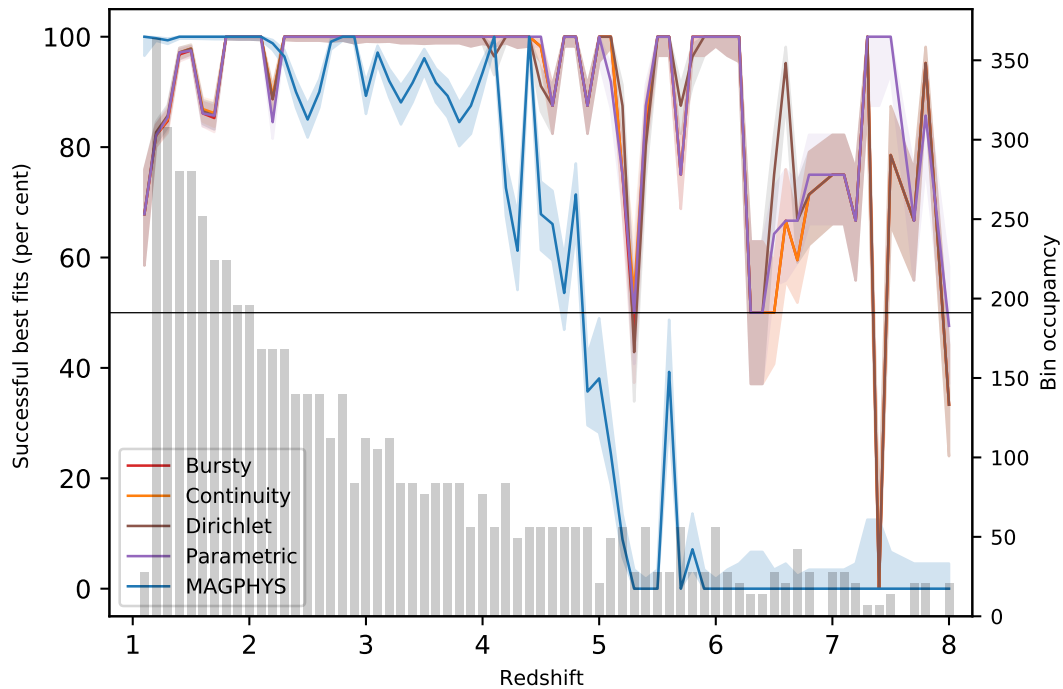


FIGURE 4.1: Percentage of successful fits by redshift averaged over bins of width  $\Delta z = 0.1$ . The lines plot the percentage of simulated SEDs successfully fitted by PROSPECTOR and MAGPHYS for each of the different SFH priors in colours defined in the legend, shaded areas in the same colour enclose the binomial standard deviation within each bin calculated using the Python package `astropy.stats`. The black horizontal line marks the 50 per cent success level for reference; the background bar chart shows the bin occupancy read from the right-hand y-axis.

the uncertainties defined as the similarly averaged 16th and 84th percentiles of the differences. Secondly, we plot the recovered values and residuals against time as each galaxy evolves.

Table 4.3 shows the average difference between the true and recovered values for the properties for each of the PROSPECTOR SFH priors, with the MAGPHYS results from Haskell et al. (2023) included for reference; the colour coding (black for  $\sigma \leq 3$  and red for  $\sigma > 3$ ) showing that in  $\approx 75$  per cent of cases there is no significant difference, on average, between the mean fitter result and the true value mean. For convenience, Figure 4.3 is included to give a visual representation of the uncertainties for the different runs. The entries show encouragingly low residual values of, on average, between 0.1 and 0.6 dex.

A more detailed view of the recovered values is given in Figures 4.4 to 4.7. These figures present the derived property values as a function of redshift and Universe age; the first four columns showing the results for the PROSPECTOR SFH priors and the last column that for MAGPHYS for reference. Each pair of rows presents the results for a specific property; in the first four pairs, the larger plot shows the true value in green and a shaded area encompassing the uncertainty of

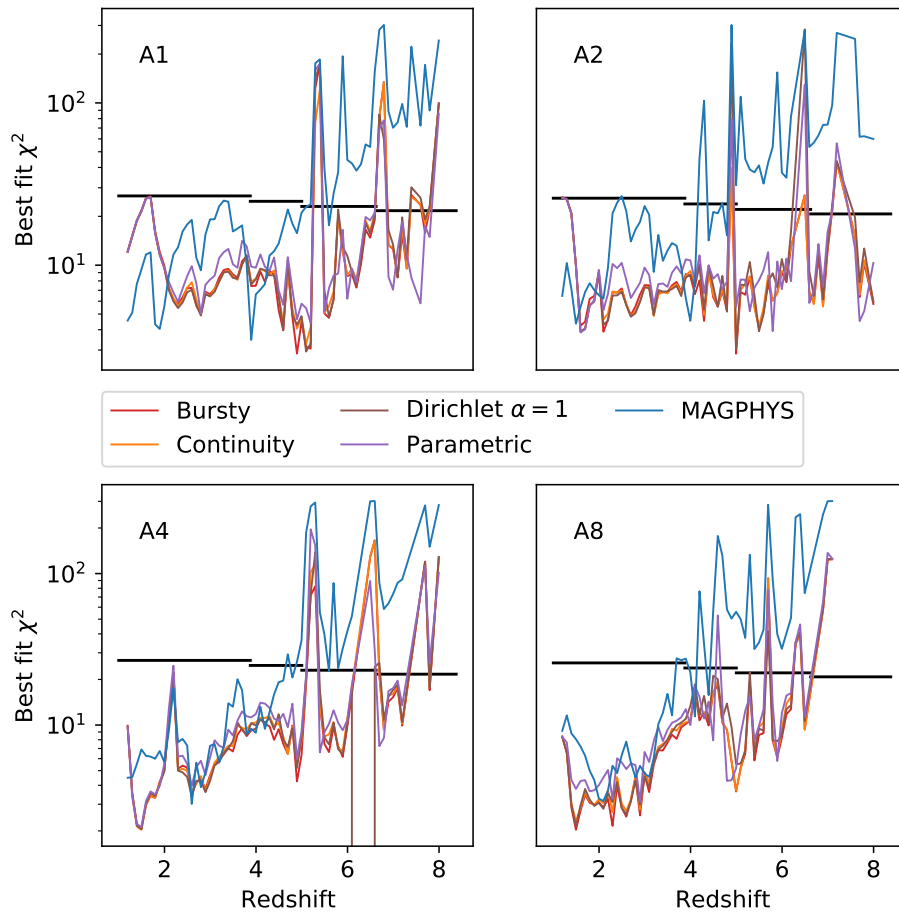


FIGURE 4.2: PROSPECTOR best-fit  $\chi^2$  values by redshift for the simulated galaxies identified in the upper left of each panel. The best-fit  $\chi^2$  values are averaged over bins of width  $\Delta z = 0.1$  and plotted for each of the PROSPECTOR SFH priors along with those for MAGPHYS - colour coded as in the central legend. The horizontal black lines in each panel define the  $\chi^2$  value below which a fit is deemed successful (see Section 4.2.4).

the derived property value for each snapshot averaged across all the snapshot's seven views; the smaller plot shows the residuals with similarly calculated uncertainties. The final pair of rows shows the evolution of  $A_V$ , here the uncertainty for each separate view is shown as overlapping grey-shaded areas.

We now look at the recovery of each property, using these figures, Figure 4.3 and Table 4.3. We look first at the results for stellar mass. Figures 4.4 to 4.7 show that stellar mass is mostly underestimated except in the early evolution of galaxies A1, A4, and A8, however, the recovered

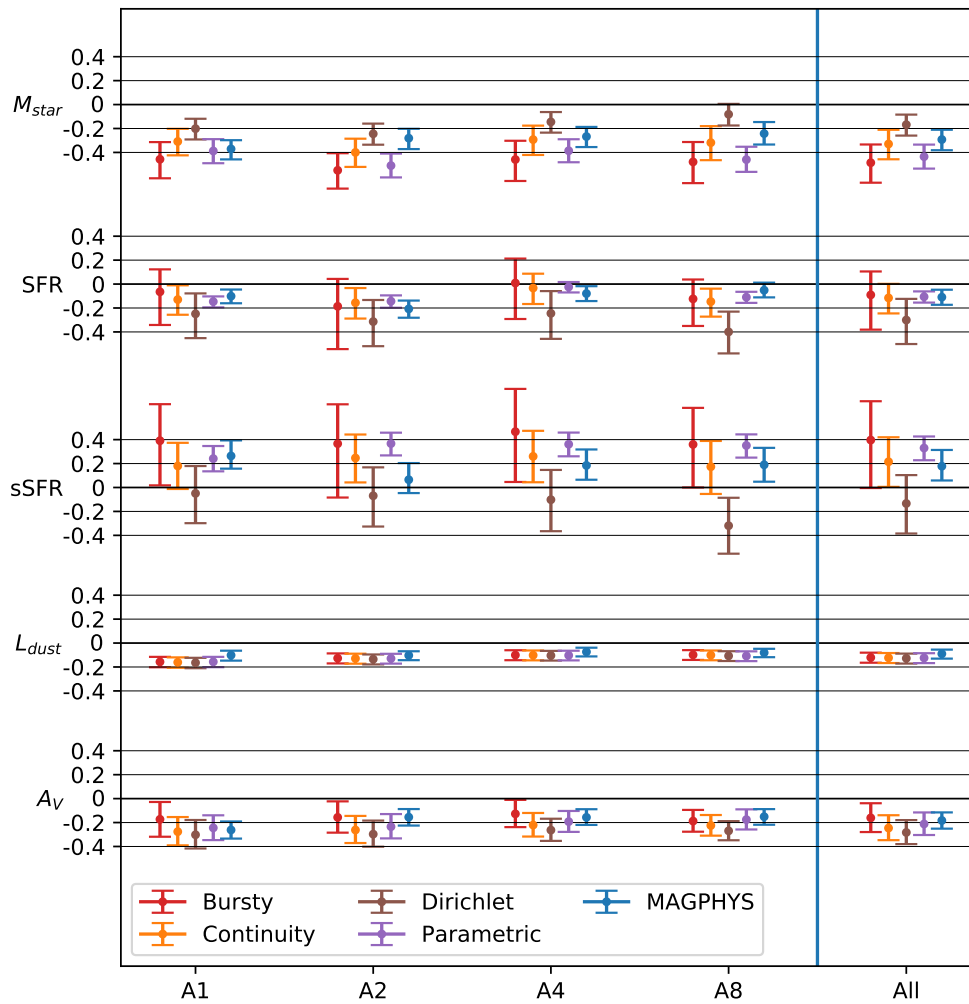


FIGURE 4.3: Visual depiction of the residuals and uncertainties returned by PROSPECTOR. Each row presents the data for a specific property (see y-axis labels), the first four columns showing the data averaged across a specific galaxy (see x-axis labels) at all redshifts, and the final column that averaged over all galaxies. The plots are colour coded to the prior as shown in the legend, with MAGPHYS added for reference. Each point plots the average of the median residual delivered by the relevant fitter/prior with the value read from the y-axis, the error bars are the 16th and 84th residual percentiles of the differences similarly averaged.

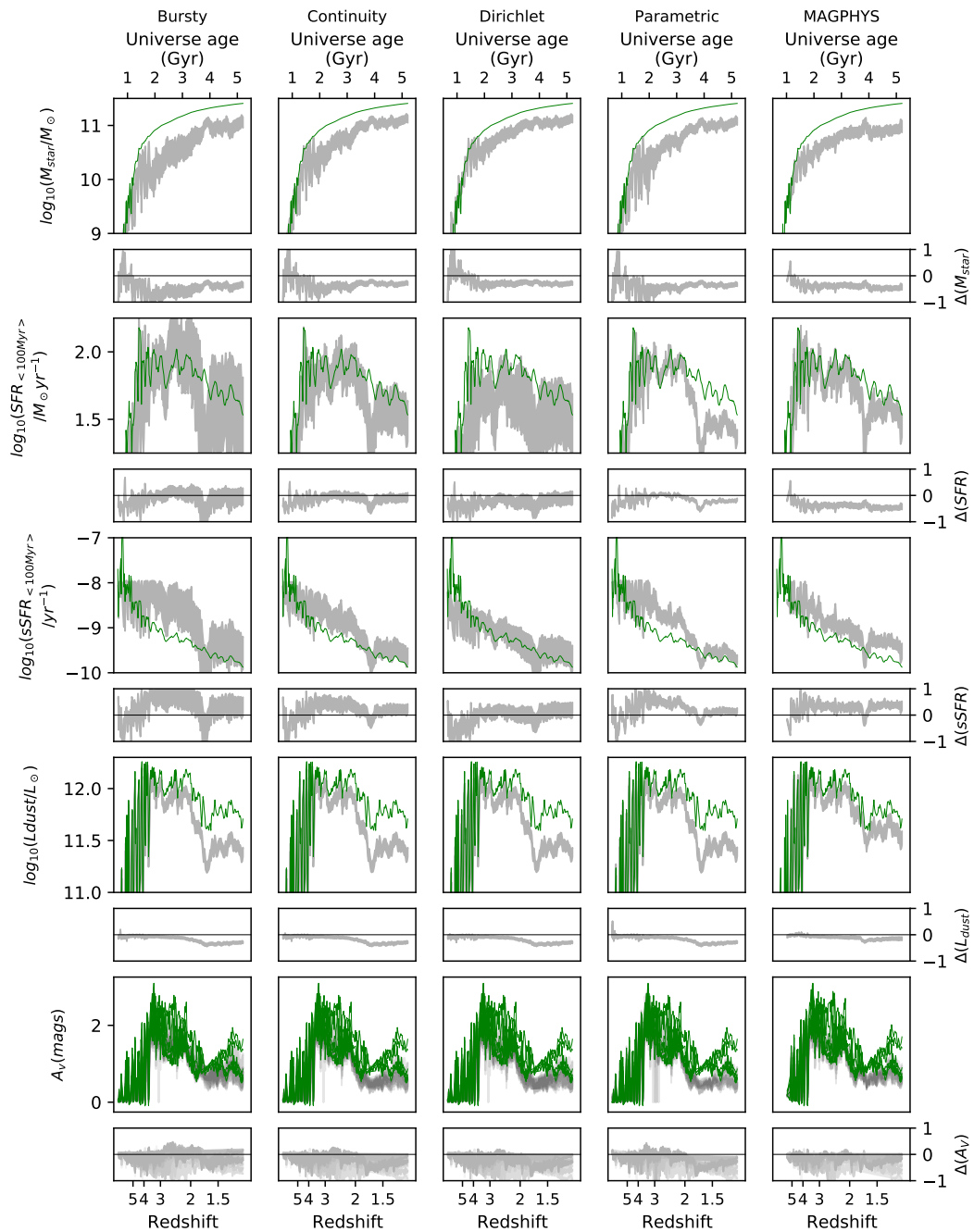


FIGURE 4.4: Evolution of properties over time for galaxy A1. The evolution of the true and derived values for each of the five properties is presented, each pair of rows showing a different property as labelled on the y-axis, and each column a different fitter/prior as shown by the column title. For the first four pairs of rows, the large panel’s grey-shaded area encloses the 16th and 84th percentiles of the derived value averaged over the seven views within each snapshot; the true value is shown in green. The smaller panels plot the residual of the derived value again enclosing the 16th and 84th percentiles of the snapshot’s seven views; the black line marks  $\Delta \log(\text{property}) = 0$ . The final pair of rows show the results for  $A_V$ , here all seven views are plotted independently as overlapping grey areas.

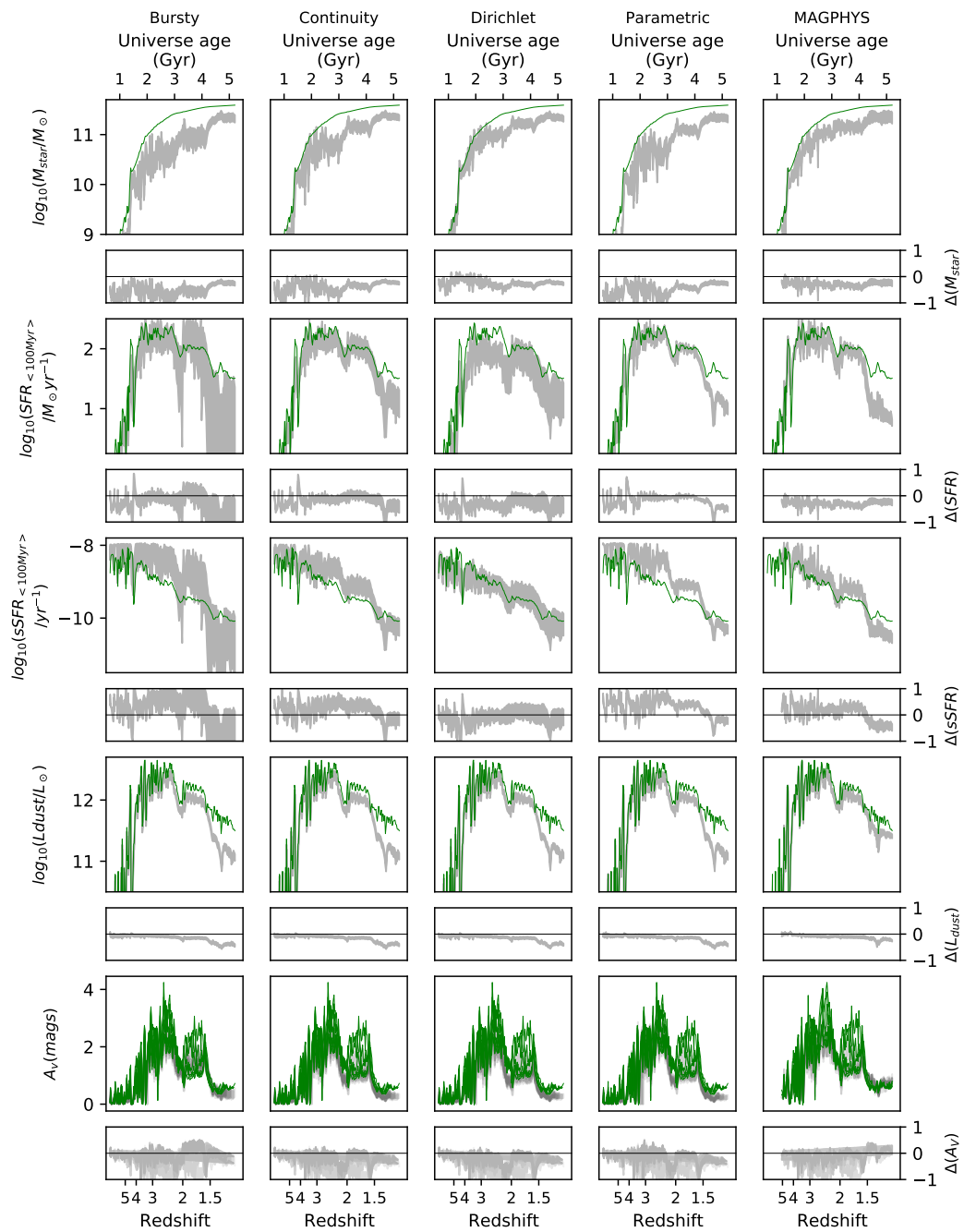


FIGURE 4.5: Evolution of properties over time for galaxy A2 - see Figure 4.4 for details.

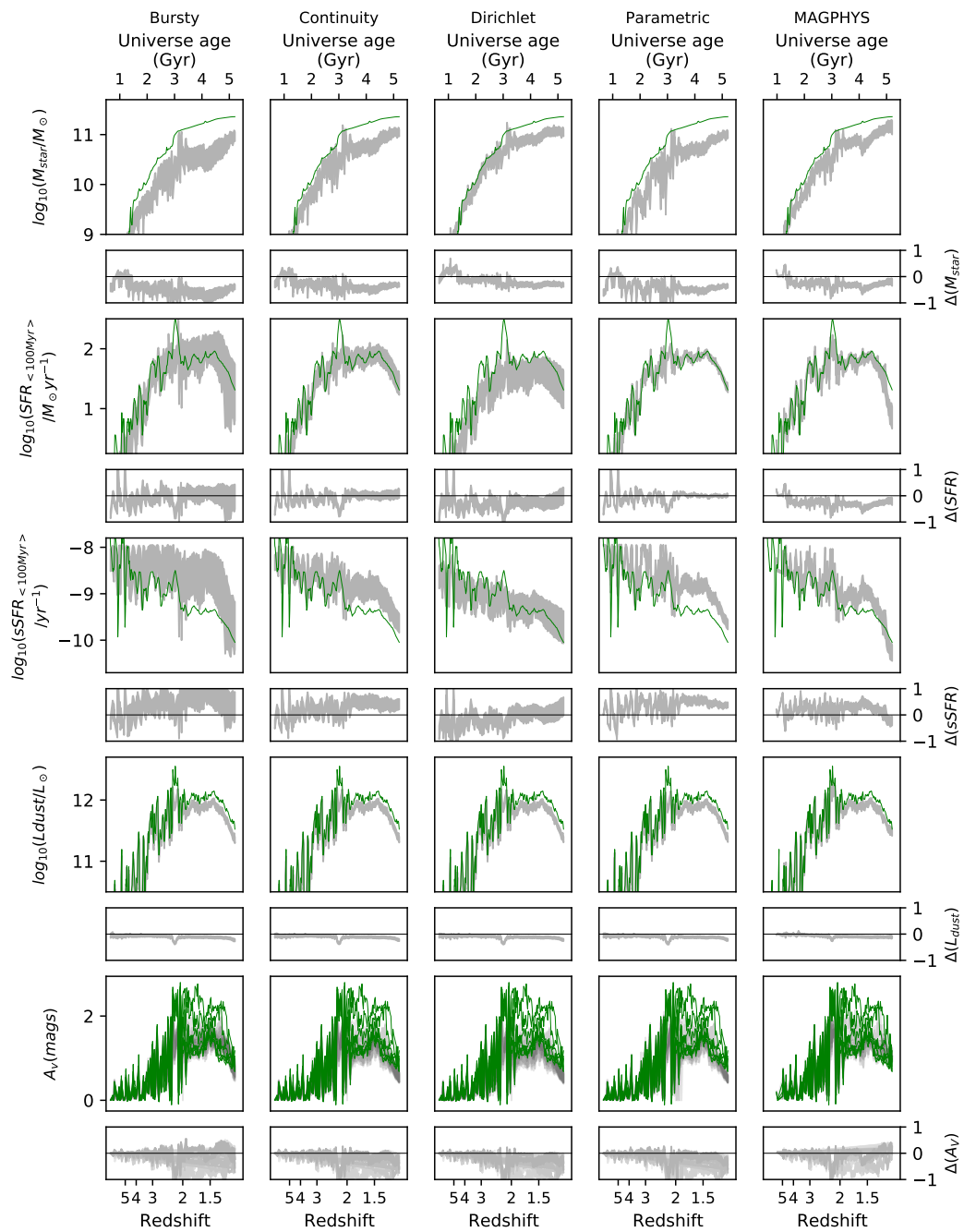


FIGURE 4.6: Evolution of properties over time for galaxy A4 - see Figure 4.4 for details.

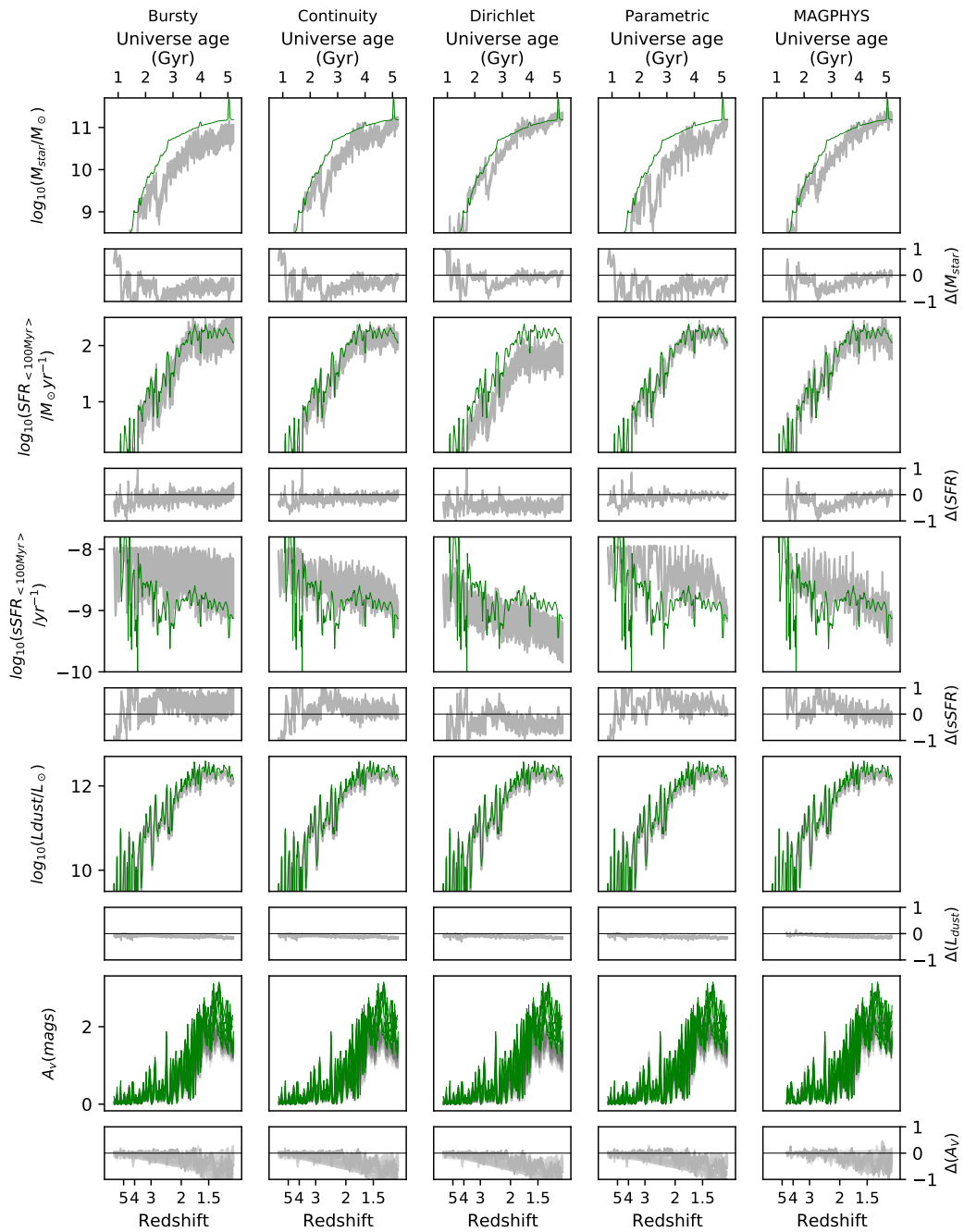


FIGURE 4.7: Evolution of properties over time for galaxy A8 - see Figure 4.4 for details.

TABLE 4.3: The average median residuals for each galaxy, property and SFH prior. Each entry shows the mean of the 50th percentile of the given property as recovered by the SFH prior shown in the column headings. The uncertainties are the 16th and 84th percentiles calculated from the true value and the appropriate percentile taken from the recovered PDF. The entries are colour coded black for  $\leq 3\sigma$  result and red for  $> 3\sigma$  result.

Galaxy	Property	Prospector				MAGPHYS
		Dirichlet	Bursty	Continuity	Parametric	
A1	$M_{\text{star}}$	-0.20 <sup>0.09</sup> <sub>0.08</sub>	<b>-0.46</b> <sup>0.16</sup> <sub>0.14</sub>	-0.31 <sup>0.12</sup> <sub>0.11</sub>	<b>-0.39</b> <sup>0.10</sup> <sub>0.10</sub>	<b>-0.37</b> <sup>0.09</sup> <sub>0.07</sub>
	SFR	-0.25 <sup>0.20</sup> <sub>0.17</sub>	-0.06 <sup>0.28</sup> <sub>0.19</sub>	-0.13 <sup>0.13</sup> <sub>0.12</sub>	<b>-0.15</b> <sup>0.05</sup> <sub>0.04</sub>	-0.10 <sup>0.06</sup> <sub>0.06</sub>
	sSFR	-0.05 <sup>0.25</sup> <sub>0.23</sub>	0.39 <sup>0.37</sup> <sub>0.31</sub>	0.18 <sup>0.19</sup> <sub>0.19</sub>	0.24 <sup>0.11</sup> <sub>0.11</sub>	0.20 <sup>0.11</sup> <sub>0.13</sub>
	$L_{\text{dust}}$	<b>-0.16</b> <sup>0.05</sup> <sub>0.04</sub>	<b>-0.16</b> <sup>0.05</sup> <sub>0.04</sub>	<b>-0.16</b> <sup>0.05</sup> <sub>0.04</sub>	<b>-0.16</b> <sup>0.05</sup> <sub>0.04</sub>	-0.10 <sup>0.05</sup> <sub>0.04</sub>
	$A_V$	-0.30 <sup>0.11</sup> <sub>0.12</sub>	-0.17 <sup>0.15</sup> <sub>0.14</sub>	-0.28 <sup>0.11</sup> <sub>0.12</sub>	-0.24 <sup>0.10</sup> <sub>0.10</sub>	<b>-0.26</b> <sup>0.07</sup> <sub>0.07</sub>
A2	$M_{\text{star}}$	-0.24 <sup>0.09</sup> <sub>0.09</sub>	<b>-0.55</b> <sup>0.14</sup> <sub>0.14</sub>	<b>-0.40</b> <sup>0.12</sup> <sub>0.11</sub>	<b>-0.51</b> <sup>0.10</sup> <sub>0.10</sub>	<b>-0.28</b> <sup>0.09</sup> <sub>0.08</sub>
	SFR	-0.31 <sup>0.21</sup> <sub>0.18</sub>	-0.19 <sup>0.36</sup> <sub>0.23</sub>	-0.16 <sup>0.13</sup> <sub>0.12</sub>	-0.14 <sup>0.05</sup> <sub>0.05</sub>	-0.21 <sup>0.07</sup> <sub>0.07</sub>
	sSFR	-0.07 <sup>0.26</sup> <sub>0.24</sub>	0.37 <sup>0.45</sup> <sub>0.33</sub>	0.25 <sup>0.20</sup> <sub>0.20</sub>	<b>0.37</b> <sup>0.10</sup> <sub>0.09</sub>	0.06 <sup>0.11</sup> <sub>0.11</sub>
	$L_{\text{dust}}$	<b>-0.13</b> <sup>0.04</sup> <sub>0.04</sub>	<b>-0.13</b> <sup>0.04</sup> <sub>0.04</sub>	<b>-0.13</b> <sup>0.04</sup> <sub>0.04</sub>	<b>-0.13</b> <sup>0.04</sup> <sub>0.04</sub>	-0.10 <sup>0.04</sup> <sub>0.03</sub>
	$A_V$	-0.30 <sup>0.10</sup> <sub>0.11</sub>	-0.16 <sup>0.13</sup> <sub>0.13</sub>	-0.26 <sup>0.11</sup> <sub>0.12</sub>	-0.23 <sup>0.10</sup> <sub>0.10</sub>	-0.15 <sup>0.07</sup> <sub>0.11</sub>
A4	$M_{\text{star}}$	-0.14 <sup>0.09</sup> <sub>0.08</sub>	-0.46 <sup>0.18</sup> <sub>0.16</sub>	-0.29 <sup>0.13</sup> <sub>0.12</sub>	<b>-0.39</b> <sup>0.10</sup> <sub>0.10</sub>	<b>-0.27</b> <sup>0.09</sup> <sub>0.08</sub>
	SFR	-0.24 <sup>0.21</sup> <sub>0.19</sub>	0.01 <sup>0.30</sup> <sub>0.20</sub>	-0.03 <sup>0.13</sup> <sub>0.12</sub>	-0.02 <sup>0.05</sup> <sub>0.04</sub>	-0.08 <sup>0.06</sup> <sub>0.06</sub>
	sSFR	-0.10 <sup>0.26</sup> <sub>0.25</sub>	0.47 <sup>0.42</sup> <sub>0.36</sub>	0.26 <sup>0.22</sup> <sub>0.21</sub>	<b>0.36</b> <sup>0.10</sup> <sub>0.10</sub>	0.18 <sup>0.12</sup> <sub>0.13</sub>
	$L_{\text{dust}}$	-0.10 <sup>0.04</sup> <sub>0.04</sub>	-0.10 <sup>0.04</sup> <sub>0.04</sub>	-0.10 <sup>0.04</sup> <sub>0.04</sub>	-0.10 <sup>0.04</sup> <sub>0.04</sub>	-0.07 <sup>0.04</sup> <sub>0.03</sub>
	$A_V$	-0.26 <sup>0.09</sup> <sub>0.10</sub>	-0.13 <sup>0.11</sup> <sub>0.12</sub>	-0.22 <sup>0.10</sup> <sub>0.10</sub>	-0.19 <sup>0.09</sup> <sub>0.09</sub>	-0.16 <sup>0.06</sup> <sub>0.07</sub>
A8	$M_{\text{star}}$	-0.08 <sup>0.09</sup> <sub>0.09</sub>	-0.48 <sup>0.18</sup> <sub>0.17</sub>	-0.32 <sup>0.15</sup> <sub>0.14</sub>	<b>-0.46</b> <sup>0.10</sup> <sub>0.11</sub>	-0.24 <sup>0.09</sup> <sub>0.10</sub>
	SFR	-0.40 <sup>0.18</sup> <sub>0.17</sub>	-0.12 <sup>0.23</sup> <sub>0.16</sub>	-0.15 <sup>0.13</sup> <sub>0.11</sub>	-0.11 <sup>0.05</sup> <sub>0.05</sub>	-0.05 <sup>0.06</sup> <sub>0.06</sub>
	sSFR	-0.32 <sup>0.23</sup> <sub>0.23</sub>	0.36 <sup>0.36</sup> <sub>0.31</sub>	0.17 <sup>0.23</sup> <sub>0.22</sub>	<b>0.35</b> <sup>0.09</sup> <sub>0.09</sub>	0.19 <sup>0.14</sup> <sub>0.14</sub>
	$L_{\text{dust}}$	-0.11 <sup>0.04</sup> <sub>0.04</sub>	-0.10 <sup>0.04</sup> <sub>0.04</sub>	-0.10 <sup>0.04</sup> <sub>0.04</sub>	-0.11 <sup>0.04</sup> <sub>0.04</sub>	-0.08 <sup>0.04</sup> <sub>0.03</sub>
	$A_V$	<b>-0.27</b> <sup>0.08</sup> <sub>0.08</sub>	-0.19 <sup>0.09</sup> <sub>0.09</sub>	-0.22 <sup>0.08</sup> <sub>0.09</sub>	-0.18 <sup>0.08</sup> <sub>0.09</sub>	-0.15 <sup>0.07</sup> <sub>0.06</sub>
All	$M_{\text{star}}$	-0.17 <sup>0.09</sup> <sub>0.08</sub>	<b>-0.49</b> <sup>0.17</sup> <sub>0.15</sub>	-0.33 <sup>0.13</sup> <sub>0.12</sub>	<b>-0.44</b> <sup>0.10</sup> <sub>0.10</sub>	<b>-0.29</b> <sup>0.09</sup> <sub>0.08</sub>
	SFR	-0.30 <sup>0.20</sup> <sub>0.18</sub>	-0.09 <sup>0.29</sup> <sub>0.20</sub>	-0.12 <sup>0.13</sup> <sub>0.12</sub>	-0.11 <sup>0.05</sup> <sub>0.04</sub>	-0.11 <sup>0.06</sup> <sub>0.06</sub>
	sSFR	-0.13 <sup>0.25</sup> <sub>0.24</sub>	0.40 <sup>0.40</sup> <sub>0.32</sub>	0.22 <sup>0.21</sup> <sub>0.20</sub>	<b>0.33</b> <sup>0.10</sup> <sub>0.10</sub>	0.18 <sup>0.12</sup> <sub>0.14</sub>
	$L_{\text{dust}}$	<b>-0.13</b> <sup>0.04</sup> <sub>0.04</sub>	-0.12 <sup>0.04</sup> <sub>0.04</sub>	-0.12 <sup>0.04</sup> <sub>0.04</sub>	<b>-0.12</b> <sup>0.04</sup> <sub>0.04</sub>	-0.09 <sup>0.04</sup> <sub>0.03</sub>
	$A_V$	-0.28 <sup>0.10</sup> <sub>0.10</sub>	-0.16 <sup>0.12</sup> <sub>0.12</sub>	-0.25 <sup>0.10</sup> <sub>0.11</sub>	-0.21 <sup>0.09</sup> <sub>0.10</sub>	-0.18 <sup>0.07</sup> <sub>0.07</sub>

value does follow the trend of true values in all cases. Looking at the PROSPECTOR nonparametric priors, Table 4.3 shows that the mean difference between the true and recovered values, averaged across all galaxies is -0.17 dex ( $1.9\sigma$ , where this statistical significance is calculated as  $\frac{\text{mean}}{(84\text{th percentile} - 16\text{th percentile}) * 0.5}$ ) for the Dirichlet prior, -0.49 dex ( $3.1\sigma$ ) for the Bursty prior, and -0.33 dex ( $2.8\sigma$ ) for the Continuity prior. It is also evident that the PROSPECTOR results are comparable to those of MAGPHYS using the same data. The PROSPECTOR results are also broadly in line with results reported in the literature when the uncertainties are taken into account, notably Leja et al. (2019), Carnall et al. (2019) and Lower et al. (2020) who all reported recoveries of stellar mass to within  $\approx 0.1$  dex and Hayward and Smith (2015), Ciesla et al. (2017) and Dudzevičiūtė et al. (2020) who reported recoveries of  $\approx 0.2$ ,  $\approx 0.1$  and  $\approx 0.5$  dex

respectively. While offsets measured in dex are part of the story, it is also critical to consider its statistical significance (as we do above), and we shall return to this topic, below.

Turning to the recovery of SFR, we again see from Table 4.3 that on average, recovery underestimates the true value. However, Figure 4.3 shows that the Bursty SFH and Continuity SFH, when averaged over all galaxies, achieve recovery of the true value within the uncertainties. Figures 4.4 to 4.7 show that PROSPECTOR follows the trend in true values, although the Parametric prior appears to deviate from the trend towards the low redshift end of the plots particularly in galaxies A1 and A2. This is likely an artefact of the unrealistically constrained uncertainties displayed by both the Parametric prior and by MAGPHYS when compared to those of the nonparametric priors (Leja et al., 2019). This result is compatible with that of Pacifici et al. (2023) which shows a wider distribution of results for the nonparametric fitters BAGPIPES and PROSPECTOR than that for MAGPHYS and CIGALE. Figure 4.3 shows that, when averaged across all galaxies, SFR is recovered well by all priors, with recoveries of 0.09 to 0.30 dex depending on the choice of SFH. These are broadly in line with the findings of Leja et al. (2019) at  $\approx 0.5$  dex using nonparametric SFH priors, and Hayward and Smith (2015) and Carnall et al. (2019) at  $\approx 0.1$  and  $\approx 0.2$  dex respectively using parametric SFH priors. We see no significant difference between the results of the nonparametric PROSPECTOR priors, this is not entirely unexpected as the recovery of SFR is strongly influenced by the assumed dust attenuation and the inclusion or exclusion of IR photometry (Pacifici et al., 2023) both of which are unchanged between these prior runs. However, Leja et al. (2019) demonstrated that SFR can be sensitive to the choice of prior, particularly over shorter timescales. Specifically, it was noted that for a declining SFR (as we have in e.g. A2 for  $z < 2$ ) the nonparametric prior should outperform a parametric prior. Despite this, Figure 4.5 reveals that all four PROSPECTOR priors exhibit similar behavior once the uncertainties are taken into account.

That the nonparametric results are also not significantly different when compared to the Parametric and MAGPHYS runs is more surprising, though both PROSPECTOR and MAGPHYS use the same dust attenuation model (Charlot and Fall, 2000). This result is, however, in agreement with Leja et al. (2019) who reported that the SFR derived by a delayed- $\tau$  model was not, in many cases, significantly different from that derived by the nonparametric Continuity prior (see Figure 12 of that work). The significance of prior choice is discussed in detail in Section 4.4.2.

Moving from SFR to sSFR, we see from Figures 4.4 to 4.7 that all runs produced similar results with the derived sSFR tending to be above the true sSFR with a difference between the true and

derived results of  $< 0.4$  dex in all but one case (Bursty prior for A4); this result is compatible with that of Hayward and Smith (2015). However, we note that based on the stellar mass formed, sSFR has an artificial upper recovered limit of  $10^{-8}$  which is an artefact of the method of calculation. Equation 4.7 shows the calculation for sSFR, noting that if all of the stellar mass has been formed in the last 100 Myr (i.e.  $M_{\text{star,current}} \approx M_{100\text{Myr,formed}}$ ), as is possible in the earliest snapshots before the return fraction becomes significant, the sSFR calculation will produce a value of  $\approx 10^{-8}$ .

$$sSFR = \frac{SFR_{100\text{Myr}}}{M_{\text{star,current}}} = \frac{M_{100\text{Myr,formed}}}{100 \times 10^6} \times \frac{1}{M_{\text{star,current}}} \approx \frac{M_{\text{star,current}}}{100 \times 10^6} \times \frac{1}{M_{\text{star,current}}} = 10^{-8} \quad (4.7)$$

We note that MAGPHYS is unable to fit at redshifts greater than 5.9, and so this trend is not visible in the MAGPHYS results.

Dust luminosity is well recovered with average residuals  $< 0.3$  dex in all cases which is consistent with Hayward and Smith (2015) and Haskell et al. (2023). The high fidelity of this result can likely be ascribed to the sampling of the FIR, particularly around the peak (Casey, 2012; Smith et al., 2013).

Finally, we look at the recovery of  $A_V$  which is also recovered well with average residuals of 0.3 mag or better. Again, the recovery of  $A_V$  follows the trend in the real values, this is particularly notable for A2 where  $A_V$  varies considerably around  $z = 2$  which PROSPECTOR mimics across all priors. There are no statistically significant differences between the different PROSPECTOR runs or with MAGPHYS.

These results show that, on average, the property values are recovered well and in line with previous works (e.g. Hayward and Smith 2015; Ciesla et al. 2017; Dudzevičiūtė et al. 2020; Lower et al. 2020; Haskell et al. 2023) but that the choice of prior has little statistically significant impact on the results, this is surprising given the results of other works - notably Leja et al. (2019), Carnall et al. (2019) and Pacifici et al. (2023) - and is discussed in Section 4.4.2.

### 4.3.3 The impact of the galaxy line-of-sight projection

The availability of different viewing angles for each snapshot within our simulations enables us to determine whether PROSPECTOR modelling is flexible enough to recover the true property value from the different projections of the galaxy while the intrinsic properties remain

unchanged. Figure 4.8 demonstrates how the difference between the true and derived property values varies with viewing angle when averaged across all snapshots in all galaxies. Each row shows a different property with the bars representing the residuals from the different fitters/priors as shown in the legend. The bars are grouped by view as indicated on the  $x$ -axis and show the mean of the residual 50th percentile as defined by Equation 4.6, the error bars show the 16th and 84th residual percentiles similarly averaged. It is evident from this that there is no consistent variation with view angle, except for  $A_V$  where the residuals show a weak tendency to vary as the angle moves towards the view corresponding to edge-on for a spiral galaxy. With the exception of  $A_V$ , all our measured properties are intrinsic to the galaxy as a whole and so are unaffected by viewing angle. During the 5 Gyr evolution of our simulated galaxies they experience a wide range of sizes and asymmetric shapes, despite this PROSPECTOR is able to satisfactorily fit the photometry and derive plausible galaxy properties. This result provides confidence that the fidelity of the results is, on average, unaffected by the different structure of dust and stellar emission presented by varying projections.

#### 4.3.4 Impact of an offset between stellar and dust emission on the recovery of property values

We now determine whether the PROSPECTOR derived values are impacted by spatial offsets between the UV emitting stars and the IR emitting dust. This is an extension of the work described in Haskell et al. (2023) for MAGPHYS, here we use the same three offset proxies as used in that work and described in Section 2.2.3. Figures 4.9 to 4.13 show how the property residuals, averaged across all galaxies, vary with these proxies: for the peak-to-peak and light-weighted offsets the residuals are averaged over equal log-spaced bins, for the Spearman correlation coefficient ( $\rho$ ) they are averaged over bins of width  $\Delta\rho = 0.1$ . Each figure presents the results for a single property and within each figure the four panels present the results for the different PROSPECTOR priors as shown by the captions. In each panel the top plot shows the relationship between the property residual and the peak-to-peak offset, the central plot shows that for the light-weighted mean offset and the last for the Spearman correlation. The coloured lines show the mean residual value within each bin, the shaded coloured areas enclose the mean 16th and 84th percentiles of the residuals. To determine if the uncertainties are reasonable we also include the 16th and 84th percentiles of the bin contents scatter, shown as the grey shaded area. The background bar chart shows the bin occupancy read from the right-hand  $y$ -axis. Note that, as in Haskell et al.

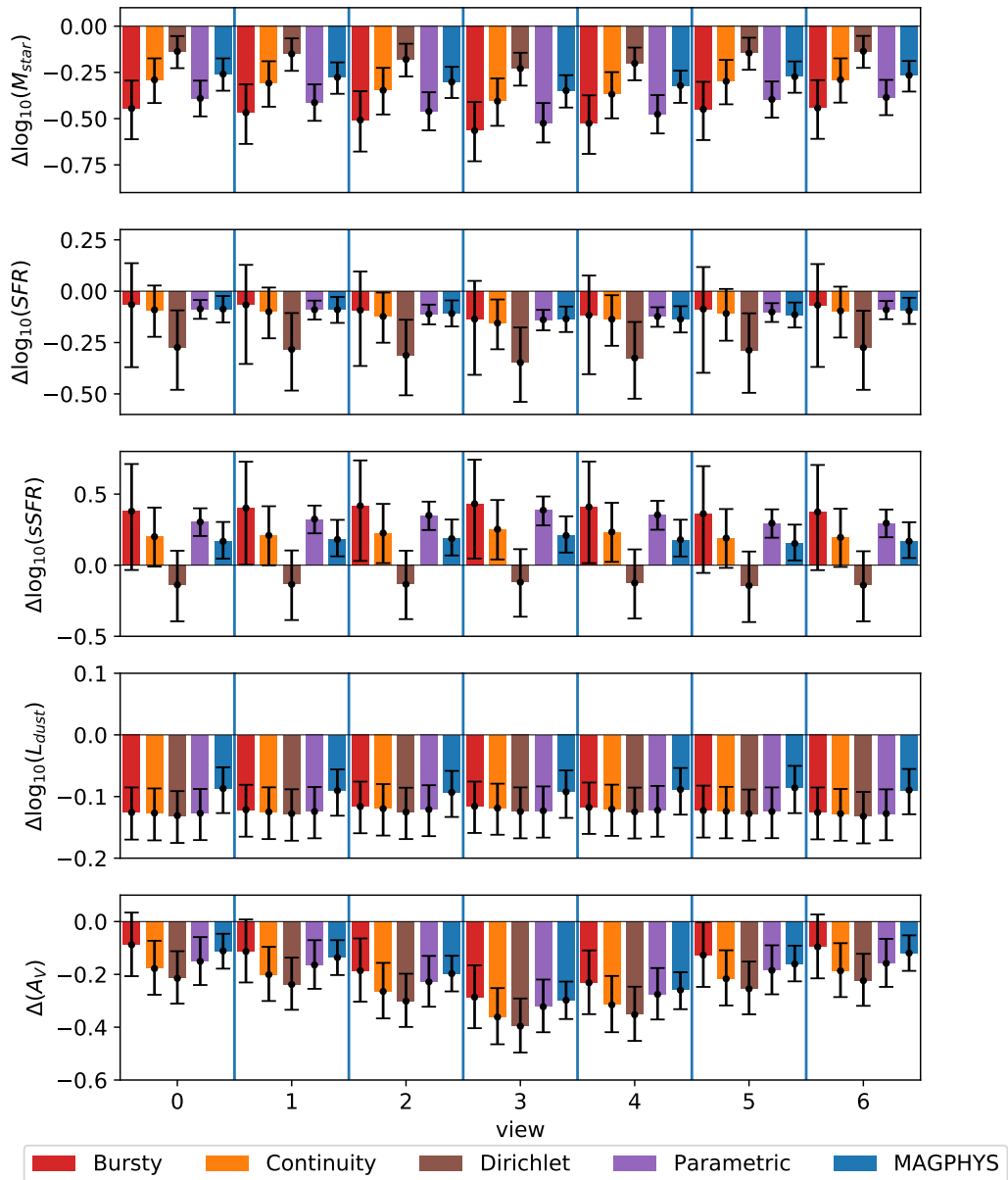


FIGURE 4.8: Average median residuals by view. Each panel shows the residual plots for the property labelled on the y-axis. The bars are grouped by view (see x-axis labels) and show the mean of the 50th percentile of the residuals averaged across all galaxies and snapshots. The bars are colour coded as per the legend. The black error bars show the 16th and 84th percentiles of the residual similarly averaged.

(2023), we have used only the brightest 20 per cent of pixels in either the UV or IR in these tests.

In all cases we see both a flat response across the range of proxy values, and a consistency between the four PROSPECTOR priors when the uncertainties are taken into account. This result is in agreement with Haskell et al. (2023) which reported similar results for MAGPHYS and reinforces the conclusion of that work that the energy-balance assumption remains valid as the stellar and FIR emission offsets vary.

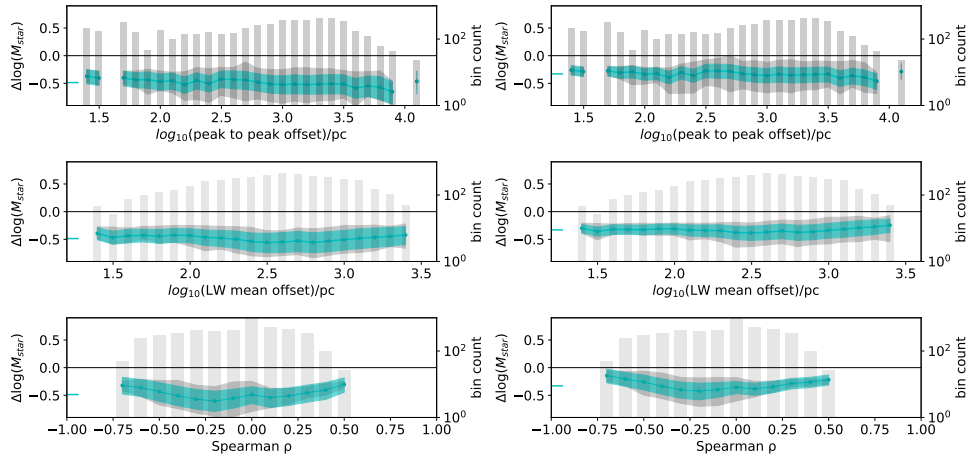
However, we note that in a number of plots there is significant scatter, the statistical significance of this scatter was measured using an F-test on each bin, defined as:

$$F = \sigma_1 / \sigma_2 \quad (4.8)$$

Where  $\sigma_1$  is the standard deviation of the scatter of data within a bin, and  $\sigma_2$  is the averaged same for the uncertainties of the data within a bin, for this test we used a significance of  $\alpha = 0.01$ . This test demonstrated that all three nonparametric priors show similar patterns of scatter significance. For stellar mass, dust luminosity and  $A_V$  the scatter was significantly greater than the error bars, indicating that the error bars may be underestimated for these properties. In contrast, SFR and sSFR show little or no significant scatter. The Parametric prior shows scatter greater than the error bars for all properties and proxy values which is in line with the findings of Leja et al. (2019) that Parametric priors have unrealistically constrained error bars.

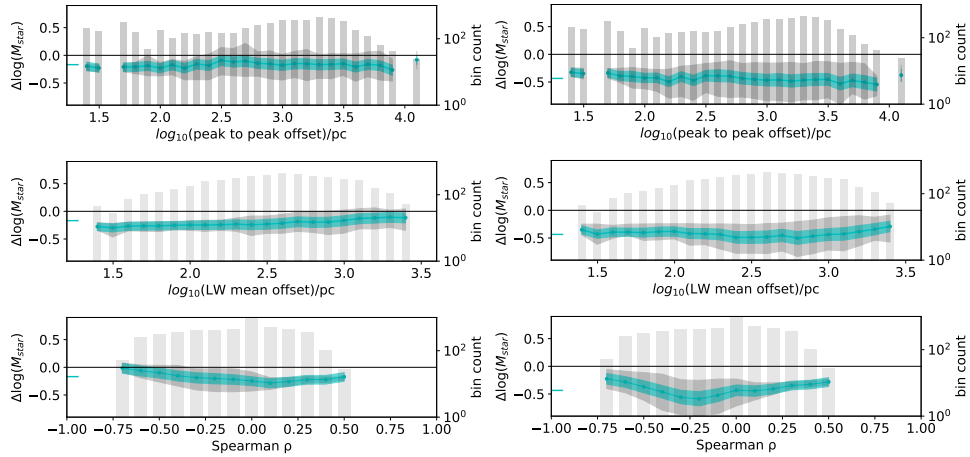
### 4.3.5 The impact of true property values

Figures 4.14 to 4.18 demonstrate how the fidelity of the derived values varies with the true values of the properties provided by the simulations. We show this by dividing the range of values into 30 equal log-spaced bins, the range of property values is determined as the maximum and minimum value for which at least one fitter/prior combination was able to find a successful fit. For all snapshots with values that fall within a bin, the average difference between the true value and the median value derived by a fitter/prior combination is shown. Also shown is the similarly averaged difference between the true value and the 16th and 84th percentiles of the derived value, and the 16th and 84th percentile values for the scatter within each bin represented by the grey-shaded area. The background bar chart shows the bin occupancy read from the right-hand y-axis. The five plots demonstrate that the four PROSPECTOR priors and MAGPHYS exhibit



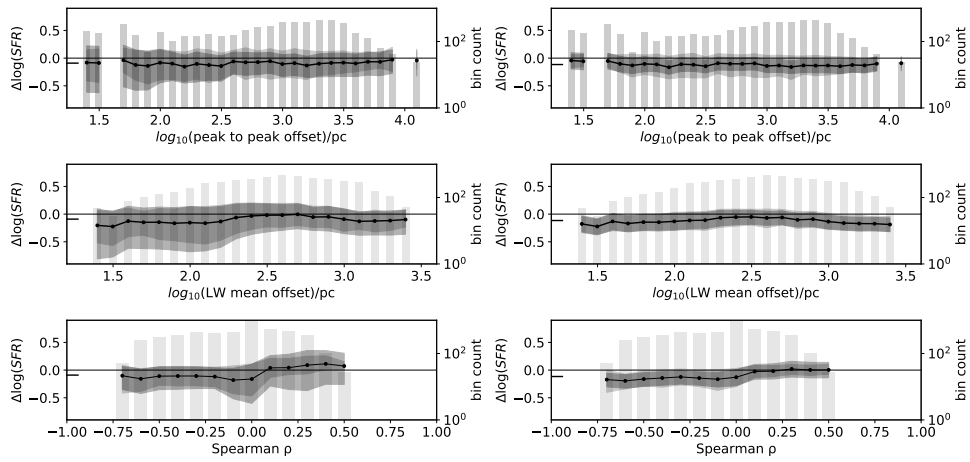
(A) PROSPECTOR Bursty prior

(B) PROSPECTOR Continuity prior

(C) PROSPECTOR Dirichlet ( $\alpha = 1$ )  
prior

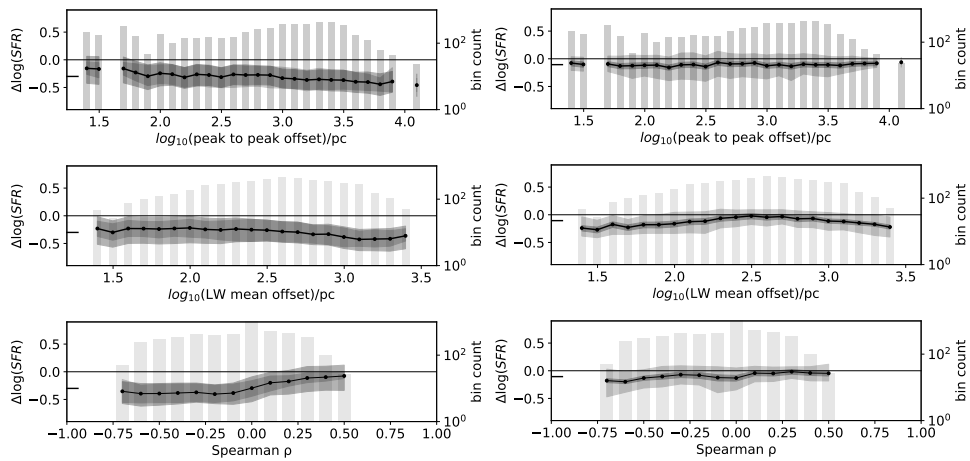
(D) PROSPECTOR Parametric prior

FIGURE 4.9: The variability of the stellar mass residual with the stellar and dust emission offset. Each panel shows how the residual of PROSPECTOR’s recovery of stellar mass varies against the proxies defined in the text for the offset between UV and FIR emitting regions. Each prior is shown in a different panel (see panel caption), in each panel the stellar mass recovery is plotted against the simple peak-to-peak proxy in the upper plot, the light-weighted mean proxy in the centre plot, and the Spearman rank correlation coefficient  $\rho$  in the lower plot. The coloured line marks the median of the difference between the true and recovered values averaged over each bin; the coloured region marks the 16th and 84th percentiles of this difference similarly averaged and the grey-shaded area the 16th and 84th percentiles of the scatter within each bin. The short coloured lines adjacent to the left-hand y-axis mark the mean value of the difference across all galaxies and snapshots for which a satisfactory fit was achieved; the background bar chart shows the bin occupancy read from the right-hand y-axis.



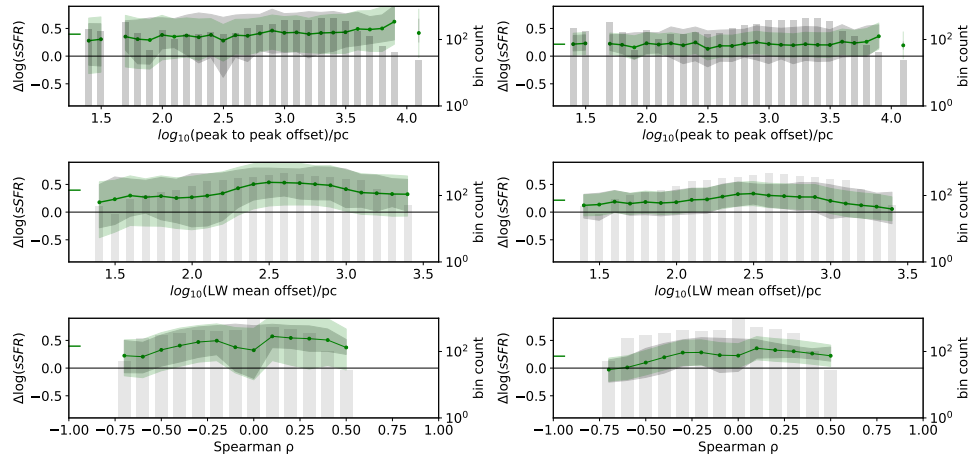
(A) PROSPECTOR Bursty prior

(B) PROSPECTOR Continuity prior

(C) PROSPECTOR Dirichlet ( $\alpha = 1$ ) prior

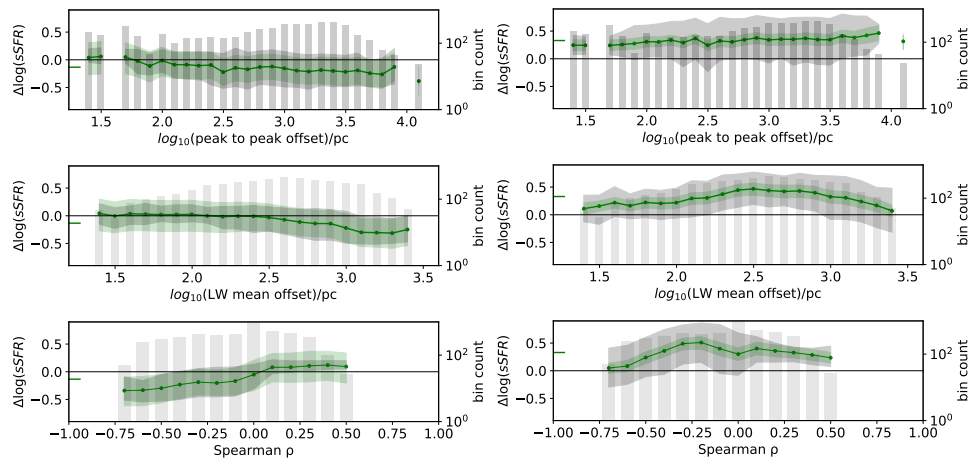
(D) PROSPECTOR Parametric prior

FIGURE 4.10: The variability of the SFR residual with the stellar and dust emission offset - see 4.9 for details.



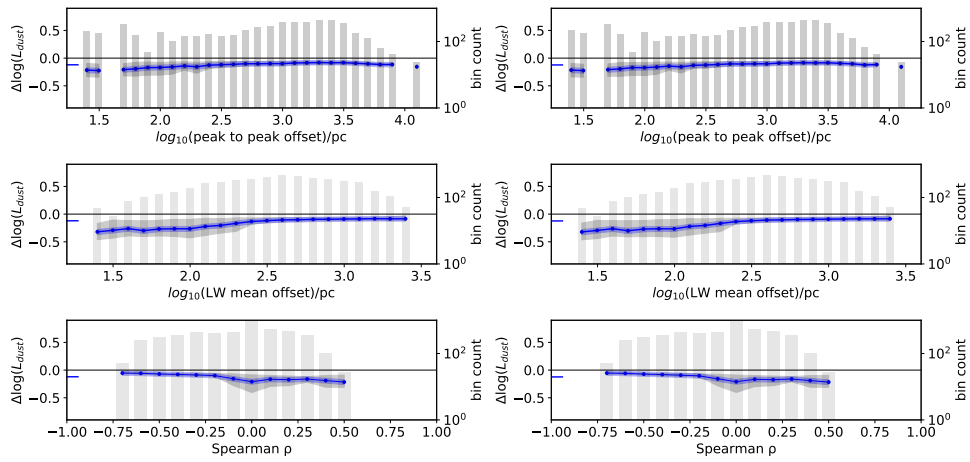
(A) PROSPECTOR Bursty prior

(B) PROSPECTOR Continuity prior

(C) PROSPECTOR Dirichlet ( $\alpha = 1$ )  
prior

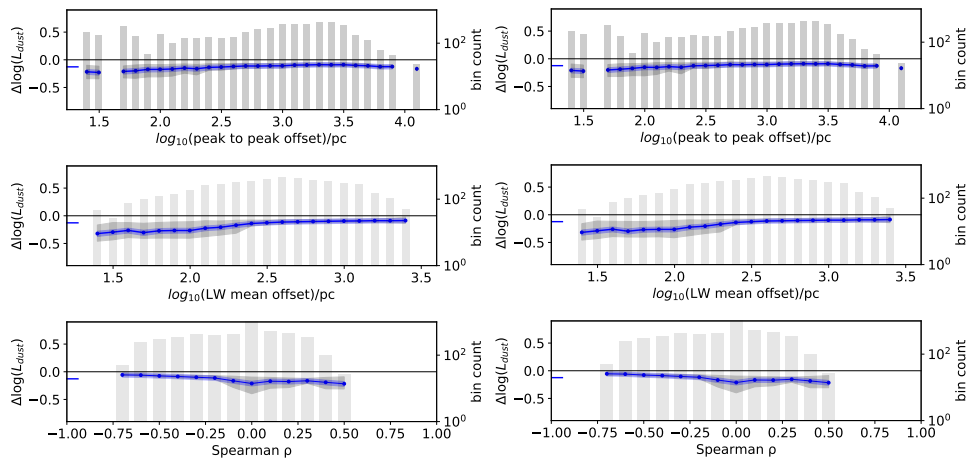
(D) PROSPECTOR Parametric prior

FIGURE 4.11: The variability of the sSFR residual with the stellar and dust emission offset - see Figure 4.9 for details.



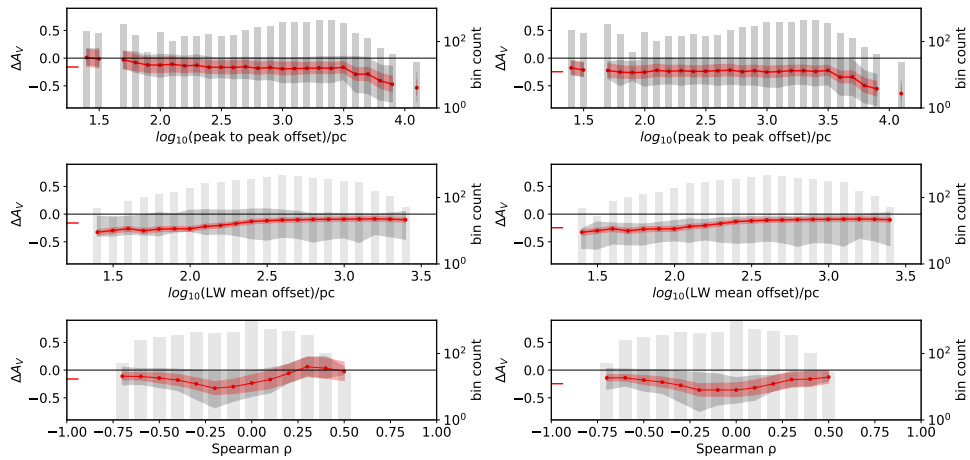
(A) PROSPECTOR Bursty prior

(B) PROSPECTOR Continuity prior

(C) PROSPECTOR Dirichlet ( $\alpha = 1$ )  
prior

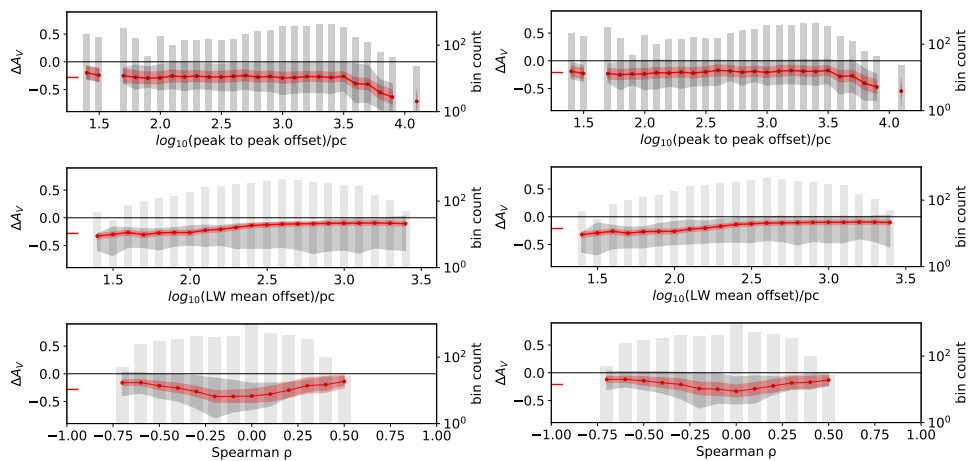
(D) PROSPECTOR Parametric prior

FIGURE 4.12: The variability of the dust luminosity residual with the stellar and dust emission offset - see Figure 4.9 for details.



(A) PROSPECTOR Bursty prior

(B) PROSPECTOR Continuity prior

(C) PROSPECTOR Dirichlet ( $\alpha = 1$ )  
prior

(D) PROSPECTOR Parametric prior

FIGURE 4.13: The variability of the  $A_V$  residual with the stellar and dust emission offset - see Figure 4.9 for details.

broad consistency, yielding comparable shapes and similar values across the derived property distributions.

Figure 4.14 presents the results for stellar mass and we can see that the fitters show remarkable consistency and that the response is approximately flat, once the uncertainties are taken into account, except at low stellar masses ( $M_{\text{star}} < 10^8 M_{\odot}$ ). These low stellar masses occur at redshifts of  $4 < z < 8$  in the simulations, a range within which the proportion of failed fits by MAGPHYS increases. A standard F-test on the variance of the scatter within each bin and that of the data ( $F = \frac{\sigma_{\text{scatter}}}{\sigma_{\text{data}}}$ ) shows that in the majority of cases the scatter is significantly greater than the error bars ( $> 68$  per cent of the bins for the nonparametric priors, 100 per cent for the parametric prior and 85 per cent for MAGPHYS) leading us to the conclusion that the error bars are underestimated in all cases.

The results for SFR are shown in Figure 4.15 and demonstrate that once again we have consistency between the fitters and a generally flat response to the changes in true SFR except for values  $\lesssim 2 \times 10^{-1} M_{\odot} \text{yr}^{-1}$  where bin occupancy is  $< 10$ . Here, the scatter is significantly greater than the error bars in fewer bins for the nonparametric priors, but again in the majority for the parametric prior and MAGPHYS.

Figure 4.16 demonstrates continued consistency between the priors, including a trend of increasing underestimation as sSFR increases, Equation 4.7 shows that sSFR will be increasingly underestimated as true sSFR rises above  $10^{-8} \text{yr}^{-1}$ . From Figures 4.4 to 4.7 we can see that sSFR is at its highest at high redshifts when this is likely to be the case and so the trend in Figure 4.16 of reducing fidelity as sSFR increases is to be expected. The trend is not visible in the MAGPHYS results as MAGPHYS was unable to find statistically significant fits for any snapshots with  $\text{sSFR} > 1.4 \times 10^{-8}$ . Of these, only 10 fell below the redshift limit after which MAGPHYS was unable to fit any snapshots ( $z \approx 5.9$ ).

Figure 4.17 presents the results for dust luminosity. The fitters and priors are remarkably consistent with the results being broadly flat when the uncertainties are taken into account. Scatter is less significant across all of the PROSPECTOR runs and MAGPHYS.

Finally, Figure 4.18 presents the results for the  $A_V$  recovery. These show that  $A_V$  becomes increasingly underestimated as the value of  $A_V$  increases for all priors and both fitters. We note that there is a correlation between  $A_V$  recovery and SFR; the upper panel of Figure 4.19 shows that the true value for  $A_V$  increases as the short-term SFR increases, and the lower panel

that the recovery of  $A_V$  deteriorates with increasing SFR, a finding which is in agreement with Wuyts et al. (2009). These figures demonstrate that recovery of  $A_V$  deteriorates with increased star-forming activity.

#### **4.3.6 The significance of scatter**

Finally, we address the issue of scatter in the plots of the residuals against both the offset proxy values (Figures 4.9 to 4.13) and the true property values (Figures 4.14 to 4.18). We commented in Section 4.2 that the method of determining the  $\chi^2_{\max}$  values, i.e. the value of  $\chi^2$  above which a fit would be deemed unsatisfactory, was derived by Smith et al. (2012) using MAGPHYS and that this derivation may not be suitable for PROSPECTOR. One explanation for the scatter could be that the  $\chi^2_{\max}$  was set too high and so poorly fitted models were being included in our averaging. We have found that the effect remained after reducing the value of  $\chi^2_{\max}$  by up to 50 per cent, suggesting that it is unlikely the value of  $\chi^2_{\max}$  is the cause of the scatter. Further investigation is required to determine the cause of the scatter which we defer to a future work.

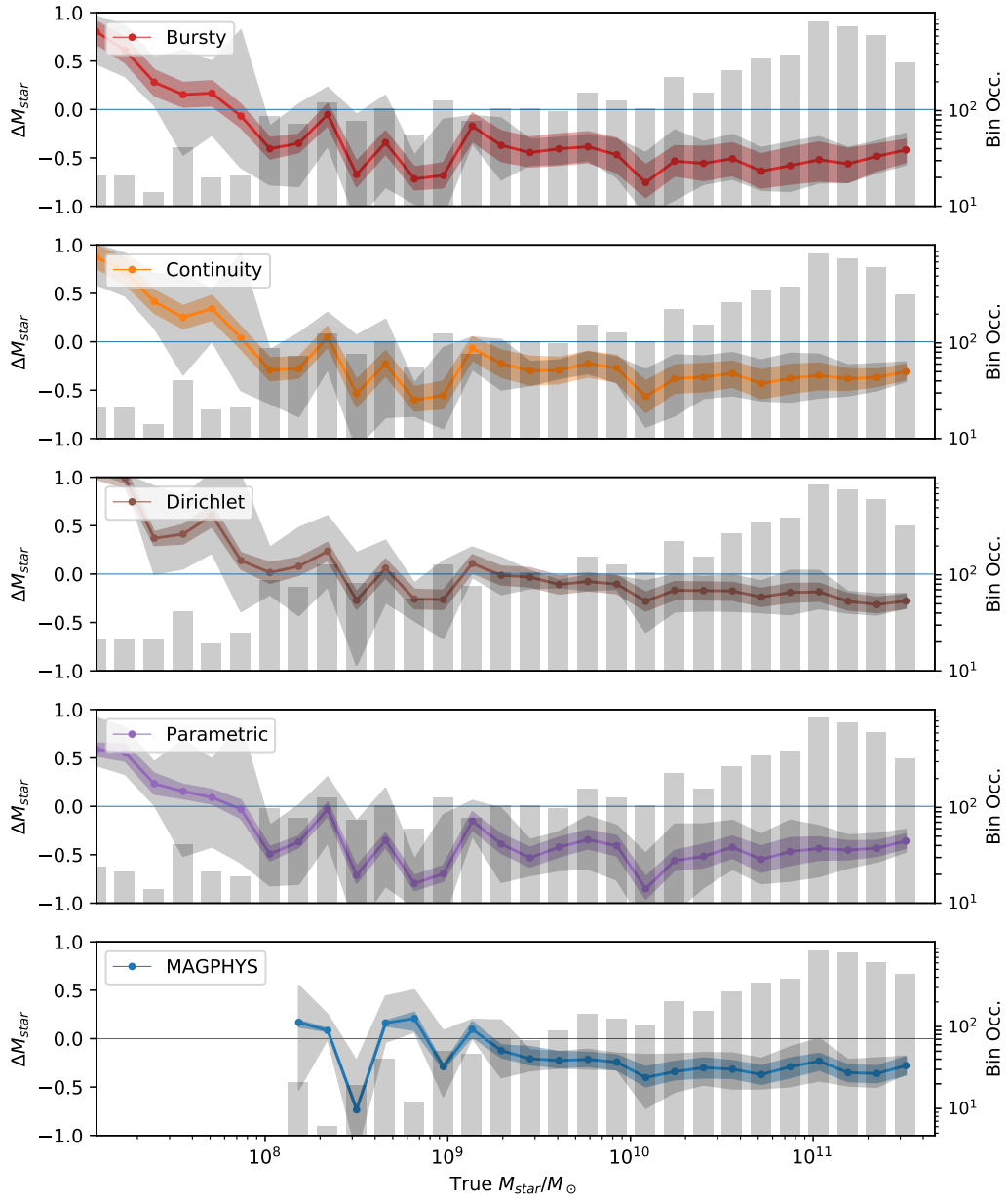


FIGURE 4.14: The variation in the stellar mass median residual value against the range of true stellar mass values available from the simulations. Each panel plots the results for the different fitters and SFH priors as shown in the label at the top left. In each panel, the coloured line plots the 50th percentile of the residual averaged over log-spaced bins of the true stellar mass values. The shaded area of the same colour shows the 16th and 84th residual percentiles similarly averaged, the grey-shaded area encloses the 16th and 84th percentiles of the scatter within each bin. The background bar chart shows the bin occupancy read from the right-hand y-axis.

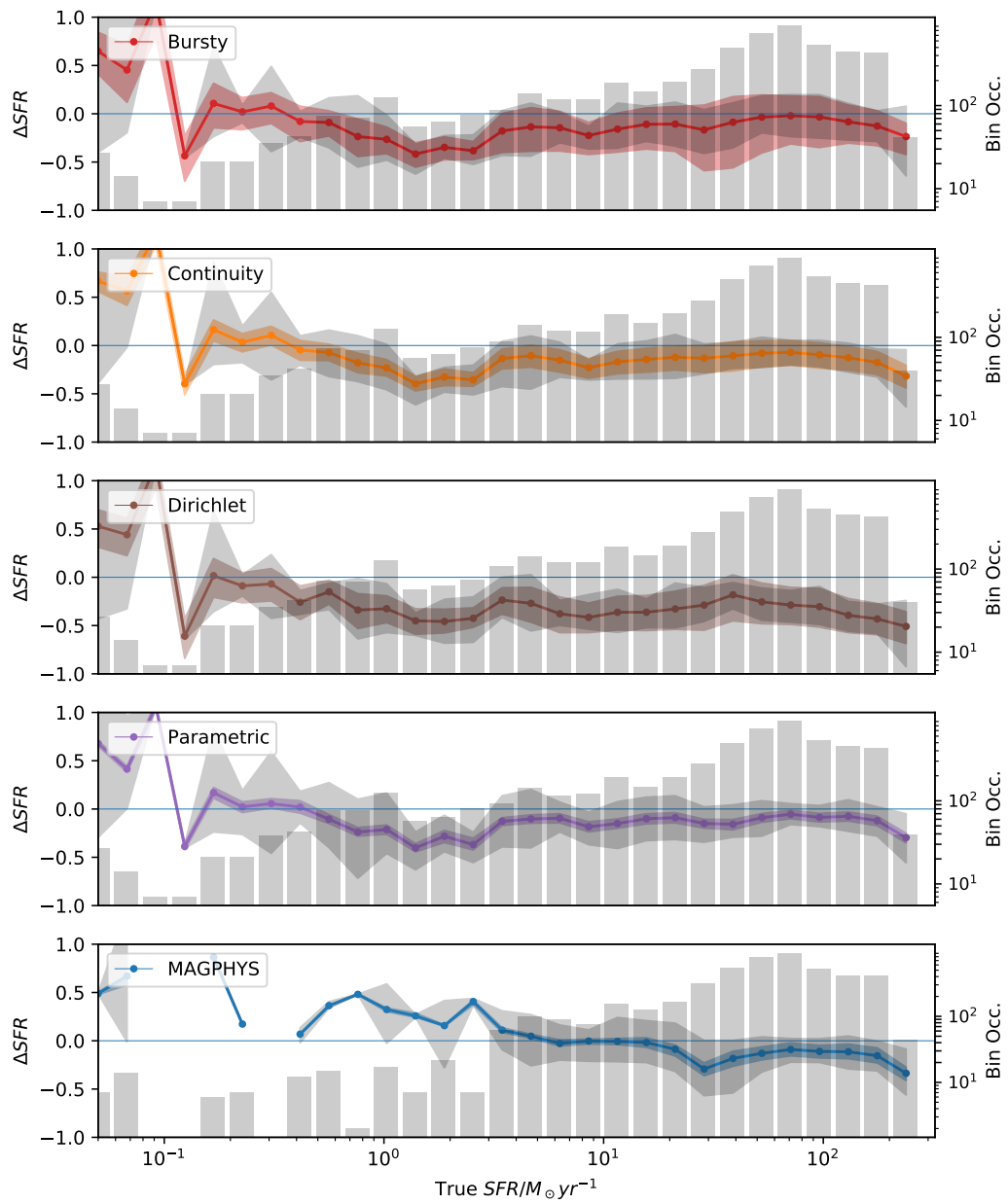


FIGURE 4.15: Plots of the variation in the SFR median recovery as a function of the range of SFR true values - see Figure 4.14 for details.

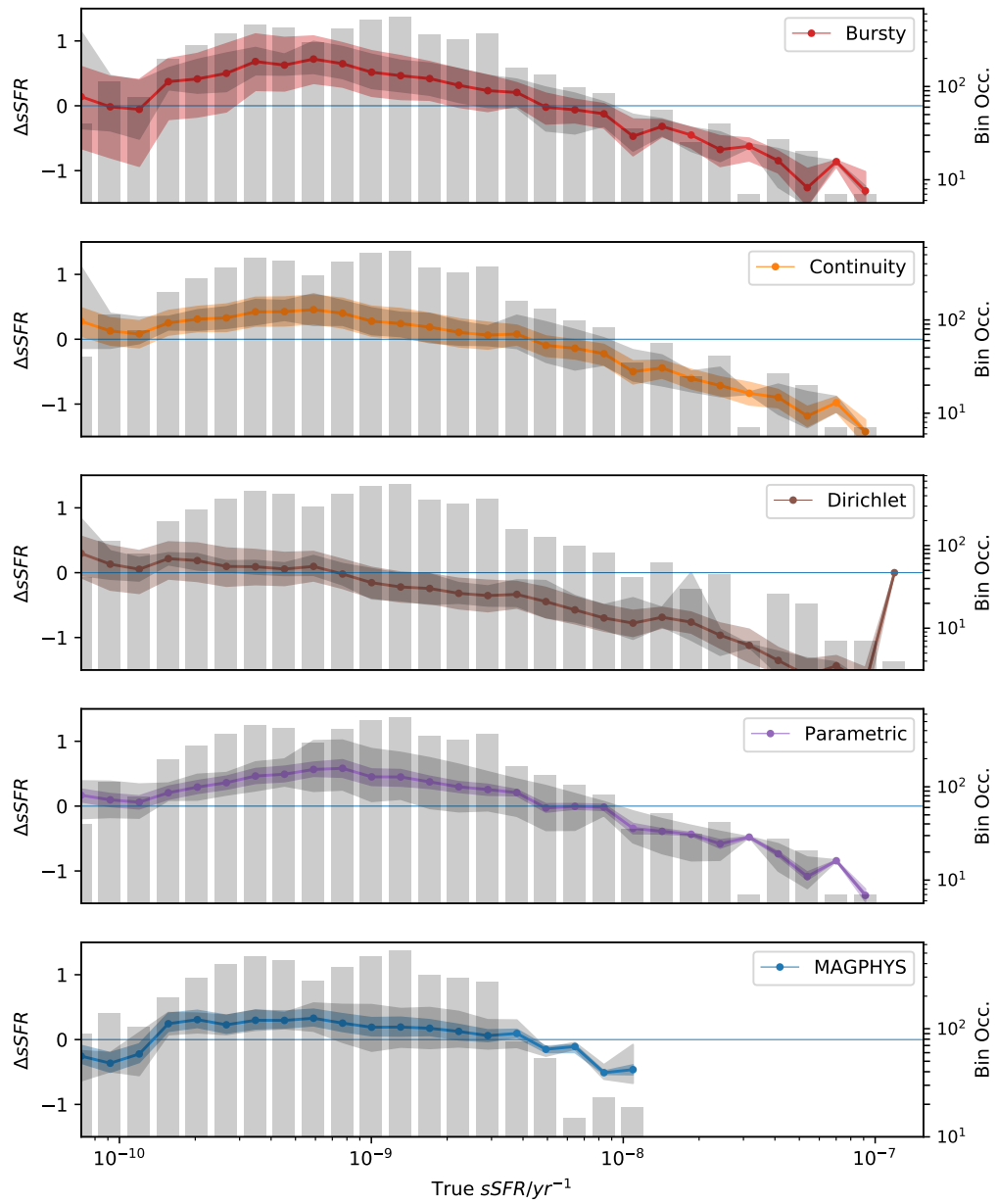


FIGURE 4.16: Plots of the variation in the sSFR median recovery as a function of the range of sSFR true values - see Figure 4.14 for details.

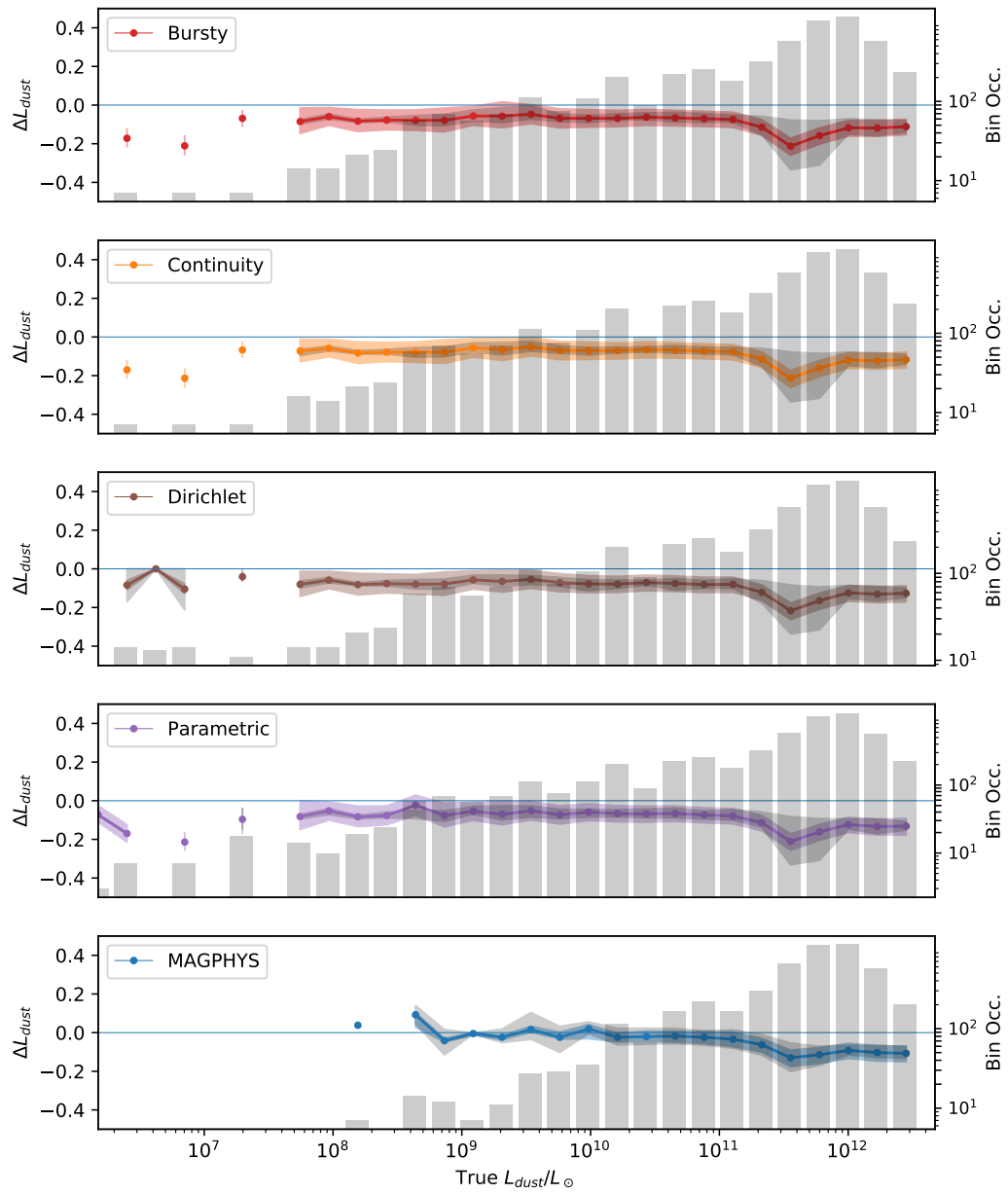


FIGURE 4.17: Plots of the variation in the dust luminosity recovery as a function of the range of dust luminosity true values - see Figure 4.14 for details.

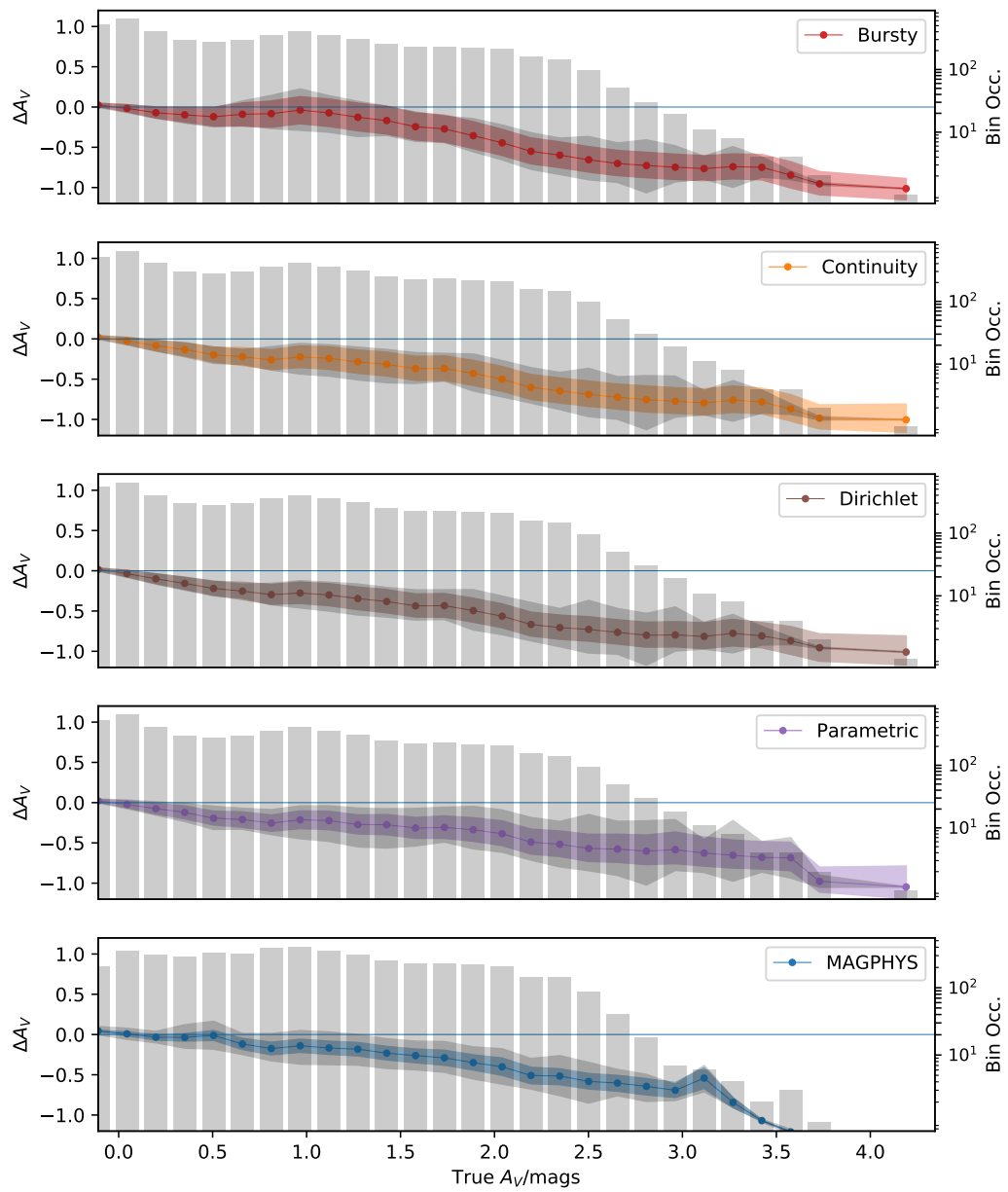


FIGURE 4.18: Plots of the variation in the  $A_V$  median recovery as a function of the range of  $A_V$  true values - see Figure 4.14 for details.

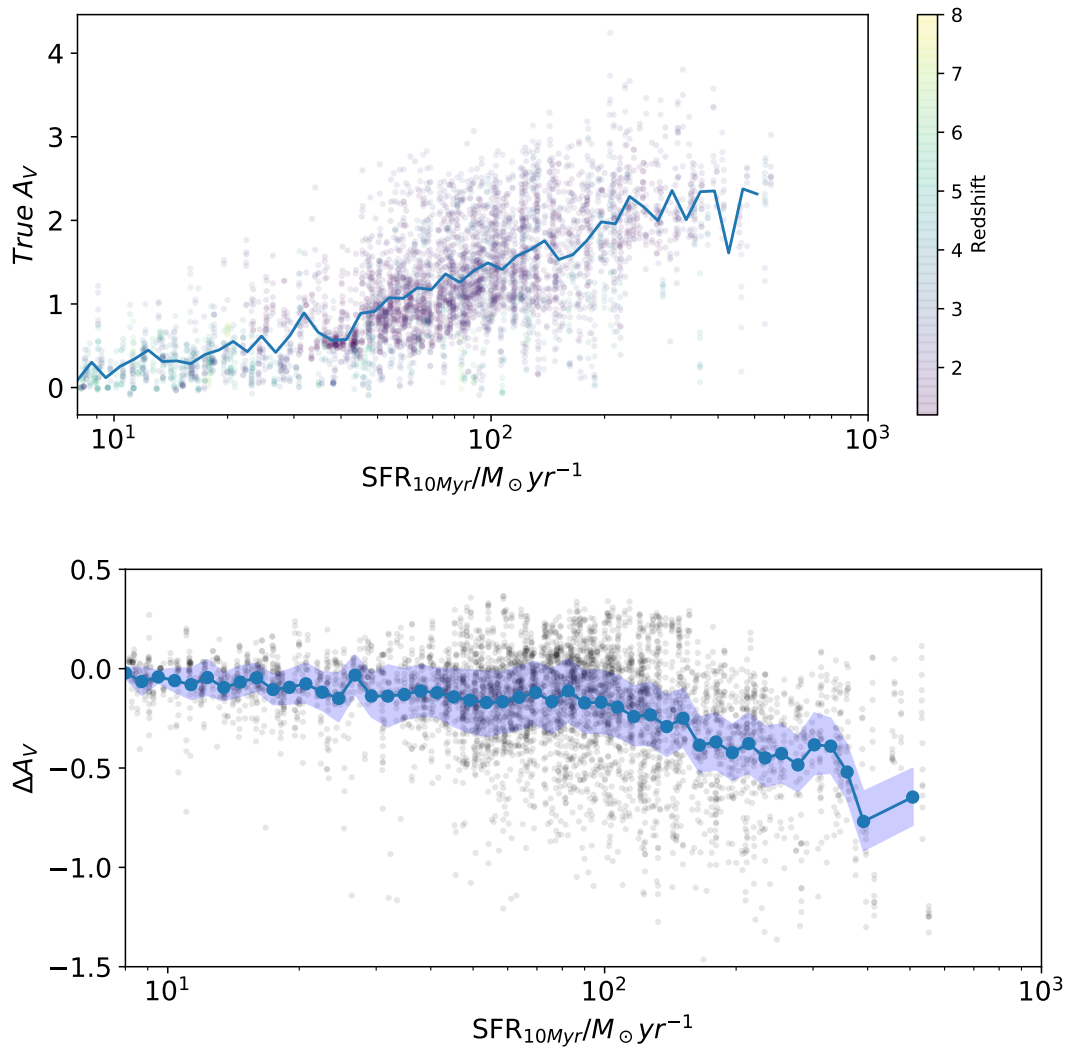


FIGURE 4.19: The relationship between  $A_V$  and the 10 Myr averaged SFR. The upper panel plots the true value of  $A_V$  against the true 10 Myr average SFR; the background points are the data, the blue line shows the trend with the data averaged over equal log-spaced bins. The lower panel plots the recovery of  $A_V$  for the Bursty SFH prior against the 10 Myr averaged SFR; the background points are the data, the blue line shows the trend in recovery accuracy averaged over equal log-spaced bins with the coloured area enclosing the 16th and 84th percentiles of the recovered accuracy similarly averaged.

## 4.4 Discussion

### 4.4.1 Why does PROSPECTOR fail to fit?

Figure 4.1 demonstrates that where PROSPECTOR was unsuccessful can be categorised into two redshift ranges, below  $z \approx 2.5$  and above  $z \approx 4.5$ . This division highlights specific failure modes associated with each redshift range. Table 4.4 classifies the failures into four distinct modes which are discussed in the following sections.

TABLE 4.4: The different fitting failure modes for PROSPECTOR. The first column shows the galaxies, the second the total number of observations of that galaxy and the third the number of unsuccessful fits. The subsequent columns show the number of unsuccessful fits in each category, these are defined and discussed in the text.

Galaxy	Total Obs	Total Fails	$M_{\text{dust}} = \text{zero}$	Low $M_{\text{dust}}/M_{\text{star}}$	$z < 2.5$ other	$z > 4.5$ other
A1	1512	122	21	89	0	12
A2	1491	136	0	129	0	7
A4	1477	79	35	14	25	5
A8	1414	67	21	149	9	23
All	5894	404	77	246	34	47

#### 4.4.1.1 Zero dust mass galaxies

Eleven snapshots comprising 77 views with  $z > 4.5$  exhibit a true dust mass of zero. While dust-free galaxies are possible at  $z > 10$  (Nath et al., 2023), their existence at lower redshifts has not been observed, suggesting that such galaxies may be unphysical (e.g. Santini et al., 2014; Popping et al., 2017). Consequently, it is, perhaps, not surprising that none of the priors are able to model zero-dust galaxies at these redshifts.

This scenario does raise an interesting point, Figure 4.20 presents the SED derived by PROSPECTOR for one of these zero dust mass galaxies. As expected, the input SED and the input unattenuated SED are identical as would be expected in the absence of dust. Despite not being able to find a satisfactory match, PROSPECTOR has also derived SED and unattenuated SED that are identical, reflecting the integrated stellar emission from a galaxy with no reddening or attenuation. However there is a visible discrepancy between the simulation and the PROSPECTOR SED in the shape of this emission. This difference decreases at lower redshifts, for example see Figure 4.21 for the input and derived SEDs of a snapshot at  $z = 1.14$  where the input and derived intrinsic SEDs are well fitted. This may highlight the effect of the energy-balance assumption and its constraining effect on UV/optical fitting, however further research is needed to establish the source of this trend.

#### 4.4.1.2 Low dust to stellar mass ratio galaxies

We now look at the failures identified in column 5 of Table 4.4. These failures are caused by a low dust to stellar mass ratio, resulting in a 100 per cent failure rate when the ratio falls below  $\approx 10^{-5}$ . Figure 4.22 illustrates this correlation between the percentage of failed fits and the dust

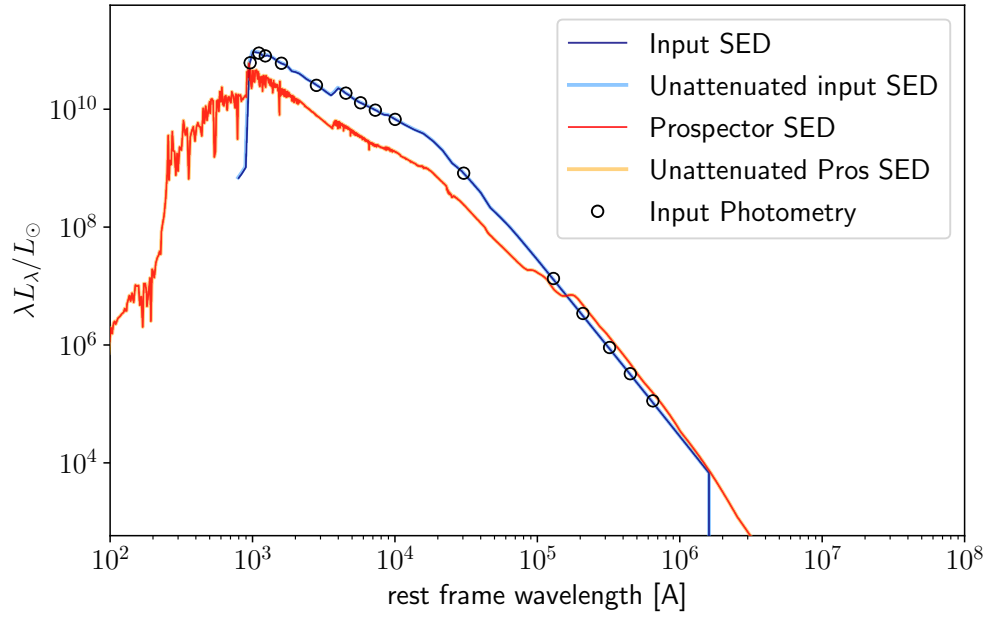


FIGURE 4.20: PROSPECTOR generated SED of a snapshot with zero true dust mass.

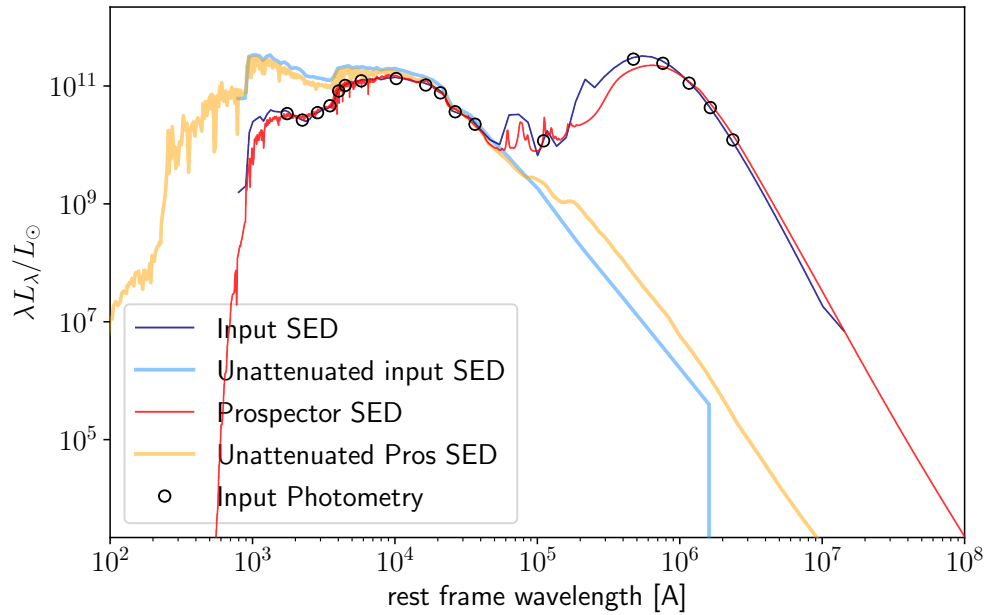


FIGURE 4.21: PROSPECTOR generated SED of a snapshot at  $z = 1.14$  showing the alignment between the true and derived unattenuated SEDs.

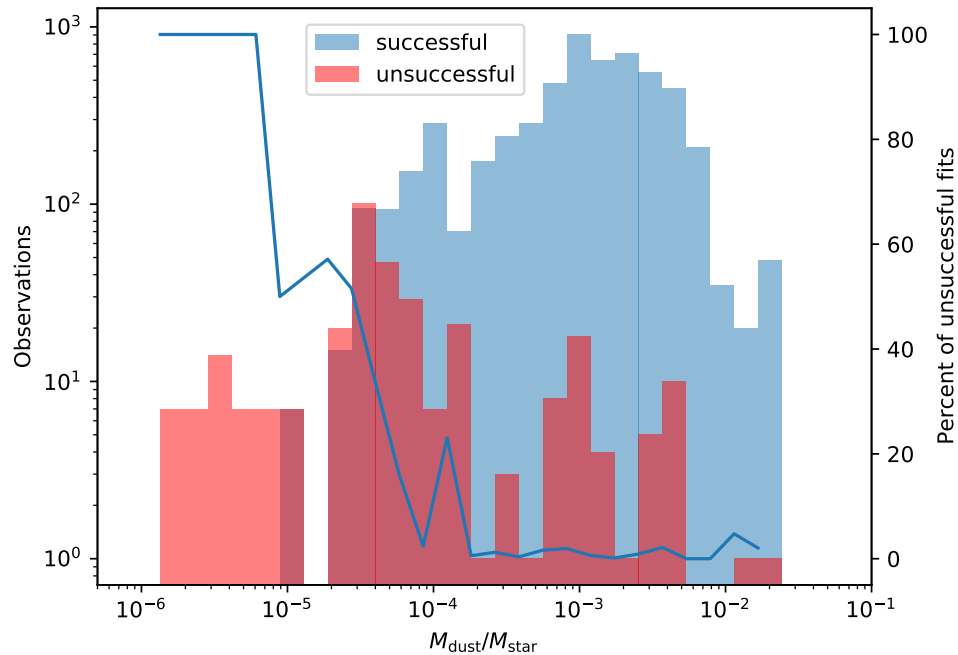


FIGURE 4.22: The percentage of PROSPECTOR failed fits against the dust to stellar mass ratio across all snapshots of all galaxies. The  $x$ -axis shows the dust to stellar mass ratio, the blue bars present the number of successful fits achieved using the Bursty SFH prior, read from the left-hand  $y$ -axis, in equal log-spaced bins; the red bars show the number of unsuccessful fits. The blue line plots the percentage of failed fits read from the right-hand  $y$ -axis.

to stellar mass ratio, suggesting a potential limitation in the PROSPECTOR’s ability to model low dust content.

Figure 4.23 demonstrates the position of failed fits on a plot of dust to stellar mass ratio against redshift; the shaded areas enclose  $2.5 < z < 4.5$  within which there are few failed fits. It is evident from this figure that the mass ratio drops to critical values predominantly in the range  $1 < z < 2.5$  making it unlikely to be related to the zero dust mass issue described above which is restricted to  $z > 4.5$ .

Several works have considered the problems of fitting SEDs to edge-on spiral galaxies (e.g. Bianchi, 2007; De Looze et al., 2012; De Geyter et al., 2014; Saftly et al., 2015). To investigate whether there is a systematic bias when recovering those views for which the apparent  $A_V$  is higher we plotted the number of failures against view; if the edge-on views of spiral galaxies were an issue, we would expect to see a peak of failed fits around view = 3 (edge-on for spiral galaxies). The results for MAGPHYS and PROSPECTOR using the Busty prior are shown in Figure 4.24, all other PROSPECTOR priors returned very similar results. We see from this no

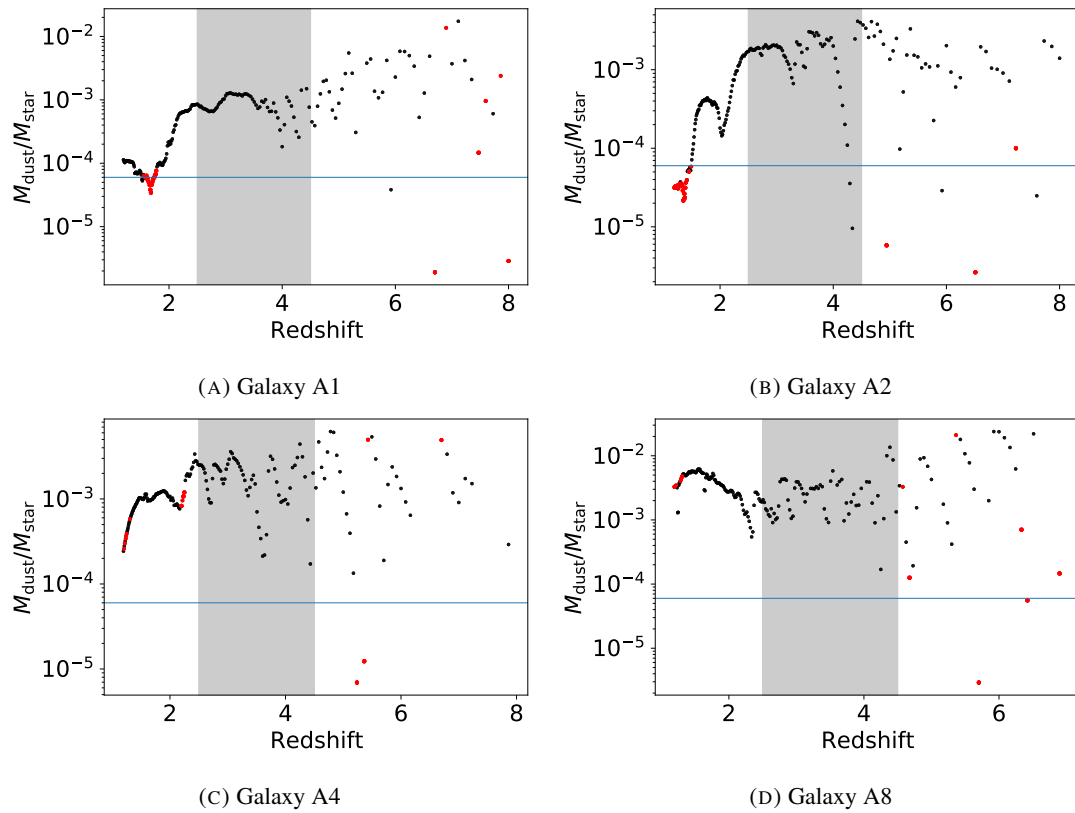


FIGURE 4.23: Plots of the dust to stellar mass ratio against redshift for each of the four galaxies. Black points mark successful fits, red points unsuccessful fits, note that failed fits due to zero dust mass have been removed. The horizontal line marks a mass ratio of  $6 \times 10^{-5}$  for reference; the shaded area encloses  $2.5 < z < 4.5$  within which there are no failed fits.

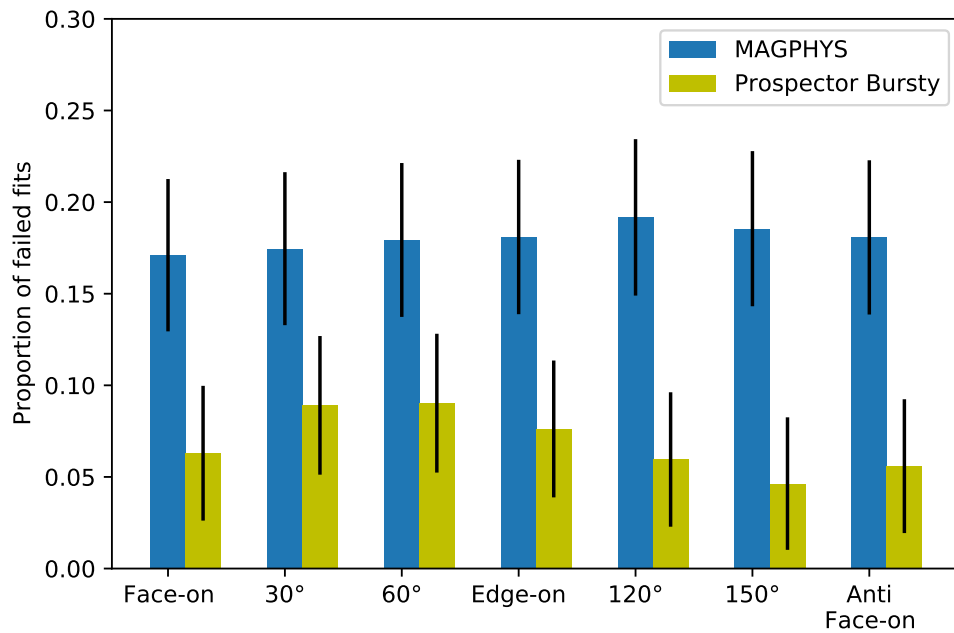


FIGURE 4.24: Bar chart showing the proportion of failed fits for each view for MAGPHYS and PROSPECTOR using the Bursty prior, with Poisson errors.

evidence of a bias towards view 3 and so conclude that the orientation is not the cause of the failures to fit.

Figures 4.4 to 4.6 show that galaxies A1, A2 and A4 suffer a considerable drop in dust luminosity in the latter stages of their evolution, however PROSPECTOR has satisfactorily fitted SEDs at the start of the loss in  $L_{\text{dust}}$  and for some considerable time after the event and is only unable to fit when the dust to stellar mass ratio falls below  $\approx 10^{-4}$ . This leads us to speculate that the issue is based on this low value rather than PROSPECTOR failing to fit the complex event that led to the loss of dust luminosity. Figure 4.25 provides an example of the input and derived SEDs for a low dust-mass snapshot of galaxy A1, with  $M_{\text{dust}}/M_{\text{star}} = 6.3 \times 10^{-5}$ , demonstrating that PROSPECTOR has been unable to fit the FIR peak, producing an SED that underestimates the IR emission. This is likely caused by the similar underestimation of the intrinsic UV/optical emission which will not provide the energy-balance assumption with enough energy to reach the true IR emission levels. This conclusion correlates with Figure 4.4 which shows that PROSPECTOR underestimates the dust luminosity at the same redshift.

Analysis of the available prior data ( $U_{\text{min}}$ ,  $\gamma_e$  and  $Q_{\text{PAH}}$ ) shows no evidence that the PDFs peak close to the bounds of the priors – indicating that the PDFs seem primarily constrained by the data rather than by the priors. While further investigation is needed to explore this issue, our preliminary conclusion is that PROSPECTOR’s dust emission model is not well-suited to reproduce atypically low dust mass.

#### 4.4.1.3 Remaining unsatisfactory fits at $z < 2.5$

Table 4.4 column 6 indicates that galaxies A4 and A8 exhibit failed fits that are not associated with the issues discussed above. Analysing the SEDs for these 34 failed fits we find that the  $\chi^2$  values are predominantly driven by discrepancies in the FIR observations around the FIR peak. Specifically, the intrinsic SED produced by PROSPECTOR tends to underestimate the corresponding SED produced by SKIRT in this area. The left-hand panel of Figure 4.26 presents the SED for view 0 of a galaxy snapshot, while the right-hand panel shows the SED for the same snapshot but from view 4. Despite the fundamental properties of the galaxy being unchanged, the difference in the fitting of the FIR peak and the associated underestimate in the intrinsic SED is evident.

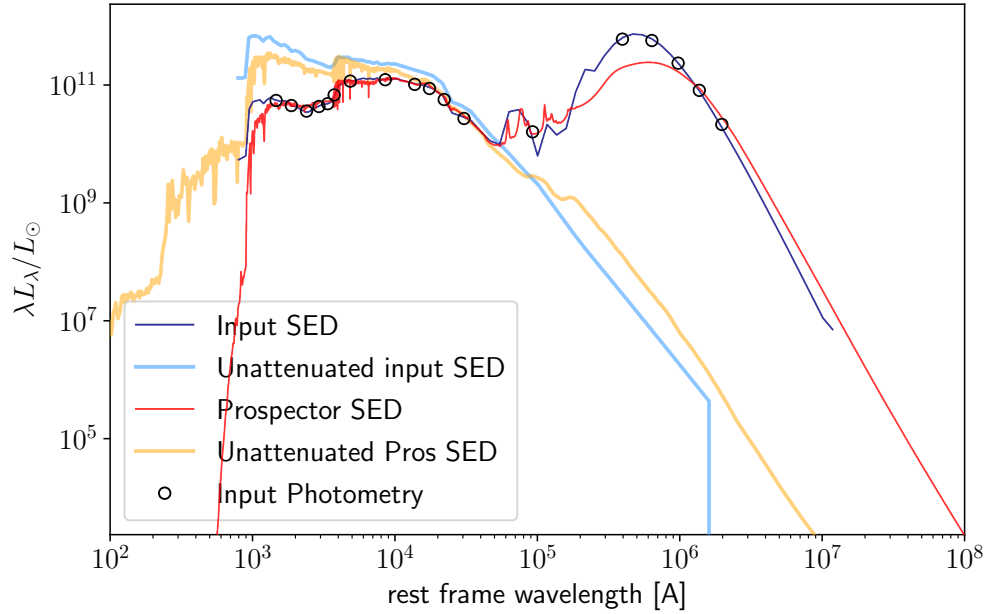


FIGURE 4.25: PROSPECTOR generated SED of galaxy A1 at  $z = 1.56$ , which was successfully fitted ( $\chi^2 = 23.8$ ) using the Bursty SFH prior, showing the underestimation of the intrinsic FIR leading to the underestimation of the IR emission in the derived SED.

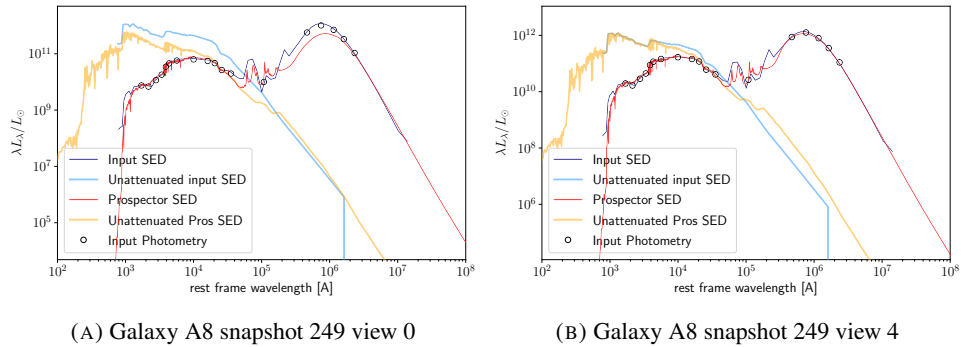


FIGURE 4.26: SEDs of two views of the same galaxy snapshot - galaxy A8, snapshot 249 at  $z = 1.2$ . The left-hand panel shows view 0 to which PROSPECTOR was unable to fit an SED, the right-hand panel shows view 4 which PROSPECTOR was successful in fitting.

Notably, in the case of the unsuccessful fit, PROSPECTOR significantly underestimates the visual extinction ( $A_V$ ), which is not observed in the successful fits. This pattern is consistent across the other failed fits in this category. Analysis shows that in the case of failed fits, the derived  $A_V$  is likely to be more underestimated when compared with successful fits. Figure 4.27 illustrates the correlation between  $A_V^{true} - A_V^{derived}$  and the failed fits with the failed fits occurring for snapshots with some of the worst  $A_V$  recovery. However, it remains unclear whether this underestimation of  $A_V$  is a symptom of the FIR mis-fit or a consequence of it. Further investigation is required to disentangle the relationship between these variables.

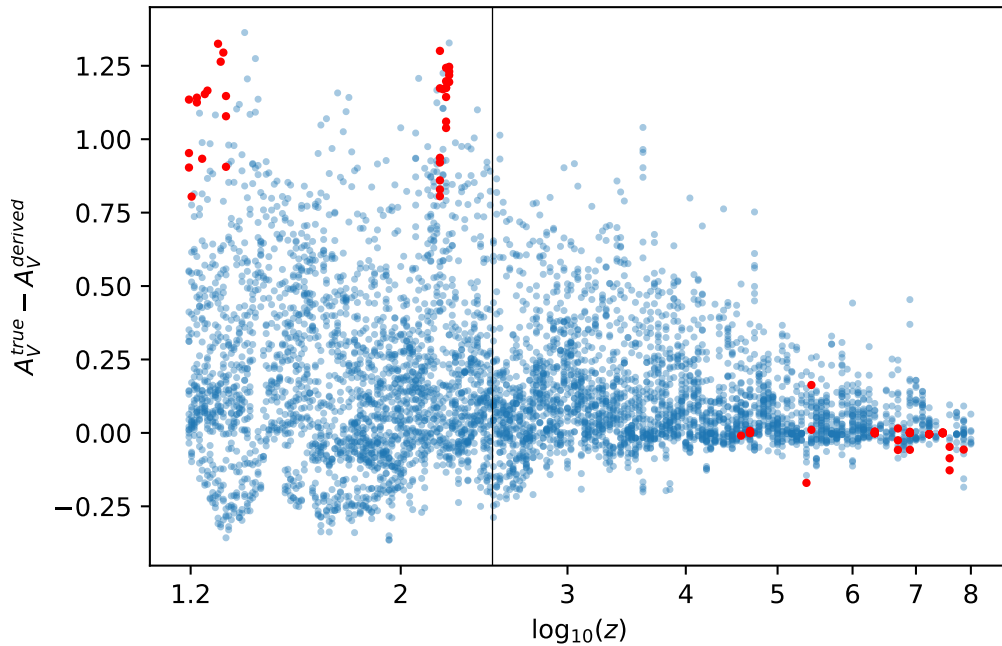


FIGURE 4.27: Plot of the difference between the true value of  $A_V$  and that derived by PROSPECTOR for all galaxies, successful fits are shown in blue, failed fits are shown in red; the vertical line marks  $z = 2.5$ , the upper end of the range for failed fits likely caused by  $A_V$  underestimation. Note that failed fits due to zero dust mass or low dust to stellar mass ratio have been removed.

#### 4.4.1.4 Remaining unsatisfactory fits at $z > 4.5$

Finally, we review the failed fits quantified in column 7 of Table 4.4, namely those in the range  $z > 4.5$  which are not accounted for by zero dust mass or very low dust to stellar mass ratio. Analysis has revealed no pattern to these fails, 35 of which are caused by PROSPECTOR failing to fit any of the views of 5 snapshots. This is, perhaps, to be expected, with the  $\chi^2$  confidence level set at 99 per cent we can expect approximately 1 per cent of cases to exceed the critical threshold even if the model is correct. These failures represent  $\approx 0.6$  per cent.

#### 4.4.1.5 Summary of fit failure modes

Our analysis of the failed fits has identified three distinct issues representing 92 per cent of the the unsuccessful outcomes. So our conclusions are:

1. A subset of the simulations are generating galaxies with zero dust mass which PROSPECTOR has been unable to model successfully;

2. The majority of failures are associated with galaxies exhibiting a low dust to stellar mass ratio compared to values reported in the literature.
3. A small number of failures in the range  $1 < z < 2.5$  are associated with PROSPECTOR underestimating  $A_V$ . This underestimation either results from, or leads to, an underestimation of the intrinsic stellar emission, preventing PROSPECTOR reproducing accurate FIR fluxes.

#### 4.4.2 The effect of prior choice on the fidelity of the derived properties.

We now examine how the choice of SED fitter and SFH prior influences the recovery of galaxy properties. As stated in Section 4.3, on average the property values are recovered well and the choice of prior has little statistically significant impact on the results, though Haskell et al. (2024) demonstrated that this averaging could hide significant areas of disagreement. This result begs further investigation as it appears to contradict findings elsewhere that the choice of non-parametric prior has an impact on the derived results, and that the flexibility of nonparametric fitters produces better quality results than those of parametric fitters (e.g. Carnall et al. 2019, Leja et al. 2019, Lower et al. 2020). Figures 4.28 to 4.32 present histograms comparing the results between each pair of priors (e.g. Continuity/Bursty, MAGPHYS/Parametric, etc.). Each histogram was constructed by taking the difference between the accuracies delivered for an observation by each prior (i.e. the difference between the residuals) and dividing by the sum of the residual errors in quadrature to produce a z-score in  $\sigma$  units for each observation. The results are plotted with a standard normal distribution overlaid in green for comparison. The large sample size ( $\approx 5894$ ) produces a low error on the mean and a subsequent high confidence in the value of the sample mean  $\mu_S$ . We see from these figures that in many cases the sample mean is within  $1\sigma$  of the true mean and the standard deviation is  $< 1\sigma$  indicating a close correspondence between the different prior results. There are, however, some exceptions to this. For  $M_{\text{star}}$  (Figure 4.28) the Dirichlet and Bursty prior results show a mean difference of  $1.8\sigma$  as do the Parametric and Dirichlet priors. In this latter case, the standard deviation is also larger than average, 1.5, and the sample distribution tail extends to at least  $5\sigma$  indicating that for some galaxies, these two priors may produce significantly different results. The plots for sSFR (Figure 4.30) show that the Dirichlet prior may also produce significantly different results when compared to the Bursty or Parametric SFHs.  $L_{\text{dust}}$  (Figure 4.31) shows remarkably tight standard deviations, and means that are between 0 and  $0.5\sigma$  of the standard distribution confirming that this property

value is well recovered across all SFH priors. Finally, Figure 4.32 demonstrates that  $A_V$  is again well recovered regardless of prior choice, though MAGPHYS may produce significantly different results from the Dirichlet prior for some galaxies.

The statistical significance of our results between the different priors can, perhaps, be attributed to our idealised test conditions where the true value is known, the SNR is constant in every band, our redshifts are entirely reliable, and we have error-free observational data. In addition, we have good spectral coverage including the FIR peak which is not the case in several studies of SED results, the papers of Pacifici et al. (2022) and Leja et al. (2017) had NIR-FIR data in only 27 and 20 per cent of their test samples respectively. Including FIR data enables the SED fitter to more accurately determine dust properties (Casey, 2012), improve the derivation of SFR (Haskell et al., 2023; Pacifici et al., 2023) and break the age/metallicity degeneracy (Walcher et al., 2011; Hayward and Smith, 2015). Section 2.3.2.3 of this thesis demonstrates the value of both full panchromatic sampling and the need for FIR coverage in particular.

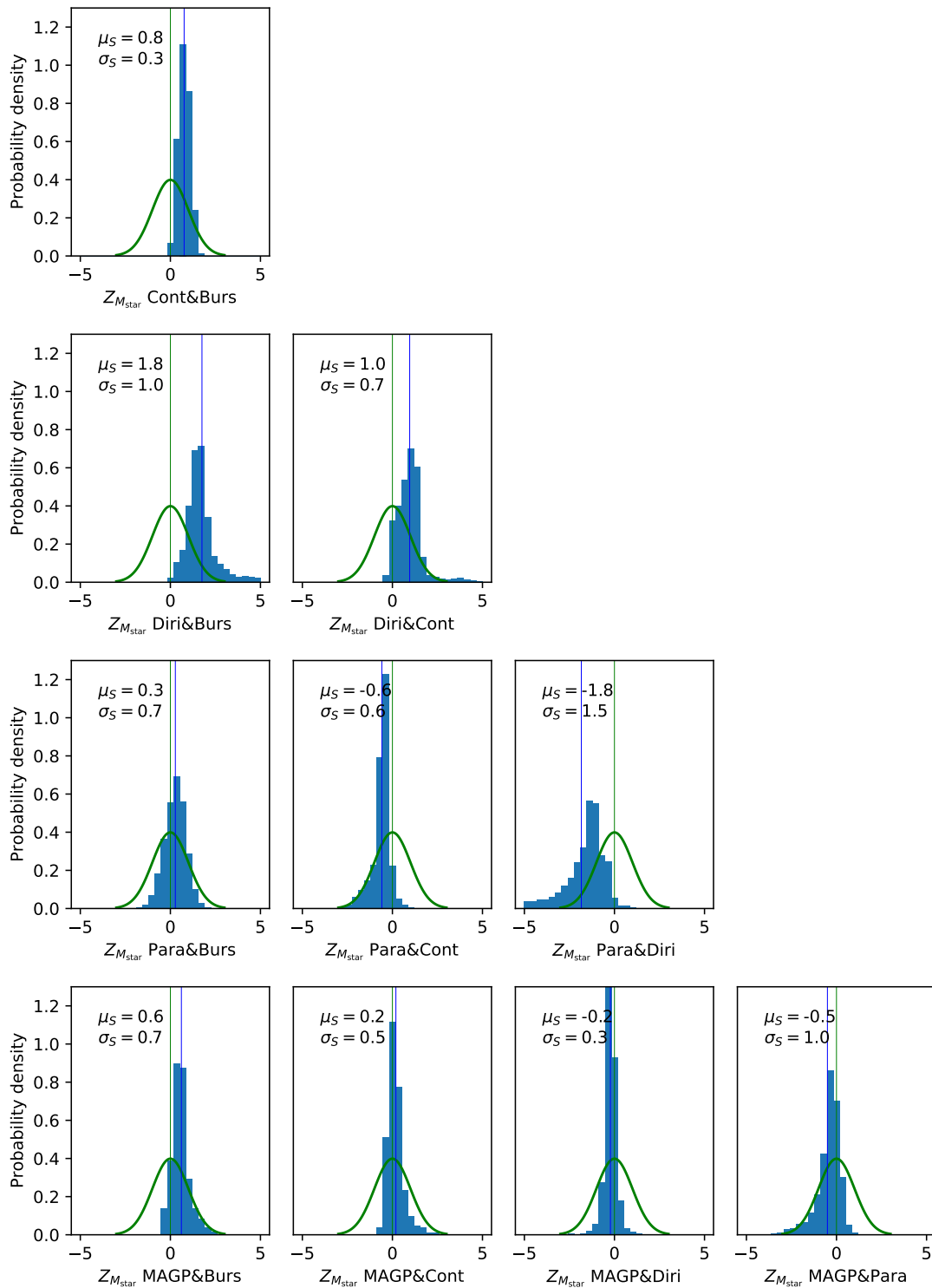


FIGURE 4.28: Z-score distributions of stellar mass for all pairs of priors, the z-scores were determined by taking the difference between the residuals (i.e. the difference in the logs of the median values) and dividing by the sum of the errors in quadrature. Each panel presents the results of comparing the accuracy of all observations (i.e. all views, all snapshots, all galaxies), the  $x$ -axis is labelled with the two priors compared in each panel (Cont=Continuity, Burs=Bursty, Diri=Dirichlet, para=PROSPECTOR parametric and MAGP=MAGPHYS), the dotted vertical line marks the sample mean which, together with the standard deviation, is shown in the legend. The standard normal distribution ( $\mu = 0$   $\sigma = 1$ ) is shown in green for reference with the zero point marked by the vertical green line.

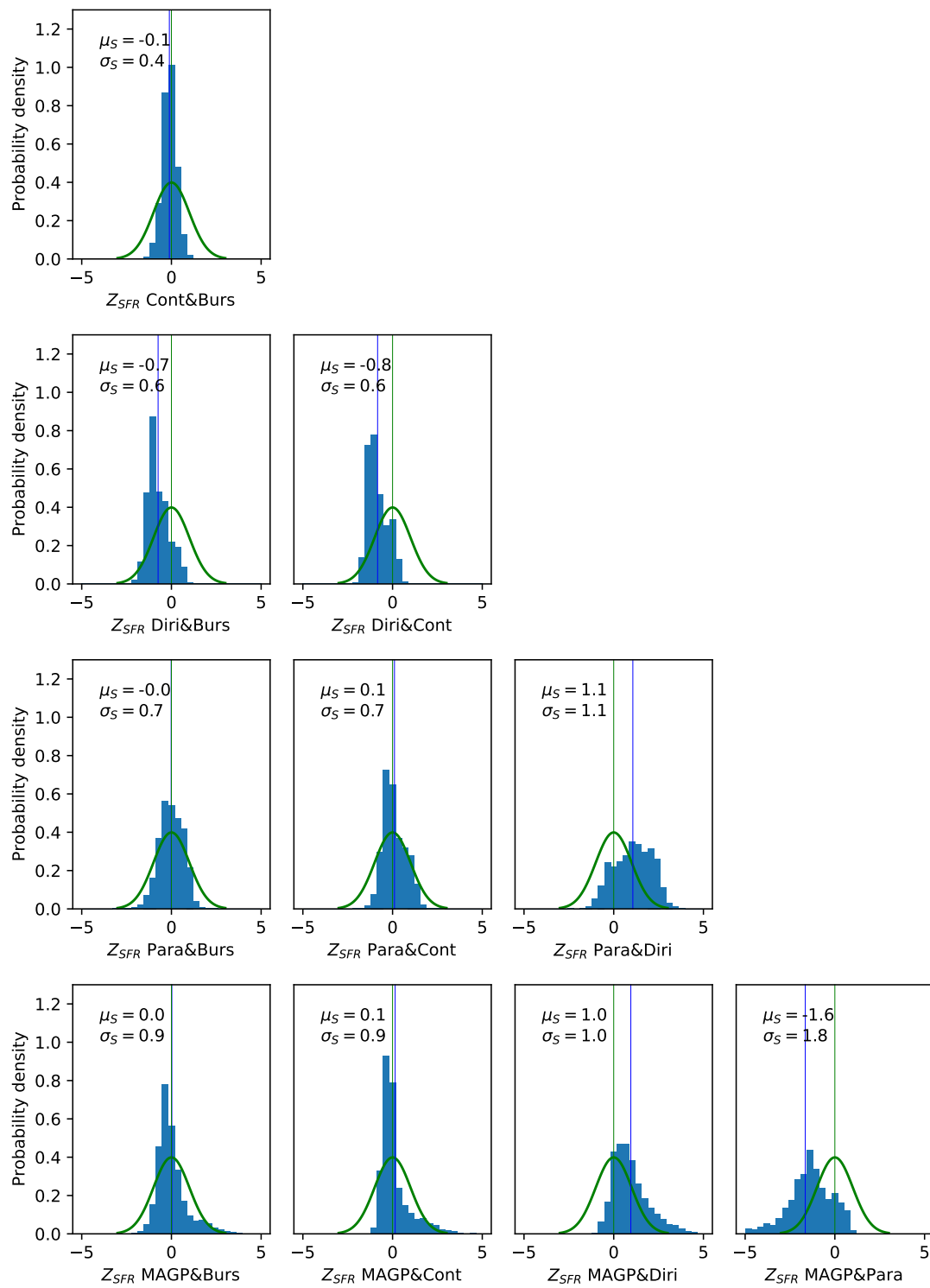


FIGURE 4.29: Plots showing the distribution of z-scores for SFR values, see Figure 4.28 for details.

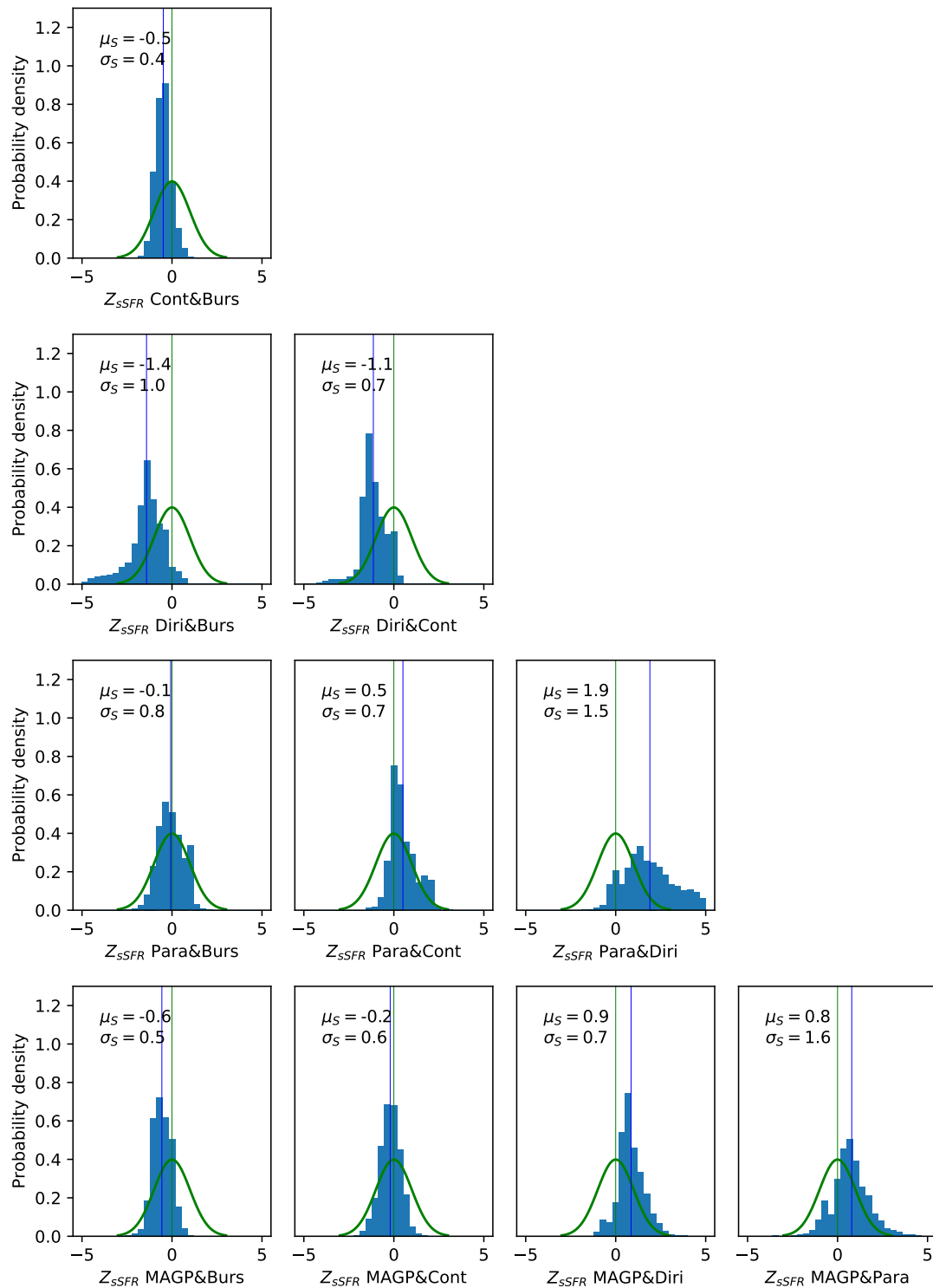


FIGURE 4.30: Plots showing the distribution of z-scores for sSFR values, see Figure 4.28 for details.

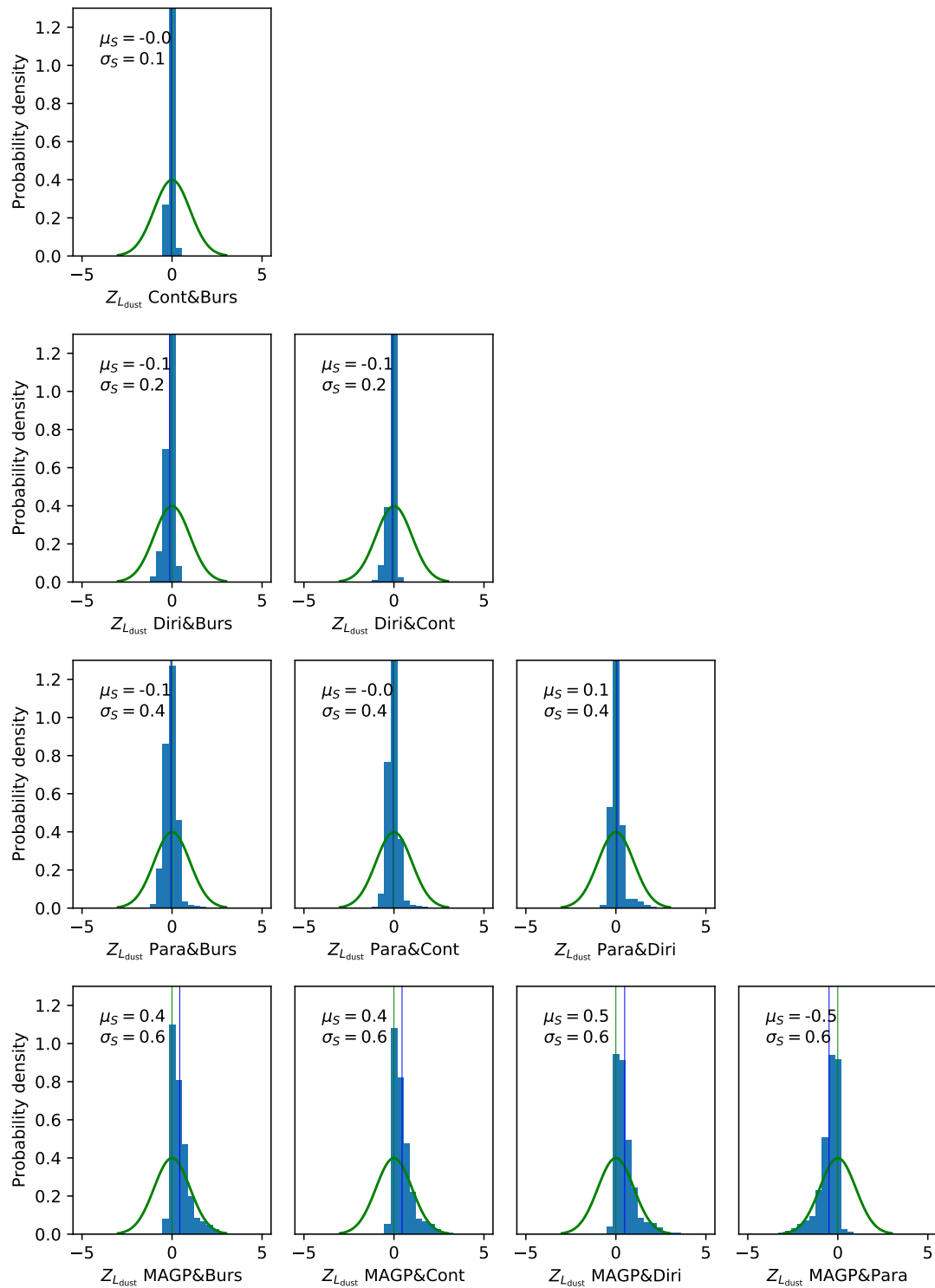


FIGURE 4.31: Plots showing the distribution of z-scores for  $L_{\text{dust}}$  values, see Figure 4.28 for details.

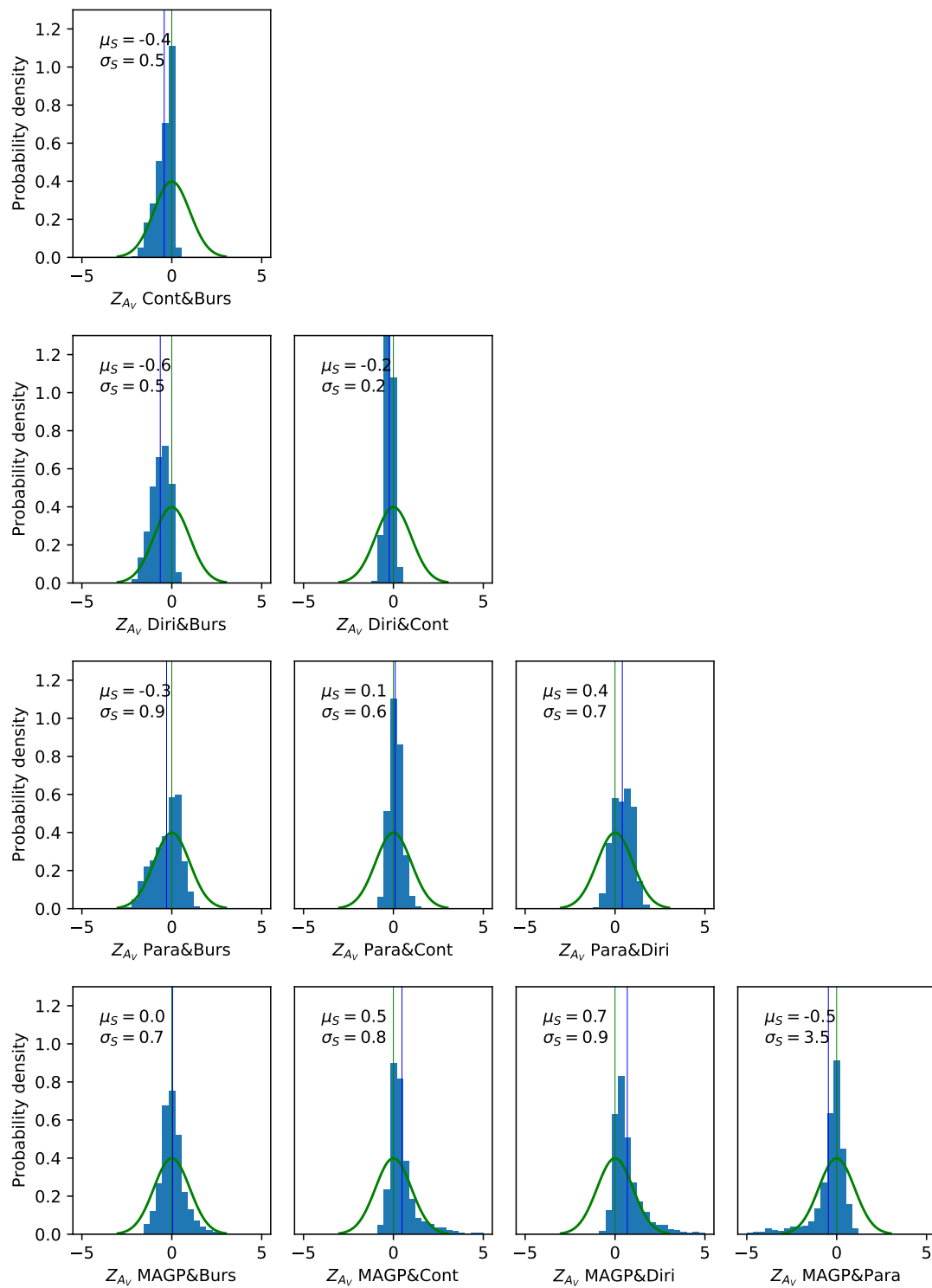


FIGURE 4.32: Plots showing the distribution of z-scores for  $A_V$  values, see Figure 4.28 for details.

### 4.4.3 How individual filters contribute to the $\chi^2$ value

Table 4.2 and Figure 4.1 demonstrated that the four SFH priors exhibit similar rates of fitting success as demonstrated by low  $\chi^2$  values, Figure 4.33 presents the mean  $\chi^2$  values for each individual filter for galaxy A1. This figure shows that, on average, all priors yield similar individual filters'  $\chi^2$  values resulting in both comparable total  $\chi^2$  and similar best-fit SEDs. The shaded area of this figure encloses the 16th and 84th percentiles of  $\chi^2$  values in each bin (i.e. the scatter) for the Bursty prior, the remaining priors presenting a similar pattern. This figure shows a small scatter ( $\leq 1$ ) for 15 of the 18 filters demonstrating that FSPS has consistently converged to locations in close proximity in the 18-dimensional observed-flux space and suggesting that the choice of SFH prior has minimal impact on the shape of the SED. However, an interesting feature is the contribution made by the PACS100 and PACS160 filters. The closeness of the mean  $\chi^2$  values from the different SFH priors shows it is unlikely that the choice of SFH is the source of this feature, Figure 4.34 provides a possible explanation. This shows the rest wavelength coverage for these filters, together with the neighbouring filters MIPS24 and SPIRE250, for  $1.2 < z < 8$  together with the average  $\chi^2$  values returned by all of the filters. We see from this that the  $\chi^2$  values appear to peak in the wavelength region  $3\mu m < \lambda < 70\mu m$ , wavelengths which include the emission from PAHs and AGN in the MIR, and from warm dust on the Wien side of the FIR. With no AGN present in the simulations, and with the AGN features of PROSPECTOR turned off, we must conclude that modelling the PAH emission is a likely cause of the high  $\chi^2$  values in the MIR. SKIRT adopts the Weingartner and Draine (2001) MW emission model which treats PAHs as small grains, whereas PROSPECTOR uses that of Draine and Li (2007) providing a more complete model for PAH emission at specific wavelengths - notably 3.3, 6.2, 7.7, 8.6 and  $11.3 \mu m$  - which correspond closely to the high  $\chi^2$  values from the MIPS24 and PACS100 filters. From this, we suggest that the high  $\chi^2$  values seen in the MIR in are likely the result of a mismatch between the SKIRT and PROSPECTOR PAH emission modelling. In the FIR, we note a feature in the Wien slope at  $\approx 20$  to  $30\mu m$  (see e.g. Figures 4.25, 4.26) which corresponds to the high  $\chi^2$  values from the PACS100 and PACS160 filters. Further work is needed to determine the source of this in the simulations, however the differing dust models may again be the cause of the mismatch at these wavelengths.

Figure 4.35 presents the average  $\chi^2$  values for each filter for the PROSPECTOR Bursty SFH prior and for MAGPHYS for galaxy A1. It is immediately apparent that MAGPHYS is, on average, less successful than PROSPECTOR at fitting the UV/optical fluxes but more successful in fitting the

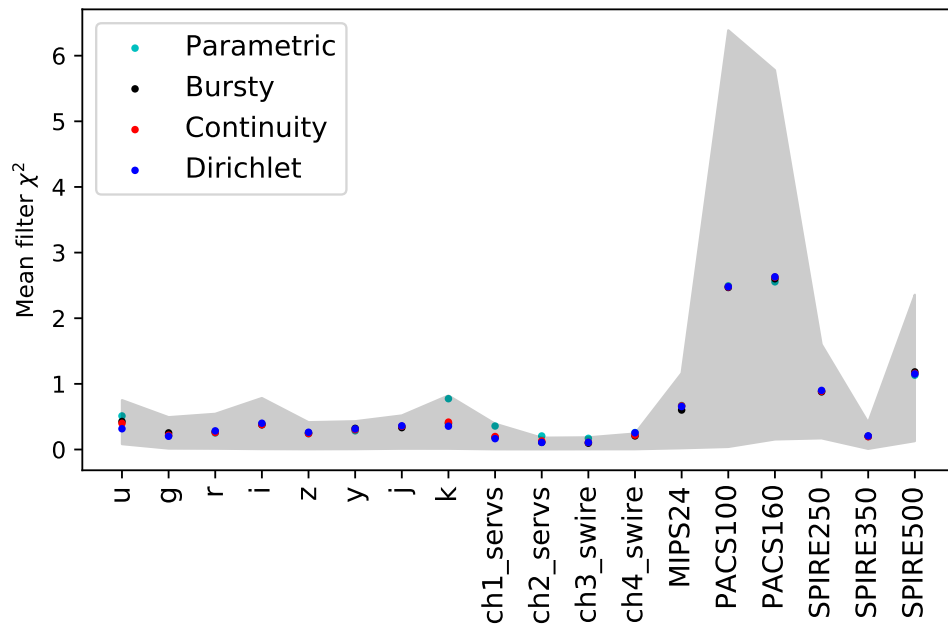


FIGURE 4.33: The mean  $\chi^2$  values for each filter produced for galaxy A1 by the four PROSPECTOR SFH priors. The grey-shaded area encloses the 16th and 84th percentiles within the Bursty prior filter  $\chi^2$ .

IR fluxes. Figure 4.36 shows that the majority of the high  $\chi^2$  values for MAGPHYS fall in the wavelength range  $10^{-1}\mu m < \lambda < 3 \times 10^{-1}\mu m$ . Both MAGPHYS and SKIRT use the Bruzual and Charlot (2003) SED for stellar emission, and so it is likely that this mismatch is caused by differing dust extinction models. MAGPHYS assumes the two component, uniform screen, model of Charlot and Fall (2000) whereas SKIRT uses the dust geometry provided by FIRE. It is possible, therefore, that the high  $\chi^2$  values experienced in the UV for MAGPHYS are caused by the effects of these different dust geometries.

The lower  $\chi^2$  values delivered by MAGPHYS in the MIR/FIR region, compared to PROSPECTOR, are interesting and may be due to configurable variables in MAGPHYS which allow prior ranges to be defined for MIR and PAH emission (da Cunha et al., 2008, and see Figure A.2). Of equal interest is the reason for PROSPECTOR providing superior fitting to MAGPHYS in the UV/optical region, we defer this to later work but note that MAGPHYS uses a MW dust law whereas PROSPECTOR uses Calzetti et al. (2000).

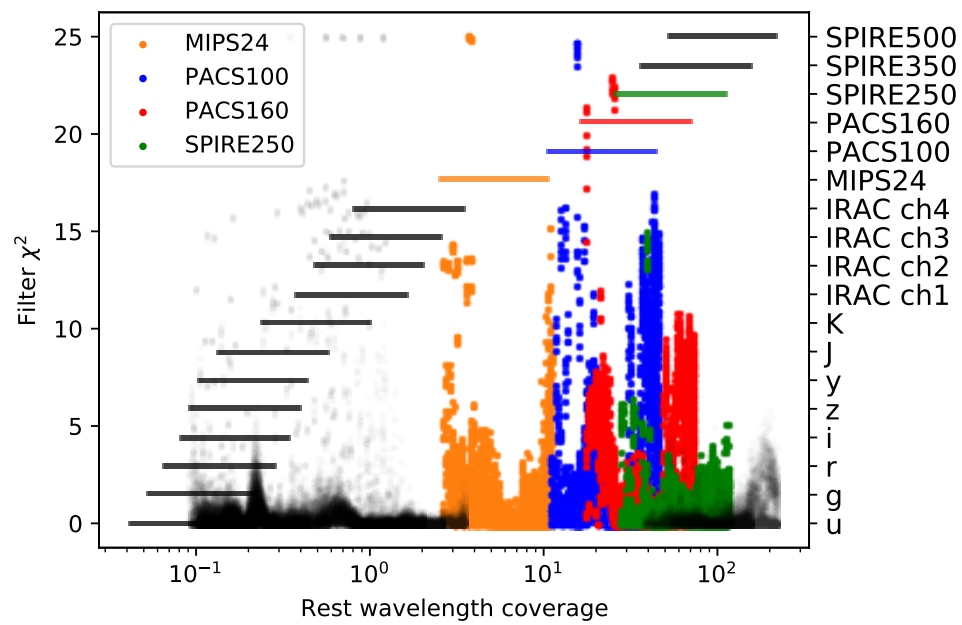


FIGURE 4.34: The rest wavelength coverage of the filters used for this work, together with the  $\chi^2$  values for the MIPS24, PACS100, PACS160, and SPIRE250 filters, delivered by the PROSPECTOR Bursty SFH prior. The named filters are colour coded as shown in the legend and their  $\chi^2$  values read from the LH y-axis, the other filters are shown in grey. The horizontal lines mark the rest frame wavelengths covered by each filter (read from the RH y-axis) over the redshift range provided by the simulations with the four named filters colour coded as shown in the legend.

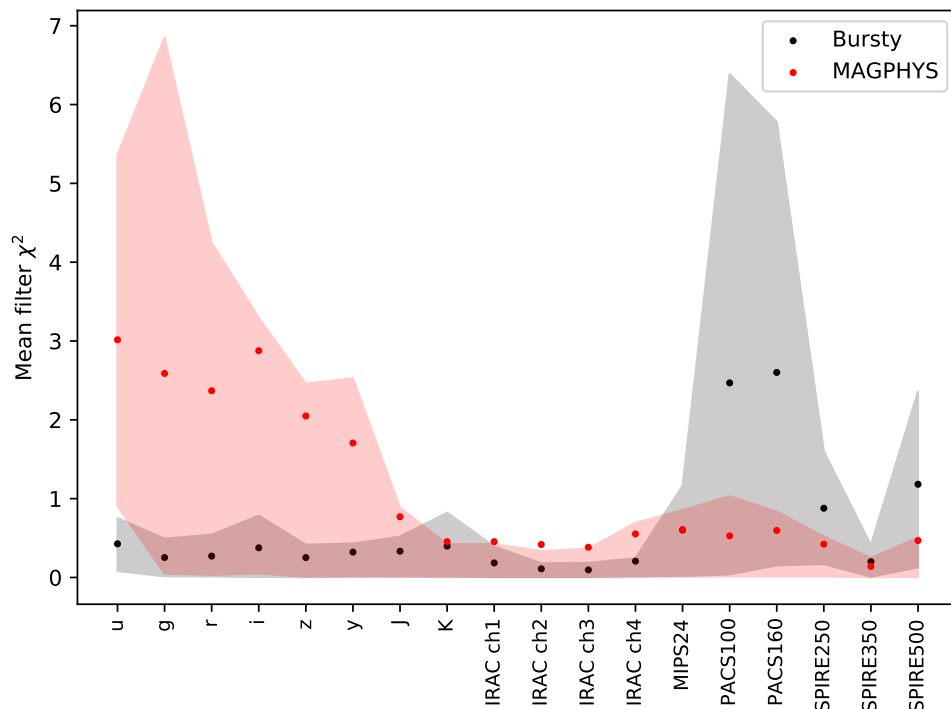


FIGURE 4.35: The mean  $\chi^2$  values for each filter produced for galaxy A1 by the Bursty non-parametric SFH prior and MAGPHYS. The grey-shaded area encloses the 16th and 84th percentiles within the Bursty prior filter  $\chi^2$ , the red area that for MAGPHYS.

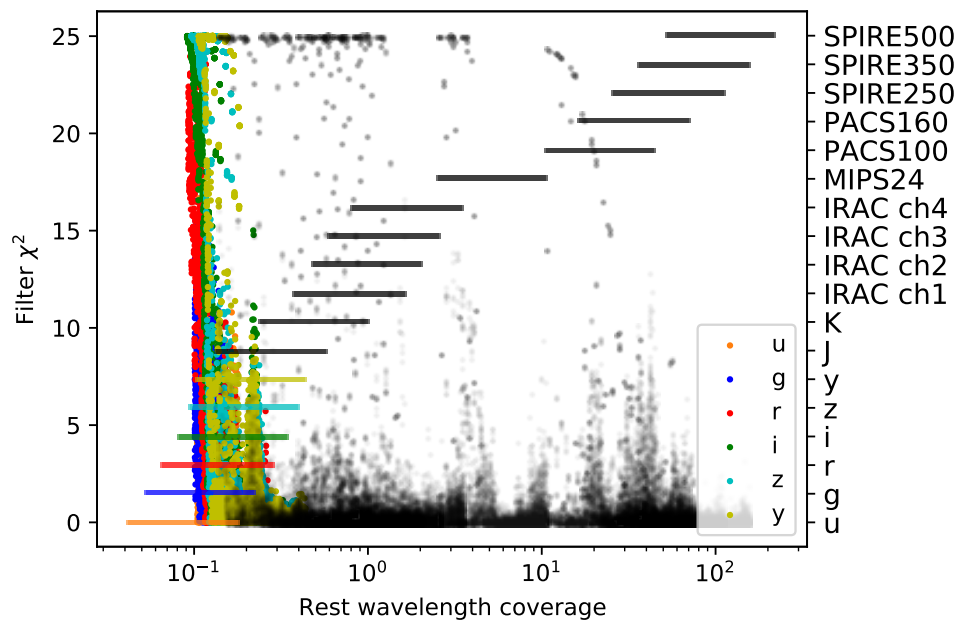


FIGURE 4.36: The rest wavelength coverage of the filters used for this work, together with the  $\chi^2$  values for the *ugrizy* filters, delivered by MAGPHYS, colour coded as shown in the legend and read from the LH y-axis; the  $\chi^2$  values for the other filters are shown in grey. The horizontal lines mark the rest frame wavelengths covered by each filter (read from the RH y-axis) over the redshift range provided by the simulations with the *ugrizy* filters colour coded as shown in the legend.

## 4.5 Summary and Conclusion

In this work we have used four cosmological zoom-in simulations from the FIRE project, generating a total of 958 galaxy snapshots sampled at approximately 25 Myr intervals, spanning redshifts from  $1 < z < 8$ . Each snapshot was observed from seven different viewing angles resulting in 6706 datasets. These were processed through the SKIRT radiative transfer software to produce redshifted SEDs which were convolved with the profiles of 18 filters covering the observed frame spectrum from UV ( $0.39 \mu m$ ) to FIR ( $500 \mu m$ ).

Of the observation datasets, 5894 were processed through the PROSPECTOR SED fitting software. This fitting procedure was performed four times using different SFH priors - three non-parametric priors using the Dirichlet and Student's t-distributions, and one parametric prior using the delayed exponentially declining SFR model. The results were compared to the true values and to those derived using MAGPHYS on the same data to enable comparisons with previous works.

We find that PROSPECTOR achieves a higher overall fit success rate compared to MAGPHYS with success rates of 93 per cent and 82 per cent respectively. This discrepancy is primarily driven by PROSPECTOR’s superior performance at high redshifts. Notably, there is no significant difference in success rates among the four PROSPECTOR priors. A small number of observations failed to fit where snapshots had zero dust mass at redshifts where such conditions have not been observed. The majority of the failed fits occurred in cases where the dust/star mass ratio of a snapshot fell below  $\approx 10^{-4}$ . We suggest that PROSPECTOR models are not well-suited to such atypically low ratios. Another subset of snapshots failed to fit due to an underestimation of  $A_V$ .

For the recovery of property values, we find:

- Stellar mass is recovered to within an average accuracy of 0.2 dex in line with previous works (Hayward and Smith, 2015; Dudzevičiūtė et al., 2020; Haskell et al., 2023). We find no significant difference in the accuracy of the results across the four PROSPECTOR priors or MAGPHYS.
- SFR is recovered to within 0.3 dex on average and sSFR to within 0.1 dex on average, though in both cases maximum differences are higher; contrary to previous works, we find the choice of prior makes no significant difference to the average fidelity of these derived values.
- $L_{\text{dust}}$  is well recovered to within 0.3 dex on average;  $A_V$  is also well recovered to within an average accuracy of 0.3 mag.

For all derived properties we find that, while the fidelity of the results using the different PROSPECTOR priors or MAGPHYS do not differ significantly in most cases when averaged across all observations, some galaxy configurations may be interpreted differently by different priors, in particular between the Dirichlet and Parametric priors, and MAGPHYS and PROSPECTOR priors. This contrasts to the findings of previous studies (e.g. Leja et al., 2019; Carnall et al., 2019; Pacifici et al., 2023) which found significant variations in derived property values depending on the choice of SED fitting tool. We suggest that this agreement may be attributed to the high quality of the data used in our study, as well as the comprehensive spectral coverage, especially the inclusion of FIR data around the peak of the FIR emission. This data coverage likely reduces the sensitivity of the results to the choice of SFH prior, leading to more consistent property estimates. However, we note that there are systematic issues between priors as demonstrated by Figures 4.28 to 4.32 possibly caused by the underestimation of uncertainties

that has been highlighted elsewhere in this chapter. This results in the delivery of similar derived property values when a large number of observations are averaged, however it hides significant differences in property values for individual galaxies as priors differ in their interpretation of similar SEDs.

We find that the fidelity with which PROSPECTOR is able to recover stellar mass, SFR, sSFR and dust luminosity does not depend strongly on the stellar and dust spatial distribution or on the degree of offset between the stellar and dust emission, as measured by any of the three proxies we use. However,  $A_V$  shows sensitivity to both the galaxy geometry and to the peak-to-peak proxy for the stellar and dust emission offset. Specifically, the accuracy of the recovered  $A_V$  value is correlated with the increasing magnitude of this offset, indicating that  $A_V$  is more affected by the spatial distribution of stars and dust than the other properties. However, we note that the variation in the scatter of our data is significantly larger than the variation in the individual data points. We interpret this as an indication that the error bars for the derived values are too narrow, suggesting that the uncertainties reported by the fitting process may be underestimated.

We find that PROSPECTOR's ability to accurately recover SFR, sSFR and dust luminosity is independent of the true values of these properties, demonstrating consistent performance at both high and low values. However, stellar mass recovery becomes less reliable for masses below  $\log_{10}(M_{\text{star}}) = 9$ . We suggest that this is due to the PROSPECTOR model underestimating the MIR emission, likely as a result of insufficient modelling of PAHs. For  $A_V$ , we observe that the fidelity of the derived value decreases as the true value increases. This decline in accuracy coincides with increased SFR and is in line with the published correlation between short-term SFR increase and  $A_V$  (Wuyts et al., 2009). As described in the previous paragraph, the scatter in the recovered data is significantly greater than that in the true data, suggesting that the error bars on the recovered values are unnaturally constrained. This indicates that the uncertainties provided by the model may not fully capture the true variability in the data.

Finally, we note that the pattern of  $\chi^2$  scores for individual filters (UV/optical for MAGPHYS and MIR for PROSPECTOR) indicates a need for further investigation.

# Chapter 5

## Summary and future work

### 5.1 Summary

In this thesis we have investigated the accuracy of the recovered properties of high redshift galaxies using two SED fitting tools - MAGPHYS (da Cunha et al., 2008) and PROSPECTOR (Leja et al., 2017). We have used 4 simulated galaxies from the FIRE project (Hopkins et al., 2018) to produce synthetic observations. We have followed the galaxies evolution from  $z \approx 8$  to  $z \approx 1$ , the simulations producing 958 snapshots at  $\approx 25$  Myr intervals, each including observations from 7 different viewing angles. The snapshots were processed through the SKIRT radiative transfer package (Baes et al., 2003) to produce  $> 6700$  SEDs of which  $\approx 5900$  had accompanying true property values.

We investigated how the properties of the simulations compared to those of real galaxies as published in the literature. Specifically, we plotted the values of stellar mass and SFR to establish the position of each snapshot on the galaxy main sequence (Tacchella et al., 2022c); we also tested the relationship between  $S_{870}$  and  $M_{\text{dust}}$  against Hayward et al. (2011); Dudzevičiūtė et al. (2020); Cochrane et al. (2023b), the relationship between  $A_V$  and redshift against Hainline et al. (2011); Dudzevičiūtė et al. (2020), and finally the offsets between the UV and FIR emission against Rujopakarn et al. (2016, 2019); Lang et al. (2019). We showed that the simulations predominantly presented dusty star-forming galaxies with properties similar to those inferred for real SMGs published in other observational works. We measured the degree of decoupling between the UV and FIR emission of each snapshot/view using three proxies: a peak-to-peak

proxy measuring the distance between the points of peak UV and peak FIR emission, a light-weighted-mean proxy measuring the distance between the centres of UV and FIR emission, and a Spearman rank coefficient (Myers and Well, 2003) comparing the degree of correlation between the UV and FIR images. To produce mock observations, we convolved the SEDs produced by SKIRT with the profiles of 18 filters in the wavelength range  $0.4\mu m \leq \lambda_{\text{eff}} \leq 482\mu m$ .

### 5.1.1 MAGPHYS and energy-balance modelling

First, we used the SED fitter MAGPHYS to process the observations, investigating the fit success rate and comparing the derived values with the known true values. We found that the proportion of observations for which MAGPHYS was able to find a statistically acceptable match with its template library reduced as redshift increased. This culminated to an inability to match SEDs at  $z > 5.9$ . We speculated this may be due to the fixed nature of the template library which becomes increasingly sparse as redshift increases, and the stochastic nature of early galaxies where bursts of star formation may dominate the spectrum. We tested this conclusion by rerunning the fitting with all observations translated to their theoretical values at  $z = 2$  and observed an improved success rate.

Using only the successfully fitted observations, we compared the derived values of stellar mass, SFR, sSFR, dust mass and dust luminosity to the true values as a function of different environmental variables. Firstly, we compared the fidelity of results to any offset between the UV and FIR emission. Several papers had suggested that the energy-balance assumption used by MAGPHYS may not apply for galaxies with clumpy dust distribution (e.g. Casey et al., 2017; Miettinen et al., 2017; Simpson et al., 2017; Buat et al., 2019). Using three proxies for the UV/FIR offset we reported that the performance of MAGPHYS remained similar over the range of stellar and dust geometries presented by the simulations. We concluded that SED fitters using this assumption remained applicable where such dust distributions are likely to be found, e.g. at high redshifts.

We also tested the fidelity of the derived values against the range of true values and found that this was not dependent on the values available from the simulations. To test the importance of panchromatic data, we re-ran the fitting using only the IR observations and, again, using only the UV/optical observations. We found that for stellar mass, SFR and dust mass the panchromatic data produced superior accuracy to the restricted data observations, with more constrained

uncertainties. For sSFR the UV/optical-only observations produced a closer average value to the truth, but with significantly greater error bars than the panchromatic run, and for dust luminosity, the FIR-only run produced a very high quality result with small errors broadly equivalent to the panchromatic run.

### 5.1.2 Averaging results hides an SED bias in SFR recovery

In chapter 3 we investigated the relative fidelity of MAGPHYS derived  $\text{SFR}_{100\text{Myr}}$  using the simulated data snapshots described in the previous chapter. We showed that MAGPHYS and PROSPECTOR produced similar levels of precision for this property when averaged over all snapshots, however, the results of MAGPHYS show a strong dependency on  $\eta = \log_{10} \left( \frac{\text{SFR}_{10\text{Myr}}}{\text{SFR}_{100\text{Myr}}} \right)$ . This resulted in MAGPHYS overestimating, or underestimating, the  $\text{SFR}_{100\text{Myr}}$  property by up to 1 dex for galaxies experiencing recent, short-term periods of enhanced star formation or quiescence. We observed a similar, but significantly weaker trend in the PROSPECTOR parametric results.

We speculated on two possible causes for this. Firstly, the MAGPHYS parametric SFH prior includes a stochastic element to model periods of increased star formation activity which may be unsuitable in some circumstances. Secondly, the dynamic nesting technique used by PROSPECTOR provides a smoother sampling of the parameter space than is possible with MAGPHYS's fixed template library. We suggested that careful consideration should be given to the choice of SED fitter when analysing galaxies with significant, recent star-forming activity

### 5.1.3 Using PROSPECTOR to derive galaxy properties

In Chapter 4 we investigated the fidelity of galaxy properties derived using PROSPECTOR with three nonparametric priors and one parametric SFH prior. Several papers have reported that non-parametric SFHs produce superior results to the parametric SFH priors (used e.g. by MAGPHYS, Carnall et al. 2019; Leja et al. 2019; Lower et al. 2020). We used the simulations previously used in Chapter 2 to enable direct comparison with values derived by MAGPHYS.

We reported that PROSPECTOR is able to fit successfully at higher redshifts than MAGPHYS and that the four priors showed very similar success rates. We showed that where it had failed to fit, the cause is likely to be local features rather than redshift per se. Specific reasons for failed fits were:

- Approximately 20 per cent of failures were occurred where galaxies with zero dust mass at redshifts where such galaxies were unlikely to exist, indicating a possible issue with the simulation or radiative transfer calculations;
- Over 60 per cent of failures occurred where galaxies exhibited  $M_{\text{dust}}/M_{\text{star}} \lesssim 10^{-5}$ , indicating a possible problem with PROSPECTOR dust model at atypically low dust masses. These failures occur at very different redshifts to those caused by zero dust mass, leading us to speculate a different underlying cause;
- 8 per cent of failures occurred where visual attenuation was underestimated by  $\gtrsim 0.75$  mag, the possible causes of which remain unclear;
- Possible causes for the remaining 12 per cent of failures, all at  $z > 4.5$  could not be determined.

We examined the values derived using the different SFH priors for stellar mass, SFR, sSFR, dust luminosity and visual attenuation. We found that, on average, all properties were recovered well with uncertainties comparable to those from MAGPHYS. Contrary to other works, we found no significant difference in the average derived values between the PROSPECTOR nonparametric, parametric and MAGPHYS runs. We compared the difference between the derived value and the true value (the residual) for every pair of fitters/priors using a z-test, for all successfully fitted observations. In most cases the difference was of statistically low significance. Some combinations produced long tails in the z-score distribution (e.g. Parametric/Dirichlet for stellar mass, SFR and sSFR, and MAGPHYS/Dirichlet for SFR) indicating that for some galaxy configurations different SFH priors may deliver significantly different results. This overall agreement is perhaps a surprising result and we speculate that it may be due to our high quality, simulated data as the real Universe is likely to provide less constrained data. Performing a similar comparison between the derived properties and the true values we found evidence that, as reported elsewhere in the literature, parametric uncertainties are under estimated resulting in large standard deviations in the z-test distribution.

Continuing the work described above to test the accuracy of the property values derived by MAGPHYS as a function of the UV/FIR emission offset, we performed the same tests on PROSPECTOR which also assumes an energy balance. Using the same three proxies, we determined that all four PROSPECTOR SFH priors showed no significant deterioration in the derived value accuracy for stellar mass, SFR, sSFR or dust luminosity. However, we reported a weak

trend for the derived visual attenuation to become less accurate as the peak-to-peak proxy increased. In related tests, we leveraged the different viewing angles provided by the simulations to determine whether the accuracy of the recovered values was dependent on the line-of-sight projection of the galaxy stellar/dust distribution. We found that stellar mass, SFR, sSFR and dust luminosity derivation were all unaffected by viewing angle. However, we reported a weak trend for visual attenuation to be affected as may be expected by the different stellar/dust distributions likely to be experienced from different angles.

Comparing a property's derived value against the true property value, we found that SFR, sSFR and dust luminosity are unaffected by the true value of the property. However, we reported a trend for the derived stellar mass to become less reliable at low values ( $M_{\text{star}} < 10^8 M_{\odot}$ ) and a correlation between the derived visual attenuation and  $\text{SFR}_{10\text{Myr}}$ .

Finally, we analysed the contributions made to a best-fit  $\chi^2$  value by each filter. We found that, for PROSPECTOR, the filters with  $23\mu\text{m} \leq \lambda_{\text{eff}} \leq 243\mu\text{m}$  contributed significantly more than other filters to the total. Over the redshift range provided by the simulations, these filters sampled in the rest frame wavelength range  $3\mu\text{m} \leq \lambda \leq 70\mu\text{m}$ . We also noted a similar issue for MAGPHYS with filters sampling in the rest frame at  $\approx 2 \times 10^{-1} \mu\text{m}$ .

We noted that, in several cases, the scatter in data values within binned data was significantly greater than the associated uncertainties. We speculated this is due to overly constrained error bars as previously reported in the literature (Leja et al., 2019).

## 5.2 Extrapolating from simulation to reality

This study is based on SEDs derived from simulated galaxies and, while this methodology offers practical advantages, it is important to recognise that the underlying assumptions and models are subject to potential biases and limitations which must be considered when attempting to extrapolate findings to observations of real galaxies. This section outlines several key sources of potential bias and their implications for the robustness of the study's conclusions.

One significant issue is the absence of nebular emission in the FIRE simulations used to construct the model SEDs. For studies focused on local galaxies, the contribution of nebular emission to broadband photometry is often negligible (Battisti et al., 2019); accordingly, some SED

fitting tools, such as the high redshift version of MAGPHYS (Battisti et al., 2019) and AGNFit-ter (see Table 1, Pacifici et al., 2023), do not include nebular emission in their default models. However, at high redshift a population of galaxies known as extreme emission line galaxies (EELGs) challenges this standard treatment of emission-line contributions (van der Wel et al., 2011; Pérez-Montero et al., 2021; Boyett et al., 2024; Llerena et al., 2024), see also Gupta et al. (2023) for the provenance of some EELGs.

EELGs are characterised by intense star formation activity and large emission line equivalent widths<sup>1</sup>, often sufficient to significantly affect broadband fluxes and hence the values of galaxy properties derived from SED fitting (Pacifici et al., 2012, 2015; Smit et al., 2014; Salmon et al., 2015). An example of such a galaxy is TN J1338-1942 (Duncan et al., 2023), which exhibits  $H_\alpha$  and [NII] emission lines with inferred EW of several hundred Ångström. Additional examples can be found in, for instance, Amorín et al. (2015) and Iglesias-Páramo et al. (2022).

The impact of high-EW emission lines on photometric analysis has also been noted in the context of the Herschel-ATLAS survey (Eales et al., 2010). Smith et al. (2012) demonstrated that for dusty, star-forming galaxies the omission of nebular emission in SED models can lead to systematic underestimation of fluxes in bands coinciding with  $H_\alpha$  emission. This again indicates the need to incorporate nebular emission in the modeling of galaxies with significant star formation activity, particularly at high redshift.

The omission of nebular emission from the FIRE simulations thus represents a limitation of the present analysis. While this shortcoming does not critically undermine the main conclusions of this study, it highlights the need for future simulations, and SED modeling, to include nebular emission in order to more accurately represent the observable properties of star-forming galaxies.

Our results show that, broadly speaking, both MAGPHYS and PROSPECTOR recovered the values of galaxy properties to within 0.5 dex. While this is impressive, it could simply be a measure of the compatibility between the models used. However, the fact that both MAGPHYS and PROSPECTOR delivered similar results up to the MAGPHYS limit of  $z \approx 5.9$  indicates this is unlikely to be the case given the differing SFHs and models used (see Table 1.1).

---

<sup>1</sup>Equivalent width (EW) is a measure of the strength of a spectral feature relative to the underlying continuum. It corresponds to the width of the continuum, typically expressed in Ångströms or nanometres, required to produce the same total flux as the line.

An important question is how the modeling used by FIRE could reflect on values derived for real galaxies. Several works have shown that FIRE simulations agree well with observations for a variety of properties at different redshifts (e.g. Hopkins et al., 2014; Faucher-Giguère et al., 2015; Muratov et al., 2017; Ma et al., 2018; Parsotan et al., 2021). Other simulations, such as EAGLE and IllustrisTNG, also show good agreement with various observed galaxy properties across different redshifts, see e.g. (Lagos et al., 2015; Pillepich et al., 2019), however FIRE’s detailed modeling of stellar feedback and the ISM provides certain advantages in replicating specific aspects of high-redshift galaxy observations. As an example, FIRE simulations resolve star formation and stellar feedback at much higher spatial and mass resolutions than large volume simulations (Hopkins et al., 2014, 2018) enabling FIRE to model the formation of individual star-forming regions (Muratov et al., 2015; Chan et al., 2018). Additionally, FIRE galaxies at high redshift have been shown to exhibit realistic properties including UV luminosities, SFR variability, gas outflow rates, and morphologies that resemble observed galaxies (Faucher-Giguère et al., 2016; Ma et al., 2018; Parsotan et al., 2021), as well as accurate modeling of processes such as galactic winds and metal enrichment (Muratov et al., 2015; Hopkins et al., 2018).

Despite these successes, it is important to exercise caution when extrapolating from simulation-based predictions to real-world galaxies. FIRE’s limited cosmological volume and specific implementation of physical models may not fully capture the diversity and statistical properties of the observed galaxy population, and its bursty SFHs and ISM conditions may not be representative of all high-redshift systems. Future advances in simulation technology, e.g. FIRE-3 (Hopkins et al., 2023b), can be expected to improve this situation.

Finally, we should consider the effect our treatment of the photometry may have upon our results. We have applied a uniform signal-to-noise ratio (SNR) of 5 in all photometric bands, simulating a clean, controlled observational environment. While this approach facilitates comparisons across models and simplifies the interpretation of recovered physical properties, it is not representative of real observational data. In practice, there are significant variations in SNR across different photometric bands. For example, optical instruments such as HST <sup>2</sup>, Euclid (Cuillandre et al., 2024), and JWST NIRCам<sup>3</sup> can achieve SNRs exceeding  $10\sigma$ , whereas FIR observations, such as those from Herschel, may yield detections at  $< 5\sigma$  (e.g. Hilton et al.,

<sup>2</sup><https://hst-docs.stsci.edu/stisihb/chapter-12-special-uses-of-stis/12-5-high-signal-to-noise-ratio-observations>

<sup>3</sup><https://jwst-docs.stsci.edu/jwst-near-infrared-camera/nircam-performance/nircam-sensitivity>

2012) particularly for faint or high-redshift sources (e.g. Margoniner and Wittman, 2008). This difference in SNR can significantly affect the ability to constrain galaxy properties; we quantified this effect in Chapter 2 by removing FIR data completely from the MAGPHYS SED fit, effectively setting uncertainties to infinity and mimicking the observational scenario where FIR detections have a very low SNR or are undetected. When the FIR information was removed, the recovery of properties dependent on the optical/NIR SED, such as stellar mass, remained relatively stable. However, parameters that depend more heavily on FIR fluxes, such as SFR, dust mass and dust luminosity, exhibited a degradation in accuracy and increased uncertainties. Given this demonstrated importance of FIR data, it is clear that including realistic photometric uncertainty in all bands is necessary if the results of fitting synthetic SEDs are to be used to calibrate those from real observations.

Notwithstanding these concerns, we now consider what future work could be undertaken to further the work discussed in this study.

### 5.3 Future work

In this study we have used photometry between rest frame  $0.4\mu m$  and  $482\mu m$ . The inclusion of a submillimetre band to improve fitting of the Rayleigh-Jeans tail may further constrain the energy-balance and improve results at higher redshifts (e.g.  $z > 4$ ).

We have highlighted two areas where the filters sampling specific rest-frame wavelengths contribute significantly to the overall fit- $\chi^2$  value. Further work is needed to determine the cause of these atypically high  $\chi^2$  values, an investigation which will need to explore the simulations, the radiative transfer package, SKIRT, and the models used by MAGPHYS and PROSPECTOR.

The scatter reported in a number of our studies indicates that the error bars for both parametric and nonparametric SFH priors may be underestimated. Leja et al. (2019) reported that using parametric SFH priors produced overly constrained uncertainties, our work extends this to include at least some results produced by nonparametric SFHs. This is an important area, affecting the validity of results derived by SED fitting, and should be investigated to determine the cause and scale of the underestimation.

Finally, many of the papers discussing potential issues with the energy-balance assumption and the improved fidelity of fitting based on nonparametric SFH priors have based their work on

real data - e.g. Leja et al. (2017); Pacifici et al. (2022). Our use of noise-free simulated photometry and precise redshifts has countered the assertions made in these and other works and further investigation using noisy, AGN-contaminated data with photometric-level redshift precision would determine the degree of bias caused by our clean data.

## 5.4 Trends in SED fitting

Current trends in a number of areas are likely to shape the usage of SED fitting as we go forward. Machine learning and AI are already starting to make an impact with the introduction of codes such as Mirkwood (Gilda et al., 2021) and ANNz (Collister and Lahav, 2004), and several recent works have cited the use of neural networks (e.g. Simet et al., 2021; Dobbels et al., 2020; Kaeufer et al., 2023; Mathews et al., 2023). These are not without their own issues, including the need for careful choice of training material, however their continued development seems likely to have considerable impact.

The models on which SED fitting relies are also evolving. Studies continue, seeking to improve our understanding of PAH emission (Narayanan et al., 2023b; Rigopoulou et al., 2024), dust emission (Triani et al., 2023), the IMF (Hennebelle and Grudić, 2024; Hutter, 2024; Yan et al., 2024) and simple stellar population modelling (Martín-Navarro and Vazdekis, 2024). In addition, work to improve the quality of simulations continues with the latest release of FIRE-2 in 2023 (Wetzel et al., 2023) and the availability of other simulations such as EAGLE (Schaye et al., 2015), IllustrisTNG (Pillepich et al., 2018), and Cosmo-OWL (Le Brun et al., 2014). Radiative transfer packages are also continuing to evolve with release 9 of SKIRT (Camps and Baes, 2020), and alternative packages such as DIRTY (Gordon et al., 2003) and Cloudy (Gunasekera et al., 2023). DIRTY is of particular interest as it attempts to cater for arbitrary distributions of radiation sources and dust (Misselt et al., 2001). These developments will (should) improve both the theoretical basis on which SED fitting relies and the ability to test against increasingly realistic simulations.

Many contemporary fitters are also continuing to evolve with X-ray (Yang et al., 2022) and low luminosity AGN (López et al., 2024) capability added to CIGALE, nebular emission added to FSPS (Byler et al., 2017) and nebular emission from the narrow-line region of AGNs added to BEAGLE (Vidal-García et al., 2024). The inclusion of spectroscopic data in the fitting process is increasingly important as higher redshift galaxies are explored by, e.g., JWST (Larson et al.,

2023) and several studies are now including this data (e.g. Yuan et al., 2019; Tacchella et al., 2022b; Topping et al., 2022; Endsley et al., 2023). New fitters such as Mirkwood (Gilda et al., 2021) and Lightning (Doore et al., 2023) are also appearing and moving forward the state-of-the-art. In parallel, studies into the sensitivity of SED results to changes in the models (e.g. Leja et al., 2019; Pacifici et al., 2022; Tortorelli et al., 2024, and Chapter 4 of this thesis) are providing insights into model choice and applicability

Finally, the improved availability of computing facilities removes some of the restrictions placed on the use of SED fitters by enabling more resource-hungry algorithms to be used. SED fitting, in general, is “embarrassingly parallel”<sup>4</sup> and so the availability of multi-processor clusters such as the University of Hertfordshire’s High Performance Cluster (UHPPC)<sup>5</sup> provides the ability to run, e.g., nonparametric, Markov Chain Monte Carlo-based fitting methods.

## 5.5 Concluding remarks

With the increasing data volume expected from future facilities (e.g. the Square Kilometre Array, the Extremely Large Telescope, the Euclid telescope, the Nancy Grace Roman Space telescope, and the Vera C. Rubin observatory) and the higher redshifts already being probed by JWST, the demand for reliable and fast galaxy analysis at high redshift will continue to grow. This study has shown that, averaging over a larger number of observations, SED fitting can produce reliable results for galaxies at high redshift — although caution is recommended for specific measurements (e.g. Haskell et al., 2024).

---

<sup>4</sup><https://www.computerhope.com/jargon/e/embarrassingly-parallel.htm>

<sup>5</sup>The UHPPC was used to provide multiple processors for the work described in Appendix A of this work and for the PROSPECTOR runs described in Chapter 4

## Appendix A

# Using spectral energy distribution fitting to create catalogues of galaxy properties

### A.1 Introduction

This Appendix describes the work done to generate catalogues of galaxy properties from existing panchromatic observational data for three deep fields: Boötes (Jannuzi et al., 1999; Williams et al., 2021), Lockman Hole (Lockman et al., 1986; Mahony et al., 2016), and the European Large Area ISO Survey field North 1 - ELAIS-N1 (Oliver et al., 2000a,b). The work was undertaken to provide complementary data to the radio frequency data collected by the LOFAR Two Metre Sky Survey project (LoTSS; van Haarlem et al., 2013).

The LoTSS project aims to survey the entire Northern sky to a resolution of at least 6" and a sensitivity of  $\approx 100 \mu\text{Jy}$  in the range 120-180 Mhz. The project saw first light on 23 May 2014, producing initial data in 2017 (Shimwell et al., 2017) and two major data releases two and five years later (DR1 and DR2; Shimwell et al., 2019, 2022).

While LoTSS is primarily focused on delivery of a wide area survey, it is also taking repeat observations of the deep fields introduced above for which high quality multi-wavelength data are already available (Tasse et al., 2021; Sabater et al., 2021).

The remainder of this Appendix provides details of the process necessary to create the MAGPHYS catalogues of galaxy properties from the raw data, with the final catalogues containing physical properties of over 849,000 galaxies.

## A.2 Method

The catalogues were created using the SED fitter MAGPHYS (da Cunha et al., 2008, 2015) to provide the physical properties for the LOFAR-detected sources. MAGPHYS is fully described in da Cunha et al. (2008) with extensions to operate at higher redshifts described in da Cunha et al. (2015); the high redshift extensions were used in this work.

Details of MAGPHYS’s fitting method and model assumptions are described in Section 2.2.2, here we describe the mechanics of running MAGPHYS and the stages it executes before SED fitting can take place. We also describe the pre- and post- processing necessary to prepare the data and create the catalogues. Figure A.1 shows the full program stack, the figures in brackets are referred to in the text.

Assembling the panchromatic observation data for processing was performed by third parties described below and is included here for information only. Observations were combined from a variety of different sources to provide UV - FIR coverage of the three survey areas – see Table A.1. For ELAIS-N1 and Lockman, UV to MIR data were combined using forced aperture photometry to produce a single set of observations - see Best et al. (2023) for details - for the Boötes field the existing catalogue of Brown et al. (2007, 2008) was used. The FIR data (McCheyne et al., 2022) were taken from the Herschel Extragalactic Legacy Project – HELP (Shirley et al., 2021) - and deblended using the XID+ Bayesian deblender (Hurley et al., 2017). Photometric redshifts were estimated using machine learning and template fitting techniques on the existing optical data (Duncan et al., 2021).

MAGPHYS requires details of the transmission profile for each filter in a specific format<sup>1</sup>, FORTRAN program P1 in Figure A.1 was written to perform this conversion while program P2 presents the output in human readable form for verification. Transmission profile information was acquired by private communication or from the SVO Filter Profile Service<sup>2</sup> (Rodrigo and Solano, 2020).

<sup>1</sup>see <https://www.iap.fr/magphys/ewExternalFiles/readme.pdf>

<sup>2</sup><http://svo2.cab.inta-csic.es/theory/fps/>

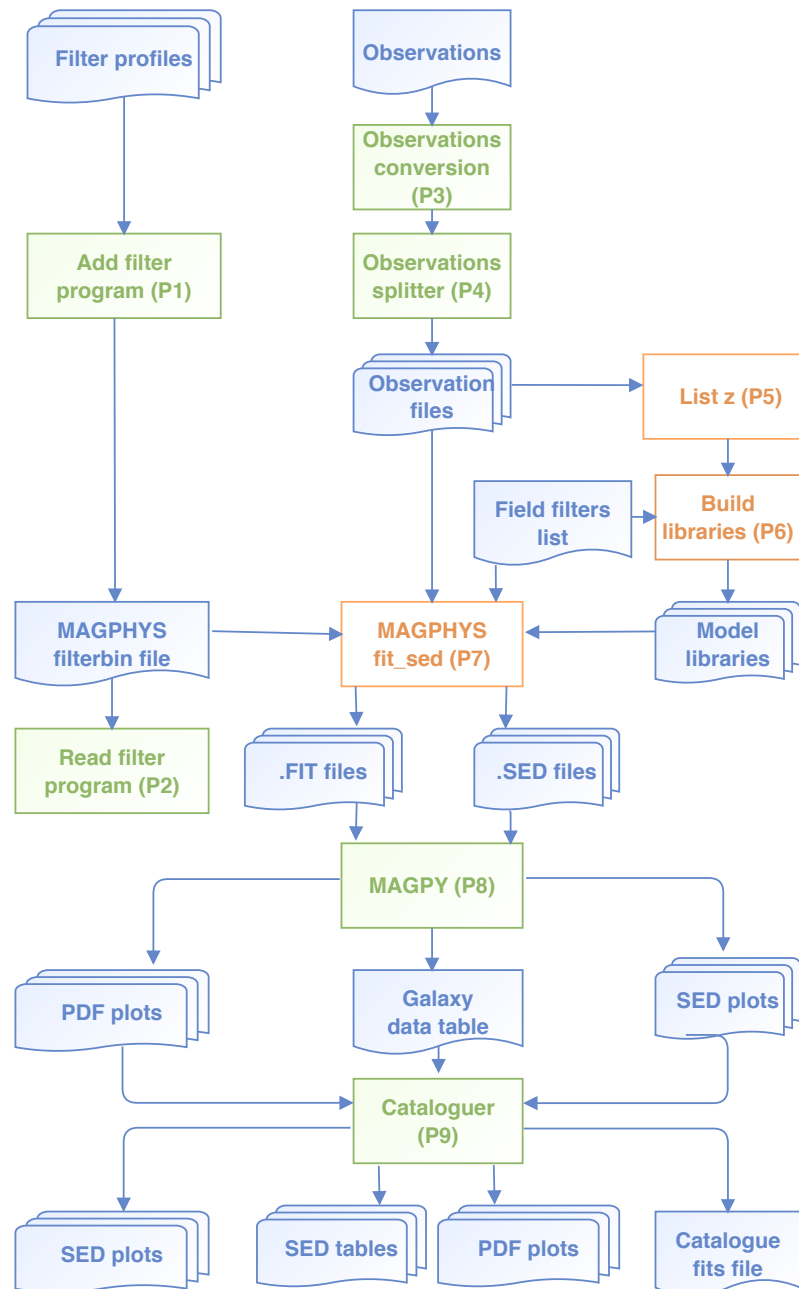


FIGURE A.1: The program stack for processing the deepfield observations. Usual flowchart notation applies; the boxes coloured green are FORTRAN or Python programs written specifically for this project, boxes coloured orange are the MAGPHYS processing suite. The numbers in brackets are referred to in the text.

Telescope	Instrument	Filter	$\lambda_{\text{eff}}(\mu\text{m})$	ELAIS-N1	Boötes	Lockman
GALEX		FUV	0.15		X	
GALEX		NUV	0.23		X	
LBT	LBC	u	0.36		X	
CFHT	Megacam	u	0.38			X
CFHT	Megacam	u	0.39	X		
KPNO	MOSAIC	Bw	0.44		X	
Subaru	HSC	g	0.46	X		
CFHT	Megacam	g	0.48			X
PanSTARRS		g	0.48	X		
Subaru	HSC	r	0.60	X		
PanSTARRS		r	0.61	X		
CFHT	Megacam	r	0.62			X
KPNO	MOSAIC	R	0.65		X	
PanSTARRS		i	0.75	X		
Subaru	HSC	i	0.76	X		
KPNO	MOSAIC	I	0.81		X	
PanSTARRS		z	0.87	X		
Subaru	HSC	z	0.89	X		
CFHT	Megacam	z	0.89			X
SDSS		z	0.89		X	
Subaru	Suprime	z	0.91		X	
Subaru	Suprime	nb921	0.92	X		
PanSTARRS		y	0.96	X		
Subaru	HSC	y	1.00	X		
LBT	LBC	y	1.04		X	
UKIRT	WFCam	J	1.24	X	X	X
NOAO	NEWFIRM	H	1.62		X	
NOAO	NEWFIRM	Ks	2.17		X	
UKIRT	WFCam	K	2.20	X	X	X
Spitzer	IRAC	I1	3.51	X	X	X
Spitzer	IRAC	I2	4.42	X	X	X
Spitzer	IRAC	I3	5.63	X	X	X
Spitzer	IRAC	I4	7.59	X	X	X
Spitzer	MIPS24		23.21	X	X	X
Herschel	PACS	100	97.90	X	X	X
Herschel	PACS	160	153.95	X	X	X
Herschel	SPIRE	250	242.82	X	X	X
Herschel	SPIRE	350	340.89	X	X	X
Herschel	SPIRE	500	482.26	X	X	X

TABLE A.1: Telescopes, instruments and filters used for the deep fields catalogues. MAGPHYS filter sets were built for each of the three survey fields using the instruments shown. Details were taken from private communications or the SVO Filter Profile Service - <http://svo2.cab.inta-csic.es/svo/theory/fps3/index.php>

Bespoke programs were written to convert the observation data for each field into a form suitable for MAGPHYS (Figure A.1 program P3). Once formatted, the data were split into files of 200 observations to enable parallel processing (Figure A.1 program P4).

MAGPHYS fits SEDs by comparing observations to those in models in prebuilt libraries. Two libraries are provided - 50,000 UV/optical models in the SFH library and 25,000 IR models in the IR library - each model containing galaxy properties together with a corresponding SED. The libraries need to be processed to calculate the expected model fluxes through the observer filters, this is done in two phases. Firstly, program P5 is run to produce a list of the redshifts appearing in the observations file. There are two options available: to compile a list of actual redshifts or to compile a list of approximate redshifts rounded to the nearest  $\Delta z = 0.01$ . This latter option produces fewer library files and was chosen for this project. The second phase comprises two programs - one for the SFH library and one for the IR - shown as P6 in Figure A.1. These programs use the filter data and the observed fluxes to create a model library for each entry in the redshift list. Parsing the appropriate library, they take each model younger than the age of the Universe at the given redshift, and compute the absolute AB magnitude through each filter. Once created, these libraries are used by the final MAGPHYS fitting phase - P7 in Figure A.1.

The output of the SED fitting phase is a pair of files for each source modelled - a file tagged .sed containing the best-fit model SED as a table, and a file tagged .fit containing details of the best-fit fluxes, the best-fit  $\chi^2$  value and the probability density functions (PDFs) of a number of properties in table form, see - <http://www.iap.fr/magphys/ewExternalFiles/readme.pdf> for details.

The MAGPHYS .fit and .sed files were processed using the MAGPY program (Figure A.1 program P8). This Python program takes as input the MAGPHYS output files producing plots of the SED and PDFs - Figure A.2 presents an example of these plots - and generating a File Image Transport System (fits) file of MAGPHYS derived galaxy data. These files contain data for each observation, including the best-fit  $\chi^2$  value and a flag indicating whether this lies outside  $\chi_{\max}^2$ , the 99% confidence value, indicating MAGPHYS has failed to find a suitable model.  $\chi_{\max}^2$  is determined by calculating the number of degrees of freedom (DoF) in the original observation, using Equation A.1 taken from Smith et al. (2012), and using standard  $\chi^2$  tables.

$$N_{\text{dof}} \approx (-2.820 \pm 0.745) + (0.661 \pm 0.132)N_{\text{bands}} + (7.91 \pm 5.50 \times 10^{-3})N_{\text{bands}}^2 \quad (\text{A.1})$$

Where  $N_{\text{dof}}$  is the resulting degrees of freedom,  $N_{\text{bands}}$  is the number of filters used in the observation.

Running multiple versions of MAGPHYS is ‘embarrassingly parallel’ in that no significant effort is needed to separate the problem into a number of parallel tasks. MAGPHYS was run on the University of Hertfordshire’s high performance cluster (UHHPC) using up to 700 parallel cores. A typical run to fit 200 galaxies on the UHHPC took between 13 and 24 hours. Output from the parallel runs was combined prior to the final catalogue build.

The CATALOGUER (Figure A.1 program P9) processes the output from MAGPHYS and MAGPY to create the catalogue; a catalogue is a directory containing five elements:

1. A README.txt file containing all relevant information;
2. A directory containing the SED plots for each galaxy
3. A directory containing the PDF plots for each galaxy
4. A directory containing the SED tables as produced by MAGPHYS for each galaxy
5. The catalogue fits file containing data on each galaxy, details can be found in Table A.2

Two sets of catalogues were created. The first, smaller, set took as input galaxies selected on the basis of a  $5\sigma$  detection at 150 MHz (Smith et al., 2021). The second set consisted of galaxies selected on the basis of their IRAC flux density - specifically those with flux density  $> 10\mu\text{Jy}$  in the  $3.6\mu\text{m}$  data from SWIRE and  $z < 1$  (Smith et al., 2021). Each set consisted of separate catalogues for the three survey fields. The smaller, radio-selected, catalogues were published in July 2020, the larger IRAC selected catalogues were published a month later. Details of the catalogues can be found in Table A.3.

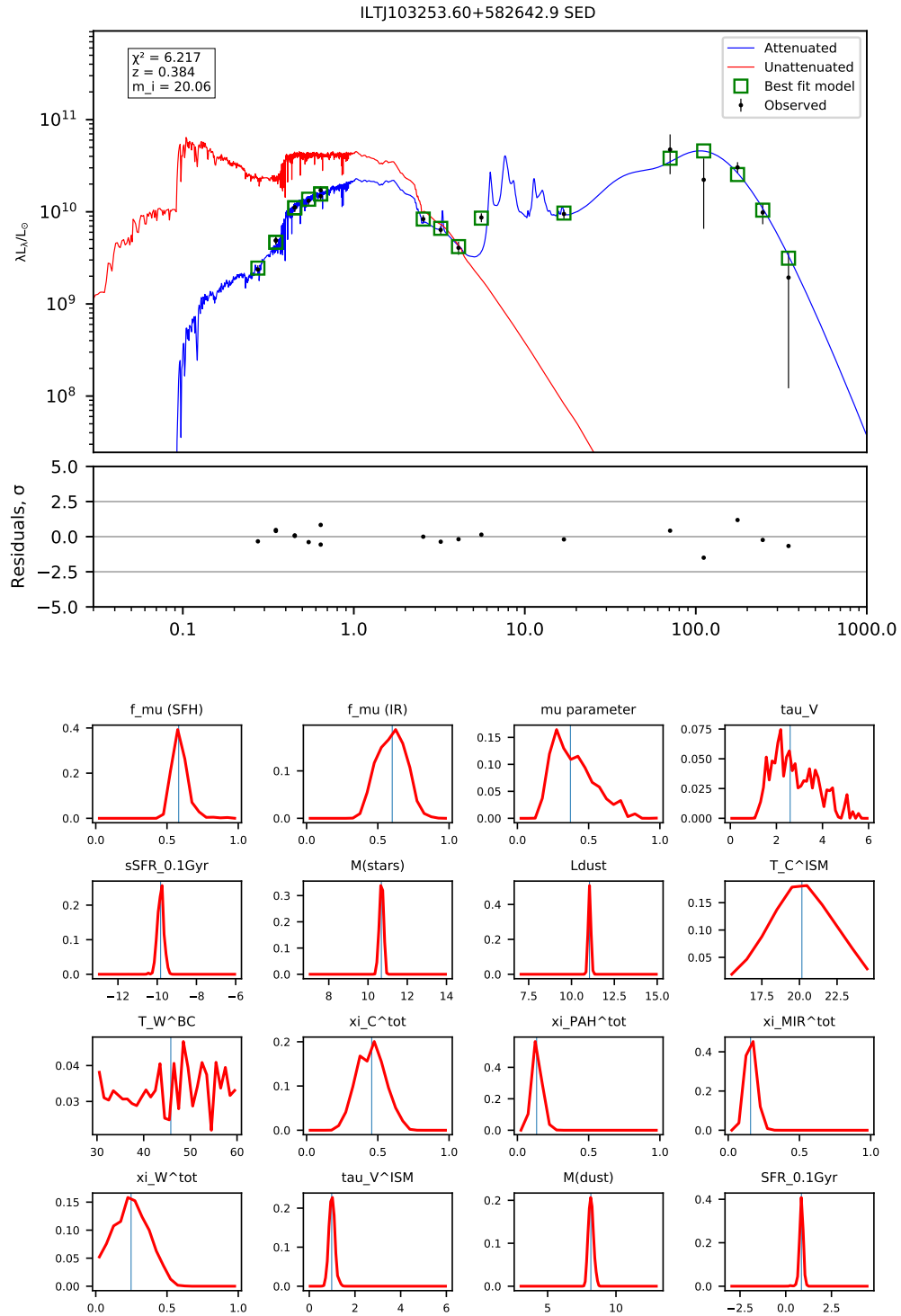


FIGURE A.2: Examples of the plots produced by MAGPY. The main plot in the upper panel is an SED produced by MAGPHYS the key to the symbols is shown in the legend. The lower part of this panel shows the residuals -  $\log_{10}(\text{model value}) - \log_{10}(\text{observed value})$  - of the observations in  $\sigma$  units for each filter. The lower panel shows the probability density functions (PDFs) of 16 of the galaxy properties returned by MAGPHYS, the blue lines mark the median. These plots are for galaxy ILTJ103253.60+582642.9 in the Lockman Hole field.

TABLE A.2: Columns in the LOFAR Deepfields catalogues. The 8 values associated with the property `fmu_sfh` are repeated for each property marked \*

Field	Value	Comment
<code>galaxy_id</code>		source id
<code>z</code>		redshift used for the fitting
<code>chi2</code>		best fit $\chi^2$ value
<code>chi2_99_flag</code>		$\chi^2$ 99 per cent confidence flag (1 = outside threshold) to identify formally bad fits.
<code>fmu_sfh</code>		fraction of total luminosity arising from ISM in optical library
	best	best-fit value
	sigma	symmetrised best fit error - defined as (84th percentile-16th percentile)/2
	bayes	Bayesian estimate of parameter value; sum of value*probability from MAGPHYS-derived pdf
	03	2.5th percentile of that parameter's PDF
	16	16th percentile
	50	50th percentile
	84	84th percentile
	98	97.5th percentile
<code>fmu_ir</code>	*	fraction of total luminosity arising from ISM in IR library
<code>mu</code>	*	fraction of <code>tau_V</code> arising from ISM
<code>tau_V</code>	*	effective dust absorption optical depth
<code>sSFR</code>	*	specific star formation rate averaged over last 0.1 Gyr
<code>M*</code>	*	mass of stars in $M_\odot$ units
<code>L<sub>dust</sub></code>	*	luminosity of dust in $L_\odot$ units
<code>TC_ISM</code>	*	temperature of cold dust in ISM in K
<code>TW BC</code>	*	temperature of warm dust in BC in K
<code>xi_C_tot</code>	*	luminosity contribution of cold dust
<code>xi_PAH_tot</code>	*	luminosity contribution of PAHs
<code>xi_MIR_tot</code>	*	luminosity contribution of hot dust
<code>xi_W_tot</code>	*	luminosity contribution of warm dust
<code>tau_V_ISM</code>	*	effective optical depth of ISM
<code>M<sub>dust</sub></code>	*	dust mass in $M_\odot$ units
<code>SFR</code>	*	star formation rate in $M_\odot \text{ yr}^{-1}$ averaged over last 0.1 Gyr

TABLE A.3: Details of the six published catalogues. The first column lists the survey field, the second the method of galaxy selection, the third the number of galaxies in the catalogue, and the fourth the percentage of galaxies to which MAGPHYS was able to satisfactorily fit an SED.

Field	Selection	Galaxies	Fit success
Boötes	150 Mhx	17102	72%
Boötes	IRAC	299495	78%
ELAIS-N1	150 Mhz	29870	92%
ELAIS-N1	IRAC	183417	90%
Lockman	150 Mhz	28836	86%
Lockman	IRAC	290672	87%

### A.3 Contribution to science

These catalogues have contributed to the following papers:

1. The LOFAR Two-metre Sky Survey Deep fields: The star formation rate – radio luminosity relation at low frequencies (Smith et al., 2021)
2. The bright end of the infrared luminosity functions and the abundance of hyperluminous infrared galaxies (Wang et al., 2021)
3. The LOFAR Two-metre Sky Survey Deep Fields. A new analysis of low-frequency radio luminosity as a star-formation tracer in the Lockman Hole region (Bonato et al., 2021)
4. The LOFAR Two-metre Sky Survey Deep fields. The mass dependence of the far-infrared radio correlation at 150MHz using deblended Herschel fluxes (McCheyne et al., 2022)
5. Cosmic evolution of low-excitation radio galaxies in the LOFAR two-metre sky survey deep fields (Kondapally et al., 2022)
6. The LOFAR Two-metre Sky Survey: the radio view of the cosmic star formation history (Cochrane et al., 2023c)
7. The LOFAR Two-meter Sky Survey: Deep Fields Data Release 1. V. Survey description, source classifications and host galaxy properties (Best et al., 2023)
8. Radio spectral properties of star-forming galaxies between 150-5000MHz in the ELAIS-N1 field (An et al., 2024)
9. The LOFAR Two-metre Sky Survey: The nature of the faint source population and SFR-radio luminosity relation using PROSPECTOR (Das et al., 2024)
10. Radio-AGN activity across the galaxy population: dependence on stellar mass, star-formation rate, and redshift (Kondapally et al., 2024).

# Bibliography

- Ahumada, R., Allende Prieto, C., Almeida, A., et al., 2020. The 16th Data Release of the Sloan Digital Sky Surveys: First Release from the APOGEE-2 Southern Survey and Full Release of eBOSS Spectra. *ApJ*, 249(1):3.
- Amorín, R., Pérez-Montero, E., Contini, T., et al., 2015. Extreme emission-line galaxies out to  $z \sim 1$  in zCOSMOS. I. Sample and characterization of global properties. *A&A*, 578:A105.
- An, F., Vaccari, M., Best, P.N., et al., 2024. Radio spectral properties of star-forming galaxies between 150 and 5000 MHz in the ELAIS-N1 field. *MNRAS*, 528(3):5346.
- Anglés-Alcázar, D., Faucher-Giguère, C.A., Quataert, E., et al., 2017. Black holes on FIRE: stellar feedback limits early feeding of galactic nuclei. *MNRAS*, 472(1):L109.
- Aniano, G., Draine, B.T., Gordon, K.D., et al., 2011. Common-Resolution Convolution Kernels for Space- and Ground-Based Telescopes. *PASP*, 123(908):1218.
- Arnaudova, M.I., Smith, D.J.B., Hardcastle, M.J., et al., 2024. Exploring the radio loudness of SDSS quasars with spectral stacking. *MNRAS*, 528(3):4547.
- Arnouts, S., Cristiani, S., Moscardini, L., et al., 1999. Measuring and modelling the redshift evolution of clustering: the Hubble Deep Field North. *MNRAS*, 310(2):540.
- Asari, N.V., Cid Fernandes, R., Stasińska, G., et al., 2007. The history of star-forming galaxies in the Sloan Digital Sky Survey. *MNRAS*, 381(1):263.
- Auld, R., Bianchi, S., Smith, M.W.L., et al., 2013. The Herschel Virgo Cluster Survey - XII. FIR properties of optically selected Virgo cluster galaxies. *MNRAS*, 428(3):1880.
- Baes, M., 2020. Panchromatic SED fitting codes and modelling techniques. In M. Boquien, E. Lusso, C. Gruppioni, and P. Tissera, editors, *Panchromatic Modelling with Next Generation Facilities*, volume 341, pages 26–34.

- Baes, M., Davies, J.I., Dejonghe, H., et al., 2003. Radiative transfer in disc galaxies - III. The observed kinematics of dusty disc galaxies. *MNRAS*, 343(4):1081.
- Baes, M., Verstappen, J., De Looze, I., et al., 2011. Efficient Three-dimensional NLTE Dust Radiative Transfer with SKIRT. *ApJ*, 196(2):22.
- Baldry, I.K., Balogh, M.L., Bower, R., et al., 2004. Color bimodality: Implications for galaxy evolution. In R.E. Allen, D.V. Nanopoulos, and C.N. Pope, editors, *The New Cosmology: Conference on Strings and Cosmology*, volume 743 of *American Institute of Physics Conference Series*, pages 106–119. AIP.
- Baldwin, C., McDermid, R.M., Kuntschner, H., et al., 2018. Comparison of stellar population model predictions using optical and infrared spectroscopy. *MNRAS*, 473(4):4698.
- Baldwin, J.A., Phillips, M.M., and Terlevich, R., 1981. Classification parameters for the emission-line spectra of extragalactic objects. *PASP*, 93:5.
- Bassini, L., Rasia, E., Borgani, S., et al., 2020. The DIANOGA simulations of galaxy clusters: characterising star formation in protoclusters. *A&A*, 642:A37.
- Battisti, A.J., da Cunha, E., Grasha, K., et al., 2019. MAGPHYS+photo-z: Constraining the Physical Properties of Galaxies with Unknown Redshifts. *ApJ*, 882(1):61.
- Baum, W.A., 1959. Population Inferences from Star Counts, Surface Brightness and Colors. *PASP*, 71(419):106.
- Baumann, D., 2009. TASI Lectures on Inflation. *arXiv e-prints*, arXiv:0907.5424.
- Beck, R., Lin, C.A., Ishida, E.E.O., et al., 2017. On the realistic validation of photometric redshifts. *MNRAS*, 468(4):4323.
- Becker, J.K., Biermann, P.L., Dreyer, J., et al., 2009. Cosmic Rays VI - Starburst galaxies at multiwavelengths. *arXiv e-prints*, arXiv:0901.1775.
- Behroozi, P.S., Wechsler, R.H., and Conroy, C., 2013. On the Lack of Evolution in Galaxy Star Formation Efficiency. *ApJ*, 762(2):L31.
- Bell, E.F. and Jong, R.S.d., 2001. Stellar mass-to-light ratios and the tully-fisher relation. *The Astrophysical Journal*.
- Bell, E.F., McIntosh, D.H., Katz, N., et al., 2003. The Optical and Near-Infrared Properties of Galaxies. I. Luminosity and Stellar Mass Functions. *ApJ*, 149(2):289.

- Bell, E.F., Wolf, C., Meisenheimer, K., et al., 2004. Nearly 5000 Distant Early-Type Galaxies in COMBO-17: A Red Sequence and Its Evolution since  $z=1$ . *ApJ*, 608(2):752.
- Bellstedt, S., Robotham, A.S.G., Driver, S.P., et al., 2020. Galaxy And Mass Assembly (GAMA): a forensic SED reconstruction of the cosmic star formation history and metallicity evolution by galaxy type. *MNRAS*, 498(4):5581.
- Bellstedt, S., Robotham, A.S.G., Driver, S.P., et al., 2021. Galaxy and mass assembly (GAMA): the inferred mass-metallicity relation from  $z = 0$  to 3.5 via forensic SED fitting. *MNRAS*, 503(3):3309.
- Bennett, C.L., Halpern, M., Hinshaw, G., et al., 2003. First-Year Wilkinson Microwave Anisotropy Probe (WMAP) Observations: Preliminary Maps and Basic Results. *ApJ*, 148(1):1.
- Benson, A.J., 2010. Galaxy formation theory. *Physics Reports*, 495(2-3):33.
- Benz, W., 1990. Smooth Particle Hydrodynamics - a Review. In J.R. Buchler, editor, *Numerical Modelling of Nonlinear Stellar Pulsations Problems and Prospects*, page 269.
- Bertelli, G., Bressan, A., Chiosi, C., et al., 1994. Theoretical isochrones from models with new radiative opacities. *A&A Supp.*, 106:275.
- Best, P.N., Kondapally, R., Williams, W.L., et al., 2023. The LOFAR Two-metre Sky Survey: Deep Fields data release 1. V. Survey description, source classifications, and host galaxy properties. *MNRAS*, 523(2):1729.
- Bianchi, S., 2007. The dust distribution in edge-on galaxies. Radiative transfer fits of V and K'-band images. *A&A*, 471(3):765.
- Bolatto, A.D., Wolfire, M., and Leroy, A.K., 2013. The CO-to-H<sub>2</sub> Conversion Factor. *Annual Review of Astronomy and Astrophysics*, 51(1):207.
- Bolzonella, M., Miralles, J.M., and Pelló, R., 2000. Photometric redshifts based on standard SED fitting procedures. *A&A*, 363:476.
- Bonato, M., Prandoni, I., De Zotti, G., et al., 2021. The LOFAR Two-metre Sky Survey Deep Fields. A new analysis of low-frequency radio luminosity as a star-formation tracer in the Lockman Hole region. *A&A*, 656:A48.

- Boquien, M., Buat, V., Burgarella, D., et al., 2022. The ALPINE-ALMA [C II] survey. Dust attenuation curves at  $z = 4.4-5.5$ . *A&A*, 663:A50.
- Boquien, M., Burgarella, D., Roehlly, Y., et al., 2019. CIGALE: a python Code Investigating GALaxy Emission. *A&A*, 622:A103.
- Bowler, R.A.A., Bourne, N., Dunlop, J.S., et al., 2018. Obscured star formation in bright  $z \approx 7$  Lyman-break galaxies. *MNRAS*, 481(2):1631.
- Bozett, K., Bunker, A.J., Curtis-Lake, E., et al., 2024. Extreme emission line galaxies detected in JADES JWST/NIRSpec - I. Inferred galaxy properties. *MNRAS*, 535(2):1796.
- Bradley, J., Dai, Z.R., Erni, R., et al., 2005. An Astronomical 2175 Å Feature in Interplanetary Dust Particles. *Science*, 307(5707):244.
- Bradley, L., Sipőcz, B., Robitaille, T., et al., 2025. astropy/photutils: 2.2.0.
- Brammer, G.B., van Dokkum, P.G., and Coppi, P., 2008. EAZY: A Fast, Public Photometric Redshift Code. *ApJ*, 686(2):1503.
- Bressan, A., Marigo, P., Girardi, L., et al., 2012. PARSEC: stellar tracks and isochrones with the PAdova and TRieste Stellar Evolution Code. *MNRAS*, 427(1):127.
- Brinchmann, J., Pettini, M., and Charlot, S., 2008. New insights into the stellar content and physical conditions of star-forming galaxies at  $z = 2-3$  from spectral modelling. *MNRAS*, 385(2):769.
- Broussard, A., Gawiser, E., and Iyer, K., 2022. Improved Measurements of Galaxy Star Formation Stochasticity from the Intrinsic Scatter of Burst Indicators. *ApJ*, 939(1):35.
- Broussard, A., Gawiser, E., Iyer, K., et al., 2019. Star Formation Stochasticity Measured from the Distribution of Burst Indicators. *ApJ*, 873(1):74.
- Brown, M.J., Clarke, T.A., Hopkins, A.M., et al., 2023. Radio continuum from the most massive early-type galaxies detected with askap racs. *Publications of the Astronomical Society of Australia*.
- Brown, M.J.I., Dey, A., Jannuzi, B.T., et al., 2007. The Evolving Luminosity Function of Red Galaxies. *ApJ*, 654(2):858.
- Brown, M.J.I., Zheng, Z., White, M., et al., 2008. Red Galaxy Growth and the Halo Occupation Distribution. *ApJ*, 682(2):937.

- Bruzual, G. and Charlot, S., 2003. Stellar population synthesis at the resolution of 2003. *MNRAS*, 344(4):1000.
- Buat, V., Ciesla, L., Boquien, M., et al., 2019. Cold dust and stellar emissions in dust-rich galaxies observed with ALMA: a challenge for SED-fitting techniques. *A&A*, 632:A79.
- Bull, P., Akrami, Y., Adamek, J., et al., 2016. Beyond  $\Lambda$  CDM: Problems, solutions, and the road ahead. *Physics of the Dark Universe*, 12:56.
- Burger, J. and Gowen, A., 2011. Data handling in hyperspectral image analysis. *Chemometrics and Intelligent Laboratory Systems*, 108(1):13. Analytical Platforms for Providing and Handling Massive Chemical Data.
- Butsky, I.S., Hummels, C.B., Hopkins, P.F., et al., 2024. Cold Gas Subgrid Model (CGSM): a two-fluid framework for modelling unresolved cold gas in galaxy simulations. *MNRAS*, 535(2):1672.
- Byler, N., Dalcanton, J.J., Conroy, C., et al., 2017. Nebular Continuum and Line Emission in Stellar Population Synthesis Models. *ApJ*, 840(1):44.
- Calistro Rivera, G., Lusso, E., Hennawi, J.F., et al., 2014. Fitting Spectral Energy Distributions of AGN - A Markov Chain Monte Carlo Approach. *arXiv e-prints*, arXiv:1401.5758.
- Calistro Rivera, G., Lusso, E., Hennawi, J.F., et al., 2016. AGNfitter: A Bayesian MCMC Approach to Fitting Spectral Energy Distributions of AGNs. *ApJ*, 833(1):98.
- Calzetti, D., 1997. Reddening and Star Formation in Starburst Galaxies. *AJ*, 113:162.
- Calzetti, D., 2001. The Dust Opacity of Star-forming Galaxies. *PASP*, 113(790):1449.
- Calzetti, D., 2013. Star Formation Rate Indicators. In J. Falcón-Barroso and J.H. Knapen, editors, *Secular Evolution of Galaxies*, page 419. Cambridge University Press.
- Calzetti, D., Armus, L., Bohlin, R.C., et al., 2000. The Dust Content and Opacity of Actively Star-forming Galaxies. *ApJ*, 533(2):682.
- Camps, P. and Baes, M., 2015. SKIRT: An advanced dust radiative transfer code with a user-friendly architecture. *Astronomy and Computing*, 9:20.
- Camps, P. and Baes, M., 2018. The Failure of Monte Carlo Radiative Transfer at Medium to High Optical Depths. *ApJ*, 861(2):80.

- Camps, P. and Baes, M., 2020. SKIRT 9: Redesigning an advanced dust radiative transfer code to allow kinematics, line transfer and polarization by aligned dust grains. *Astronomy and Computing*, 31:100381.
- Capak, P., Aussel, H., Ajiki, M., et al., 2007. The First Release COSMOS Optical and Near-IR Data and Catalog. *ApJ*, 172(1):99.
- Cappellari, M., 2023. Full spectrum fitting with photometry in PPXF: stellar population versus dynamical masses, non-parametric star formation history and metallicity for 3200 LEGA-C galaxies at redshift  $z \approx 0.8$ . *MNRAS*, 526(3):3273.
- Cardelli, J.A., Clayton, G.C., and Mathis, J.S., 1989. The Relationship between Infrared, Optical, and Ultraviolet Extinction. *ApJ*, 345:245.
- Carnall, A.C., Leja, J., Johnson, B.D., et al., 2019. How to Measure Galaxy Star Formation Histories. I. Parametric Models. *ApJ*, 873(1):44.
- Carnall, A.C., McLure, R.J., Dunlop, J.S., et al., 2018. Inferring the star formation histories of massive quiescent galaxies with BAGPIPES: evidence for multiple quenching mechanisms. *MNRAS*, 480(4):4379.
- Carrasco Kind, M. and Brunner, R.J., 2014. Exhausting the information: novel bayesian combination of photometric redshift pdfs. *Monthly Notices of the Royal Astronomical Society*, 442(4):3380.
- Carroll, B.W. and Ostlie, D.A., 2017. *An introduction to modern astrophysics, Second Edition*. Person.
- Casey, C.M., 2012. Far-infrared spectral energy distribution fitting for galaxies near and far. *MNRAS*, 425(4):3094.
- Casey, C.M., Cooray, A., Killi, M., et al., 2017. Near-infrared MOSFIRE Spectra of Dusty Star-forming Galaxies at  $0.2 < z < 4$ . *ApJ*, 840(2):101.
- Cattaneo, A., Dekel, A., Faber, S.M., et al., 2008. Downsizing by shutdown in red galaxies. *MNRAS*, 389(2):567.
- Cautun, M., van de Weygaert, R., Jones, B.J.T., et al., 2014. Evolution of the cosmic web. *MNRAS*, 441(4):2923.
- Chabrier, G., 2003. Galactic Stellar and Substellar Initial Mass Function. *PASP*, 115(809):763.

- Chabrier, G., 2005. The Initial Mass Function: From Salpeter 1955 to 2005. In E. Corbelli, F. Palla, and H. Zinnecker, editors, *The Initial Mass Function 50 Years Later*, volume 327 of *Astrophysics and Space Science Library*, page 41.
- Chan, T.K., Kereš, D., Wetzel, A., et al., 2018. The origin of ultra diffuse galaxies: stellar feedback and quenching. *MNRAS*, 478(1):906.
- Charlot, S. and Fall, S.M., 2000. A Simple Model for the Absorption of Starlight by Dust in Galaxies. *ApJ*, 539(2):718.
- Chen, C.C., Hodge, J.A., Smail, I., et al., 2017. A Spatially Resolved Study of Cold Dust, Molecular Gas, H II Regions, and Stars in the  $z = 2.12$  Submillimeter Galaxy ALESS67.1. *ApJ*, 846(2):108.
- Cheng, C., Huang, J.S., Smail, I., et al., 2023. JWST's PEARLS: A JWST/NIRCam View of ALMA Sources. *ApJ*, 942(1):L19.
- Choudhuri, S., Ghosh, A., Roy, N., et al., 2020. All-sky angular power spectrum - I. Estimating brightness temperature fluctuations using the 150-MHz TGSS survey. *MNRAS*, 494(2):1936.
- Chu, Y.Q. and Cui, X.Q., 1996. The LAMOST Project. In N. Kaifu, editor, *Ground-Based Astronomy in Asia*, page 327.
- Ciesla, L., Charmandaris, V., Georgakakis, A., et al., 2015. Constraining the properties of AGN host galaxies with spectral energy distribution modelling. *A&A*, 576:A10.
- Ciesla, L., Elbaz, D., and Fensch, J., 2017. The SFR- $M_*$  main sequence archetypal star-formation history and analytical models. *A&A*, 608:A41.
- Cimatti, A., Bianchi, S., Ferrara, A., et al., 1997. On the dust extinction in high- $z$  galaxies and the case of extremely red objects. *MNRAS*, 290(3):L43.
- Cimatti, A., Fraternali, F., and Nipoti, C., 2020. *Introduction to galaxy formation and evolution: from primordial gas to present-day galaxies*. Cambridge University Press,.
- Cochrane, R.K., Anglés-Alcázar, D., Cullen, F., et al., 2023a. Disappearing galaxies: the orientation dependence of JWST-bright, HST-dark, star-forming galaxy selection. *arXiv e-prints*, arXiv:2310.08829.

- Cochrane, R.K., Best, P.N., Smail, I., et al., 2021. Resolving a dusty, star-forming SHiZELS galaxy at  $z = 2.2$  with HST, ALMA, and SINFONI on kiloparsec scales. *MNRAS*, 503(2):2622.
- Cochrane, R.K., Hayward, C.C., Anglés-Alcázar, D., et al., 2019. Predictions for the spatial distribution of the dust continuum emission in  $1 < z < 5$  star-forming galaxies. *MNRAS*, 488(2):1779.
- Cochrane, R.K., Hayward, C.C., Anglés-Alcázar, D., et al., 2022. Predicting sub-millimeter flux densities from global galaxy properties. *MNRAS*.
- Cochrane, R.K., Hayward, C.C., Anglés-Alcázar, D., et al., 2023b. Predicting sub-millimetre flux densities from global galaxy properties. *MNRAS*, 518(4):5522.
- Cochrane, R.K., Kondapally, R., Best, P.N., et al., 2023c. The LOFAR Two-metre Sky Survey: the radio view of the cosmic star formation history. *MNRAS*, 523(4):6082.
- Coil, A.L., Aird, J., Reddy, N., et al., 2015. The MOSDEF Survey: Optical Active Galactic Nucleus Diagnostics at  $z \sim 2.3$ . *ApJ*, 801(1):35.
- Colless, M., Dalton, G., Maddox, S., et al., 2001. The 2dF Galaxy Redshift Survey: spectra and redshifts. *MNRAS*, 328(4):1039.
- Collister, A.A. and Lahav, O., 2004. ANNz: Estimating Photometric Redshifts Using Artificial Neural Networks. *PASP*, 116(818):345.
- Colman, T. and Teysier, R., 2019. On the origin of the peak of the stellar initial mass function: exploring the tidal screening theory. *Monthly Notices of the Royal Astronomical Society*.
- Condon, J.J., 1992. Radio emission from normal galaxies. *Annual Review of Astronomy and Astrophysics*, 30:575.
- Condon, J.J., Condon, M.A., Gisler, G., et al., 1982. Strong radio sources in bright spiral galaxies. II. Rapid star formation and galaxy-galaxy interactions. *ApJ*, 252:102.
- Conroy, C., 2013. Modeling the Panchromatic Spectral Energy Distributions of Galaxies. *Annual Review of Astronomy and Astrophysics*, 51(1):393.
- Conroy, C. and Gunn, J.E., 2010a. FSPS: Flexible Stellar Population Synthesis. Astrophysics Source Code Library, record ascl:1010.043.

- Conroy, C. and Gunn, J.E., 2010b. The Propagation of Uncertainties in Stellar Population Synthesis Modeling. III. Model Calibration, Comparison, and Evaluation. *ApJ*, 712(2):833.
- Conroy, C., Gunn, J.E., and White, M., 2009. The Propagation of Uncertainties in Stellar Population Synthesis Modeling. I. The Relevance of Uncertain Aspects of Stellar Evolution and the Initial Mass Function to the Derived Physical Properties of Galaxies. *ApJ*, 699(1):486.
- Conroy, C., White, M., and Gunn, J.E., 2010. The Propagation of Uncertainties in Stellar Population Synthesis Modeling. II. The Challenge of Comparing Galaxy Evolution Models to Observations. *ApJ*, 708(1):58.
- Conselice, C.J., 2003. Observing Massive Galaxy Formation. In C.M. Boily, P. Patsis, S. Portegies Zwart, R. Spurzem, and C. Theis, editors, *EAS Publications Series*, volume 10 of *EAS Publications Series*, page 101.
- Conselice, C.J., 2014. The Evolution of Galaxy Structure Over Cosmic Time. *Annual Review of Astronomy and Astrophysics*, 52:291.
- Courteau, S., Cappellari, M., de Jong, R.S., et al., 2014. Galaxy masses. *Reviews of Modern Physics*, 86(1):47.
- Cowie, L.L., Songaila, A., Hu, E.M., et al., 1996. New Insight on Galaxy Formation and Evolution From Keck Spectroscopy of the Hawaii Deep Fields. *AJ*, 112:839.
- Crain, R.A., Schaye, J., Bower, R.G., et al., 2015. The EAGLE simulations of galaxy formation: calibration of subgrid physics and model variations. *MNRAS*, 450(2):1937.
- Cram, L., Hopkins, A., Mobasher, B., et al., 1998. Star Formation Rates in Faint Radio Galaxies. *ApJ*, 507(1):155.
- Croft, R.A.C., Weinberg, D.H., Bolte, M., et al., 2002. Toward a Precise Measurement of Matter Clustering: Ly $\alpha$  Forest Data at Redshifts 2-4. *ApJ*, 581(1):20.
- Croton, D.J., Colless, M., Gaztañaga, E., et al., 2004. The 2dF Galaxy Redshift Survey: voids and hierarchical scaling models. *MNRAS*, 352(3):828.
- Cui, W., Knebe, A., Yepes, G., et al., 2018. The Three Hundred project: a large catalogue of theoretically modelled galaxy clusters for cosmological and astrophysical applications. *MNRAS*, 480(3):2898.

- Cuillandre, J.C., Bertin, E., Bolzonella, M., et al., 2024. Euclid: Early Release Observations – Programme overview and pipeline for compact- and diffuse-emission photometry. *arXiv e-prints*, arXiv:2405.13496.
- da Cunha, E., Charlot, S., and Elbaz, D., 2008. A simple model to interpret the ultraviolet, optical and infrared emission from galaxies. *MNRAS*, 388(4):1595.
- da Cunha, E., Walter, F., Smail, I.R., et al., 2015. An ALMA Survey of Sub-millimeter Galaxies in the Extended Chandra Deep Field South: Physical Properties Derived from Ultraviolet-to-radio Modeling. *ApJ*, 806(1):110.
- Dahlen, T., Mobasher, B., Faber, S.M., et al., 2013. A Critical Assessment of Photometric Redshift Methods: A CANDELS Investigation. *ApJ*, 775(2):93.
- Dai, Y.S., Wilkes, B.J., Bergeron, J., et al., 2018. Is there a relationship between AGN and star formation in IR-bright AGNs? *MNRAS*, 478(3):4238.
- Dale, D.A., Helou, G., Magdis, G.E., et al., 2014. A Two-parameter Model for the Infrared/Submillimeter/Radio Spectral Energy Distributions of Galaxies and Active Galactic Nuclei. *ApJ*, 784(1):83.
- Dalton, G., Trager, S.C., Abrams, D.C., et al., 2012. WEAVE: the next generation wide-field spectroscopy facility for the William Herschel Telescope. In I.S. McLean, S.K. Ramsay, and H. Takami, editors, *Ground-based and Airborne Instrumentation for Astronomy IV*, volume 8446 of *Society of Photo-Optical Instrumentation Engineers (SPIE) Conference Series*, page 84460P.
- Das, S., Smith, D.J.B., Haskell, P., et al., 2024. The LOFAR Two-metre Sky Survey: The nature of the faint source population and SFR-radio luminosity relation using PROSPECTOR. *MNRAS*.
- Davé, R., Anglés-Alcázar, D., Narayanan, D., et al., 2019. SIMBA: Cosmological simulations with black hole growth and feedback. *MNRAS*, 486(2):2827.
- de Chambure, D., Lainé, R., van Katwijk, K., et al., 1999. XMM's X-ray telescopes. *ESA Bulletin*, 100:30.
- De Geyter, G., Baes, M., Camps, P., et al., 2014. The distribution of interstellar dust in CALIFA edge-on galaxies via oligochromatic radiative transfer fitting. *MNRAS*, 441(1):869.

- De Looze, I., Baes, M., Bendo, G.J., et al., 2012. The dust energy balance in the edge-on spiral galaxy NGC 4565. *MNRAS*, 427(4):2797.
- de Sitter, W., 1917. On the relativity of inertia. Remarks concerning Einstein's latest hypothesis. *Koninklijke Nederlandse Akademie van Wetenschappen Proceedings Series B Physical Sciences*, 19:1217.
- De Vaucouleurs, G., 1959. Classification and morphology of external galaxies. In *Astrophysik iv: Sternsysteme/astrophysics iv: Stellar systems*, pages 275–310. Springer.
- Delvecchio, I., Daddi, E., Sargent, M.T., et al., 2021. The infrared-radio correlation of star-forming galaxies is strongly  $M_*$ -dependent but nearly redshift-invariant since  $z \sim 4$ . *A&A*, 647:A123.
- Diemer, B., Sparre, M., Abramson, L.E., et al., 2017. Log-normal Star Formation Histories in Simulated and Observed Galaxies. *ApJ*, 839(1):26.
- Dobbels, W., Baes, M., Viaene, S., et al., 2020. Predicting the global far-infrared SED of galaxies via machine learning techniques. *A&A*, 634:A57.
- Dome, T., Tacchella, S., Fialkov, A., et al., 2024. Mini-quenching of  $z = 4-8$  galaxies by bursty star formation. *MNRAS*, 527(2):2139.
- Doore, K., Monson, E.B., Eufrazio, R.T., et al., 2023. Lightning: An X-Ray to Submillimeter Galaxy SED-fitting Code with Physically Motivated Stellar, Dust, and AGN Models. *ApJ*, 266(2):39.
- Dotter, A., 2016. MESA Isochrones and Stellar Tracks (MIST) 0: Methods for the Construction of Stellar Isochrones. *ApJ*, 222(1):8.
- Dotter, A., Chaboyer, B., Jevremović, D., et al., 2008. The Dartmouth Stellar Evolution Database. *ApJ*, 178(1):89.
- Draine, B.T., 2003. Interstellar Dust Grains. *Annual Review of Astronomy and Astrophysics*, 41:241.
- Draine, B.T., 2011. *Physics of the Interstellar and Intergalactic Medium*. Princeton University Press.
- Draine, B.T., Dale, D.A., Bendo, G., et al., 2007. Dust Masses, PAH Abundances, and Starlight Intensities in the SINGS Galaxy Sample. *ApJ*, 663(2):866.

- Draine, B.T. and Lee, H.M., 1984. Optical Properties of Interstellar Graphite and Silicate Grains. *ApJ*, 285:89.
- Draine, B.T. and Li, A., 2007. Infrared Emission from Interstellar Dust. IV. The Silicate-Graphite-PAH Model in the Post-Spitzer Era. *ApJ*, 657(2):810.
- Driver, S.P. and Robotham, A.S., 2010. Quantifying cosmic variance. *Monthly Notices of the Royal Astronomical Society*, 407(4):2131.
- Drory, N., Bender, R., and Hopp, U., 2004. Comparing Spectroscopic and Photometric Stellar Mass Estimates. *ApJ*, 616(2):L103.
- Dubois, Y., Beckmann, R., Bournaud, F., et al., 2021. Introducing the NEWHORIZON simulation: Galaxy properties with resolved internal dynamics across cosmic time. *A&A*, 651:A109.
- Dubois, Y., Pichon, C., Welker, C., et al., 2014. Dancing in the dark: galactic properties trace spin swings along the cosmic web. *MNRAS*, 444(2):1453.
- Dudzevičiūtė, U., Smail, I., Swinbank, A.M., et al., 2020. An ALMA survey of the SCUBA-2 CLS UDS field: physical properties of 707 sub-millimetre galaxies. *MNRAS*, 494(3):3828.
- Duncan, K.J., Brown, M.J.I., Williams, W.L., et al., 2018a. Photometric redshifts for the next generation of deep radio continuum surveys - I. Template fitting. *MNRAS*, 473(2):2655.
- Duncan, K.J., Jarvis, M.J., Brown, M.J.I., et al., 2018b. Photometric redshifts for the next generation of deep radio continuum surveys - II. Gaussian processes and hybrid estimates. *MNRAS*, 477(4):5177.
- Duncan, K.J., Kondapally, R., Brown, M.J.I., et al., 2021. The LOFAR Two-meter Sky Survey: Deep Fields Data Release 1. IV. Photometric redshifts and stellar masses. *A&A*, 648:A4.
- Duncan, K.J., Windhorst, R.A., Koekemoer, A.M., et al., 2023. JWST's PEARLS: TN J1338-1942 - I. Extreme jet-triggered star formation in a  $z = 4.11$  luminous radio galaxy. *MNRAS*, 522(3):4548.
- Dunne, L., Eales, S., Edmunds, M., et al., 2000. The SCUBA Local Universe Galaxy Survey - I. First measurements of the submillimetre luminosity and dust mass functions. *MNRAS*, 315(1):115.

- Dwek, E., Arendt, R.G., Hauser, M.G., et al., 1998. The COBE Diffuse Infrared Background Experiment Search for the Cosmic Infrared Background: IV. Cosmological Implications. *ApJ*, 508(1):106.
- Dye, S., 2008. Star formation histories from multiband photometry: a new approach. *MNRAS*, 389(3):1293.
- Eales, S., Dunne, L., Clements, D., et al., 2010. The Herschel ATLAS. *PASP*, 122(891):499.
- Eggen, O.J., Lynden-Bell, D., and Sandage, A.R., 1962. Evidence from the motions of old stars that the Galaxy collapsed. *ApJ*, 136:748.
- Einstein, A., 1917. Kosmologische Betrachtungen zur allgemeinen Relativitätstheorie. *Sitzungsberichte der Königlich Preussischen Akademie der Wissenschaften*, pages 142–152.
- Elbaz, D., Daddi, E., Le Borgne, D., et al., 2007. The reversal of the star formation-density relation in the distant universe. *A&A*, 468(1):33.
- Endsley, R., Stark, D.P., Whitler, L., et al., 2023. A JWST/NIRCam study of key contributors to reionization: the star-forming and ionizing properties of UV-faint  $z$  7-8 galaxies. *MNRAS*, 524(2):2312.
- Faisst, A.L., Capak, P.L., Emami, N., et al., 2019. The Recent Burstiness of Star Formation in Galaxies at  $z \sim 4.5$  from  $H\alpha$  Measurements. *ApJ*, 884(2):133.
- Falcón-Barroso, J., Sánchez-Blázquez, P., Vazdekis, A., et al., 2011. An updated MILES stellar library and stellar population models. *A&A*, 532:A95.
- Fall, S.M. and Efstathiou, G., 1980. Formation and rotation of disc galaxies with haloes. *MNRAS*, 193:189.
- Faucher, N. and Blanton, M.R., 2024. Testing the Accuracy of Spectral Energy Distribution Modeling Techniques Using the NIHAO-SKIRT-Catalog. *ApJ*, 975(2):220.
- Faucher-Giguère, C.A., 2018. A model for the origin of bursty star formation in galaxies. *MNRAS*, 473(3):3717.
- Faucher-Giguère, C.A., Feldmann, R., Quataert, E., et al., 2016. A stellar feedback origin for neutral hydrogen in high-redshift quasar-mass haloes. *MNRAS*, 461(1):L32.
- Faucher-Giguère, C.A., Hopkins, P.F., Kereš, D., et al., 2015. Neutral hydrogen in galaxy haloes at the peak of the cosmic star formation history. *MNRAS*, 449(1):987.

- Feldmann, R., Hopkins, P.F., Quataert, E., et al., 2016. The formation of massive, quiescent galaxies at cosmic noon. *MNRAS*, 458(1):L14.
- Fernández-Soto, A., Lanzetta, K.M., Chen, H.W., et al., 2001. On the Compared Accuracy and Reliability of Spectroscopic and Photometric Redshift Measurements. *ApJ*, 135(1):41.
- Few, C.G., Dobbs, C., Pettitt, A., et al., 2016. Testing hydrodynamics schemes in galaxy disc simulations. *MNRAS*, 460(4):4382.
- Fields, B.D., Molaro, P., and Sarkar, S., 2014. Big-Bang Nucleosynthesis. *arXiv e-prints*, arXiv:1412.1408.
- Fitzpatrick, E.L., 1986. An average interstellar extinction curve for the Large Magellanic Cloud. *AJ*, 92:1068.
- Flores Velázquez, J.A., Gurvich, A.B., Faucher-Giguère, C.A., et al., 2021a. The time-scales probed by star formation rate indicators for realistic, bursty star formation histories from the FIRE simulations. *MNRAS*, 501(4):4812.
- Flores Velázquez, J.A., Gurvich, A.B., Faucher-Giguère, C.A., et al., 2021b. The time-scales probed by star formation rate indicators for realistic, bursty star formation histories from the FIRE simulations. *MNRAS*, 501(4):4812.
- Fontana, A., D’Odorico, S., Poli, F., et al., 2000. Photometric Redshifts and Selection of High-Redshift Galaxies in the NTT and Hubble Deep Fields. *AJ*, 120(5):2206.
- Forbes, D.A., Sánchez-Blázquez, P., and Proctor, R., 2005. The correlation of metallicity gradient with galaxy mass. *MNRAS*, 361(1):L6.
- Gallazzi, A. and Bell, E.F., 2009. Stellar Mass-to-Light Ratios from Galaxy Spectra: How Accurate Can They Be? *ApJ*, 185(2):253.
- Gallazzi, A., Charlot, S., Brinchmann, J., et al., 2005. The ages and metallicities of galaxies in the local universe. *MNRAS*, 362(1):41.
- Gardner, J.P., 2009. The James Webb Space Telescope. In T. Onaka, G.J. White, T. Nakagawa, and I. Yamamura, editors, *AKARI, a Light to Illuminate the Misty Universe*, volume 418 of *Astronomical Society of the Pacific Conference Series*, page 365.

- Gawiser, E., 2006. Galaxy Formation. In S.J. Kannappan, S. Redfield, J.E. Kessler-Silacci, M. Landriau, and N. Drory, editors, *New Horizons in Astronomy: Frank N. Bash Symposium*, volume 352 of *Astronomical Society of the Pacific Conference Series*, page 177.
- Gebek, A., Trčka, A., Baes, M., et al., 2024. The many colours of the TNG100 simulation. *MNRAS*, 531(4):3839.
- Gehrz, R., 1989. Sources of Stardust in the Galaxy. In L.J. Allamandola and A.G.G.M. Tielens, editors, *Interstellar Dust*, volume 135, page 445.
- Gehrz, R.D., Roellig, T.L., Werner, M.W., et al., 2007. The NASA Spitzer Space Telescope. *Review of Scientific Instruments*, 78(1):011302.
- Gil de Paz, A., Boissier, S., Madore, B.F., et al., 2007. The GALEX Ultraviolet Atlas of Nearby Galaxies. *ApJ*, 173(2):185.
- Gilbank, D.G., Yee, H.K.C., Ellingson, E., et al., 2008. The Red-Sequence Luminosity Function in Galaxy Clusters since  $z \sim 1$ . *ApJ*, 673(2):742.
- Gilda, S., Lower, S., and Narayanan, D., 2021. MIRKWOOD: Fast and Accurate SED Modeling Using Machine Learning. *ApJ*, 916(1):43.
- Gingold, R.A. and Monaghan, J.J., 1977. Smoothed particle hydrodynamics: theory and application to non-spherical stars. *MNRAS*, 181:375.
- Ginolfi, M., Graziani, L., Schneider, R., et al., 2018. Where does galactic dust come from? *MNRAS*, 473(4):4538.
- Giovanelli, R., Haynes, M.P., Kent, B.R., et al., 2005. The Arecibo Legacy Fast ALFA Survey. I. Science Goals, Survey Design, and Strategy. *AJ*, 130(6):2598.
- Girardi, L., Bressan, A., Bertelli, G., et al., 2000. Evolutionary tracks and isochrones for low- and intermediate-mass stars: From 0.15 to 7  $M_{sun}$ , and from  $Z=0.0004$  to 0.03. *A&A Supp.*, 141:371.
- Gnedin, N.Y., Tassis, K., and Kravtsov, A.V., 2009. Modeling Molecular Hydrogen and Star Formation in Cosmological Simulations. *ApJ*, 697(1):55.
- Gómez-Guijarro, C., Toft, S., Karim, A., et al., 2018. Starburst to Quiescent from HST/ALMA: Stars and Dust Unveil Minor Mergers in Submillimeter Galaxies at  $z \sim 4.5$ . *ApJ*, 856(2):121.

- Gondhalekar, P.M., 1981. Ultraviolet Astronomy with the International Ultraviolet Explorer. *Bulletin of the Astronomical Society of India*, 9:112.
- Gordon, K.D., Clayton, G.C., Misselt, K.A., et al., 2003. A Quantitative Comparison of the Small Magellanic Cloud, Large Magellanic Cloud, and Milky Way Ultraviolet to Near-Infrared Extinction Curves. *ApJ*, 594(1):279.
- Gray, R. and Dunning-Davies, J., 2008. A review of redshift and its interpretation in cosmology and astrophysics. *arXiv e-prints*, arXiv:0806.4085.
- Guerra, J., Molinari, E., Lodi, M., et al., 2016. WAS: the data archive for the WEAVE spectrograph. In G. Chiozzi and J.C. Guzman, editors, *Software and Cyberinfrastructure for Astronomy IV*, volume 9913 of *Society of Photo-Optical Instrumentation Engineers (SPIE) Conference Series*, page 99131X.
- Gunasekera, C.M., van Hoof, P.A.M., Chatzikos, M., et al., 2023. The 23.01 Release of Cloudy. *Research Notes of the American Astronomical Society*, 7(11):246.
- Guo, Y., Rafelski, M., Faber, S.M., et al., 2016. The Bursty Star Formation Histories of Low-mass Galaxies at  $0.4 < z < 1$  Revealed by Star Formation Rates Measured From  $H\beta$  and FUV. *ApJ*, 833(1):37.
- Gupta, A., Jaiswar, R., Rodriguez-Gomez, V., et al., 2023. MOSEL Survey: JWST Reveals Major Mergers/strong Interactions Drive the Extreme Emission Lines in the Early Universe. *ApJ*, 957(2):L35.
- Guth, A.H., 1981. Inflationary universe: A possible solution to the horizon and flatness problems. *Physical Review D*, 23(2):347.
- Hainline, L.J., Blain, A.W., Smail, I., et al., 2011. The Stellar Mass Content of Submillimeter-selected Galaxies. *ApJ*, 740(2):96.
- Harvey, T., Conselice, C., Adams, N.J., et al., 2024. EPOCHS IV: SED Modelling Assumptions and their impact on the Stellar Mass Function at  $6.5 < z < 13.5$  using PEARLS and public JWST observations. *arXiv e-prints*, arXiv:2403.03908.
- Haskell, P., Das, S., Smith, D.J.B., et al., 2024. Beware the recent past: a bias in spectral energy distribution modelling due to bursty star formation. *MNRAS*, 530(1):L7.

- Haskell, P., Smith, D.J.B., Cochrane, R.K., et al., 2023. Energy balance SED modelling can be effective at high redshifts regardless of UV-FIR offsets. *MNRAS*, 525(1):1535.
- Hauser, M.G., Arendt, R.G., Kelsall, T., et al., 1998. The COBE Diffuse Infrared Background Experiment Search for the Cosmic Infrared Background. I. Limits and Detections. *ApJ*, 508(1):25.
- Hayward, C.C. and Hopkins, P.F., 2017. How stellar feedback simultaneously regulates star formation and drives outflows. *MNRAS*, 465(2):1682.
- Hayward, C.C., Kereš, D., Jonsson, P., et al., 2011. What Does a Submillimeter Galaxy Selection Actually Select? The Dependence of Submillimeter Flux Density on Star Formation Rate and Dust Mass. *ApJ*, 743(2):159.
- Hayward, C.C. and Smith, D.J.B., 2015. Should we believe the results of ultraviolet-millimetre galaxy spectral energy distribution modelling? *MNRAS*, 446(2):1512.
- Hennebelle, P. and Grudić, M.Y., 2024. The Physical Origin of the Stellar Initial Mass Function. *Annual Review of Astronomy and Astrophysics*, 62(1):63.
- Herschel, W., 1802. Catalogue of 500 New Nebulae, Nebulous Stars, Planetary Nebulae, and Clusters of Stars; With Remarks on the Construction of the Heavens. *Philosophical Transactions of the Royal Society of London Series I*, 92:477.
- Hidaka, J., Mathews, G.J., Kajino, T., et al., 2015. Equation of state of proto-neutron star and failed supernova neutrino. In *Proceedings of the Conference on Advances in Radioactive Isotope Science (ARIS2014)*, page 030137.
- Hidalgo, S.L., Pietrinferni, A., Cassisi, S., et al., 2018. The Updated BaSTI Stellar Evolution Models and Isochrones. I. Solar-scaled Calculations. *ApJ*, 856(2):125.
- Higson, E., Handley, W., Hobson, M., et al., 2019. Dynamic nested sampling: an improved algorithm for parameter estimation and evidence calculation. *Statistics and Computing*, 29(5):891.
- Hildebrand, R.H., 1983. The determination of cloud masses and dust characteristics from submillimetre thermal emission. *Quarterly Journal of the Royal Astronomical Society*, 24:267.
- Hilton, M., Conselice, C.J., Roseboom, I.G., et al., 2012. Herschel observations of a  $z \sim 2$  stellar mass selected galaxy sample drawn from the GOODS NICMOS Survey. *MNRAS*, 425(1):540.

- Hodge, J.A., Smail, I., Walter, F., et al., 2019. ALMA Reveals Potential Evidence for Spiral Arms, Bars, and Rings in High-redshift Submillimeter Galaxies. *ApJ*, 876(2):130.
- Hodge, J.A., Swinbank, A.M., Simpson, J.M., et al., 2016. Kiloparsec-scale Dust Disks in High-redshift Luminous Submillimeter Galaxies. *ApJ*, 833(1):103.
- Hogg, D.W., 1999. Distance measures in cosmology. *arXiv e-prints*, astro-ph/9905116.
- Hogg, D.W., Baldry, I.K., Blanton, M.R., et al., 2002. The K correction. *arXiv e-prints*, astro-ph/0210394.
- Hopkins, P.F., 2015. A new class of accurate, mesh-free hydrodynamic simulation methods. *MNRAS*, 450(1):53.
- Hopkins, P.F., Gurvich, A.B., Shen, X., et al., 2023a. What causes the formation of discs and end of bursty star formation? *MNRAS*, 525(2):2241.
- Hopkins, P.F., Kereš, D., Oñorbe, J., et al., 2014. Galaxies on FIRE (Feedback In Realistic Environments): stellar feedback explains cosmologically inefficient star formation. *MNRAS*, 445(1):581.
- Hopkins, P.F. and Raives, M.J., 2016. Accurate, meshless methods for magnetohydrodynamics. *MNRAS*, 455(1):51.
- Hopkins, P.F., Wetzel, A., Kereš, D., et al., 2018. FIRE-2 simulations: physics versus numerics in galaxy formation. *MNRAS*, 480(1):800.
- Hopkins, P.F., Wetzel, A., Wheeler, C., et al., 2023b. FIRE-3: updated stellar evolution models, yields, and microphysics and fitting functions for applications in galaxy simulations. *MNRAS*, 519(2):3154.
- Hoyle, F., 1948. A New Model for the Expanding Universe. *MNRAS*, 108:372.
- Hoyle, F. and Wickramasinghe, N.C., 1967. Impurities in Interstellar Grains. *Nature*, 214(5092):969.
- Hubble, E., 1929. A Relation between Distance and Radial Velocity among Extra-Galactic Nebulae. *Proceedings of the National Academy of Science*, 15(3):168.
- Hubble, E.P., 1936. *Realm of the Nebulae*.

- Hunt, L.K., De Looze, I., Boquien, M., et al., 2019. Comprehensive comparison of models for spectral energy distributions from 0.1  $\mu\text{m}$  to 1 mm of nearby star-forming galaxies. *A&A*, 621:A51.
- Hurley, P.D., Oliver, S., Betancourt, M., et al., 2017. HELP: XID+, the probabilistic de-blender for Herschel SPIRE maps. *MNRAS*, 464(1):885.
- Husser, T.O., Wende-von Berg, S., Dreizler, S., et al., 2013. A new extensive library of PHOENIX stellar atmospheres and synthetic spectra. *A&A*, 553:A6.
- Hutter, A., 2024. Early galaxy evolution with a varying stellar initial mass function. In *EAS2024, European Astronomical Society Annual Meeting*, page 1401.
- Iglesias-Páramo, J., Arroyo, A., Kehrig, C., et al., 2022. The miniJPAS survey: A search for extreme emission-line galaxies. *A&A*, 665:A95.
- Iglesias-Páramo, J., Vílchez, J.M., Galbany, L., et al., 2013. Aperture corrections for disk galaxy properties derived from the CALIFA survey. Balmer emission lines in spiral galaxies. *A&A*, 553:L7.
- Ikuta, C., 2007. Model colour-magnitude diagrams of elliptical galaxies. *A&A*, 472(1):77.
- Ilbert, O., Arnouts, S., McCracken, H.J., et al., 2006. Accurate photometric redshifts for the CFHT legacy survey calibrated using the VIMOS VLT deep survey. *A&A*, 457(3):841.
- Iyer, K.G., Gawiser, E., Faber, S.M., et al., 2019. Nonparametric Star Formation History Reconstruction with Gaussian Processes. I. Counting Major Episodes of Star Formation. *ApJ*, 879(2):116.
- Iyer, K.G., Tacchella, S., Genel, S., et al., 2020. The diversity and variability of star formation histories in models of galaxy evolution. *MNRAS*, 498(1):430.
- Jannuzi, B.T., Dey, A., and NDWFS Team, 1999. The NOAO Deep Wide-Field Survey. In *American Astronomical Society Meeting Abstracts*, volume 195 of *American Astronomical Society Meeting Abstracts*, page 12.07.
- Jansky, K.G., 1933. Radio Waves from Outside the Solar System. *Nature*, 132(3323):66.
- Ji, X. and Yan, R., 2020. Constraining photoionization models with a reprojected optical diagnostic diagram. *Monthly Notices of the Royal Astronomical Society*, 499(4):5749.

- Jiménez-Teja, Y., Benítez, N., Molino, A., et al., 2015. Accurate PSF-matched photometry and photometric redshifts for the extreme deep field with the Chebyshev-Fourier functions. *MNRAS*, 453(1):1136.
- Johnson, B.D., Leja, J., Conroy, C., et al., 2021. Stellar Population Inference with Prospector. *ApJ*, 254(2):22.
- Jonsson, P., 2006. SUNRISE: polychromatic dust radiative transfer in arbitrary geometries. *MNRAS*, 372(1):2.
- Juhász, A., Bouwman, J., Henning, T., et al., 2010. Dust Evolution in Protoplanetary Disks Around Herbig Ae/Be Stars—the Spitzer View. *ApJ*, 721(1):431.
- Juneau, S., Bournaud, F., Charlot, S., et al., 2014. Active Galactic Nuclei Emission Line Diagnostics and the Mass-Metallicity Relation up to Redshift  $z \sim 2$ : The Impact of Selection Effects and Evolution. *ApJ*, 788(1):88.
- Kaeufer, T., Woitke, P., Min, M., et al., 2023. Analysing the SEDs of protoplanetary disks with machine learning. *A&A*, 672:A30.
- Kajisawa, M. and Yamada, T., 2001. When Did the Hubble Sequence Appear?: Morphology, Color, and Number-Density Evolution of the Galaxies in the Hubble Deep Field North. *Publications of the Astronomical Society of Japan*, 53(5):833.
- Kartaltepe, J.S., Sanders, D., Le Floch, E., et al., 2010. A multiwavelength study of a sample of 70  $\mu\text{m}$  selected galaxies in the cosmos field. ii. the role of mergers in galaxy evolution. *The Astrophysical Journal*, 721(1):98.
- Katz, H., Galligan, T.P., Kimm, T., et al., 2019. Probing cosmic dawn with emission lines: predicting infrared and nebular line emission for ALMA and JWST. *MNRAS*, 487(4):5902.
- Kauffmann, G. and Haehnelt, M., 2000. A unified model for the evolution of galaxies and quasars. *MNRAS*, 311(3):576.
- Kauffmann, G., Heckman, T.M., Tremonti, C., et al., 2003a. The host galaxies of active galactic nuclei. *MNRAS*, 346(4):1055.
- Kauffmann, G., Heckman, T.M., White, S.D.M., et al., 2003b. Stellar masses and star formation histories for  $10^5$  galaxies from the Sloan Digital Sky Survey. *MNRAS*, 341(1):33.

- Kaviraj, S., Devriendt, J.E.G., Ferreras, I., et al., 2005. The elliptical galaxy colour-magnitude relation as a discriminant between the monolithic and merger paradigms. *MNRAS*, 360(1):60.
- Kelly, A.J., Jenkins, A., Deason, A., et al., 2022. Apostle-Auriga: effects of different subgrid models on the baryon cycle around Milky Way-mass galaxies. *MNRAS*, 514(3):3113.
- Kelsall, T., Weiland, J.L., Franz, B.A., et al., 1998. The COBE Diffuse Infrared Background Experiment Search for the Cosmic Infrared Background. II. Model of the Interplanetary Dust Cloud. *ApJ*, 508(1):44.
- Kennicutt, Robert C., J., 1998a. Star Formation in Galaxies Along the Hubble Sequence. *Annual Review of Astronomy and Astrophysics*, 36:189.
- Kennicutt, Robert C., J., Armus, L., Bendo, G., et al., 2003. SINGS: The SIRTf Nearby Galaxies Survey. *PASP*, 115(810):928.
- Kennicutt, Robert C., J., Calzetti, D., Walter, F., et al., 2007. Star Formation in NGC 5194 (M51a). II. The Spatially Resolved Star Formation Law. *ApJ*, 671(1):333.
- Kennicutt, Robert C., J., Hao, C.N., Calzetti, D., et al., 2009. Dust-corrected Star Formation Rates of Galaxies. I. Combinations of H $\alpha$  and Infrared Tracers. *ApJ*, 703(2):1672.
- Kennicutt, R.C., 1998b. The Global Schmidt Law in Star-forming Galaxies. *ApJ*, 498(2):541.
- Kennicutt, R.C., Calzetti, D., Aniano, G., et al., 2011. KINGFISH—Key Insights on Nearby Galaxies: A Far-Infrared Survey with Herschel: Survey Description and Image Atlas. *PASP*, 123(910):1347.
- Kennicutt, R.C. and Evans, N.J., 2012. Star Formation in the Milky Way and Nearby Galaxies. *Annual Review of Astronomy and Astrophysics*, 50:531.
- Kewley, L.J., Dopita, M.A., Sutherland, R.S., et al., 2001. Theoretical Modeling of Starburst Galaxies. *ApJ*, 556(1):121.
- Kewley, L.J., Jansen, R.A., and Geller, M.J., 2005. Aperture Effects on Star Formation Rate, Metallicity, and Reddening. *PASP*, 117(829):227.
- Klaas, U., Walker, H.J., Müller, T.G., et al., 2006. Multi-aperture photometry of extended IR sources with ISOPHOT. I. The nature of extended IR emission of planetary Nebulae. *A&A*, 452(2):523.

- Kokorev, V.I., Magdis, G.E., Davidzon, I., et al., 2021. The Evolving Interstellar Medium of Star-forming Galaxies, as Traced by Stardust. *ApJ*, 921(1):40.
- Kondapally, R., Best, P.N., Cochrane, R.K., et al., 2022. Cosmic evolution of low-excitation radio galaxies in the LOFAR two-metre sky survey deep fields. *MNRAS*, 513(3):3742.
- Kondapally, R., Best, P.N., Duncan, K.J., et al., 2024. Radio-AGN activity across the galaxy population: dependence on stellar mass, star-formation rate, and redshift. *MNRAS*.
- Kondapally, R., Best, P.N., Hardcastle, M.J., et al., 2021. The LOFAR Two-meter Sky Survey: Deep Fields Data Release 1. III. Host-galaxy identifications and value added catalogues. *A&A*, 648:A3.
- Krieger, A. and Wolf, S., 2023. Improving Monte Carlo radiative transfer simulations: A shift of framework. *A&A*, 680:A67.
- Kriek, M. and Conroy, C., 2013. The Dust Attenuation Law in Distant Galaxies: Evidence for Variation with Spectral Type. *ApJ*, 775(1):L16.
- Kroupa, P., 2001. On the variation of the initial mass function. *MNRAS*, 322(2):231.
- Kroupa, P. and Jerabkova, T., 2019. The Salpeter IMF and its descendants. *Nature Astronomy*, 3:482.
- Kuijken, K., 2008. GaaP: PSF- and aperture-matched photometry using shapelets. *A&A*, 482(3):1053.
- Lagos, C.d.P., Crain, R.A., Schaye, J., et al., 2015. Molecular hydrogen abundances of galaxies in the EAGLE simulations. *MNRAS*, 452(4):3815.
- Laigle, C., Pichon, C., Arnouts, S., et al., 2018. COSMOS2015 photometric redshifts probe the impact of filaments on galaxy properties. *MNRAS*, 474(4):5437.
- Lang, P., Schinnerer, E., Smail, I., et al., 2019. Revealing the Stellar Mass and Dust Distributions of Submillimeter Galaxies at Redshift 2. *ApJ*, 879(1):54.
- Larson, R.B. and Bromm, V., 2001. The first stars in the universe. *Scientific American*, 285(6):64.
- Larson, R.B. and Tinsley, B.M., 1978. Star formation rates in normal and peculiar galaxies. *ApJ*, 219:46.

- Larson, R.L., Hutchison, T.A., Bagley, M., et al., 2023. Spectral Templates Optimal for Selecting Galaxies at  $z \gtrsim 8$  with the JWST. *ApJ*, 958(2):141.
- Le Borgne, J.F., Bruzual, G., Pelló, R., et al., 2003. STELIB: A library of stellar spectra at  $R \sim 2000$ . *A&A*, 402:433.
- Le Brun, A.M.C., McCarthy, I.G., Schaye, J., et al., 2014. Towards a realistic population of simulated galaxy groups and clusters. *MNRAS*, 441(2):1270.
- Lee, D., Baes, M., Seon, K.I., et al., 2016. Radiative transfer in disc galaxies - V. The accuracy of the KB approximation. *MNRAS*, 463(3):2912.
- Lee, K.W., 2014. Initial mass function and star formation history in the small magellanic cloud. *Journal of the Korean Earth Science Society*.
- Lee, S.K., Idzi, R., Ferguson, H.C., et al., 2009. Biases and Uncertainties in Physical Parameter Estimates of Lyman Break Galaxies from Broadband Photometry. *ApJ*, 184(1):100.
- Lee, S.K.J., 2010. *Constraining physical properties and star-formation histories of star-forming galaxies at high-redshift*. Ph.D. thesis, Johns Hopkins University, Maryland.
- Leja, J., Carnall, A.C., Johnson, B.D., et al., 2019. How to Measure Galaxy Star Formation Histories. II. Nonparametric Models. *ApJ*, 876(1):3.
- Leja, J., Johnson, B.D., Conroy, C., et al., 2017. Deriving Physical Properties from Broadband Photometry with Prospector: Description of the Model and a Demonstration of its Accuracy Using 129 Galaxies in the Local Universe. *ApJ*, 837(2):170.
- Lemaître, G., 1927. Un univers homogène de masse constante et de rayon croissant rendant compte de la vitesse radiale des nébuleuses extragalactiques. *Annales de la Société Scientifique de Bruxelles*, A47:49.
- Lennox, J., 2001. *Aristotle's Philosophy of Biology*. Cambridge University Press,.
- Li, H., Vogelsberger, M., Marinacci, F., et al., 2020. The effects of subgrid models on the properties of giant molecular clouds in galaxy formation simulations. *MNRAS*, 499(4):5862.
- Lilly, S.J., Le Brun, V., Maier, C., et al., 2009. The zCOSMOS 10k-Bright Spectroscopic Sample. *ApJ*, 184(2):218.
- Lindholmer, M.O. and Pimblet, K.A., 2019. Redshift measurement through star formation. *A&A*, 629:A7.

- Lintott, C.J., Ferreras, I., and Lahav, O., 2006. Massive Elliptical Galaxies: From Cores to Halos. *ApJ*, 648(2):826.
- Liu, D., 2020. michi2: SED and SLED fitting tool. Astrophysics Source Code Library, record ascl:2005.002.
- Liu, D., Daddi, E., Schinnerer, E., et al., 2021. CO Excitation, Molecular Gas Density, and Interstellar Radiation Field in Local and High-redshift Galaxies. *ApJ*, 909(1):56.
- Llerena, M., Amorín, R., Pentericci, L., et al., 2024. Physical properties of extreme emission-line galaxies at  $z \sim 4-9$  from the JWST CEERS survey. *A&A*, 691:A59.
- Lo Faro, B., Buat, V., Roehlly, Y., et al., 2017. Characterizing the UV-to-NIR shape of the dust attenuation curve of IR luminous galaxies up to  $z \sim 2$ . *MNRAS*, 472(2):1372.
- Lockman, F.J., Jahoda, K., and McCammon, D., 1986. The Structure of Galactic H I in Directions of Low Total Column Density. *ApJ*, 302:432.
- Looser, T.J., D'Eugenio, F., Maiolino, R., et al., 2023. JADES: Differing assembly histories of galaxies – Observational evidence for bursty SFHs and (mini-)quenching in the first billion years of the Universe. *arXiv e-prints*, arXiv:2306.02470.
- López, I.E., Yang, G., Mountrichas, G., et al., 2024. A Cigale module tailored (not only) for Low-Luminosity AGN. *arXiv e-prints*, arXiv:2404.16938.
- Lower, S., Narayanan, D., Leja, J., et al., 2020. How Well Can We Measure the Stellar Mass of a Galaxy: The Impact of the Assumed Star Formation History Model in SED Fitting. *ApJ*, 904(1):33.
- Ma, X., Hayward, C.C., Casey, C.M., et al., 2019. Dust attenuation, dust emission, and dust temperature in galaxies at  $z \geq 5$ : a view from the FIRE-2 simulations. *MNRAS*, 487(2):1844.
- Ma, X., Hopkins, P.F., Garrison-Kimmel, S., et al., 2018. Simulating galaxies in the reionization era with FIRE-2: galaxy scaling relations, stellar mass functions, and luminosity functions. *MNRAS*, 478(2):1694.
- Madau, P., 1995. Radiative Transfer in a Clumpy Universe: The Colors of High-Redshift Galaxies. *ApJ*, 441:18.
- Madau, P. and Dickinson, M., 2014. Cosmic Star-Formation History. *Annual Review of Astronomy and Astrophysics*, 52:415.

- Madau, P., Ferguson, H.C., Dickinson, M.E., et al., 1996. High-redshift galaxies in the Hubble Deep Field: colour selection and star formation history to  $z=4$ . *MNRAS*, 283(4):1388.
- Mahony, E.K., Morganti, R., Prandoni, I., et al., 2016. The Lockman Hole project: LO-FAR observations and spectral index properties of low-frequency radio sources. *MNRAS*, 463(3):2997.
- Małek, K., Buat, V., Roehlly, Y., et al., 2018. HELP: modelling the spectral energy distributions of Herschel detected galaxies in the ELAIS N1 field. *A&A*, 620:A50.
- Mao, Y.W., Kong, X., and Lin, L., 2014. Characterizing Ultraviolet and Infrared Observational Properties for Galaxies. II. Features of Attenuation Law. *ApJ*, 789(1):76.
- Maraston, C., 2005. Evolutionary population synthesis: models, analysis of the ingredients and application to high- $z$  galaxies. *MNRAS*, 362(3):799.
- Margoniner, V.E. and Wittman, D.M., 2008. Photometric Redshifts and Signal-to-Noise Ratios. *ApJ*, 679(1):31.
- Marigo, P., Girardi, L., Bressan, A., et al., 2008. Evolution of asymptotic giant branch stars. II. Optical to far-infrared isochrones with improved TP-AGB models. *A&A*, 482(3):883.
- Martin, D.C., 2007. Quenching Star Formation in the Green Valley. Keck Observatory Archive DEIMOS, id.C245D.
- Martin, D.C., Fanson, J., Schiminovich, D., et al., 2005. The Galaxy Evolution Explorer: A Space Ultraviolet Survey Mission. *ApJ*, 619(1):L1.
- Martín-Navarro, I. and Vazdekis, A., 2024. Counting stars from the integrated spectra of galaxies. *A&A*, 691:L10.
- Mathews, E.P., Leja, J., Speagle, J.S., et al., 2023. As Simple as Possible but No Simpler: Optimizing the Performance of Neural Net Emulators for Galaxy SED Fitting. *ApJ*, 954(2):132.
- Mathis, J.S., Rumpl, W., and Nordsieck, K.H., 1977. The size distribution of interstellar grains. *ApJ*, 217:425.
- Mattig, W., 1958. Über den Zusammenhang zwischen Rotverschiebung und scheinbarer Helligkeit. *Astronomische Nachrichten*, 284:109.

- McCheyne, I., Oliver, S., Sargent, M., et al., 2022. The LOFAR Two-metre Sky Survey Deep fields. The mass dependence of the far-infrared radio correlation at 150 MHz using deblended Herschel fluxes. *A&A*, 662:A100.
- Meiksin, A.A., 2009. The physics of the intergalactic medium. *Reviews of Modern Physics*, 81(4):1405.
- Merrifield, M.R., Forbes, D.A., and Terlevich, A.I., 2000. The black hole mass-galaxy age relation. *MNRAS*, 313(2):L29.
- Michałowski, M.J., Hayward, C.C., Dunlop, J.S., et al., 2014. Determining the stellar masses of submillimetre galaxies: the critical importance of star formation histories. *A&A*, 571:A75.
- Michałowski, M.J., Watson, D., and Hjorth, J., 2010. Rapid Dust Production in Submillimeter Galaxies at  $z \gtrsim 4$ ? *ApJ*, 712(2):942.
- Miettinen, O., Delvecchio, I., Smolčić, V., et al., 2017. An ALMA survey of submillimetre galaxies in the COSMOS field: Physical properties derived from energy balance spectral energy distribution modelling. *A&A*, 606:A17.
- Misselt, K.A., Gordon, K.D., Clayton, G.C., et al., 2001. The DIRTY Model. II. Self-consistent Treatment of Dust Heating and Emission in a Three-dimensional Radiative Transfer Code. *ApJ*, 551(1):277.
- Mitchell, P.D., Lacey, C.G., Baugh, C.M., et al., 2013. How well can we really estimate the stellar masses of galaxies from broad-band photometry? *MNRAS*, 435(1):87.
- Mobasher, B., Dahlen, T., Ferguson, H.C., et al., 2015. A Critical Assessment of Stellar Mass Measurement Methods. *ApJ*, 808(1):101.
- Motha, N. and Razzaque, S., 2021. Modelling of synchrotron emission from galaxies and extragalactic radio background. In *High Energy Astrophysics in Southern Africa*, page 14.
- Muñoz-Mateos, J.C., Gil de Paz, A., Boissier, S., et al., 2009. Radial Distribution of Stars, Gas, and Dust in Singalaxies. II. Derived Dust Properties. *ApJ*, 701(2):1965.
- Mullaney, J.R., Pannella, M., Daddi, E., et al., 2012. GOODS-Herschel: the far-infrared view of star formation in active galactic nucleus host galaxies since  $z \approx 3$ . *MNRAS*, 419(1):95.

- Muratov, A.L., Kereš, D., Faucher-Giguère, C.A., et al., 2015. Gusty, gaseous flows of FIRE: galactic winds in cosmological simulations with explicit stellar feedback. *MNRAS*, 454(3):2691.
- Muratov, A.L., Kereš, D., Faucher-Giguère, C.A., et al., 2017. Metal flows of the circumgalactic medium, and the metal budget in galactic haloes. *MNRAS*, 468(4):4170.
- Myers, J.L. and Well, A.A., 2003. *Research design and statistical analysis*. Lawrence Erlbaum Associates.
- Nagaraj, G., Forbes, J.C., Leja, J., et al., 2022. A Bayesian Population Model for the Observed Dust Attenuation in Galaxies. *ApJ*, 932(1):54.
- Narayanan, D., Conroy, C., Davé, R., et al., 2018. A Theory for the Variation of Dust Attenuation Laws in Galaxies. *ApJ*, 869(1):70.
- Narayanan, D., Lower, S., Torrey, P., et al., 2023a. Outshining by Recent Star Formation Prevents the Accurate Measurement of High- $z$  Galaxy Stellar Masses. *arXiv e-prints*, arXiv:2306.10118.
- Narayanan, D., Smith, J.D.T., Hensley, B.S., et al., 2023b. A Framework for Modeling Polycyclic Aromatic Hydrocarbon Emission in Galaxy Evolution Simulations. *ApJ*, 951(2):100.
- Natale, G., Tuffs, R.J., Xu, C.K., et al., 2012. The dust emission SED of X-ray emitting regions in Stephan's Quintet. In R.J. Tuffs and C.C. Popescu, editors, *The Spectral Energy Distribution of Galaxies - SED 2011*, volume 284, pages 337–341.
- Nath, B.B., Vasiliev, E.O., Drozdov, S.A., et al., 2023. Dust-free starburst galaxies at redshifts  $z \lesssim 10$ . *MNRAS*, 521(1):662.
- Nayyeri, H., Hemmati, S., Mobasher, B., et al., 2017. CANDELS Multi-wavelength Catalogs: Source Identification and Photometry in the CANDELS COSMOS Survey Field. *ApJ*, 228(1):7.
- Nersesian, A., Zibetti, S., D'Eugenio, F., et al., 2023. Non-parametric galaxy morphology from stellar and nebular emission with the CALIFA sample. *A&A*, 673:A63.
- Neugebauer, G. and Leighton, R.B., 1969. *Two-micron sky survey. A preliminary catalogue*. NASA SP, Washington: NASA, 1969.

- Nobels, F.S.J., Schaye, J., Schaller, M., et al., 2024. Tests of subgrid models for star formation using simulations of isolated disc galaxies. *MNRAS*, 532(3):3299.
- Noeske, K.G., Faber, S.M., Weiner, B.J., et al., 2007a. Star Formation in AEGIS Field Galaxies since  $z=1.1$ : Staged Galaxy Formation and a Model of Mass-dependent Gas Exhaustion. *ApJ*, 660(1):L47.
- Noeske, K.G., Weiner, B.J., Faber, S.M., et al., 2007b. Star Formation in AEGIS Field Galaxies since  $z=1.1$ : The Dominance of Gradually Declining Star Formation, and the Main Sequence of Star-forming Galaxies. *ApJ*, 660(1):L43.
- Noll, S., Burgarella, D., Giovannoli, E., et al., 2009. Analysis of galaxy spectral energy distributions from far-UV to far-IR with CIGALE: studying a SINGS test sample. *A&A*, 507(3):1793.
- Ogando, R.L.C., Maia, M.A.G., Chiappini, C., et al., 2005. Do Observed Metallicity Gradients of Early-Type Galaxies Support a Hybrid Formation Scenario? *ApJ*, 632(2):L61.
- Oliver, S., Rowan-Robinson, M., Alexander, D.M., et al., 2000a. The European Large Area ISO Survey - I. Goals, definition and observations. *MNRAS*, 316(4):749.
- Oliver, S., Serjeant, S., Efstathiou, A., et al., 2000b. The European Large Area ISO Survey (ELAIS): Latest Results. In D. Lemke, M. Stickel, and K. Wilke, editors, *ISO Survey of a Dusty Universe*, volume 548, page 28. Springer Link.
- Olsen, K.P., 2015. Observing and Simulating Galaxy Evolution - from X-ray to Millimeter Wavelengths. *arXiv e-prints*, arXiv:1509.02991.
- Osterbrock, D.E. and Ferland, G.J., 2006. *Astrophysics of gaseous nebulae and active galactic nuclei*. University of Science Books.
- Pacifici, C., Charlot, S., Blaizot, J., et al., 2012. Relative merits of different types of rest-frame optical observations to constrain galaxy physical parameters. *MNRAS*, 421(3):2002.
- Pacifici, C., da Cunha, E., Charlot, S., et al., 2015. On the importance of using appropriate spectral models to derive physical properties of galaxies at  $0.7 < z < 2.8$ . *MNRAS*, 447(1):786.
- Pacifici, C., Iyer, K.G., Mobasher, B., et al., 2022. The Art of Measuring Physical Parameters in Galaxies: A Critical Assessment of Spectral Energy Distribution Fitting Techniques. *arXiv e-prints*, arXiv:2212.01915.

- Pacifici, C., Iyer, K.G., Mobasher, B., et al., 2023. The Art of Measuring Physical Parameters in Galaxies: A Critical Assessment of Spectral Energy Distribution Fitting Techniques. *ApJ*, 944(2):141.
- Pakmor, R., Springel, V., Coles, J.P., et al., 2023. The MillenniumTNG Project: the hydrodynamical full physics simulation and a first look at its galaxy clusters. *MNRAS*, 524(2):2539.
- Papastergis, E., Giovanelli, R., Haynes, M.P., et al., 2013. The Clustering of ALFALFA Galaxies: Dependence on H I Mass, Relationship with Optical Samples, and Clues of Host Halo Properties. *ApJ*, 776(1):43.
- Parravano, A., McKee, C.F., and Hollenbach, D.J., 2011. An Initial Mass Function for Individual Stars in Galactic Disks. I. Constraining the Shape of the Initial Mass Function. *ApJ*, 726(1):27.
- Parsotan, T., Cochrane, R.K., Hayward, C.C., et al., 2021. Realistic mock observations of the sizes and stellar mass surface densities of massive galaxies in FIRE-2 zoom-in simulations. *MNRAS*, 501(2):1591.
- Patidar, S., Khaire, V., and Narayanan, A., 2024. Tracing Baryons in the Warm Hot Intergalactic Medium using Broad Lyman- $\alpha$  Absorbers. In *42nd meeting of the Astronomical Society of India (ASI)*, volume 42, page P78.
- Patiri, S.G., Betancort-Rijo, J.E., Prada, F., et al., 2006. Statistics of voids in the two-degree Field Galaxy Redshift Survey. *MNRAS*, 369(1):335.
- Pavia, Donald and Kriz, G., Lampman, G., and Vyvyan, J., 2012. *Introduction to Spectroscopy*. Brookes Cole.
- Pearson, K., 1900. On the criterion that a given system of deviations from the probable in the case of a correlated system of variables is such that it can be reasonably supposed to have arisen from random sampling. *Phil. Mag. Series 5*, 50(157).
- Pellegrini, E.W., Oey, M.S., Winkler, P.F., et al., 2012. The Optical Depth of H II Regions in the Magellanic Clouds. *ApJ*, 755(1):40.
- Pentericci, L., McLure, R.J., Garilli, B., et al., 2018. The VANDELS ESO public spectroscopic survey: Observations and first data release. *A&A*, 616:A174.
- Penzias, A.A. and Wilson, R.W., 1965. A Measurement of Excess Antenna Temperature at 4080 Mc/s. *Astrophys. J.*, 142:419.

- Pérez-Montero, E., Amorín, R., Sánchez Almeida, J., et al., 2021. Extreme emission-line galaxies in SDSS - I. Empirical and model-based calibrations of chemical abundances. *MNRAS*, 504(1):1237.
- Perlmutter, S., Aldering, G., Goldhaber, G., et al., 1999. Measurements of  $\Omega$  and  $\Lambda$  from 42 High-Redshift Supernovae. *ApJ*, 517(2):565.
- Petrosian, V., 1976. Surface Brightness and Evolution of Galaxies. *ApJ*, 210:L53.
- Pforr, J., Maraston, C., and Tonini, C., 2012. Recovering galaxy stellar population properties from broad-band spectral energy distribution fitting. *MNRAS*, 422(4):3285.
- Phillipps, S., Bremer, M.N., Hopkins, A.M., et al., 2019. Galaxy and Mass Assembly (GAMA): time-scales for galaxies crossing the green valley. *MNRAS*, 485(4):5559.
- Pilbratt, G.L., 2003. Herschel Space Observatory mission overview. In J.C. Mather, editor, *IR Space Telescopes and Instruments*, volume 4850 of *Society of Photo-Optical Instrumentation Engineers (SPIE) Conference Series*, pages 586–597.
- Pillepich, A., Nelson, D., Springel, V., et al., 2019. First results from the TNG50 simulation: the evolution of stellar and gaseous discs across cosmic time. *MNRAS*, 490(3):3196.
- Pillepich, A., Springel, V., Nelson, D., et al., 2018. Simulating galaxy formation with the IllustrisTNG model. *MNRAS*, 473(3):4077.
- Planck Collaboration, Ade, P.A.R., Aghanim, N., et al., 2011. Planck early results. I. The Planck mission. *A&A*, 536:A1.
- Planck Collaboration, Ade, P.A.R., Aghanim, N., et al., 2016. Planck 2015 results. XIII. Cosmological parameters. *A&A*, 594:A13.
- Planck Collaboration, Fermi Collaboration, Ade, P.A.R., et al., 2015. Planck intermediate results. XXVIII. Interstellar gas and dust in the Chamaeleon clouds as seen by Fermi LAT and Planck. *A&A*, 582:A31.
- Popping, G., Somerville, R.S., and Galametz, M., 2017. The dust content of galaxies from  $z = 0$  to  $z = 9$ . *MNRAS*, 471(3):3152.
- Prevot, M.L., Lequeux, J., Maurice, E., et al., 1984. The typical interstellar extinction in the Small Magellanic Cloud. *A&A*, 132:389.

- Prugniel, P. and Soubiran, C., 2001. A database of high and medium-resolution stellar spectra. *A&A*, 369:1048.
- Raiter, A., Fosbury, R.A.E., and Teimoorinia, H., 2010. Ly $\alpha$  emitters in the GOODS-S field. A powerful pure nebular SED with N IV] emission at  $z = 5.563$ . *A&A*, 510:A109.
- Rawlings, M.G., Juvela, M., Mattila, K., et al., 2005. ISO observations of 3-200  $\mu\text{m}$  emission by three dust populations in an isolated local translucent cloud. *MNRAS*, 356(3):810.
- Reber, G., 1944. Cosmic Static. In *Class. Radio Astron.*, pages 61–69. Springer Netherlands, Dordrecht.
- Reddy, N.A., Kriek, M., Shapley, A.E., et al., 2015. The MOSDEF Survey: Measurements of Balmer Decrements and the Dust Attenuation Curve at Redshifts  $z \sim 1.4$ -2.6. *ApJ*, 806(2):259.
- Rieke, G.H., Alonso-Herrero, A., Weiner, B.J., et al., 2009. Determining Star Formation Rates for Infrared Galaxies. *ApJ*, 692(1):556.
- Riess, A.G., Filippenko, A.V., Challis, P., et al., 1998. Observational Evidence from Supernovae for an Accelerating Universe and a Cosmological Constant. *AJ*, 116(3):1009.
- Rigopoulou, D., Donnan, F.R., García-Bernete, I., et al., 2024. Polycyclic aromatic hydrocarbon emission in galaxies as seen with JWST. *MNRAS*, 532(2):1598.
- Robotham, A.S.G., Bellstedt, S., Lagos, C.d.P., et al., 2020. ProSpect: generating spectral energy distributions with complex star formation and metallicity histories. *MNRAS*, 495(1):905.
- Rodrigo, C. and Solano, E., 2020. The SVO Filter Profile Service. In *XIV.0 Scientific Meeting (virtual) of the Spanish Astronomical Society*, page 182.
- Roebuck, E., Sajina, A., Hayward, C.C., et al., 2019. Simulations Find Our Accounting of Dust-obscured Star Formation May Be Incomplete. *ApJ*, 881(1):18.
- Roediger, J.C. and Courteau, S., 2015. On the uncertainties of stellar mass estimates via colour measurements. *MNRAS*, 452(3):3209.
- Rosario, D.J., Mendel, J.T., Ellison, S.L., et al., 2016. Local SDSS galaxies in the Herschel Stripe 82 survey: a critical assessment of optically derived star formation rates. *MNRAS*, 457(3):2703.
- Rujopakarn, W., Daddi, E., Rieke, G.H., et al., 2019. ALMA 200 pc Resolution Imaging of Smooth Cold Dusty Disks in Typical  $z \sim 3$  Star-forming Galaxies. *ApJ*, 882(2):107.

- Rujopakarn, W., Dunlop, J.S., Rieke, G.H., et al., 2016. VLA and ALMA Imaging of Intense Galaxy-wide Star Formation in  $z \sim 2$  Galaxies. *ApJ*, 833(1):12.
- Sabater, J., Best, P.N., Tasse, C., et al., 2021. The LOFAR Two-meter Sky Survey: Deep Fields Data Release 1. II. The ELAIS-N1 LOFAR deep field. *A&A*, 648:A2.
- Saftly, W., Baes, M., De Geyter, G., et al., 2015. Large and small-scale structures and the dust energy balance problem in spiral galaxies. *A&A*, 576:A31.
- Salim, S., 2014. Green Valley Galaxies. *Serbian Astronomical Journal*, 189:1.
- Salim, S., Rich, R.M., Charlot, S., et al., 2007. UV Star Formation Rates in the Local Universe. *ApJ*, 173(2):267.
- Salmon, B., Papovich, C., Finkelstein, S.L., et al., 2015. The Relation between Star Formation Rate and Stellar Mass for Galaxies at  $3.5 \leq z \leq 6.5$  in CANDELS. *ApJ*, 799(2):183.
- Salpeter, E.E., 1955. The Luminosity Function and Stellar Evolution. *ApJ*, 121:161.
- Sánchez, C., Carrasco Kind, M., Lin, H., et al., 2014. Photometric redshift analysis in the Dark Energy Survey Science Verification data. *MNRAS*, 445(2):1482.
- Sánchez, S.F., Lugo-Aranda, A.Z., Sánchez Almeida, J., et al., 2024. WHaD diagram: Classifying the ionizing source with one single emission line. *A&A*, 682:A71.
- Sánchez-Blázquez, P., Peletier, R.F., Jiménez-Vicente, J., et al., 2006. Medium-resolution Isaac Newton Telescope library of empirical spectra. *MNRAS*, 371(2):703.
- Sandage, A., 1961. *The Hubble Atlas of Galaxies*. Carnegie Institute of Washington.
- Sandage, A., Sandage, M., and Kristian, J., 1975. *Galaxies and the universe*. University of Chicago Press.
- Sanders, D.B. and Mirabel, I.F., 1996. Luminous Infrared Galaxies. *Annual Review of Astronomy and Astrophysics*, 34:749.
- Santini, P., Maiolino, R., Magnelli, B., et al., 2014. The evolution of the dust and gas content in galaxies. *A&A*, 562:A30.
- Scannapieco, E., Silk, J., and Bouwens, R., 2005. AGN Feedback Causes Downsizing. *ApJ*, 635(1):L13.

- Schaller, M., Dalla Vecchia, C., Schaye, J., et al., 2015. The EAGLE simulations of galaxy formation: the importance of the hydrodynamics scheme. *MNRAS*, 454(3):2277.
- Schaye, J., Crain, R.A., Bower, R.G., et al., 2015. The EAGLE project: simulating the evolution and assembly of galaxies and their environments. *MNRAS*, 446(1):521.
- Schmidt, K., Treu, T., Brammer, G., et al., 2014. Through the looking glass: Hst spectroscopy of faint galaxies lensed by the frontier fields cluster macsj0717. 5+ 3745. *The Astrophysical Journal Letters*, 782(2):L36.
- Schreiber, C., Pannella, M., Elbaz, D., et al., 2015. The Herschel view of the dominant mode of galaxy growth from  $z = 4$  to the present day. *A&A*, 575:A74.
- Scranton, R., Connolly, A.J., Szalay, A.S., et al., 2005. Photometric Covariance in Multi-Band Surveys: Understanding the Photometric Error in the SDSS. *arXiv e-prints*, astro-ph/0508564.
- Searle, L., Sargent, W.L.W., and Bagnuolo, W.G., 1973. The History of Star Formation and the Colors of Late-Type Galaxies. *ApJ*, 179:427.
- Seillé, L.M., Buat, V., Haddad, W., et al., 2022. Spatial disconnection between stellar and dust emissions: The test of the Antennae Galaxies (Arp 244). *A&A*, 665:A137.
- Selina, R.J., Murphy, E.J., McKinnon, M., et al., 2018. The Next-Generation Very Large Array: a technical overview. In H.K. Marshall and J. Spyromilio, editors, *Ground-based and Airborne Telescopes VII*, volume 10700 of *Society of Photo-Optical Instrumentation Engineers (SPIE) Conference Series*, page 107001O.
- Semenov, V.A., 2024. Capturing Turbulence with Numerical Dissipation: a Simple Dynamical Model for Unresolved Turbulence in Hydrodynamic Simulations. *arXiv e-prints*, arXiv:2410.23339.
- Shapley, A.E., Sanders, R.L., Shao, P., et al., 2019. The MOSDEF Survey: Sulfur Emission-line Ratios Provide New Insights into Evolving Interstellar Medium Conditions at High Redshift. *ApJ*, 881(2):L35.
- Shimono, A., Tamura, N., Sugai, H., et al., 2012. The system software development for prime focus spectrograph on Subaru Telescope. In N.M. Radziwill and G. Chiozzi, editors, *Software and Cyberinfrastructure for Astronomy II*, volume 8451 of *Society of Photo-Optical Instrumentation Engineers (SPIE) Conference Series*, page 84513F.

- Shimwell, T.W., Hardcastle, M.J., Tasse, C., et al., 2022. VizieR Online Data Catalog: LOFAR Two-metre Sky Survey (LoTSS) DR2 (Shimwell+, 2022). VizieR On-line Data Catalog: J/A+A/659/A1. Originally published in: 2022A&A...659A...1S.
- Shimwell, T.W., Röttgering, H.J.A., Best, P.N., et al., 2017. The LOFAR Two-metre Sky Survey. I. Survey description and preliminary data release. *A&A*, 598:A104.
- Shimwell, T.W., Tasse, C., Hardcastle, M.J., et al., 2019. The LOFAR Two-metre Sky Survey. II. First data release. *A&A*, 622:A1.
- Shirley, R., Duncan, K., Campos Varillas, M.C., et al., 2021. HELP: the Herschel Extragalactic Legacy Project. *MNRAS*, 507(1):129.
- Silva, L., Granato, G.L., Bressan, A., et al., 1998. Modeling the Effects of Dust on Galactic Spectral Energy Distributions from the Ultraviolet to the Millimeter Band. *ApJ*, 509(1):103.
- Simet, M., Chartab, N., Lu, Y., et al., 2021. Comparison of Observed Galaxy Properties with Semianalytic Model Predictions Using Machine Learning. *ApJ*, 908(1):47.
- Simha, V., Weinberg, D.H., Conroy, C., et al., 2014. Parametrising Star Formation Histories. *arXiv e-prints*, arXiv:1404.0402.
- Simpson, J.M., Smail, I., Swinbank, A.M., et al., 2017. The SCUBA-2 Cosmology Legacy Survey: Multi-wavelength Properties of ALMA-identified Submillimeter Galaxies in UKIDSS UDS. *ApJ*, 839(1):58.
- Skilling, J., 2004. Nested Sampling. In R. Fischer, R. Preuss, and U.V. Toussaint, editors, *Bayesian Inference and Maximum Entropy Methods in Science and Engineering: 24th International Workshop on Bayesian Inference and Maximum Entropy Methods in Science and Engineering*, volume 735 of *American Institute of Physics Conference Series*, pages 395–405.
- Smit, R., Bouwens, R.J., Labbé, I., et al., 2014. Evidence for Ubiquitous High-equivalent-width Nebular Emission in  $z \sim 7$  Galaxies: Toward a Clean Measurement of the Specific Star-formation Rate Using a Sample of Bright, Magnified Galaxies. *ApJ*, 784(1):58.
- Smith, D.J. and Hayward, C.C., 2018. Panchromatic SED modelling of spatially resolved galaxies. *MNRAS*, 476(2):1705.
- Smith, D.J.B., Dunne, L., da Cunha, E., et al., 2012. Herschel-ATLAS: multi-wavelength SEDs and physical properties of 250  $\mu\text{m}$  selected galaxies at  $z \lesssim 0.5$ . *MNRAS*, 427(1):703.

- Smith, D.J.B., Hardcastle, M.J., Jarvis, M.J., et al., 2013. Isothermal dust models of Herschel-ATLAS galaxies. *MNRAS*, 436(3):2435.
- Smith, D.J.B., Haskell, P., Gürkan, G., et al., 2021. The LOFAR Two-metre Sky Survey Deep Fields. The star-formation rate-radio luminosity relation at low frequencies. *A&A*, 648:A6.
- Smith, D.J.B. and Hayward, C.C., 2015. Deriving star formation histories from photometry using energy balance spectral energy distribution modelling. *MNRAS*, 453(2):1597.
- Snyder, G.F., Torrey, P., Lotz, J.M., et al., 2015. Galaxy morphology and star formation in the Illustris Simulation at  $z = 0$ . *MNRAS*, 454(2):1886.
- Solarz, A., Takeuchi, T.T., and Pollo, A., 2016. Total infrared luminosity estimation from local galaxies in AKARI all sky survey. *A&A*, 592:A155.
- Somerville, R.S. and Davé, R., 2015. Physical Models of Galaxy Formation in a Cosmological Framework. *Annual Review of Astronomy and Astrophysics*, 53:51.
- Sorba, R. and Sawicki, M., 2015. Missing stellar mass in SED fitting: spatially unresolved photometry can underestimate galaxy masses. *MNRAS*, 452(1):235.
- Sparke, L.S. and Gallagher, John S., I., 2007. *Galaxies in the Universe*. Cambridge University Press.
- Sparre, M., Hayward, C.C., Feldmann, R., et al., 2017. (Star)bursts of FIRE: observational signatures of bursty star formation in galaxies. *MNRAS*, 466(1):88.
- Speagle, J.S., 2020. DYNESTY: a dynamic nested sampling package for estimating Bayesian posteriors and evidences. *MNRAS*, 493(3):3132.
- Speagle, J.S., Steinhardt, C.L., Capak, P.L., et al., 2014. A Highly Consistent Framework for the Evolution of the Star-Forming “Main Sequence” from  $z \sim 0-6$ . *ApJ*, 214(2):15.
- Spergel, D.N., Verde, L., Peiris, H.V., et al., 2003. First-Year Wilkinson Microwave Anisotropy Probe (WMAP) Observations: Determination of Cosmological Parameters. *ApJ*, 148(1):175.
- Springel, V., 2005. The cosmological simulation code GADGET-2. *MNRAS*, 364(4):1105.
- Springel, V., 2010. E pur si muove: Galilean-invariant cosmological hydrodynamical simulations on a moving mesh. *MNRAS*, 401(2):791.

- Springel, V., 2011. Moving-mesh hydrodynamics with the AREPO code. In J. Alves, B.G. Elmegreen, J.M. Girart, and V. Trimble, editors, *Computational Star Formation*, volume 270 of *IAU Symposium*, pages 203–206.
- Springel, V., Yoshida, N., and White, S.D.M., 2001. GADGET: a code for collisionless and gasdynamical cosmological simulations. *NewA*, 6(2):79.
- Stecher, T.P., 1965. Interstellar Extinction in the Ultraviolet. *ApJ*, 142:1683.
- Stern, J., Faucher-Giguère, C.A., Fielding, D., et al., 2021. Virialization of the Inner CGM in the FIRE Simulations and Implications for Galaxy Disks, Star Formation, and Feedback. *ApJ*, 911(2):88.
- Suess, K.A., Leja, J., Johnson, B.D., et al., 2022. Recovering the Star Formation Histories of Recently Quenched Galaxies: The Impact of Model and Prior Choices. *ApJ*, 935(2):146.
- Tacchella, S., Conroy, C., Faber, S.M., et al., 2022a. Fast, Slow, Early, Late: Quenching Massive Galaxies at  $z \sim 0.8$ . *ApJ*, 926(2):134.
- Tacchella, S., Finkelstein, S.L., Bagley, M., et al., 2022b. On the Stellar Populations of Galaxies at  $z = 9-11$ : The Growth of Metals and Stellar Mass at Early Times. *ApJ*, 927(2):170.
- Tacchella, S., Finkelstein, S.L., Bagley, M., et al., 2022c. On the Stellar Populations of Galaxies at  $z = 9-11$ : The Growth of Metals and Stellar Mass at Early Times. *ApJ*, 927(2):170.
- Tacchella, S., Smith, A., Kannan, R., et al., 2022d. H  $\alpha$  emission in local galaxies: star formation, time variability, and the diffuse ionized gas. *MNRAS*, 513(2):2904.
- Tarenghi, M., 2008. The Atacama Large Millimeter/Submillimeter Array: overview & status. *Ap&SS*, 313(1-3):1.
- Tasse, C., Shimwell, T., Hardcastle, M.J., et al., 2021. The LOFAR Two-meter Sky Survey: Deep Fields Data Release 1. I. Direction-dependent calibration and imaging. *A&A*, 648:A1.
- Terao, Y., Spitler, L.R., Motohara, K., et al., 2022. A Selection of H $\alpha$  Emitters at  $z = 2.1-2.5$  Using the K<sub>s</sub>-band Photometry of ZFOURGE. *ApJ*, 941(1):70.
- Teyssier, R., 2002. Cosmological hydrodynamics with adaptive mesh refinement. A new high resolution code called RAMSES. *A&A*, 385:337.

- Thomas, S.J., Barr, J., Callahan, S., et al., 2020. Vera C. Rubin Observatory: telescope and site status. In H.K. Marshall, J. Spyromilio, and T. Usuda, editors, *Ground-based and Airborne Telescopes VIII*, volume 11445 of *Society of Photo-Optical Instrumentation Engineers (SPIE) Conference Series*, page 114450I.
- Thorne, J.E., Robotham, A.S.G., Bellstedt, S., et al., 2022. DEVILS: cosmic evolution of SED-derived metallicities and their connection to star formation histories. *MNRAS*, 517(4):6035.
- Tielens, A.G.G.M., 2005. *The Physics and Chemistry of the Interstellar Medium*. Cambridge University Press.
- Tielens, A.G.G.M., 2008. Interstellar polycyclic aromatic hydrocarbon molecules. *Annual Review of Astronomy and Astrophysics*, 46:289.
- Tinsley, B.M., 1968. Evolution of the Stars and Gas in Galaxies. *ApJ*, 151:547.
- Tinsley, B.M., 1972. Stellar Evolution in Elliptical Galaxies. *ApJ*, 178:319.
- Tody, D., 1986. The IRAF Data Reduction and Analysis System. In D.L. Crawford, editor, *Instrumentation in astronomy VI*, volume 627 of *Society of Photo-Optical Instrumentation Engineers (SPIE) Conference Series*, page 733.
- Topping, M.W., Stark, D.P., Endsley, R., et al., 2022. Searching for Extremely Blue UV Continuum Slopes at  $z = 7-11$  in JWST/NIRCam Imaging: Implications for Stellar Metallicity and Ionizing Photon Escape in Early Galaxies. *ApJ*, 941(2):153.
- Torrey, P., Snyder, G.F., Vogelsberger, M., et al., 2015. Synthetic galaxy images and spectra from the Illustris simulation. *MNRAS*, 447(3):2753.
- Tortorelli, L., McCullough, J., and Gruen, D., 2024. Impact of stellar population synthesis choices on forward modelling-based redshift distribution estimates. *A&A*, 689:A144.
- Trayford, J.W., Lagos, C.d.P., Robotham, A.S.G., et al., 2020. Fade to grey: systematic variation of galaxy attenuation curves with galaxy properties in the EAGLE simulations. *MNRAS*, 491(3):3937.
- Trayford, J.W., Theuns, T., Bower, R.G., et al., 2016. It is not easy being green: the evolution of galaxy colour in the EAGLE simulation. *MNRAS*, 460(4):3925.
- Triani, D.P., Croton, D.J., Sinha, M., et al., 2023. Dust contribution to the panchromatic galaxy emission. *MNRAS*, 519(2):2500.

- Trouille, L., Barger, A.J., and Tremonti, C., 2011. The OPTX Project. V. Identifying Distant Active Galactic Nuclei. *ApJ*, 742(1):46.
- Tully, R.B. and Fisher, J.R., 1977. A new method of determining distances to galaxies. *A&A*, 54:661.
- Turner, M.S., 1999. Large-scale structure from quantum fluctuations in the early universe. *Philosophical Transactions of the Royal Society of London Series A*, 357(1750):7.
- van der Wel, A., Straughn, A.N., Rix, H.W., et al., 2011. Extreme Emission-line Galaxies in CANDELS: Broadband-selected, Starbursting Dwarf Galaxies at  $z < 1$ . *ApJ*, 742(2):111.
- van Haarlem, M.P., Wise, M.W., Gunst, A.W., et al., 2013. LOFAR: The LOw-Frequency ARray. *A&A*, 556:A2.
- Vassiliadis, E. and Wood, P.R., 1994. Post-Asymptotic Giant Branch Evolution of Low- to Intermediate-Mass Stars. *ApJ*, 92:125.
- Verstocken, S., Van De Putte, D., Camps, P., et al., 2017. SKIRT: Hybrid parallelization of radiative transfer simulations. *Astronomy and Computing*, 20:16.
- Vidal-García, A., Plat, A., Curtis-Lake, E., et al., 2024. BEAGLE-AGN I: simultaneous constraints on the properties of gas in star-forming and AGN narrow-line regions in galaxies. *MNRAS*, 527(3):7217.
- Vogelsberger, M., Genel, S., Springel, V., et al., 2014. Introducing the Illustris Project: simulating the coevolution of dark and visible matter in the Universe. *MNRAS*, 444(2):1518.
- Vogelsberger, M., Marinacci, F., Torrey, P., et al., 2020. Cosmological simulations of galaxy formation. *Nature Reviews Physics*, 2(1):42.
- Walcher, J., Groves, B., Budavári, T., et al., 2011. Fitting the integrated spectral energy distributions of galaxies. *Ap&SS*, 331:1.
- Walker, L.M., Butterfield, N., Johnson, K., et al., 2013. The Optical Green Valley versus Mid-infrared Canyon in Compact Groups. *ApJ*, 775(2):129.
- Wall, J.V. and Jenkins, C.R., 2003. *Practical Statistics for Astronomers*, volume 3. Cambridge.
- Wang, B., Leja, J., Atek, H., et al., 2023. Quantifying the Effects of Known Unknowns on Inferred High-redshift Galaxy Properties: Burstiness, the IMF, and Nebular Physics. *arXiv e-prints*, arXiv:2310.06781.

- Wang, L., Gao, F., Best, P.N., et al., 2021. The bright end of the infrared luminosity functions and the abundance of hyperluminous infrared galaxies. *A&A*, 648:A8.
- Wang, Y., Napolitano, N.R., Cui, W., et al., 2022. A stochastic model to reproduce the star formation history of individual galaxies in hydrodynamic simulations. *MNRAS*, 515(3):3249.
- Weingartner, J.C. and Draine, B.T., 2001. Dust Grain-Size Distributions and Extinction in the Milky Way, Large Magellanic Cloud, and Small Magellanic Cloud. *ApJ*, 548(1):296.
- Weisskopf, M., 2000. The Chandra X-Ray Observatory Overview. In *APS April Meeting Abstracts*, APS Meeting Abstracts, page J8.001.
- Wellons, S., Faucher-Giguère, C.A., Anglés-Alcázar, D., et al., 2020. Measuring dynamical masses from gas kinematics in simulated high-redshift galaxies. *MNRAS*, 497(4):4051.
- Wetzel, A., Hayward, C.C., Sanderson, R.E., et al., 2023. Public Data Release of the FIRE-2 Cosmological Zoom-in Simulations of Galaxy Formation. *ApJ*, 265(2):44.
- White, S.D.M. and Rees, M.J., 1978. Core condensation in heavy halos: a two-stage theory for galaxy formation and clustering. *MNRAS*, 183:341.
- Wilkins, S.M., Gonzalez-Perez, V., Baugh, C.M., et al., 2013. Single-colour diagnostics of the mass-to-light ratio - I. Predictions from galaxy formation models. *MNRAS*, 431(1):430.
- Wilkinson, D.M., Maraston, C., Goddard, D., et al., 2017. FIREFLY (Fitting Iteratively For Likelihood analysis): a full spectral fitting code. *MNRAS*, 472(4):4297.
- Williams, W.L., de Gasperin, F., Hardcastle, M.J.H., et al., 2021. The LOFAR LBA Sky Survey: Deep Fields. I. The Boötes Field. *A&A*, 655:A40.
- Witt, A.N. and Gordon, K.D., 2000. Multiple Scattering in Clumpy Media. II. Galactic Environments. *ApJ*, 528(2):799.
- Woodrum, C., Rieke, M., Ji, Z., et al., 2023. JADES: Using NIRCcam Photometry to Investigate the Dependence of Stellar Mass Inferences on the IMF in the Early Universe. *arXiv e-prints*, arXiv:2310.18464.
- Worthey, G., 1994. Comprehensive Stellar Population Models and the Disentanglement of Age and Metallicity Effects. *ApJ*, 95:107.
- Worthey, G. and Dotter, A., 2009. Comparison of alpha-element-enhanced simple stellar population models with milky way globular clusters. *The Astronomical Journal*.

- Wuyts, S., Franx, M., Cox, T.J., et al., 2009. Recovering Stellar Population Properties and Redshifts from Broadband Photometry of Simulated Galaxies: Lessons for SED Modeling. *ApJ*, 696(1):348.
- Wyder, T.K., Martin, D.C., Schiminovich, D., et al., 2007. The UV-Optical Galaxy Color-Magnitude Diagram. I. Basic Properties. *ApJ*, 173(2):293.
- Yan, Z., Li, J., Kroupa, P., et al., 2024. The Variation in the Galaxy-wide Initial Mass Function for Low-mass Stars: Modeling and Observational Insights. *ApJ*, 969(2):95.
- Yang, G., Boquien, M., Brandt, W.N., et al., 2022. Fitting AGN/Galaxy X-Ray-to-radio SEDs with CIGALE and Improvement of the Code. *ApJ*, 927(2):192.
- York, D.G., Adelman, J., Anderson, John E., J., et al., 2000. The Sloan Digital Sky Survey: Technical Summary. *AJ*, 120(3):1579.
- Yuan, F.T., Burgarella, D., Corre, D., et al., 2019. Properties of LBGs with [OIII] detection at  $z \sim 3.5$ . The importance of including nebular emission data in SED fitting. *A&A*, 631:A123.
- Zhang, H.X., Gao, Y., and Kong, X., 2010. Star formation histories within the Antennae galaxies (Arp244). *MNRAS*, 401(3):1839.
- Zhuang, M.Y. and Shen, Y., 2024. Characterization of JWST NIRCcam PSFs and Implications for AGN+host Image Decomposition. *ApJ*, 962(2):139.
- Zinn, P.C., Middelberg, E., Norris, R.P., et al., 2013. Active Galactic Nucleus Feedback Works Both Ways. *ApJ*, 774(1):66.